

2-9-2011

A Critical Evaluation of Computational Fracture Using a Smeared Crack Approach in MPM

Jason Sanchez

Follow this and additional works at: https://digitalrepository.unm.edu/me_etds

Recommended Citation

Sanchez, Jason. "A Critical Evaluation of Computational Fracture Using a Smeared Crack Approach in MPM." (2011).
https://digitalrepository.unm.edu/me_etds/8

This Dissertation is brought to you for free and open access by the Engineering ETDs at UNM Digital Repository. It has been accepted for inclusion in Mechanical Engineering ETDs by an authorized administrator of UNM Digital Repository. For more information, please contact disc@unm.edu.

Jason Sanchez

Candidate

Mechanical Engineering

Department

This dissertation is approved, and it is acceptable in quality and form for publication on microfilm:

Approved by the Dissertation Committee:

Tariq Khraishi

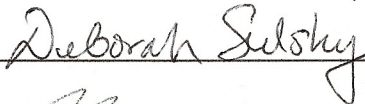


, Chairperson

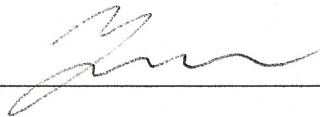
Howard Schreyer



Deborah Sulsky



Yu-Lin Shen



Accepted:

Dean, Graduate School

Date

A Critical Evaluation of Computational Fracture Using a Smeared Crack Approach in MPM

by

Jason Sanchez

B.S., New Mexico Tech, 2000

M.S., University of New Mexico, 2006

DISSERTATION

Submitted in Partial Fulfillment of the
Requirements for the Degree of

Doctor of Philosophy
Engineering

The University of New Mexico

Albuquerque, New Mexico

December, 2010

©2010, Jason Sanchez

Dedication

*To Christine Aurelia Sanchez
May 14, 1932 - November 2, 2008*

Acknowledgments

I would like to thank my advisors and friends, Buck Schreyer and Deborah Sulsky, for their teaching, support, guidance and patience throughout my entire graduate school experience. I would also like to thank Tariq Khraishi and Yu-Lin Shen for all their support and always helpful advise. I would like to acknowledge Professors Arup Maji and Xavier Oliver. I would also like to acknowledge attendees of the weekly group meeting including Kara Peterson, Tyler ("Big T") Baker and Pedro Madrid.

Support of family and friends has been invaluable. I want to say thank you to my dad, Al, stepmom, Sara, brother, Michael, and stepsister, Elisa for their love and moral support. I thank my good friend, Dr. Joe Cormier, for his solidarity. I thank my good friends Tony Silva and Eric Armijo. I also want to thank Melissa Saavedra.

A Critical Evaluation of Computational Fracture Using a Smearred Crack Approach in MPM

by

Jason Sanchez

ABSTRACT OF DISSERTATION

Submitted in Partial Fulfillment of the
Requirements for the Degree of

Doctor of Philosophy
Engineering

The University of New Mexico

Albuquerque, New Mexico

December, 2010

A Critical Evaluation of Computational Fracture Using a Smearred Crack Approach in MPM

by

Jason Sanchez

B.S., New Mexico Tech, 2000

M.S., University of New Mexico, 2006

PhD, Engineering, University of New Mexico, 2010

Abstract

An evaluation of the smeared crack representation of material failure using the material-point method (MPM) as a feasible computational failure approach is performed. The spatial discretization in MPM is defined by a grid of cells that represent space and a set of points that represent the deformable solid. A grid orientation bias in the numerical results is demonstrated. Solution accuracy is lost when failure surface and grid line orientations are not aligned. Causes of the grid orientation dependence are identified, but the problem remains unresolved. Limited use of the smeared crack approach in MPM for solving problems of material failure is advised.

Contents

List of Figures	xi
List of Tables	xvi
1 Introduction	1
2 A Review of Various Computational Material Failure Approaches	4
2.1 Quasi-brittle Material Failure	5
2.2 Modeling Strain Softening in a Continuum	7
2.2.1 Physical Aspects of Strain Softening	7
2.2.2 Mathematical Aspects of Strain Softening	9
2.3 Discrete Constitutive Models	11
2.4 Continuous and Discontinuous Representation of Material Failure . .	15
2.4.1 The Smearred Crack Approach	16
2.4.2 Non-Classical Continuum Descriptions	19
2.4.3 The Embedded Discontinuity Approach	22
2.4.4 Discontinuous Failure Representations	25
3 The Governing Equations	30
3.1 Introduction	31
3.2 The Geometry of Deformation	31
3.3 Representation of Quantities and their Time Derivatives	41

Contents

3.4	Conservation of Mass	46
3.5	Conservation of Momentum	48
3.5.1	Weak Form of the Linear Momentum Balance	52
3.5.2	Strong Discontinuity Kinematics	53
3.5.3	Elastic De-cohesive Constitutive Model for Geological Materials	56
3.5.4	A Continuum Representation of Material Failure	69
3.6	The Initial Boundary Value Problem	71
4	Numerical Modeling with the Material-point Method	73
4.1	Introduction	74
4.2	The Discrete MPM Equations	75
4.3	General Implementation of MPM	81
4.4	Two Dimensional & Axisymmetric Implementation of MPM	84
4.5	Numerical Implementation of the Elastic De-cohesive Constitutive Model	92
5	Evaluation of the Smeared Crack Approach in MPM	106
5.1	Introduction	107
5.2	Case Study Problem: 2-D Elastic De-cohesive Bar in Tension	107
5.2.1	The Analytical Solution	108
5.2.2	Problem Setup and Other Computational Considerations	115
5.3	A Preliminary Study of Mesh Orientation Bias in MPM Results	127
5.4	The Baseline Failure Simulation	130
5.5	Mesh Dependency in Smeared Crack MPM Results	139
5.5.1	The Mesh Orientation Bias	139
5.5.2	Analysis of the Stress Computation	152
5.5.3	Stiffening and Crack Pattern Dispersion Effects	168
5.5.4	Use of Embedded Discontinuities in MPM	185

6 Conclusion	193
A Non-Linear Solution Methods for Implicit Dynamics in MPM	196
A.1 Implicit Solution of Non-linear MPM Equations	197
A.2 GMRES	201
A.3 Evaluation of the Implicit Non-linear Function and its Directional Derivative	211
B Quasi-Static MPM	213
B.1 Governing Equations	214
B.2 The Discrete MPM Equations	215
B.3 Numerical Implementation of Quasi-static MPM	218
B.4 Evaluation of the Implicit Non-linear Function and its Directional Derivative	221
C Preliminary Studies of Fracture Energy Size Effect Simulation	223
C.1 Measurement of Fracture Energy	224
C.2 A Modification to the Classical Multiple Smearred Crack Approach . .	228
C.3 CTS problem Setup in MPM	231
C.4 Simulation of the Ideal Failure of the CTS	234
C.5 Preliminary Results for Fracture Energy Size Effect Simulation	236
References	240

List of Figures

2.1	Illustration of FPZ for ductile (right) and quasi-brittle (left) materials	6
2.2	Discrete crack surface and associated local crack basis	12
2.3	Linear softening law used for a discrete constitutive model	13
3.1	Illustration of a Deformation of a Solid Body	32
3.2	Illustration of a Deformation of a Volume Element	35
3.3	Illustration of a Deformation of an Area Element	38
3.4	Illustration of strong discontinuity kinematics concept	55
4.1	2-D Master Element	85
4.2	Multiple smeared crack concept	99
5.1	Illustration of the elastic de-cohesive tensile bar problem	108
5.2	Illustration of $P - \delta$ response of the elastic de-cohesive tensile bar problem	109
5.3	Baseline ($\alpha = 0^\circ$) MPM configurations of tensile bar problem	117
5.4	MPM configurations of bar problem for $\alpha = 45^\circ$	117
5.5	MPM configuration key	118
5.6	Comparison of the placement of rigid material points for applying velocity boundary conditions	126
5.7	MPM configurations of baseline elastic bar in tension problem . . .	128
5.8	MPM convergence study for the baseline configuration elastic bar . .	128

List of Figures

5.9	Convergence behavior comparison of elastic bar problem in MPM with different α	129
5.10	Baseline MPM configurations of tensile bar with area of weakness . .	133
5.11	Post failure $[[u]]_n/u_0$ plots of tensile bar with area of weakness . . .	133
5.12	MPM solutions of baseline tensile bar problem with area of weakness	134
5.13	Baseline MPM configurations of tensile bar with plane of weakness .	135
5.14	Post failure $[[u]]_n/u_0$ plots of tensile bar with plane of weakness . . .	135
5.15	MPM solutions for baseline tensile bar problem with plane of weakness	136
5.16	Baseline MPM configurations of tensile bar with one weak point . .	137
5.17	Post failure $[[u]]_n/u_0$ plots of tensile bar with one weak point	137
5.18	MPM solutions for baseline tensile bar problem with one weak point	138
5.19	Baseline configuration of tensile bar	143
5.20	$\alpha = 45^\circ$ configuration of tensile bar	143
5.21	P and W_f vs. δ response for baseline tensile bar case	144
5.22	P and W_f vs. δ response for $\alpha = 45^\circ$ tensile bar case	144
5.23	$[[u_n]]/u_0$ for baseline tensile bar case at failure	145
5.24	$[[u_n]]/u_0$ for $\alpha = 45^\circ$ tensile bar case at failure	145
5.25	σ_{xx}/τ_{nf} for baseline tensile bar case during elastic deformation . . .	146
5.26	σ_{nn}/τ_{nf} for $\alpha = 45^\circ$ tensile bar case during elastic deformation . . .	146
5.27	σ_{yy}/τ_{nf} for baseline tensile bar case during elastic deformation . . .	147
5.28	σ_{tt}/τ_{nf} for $\alpha = 45^\circ$ tensile bar case during elastic deformation	147
5.29	σ_{xy}/τ_{nf} for baseline tensile bar case during elastic deformation . . .	148
5.30	σ_{nt}/τ_{nf} for $\alpha = 45^\circ$ tensile bar case during elastic deformation	148
5.31	σ_{xx}/τ_{nf} for baseline tensile bar case during softening	149
5.32	σ_{nn}/τ_{nf} for $\alpha = 45^\circ$ tensile bar case during softening	149
5.33	σ_{yy}/τ_{nf} for baseline tensile bar case during softening	150
5.34	σ_{tt}/τ_{nf} for $\alpha = 45^\circ$ tensile bar case during softening	150
5.35	σ_{xy}/τ_{nf} for baseline tensile bar case during softening	151

List of Figures

5.36	σ_{nt}/τ_{nf} for $\alpha = 45^\circ$ tensile bar case during softening	151
5.37	Illustration of a general pure mode I failure for a single material point in 2-D	153
5.38	Illustration of a pure mode I failure for a single material point in 2-D for $\alpha = 0$	164
5.39	$\alpha = 45^\circ$ configuration of tensile bar with a non-uniform in-cell ma- terial point distribution	171
5.40	$\alpha = 45^\circ$ configuration of tensile bar with a uniform in-cell material point distribution	171
5.41	σ_{nn}/τ_{nf} for $\alpha = 45^\circ$ configuration with a non-uniform in-cell material point distribution during elastic deformation	172
5.42	σ_{nn}/τ_{nf} for $\alpha = 45^\circ$ configuration with a uniform in-cell material point distribution during elastic deformation	172
5.43	σ_{tt}/τ_{nf} for $\alpha = 45^\circ$ configuration with a non-uniform in-cell material point distribution during elastic deformation	173
5.44	σ_{tt}/τ_{nf} for $\alpha = 45^\circ$ configuration with a uniform in-cell material point distribution during elastic deformation	173
5.45	σ_{nt}/τ_{nf} for $\alpha = 45^\circ$ configuration with a non-uniform in-cell material point distribution during elastic deformation	174
5.46	σ_{nt}/τ_{nf} for $\alpha = 45^\circ$ configuration with a uniform in-cell material point distribution during elastic deformation	174
5.47	σ_{nn}/τ_{nf} for $\alpha = 45^\circ$ configuration with a non-uniform in-cell material point distribution during elastic deformation	175
5.48	Convergence behavior comparison of elastic bar problem in MPM with a uniform in-cell material point distribution for different α . . .	176
5.49	Convergence behavior comparison of elastic bar problem in MPM with a non-uniform in-cell material point distribution for different α	176

List of Figures

5.50	P and W_f vs. δ response for $\alpha = 45^\circ$ tensile bar case with a non-uniform in-cell material point distribution	180
5.51	P and W_f vs. δ response for $\alpha = 45^\circ$ tensile bar case with a uniform in-cell material point distribution	180
5.52	$[[u_n]]/u_0$ for $\alpha = 45^\circ$ configuration with a uniform in-cell material point distribution during softening	181
5.53	σ_{nn}/τ_{nf} for $\alpha = 45^\circ$ configuration with a uniform in-cell material point distribution during softening	181
5.54	σ_{tt}/τ_{nf} for $\alpha = 45^\circ$ configuration with a uniform in-cell material point distribution during softening	182
5.55	σ_{nt}/τ_{nf} for $\alpha = 45^\circ$ configuration with a uniform in-cell material point distribution during softening	182
5.56	Close up of $[[u_n]]/u_0$ for $\alpha = 45^\circ$ configuration during softening . . .	183
5.57	Illustration of a compatible deformation of grid cells	183
5.58	Close up of σ_{nt}/τ_{nf} in softening region for $\alpha = 45^\circ$ configuration during softening	184
5.59	Illustration of strong discontinuity kinematics concept	187
5.60	Illustration of the set of elements, \mathcal{J} , intersected by the discontinuity taken from [44]	188
5.61	Illustration of an element with an embedded discontinuity, $e \in \mathcal{J}$	188
C.1	Illustration of Work of Fracture Method for Measuring G_f	225
C.2	Experimental Concrete Fracture Data Taken from Wittmann et. al. 1990 [77]	225
C.3	Idealized tension test of a representative volume of inhomogeneous material to obtain mode I G_f^*	227
C.4	Compact tension specimen geometry [78]	231
C.5	MPM configuration of CTS for $b = 15\text{ cm}$	233
C.6	Ideal CTS failure results for $b = 15\text{ cm}$	236

List of Figures

C.7	P vs. δ response for the ideal CTS failure	238
C.8	P vs. δ response for CTS failure using multiple cracks	238

List of Tables

5.1	Bar problem data	118
5.2	Convergence rate results for elastic tensile bar problem	129
C.1	Compact tension specimen problem data	233
C.2	Results for G_f computed from simulations	239

Chapter 1

Introduction

Chapter 1. Introduction

Valid computational capabilities are necessary for accurately predicting the failure of solid material for a wide range of critical engineering applications. Prediction of quasi-brittle fracture in concrete structures is required for the design of safe and reliable structures. National defense applications require assessments of fragmentation of structures due to impact and blast loading. Simulation of breakages can be used to improve the successful production of parts in certain manufacturing processes. Such capabilities could also provide assessments of landslide danger due to soil instability. A number of computational fracture methods have been applied to the aforementioned problems. These techniques differ from each other by the manner in which material failure is represented. Although some methods have proven successful for solving certain types of problems, there is no standard approach that is applicable to all problems of material failure. Recently, a computational fracture method has been utilized to simulate the formation of leads (cracks) in sea ice as part of a larger climate modeling effort [70], [47]. The particular method employed for this work is a smeared crack representation of material failure using the material-point method (MPM) for solving solid mechanics problems. The focus of the present research is to evaluate the smeared crack approach in MPM as a computational failure method.

Any robust numerical solution method must demonstrate convergence of solutions with respect to the discretization of the spatial domain of the problem. Furthermore, convergence must be observed regardless of how the spatial discretization is structured. MPM incorporates two spatial discretizations. A grid of finite elements represents space and a set of points corresponding to discrete point masses represent a deformable solid body. The goal of this study is to determine whether or not smeared-crack MPM results are independent of the relative orientation between the spatial grid and the body of material points. It is hypothesized that such a dependence does exist based on findings for quasi-brittle fracture applications of the finite element method (FEM) using a smeared crack failure representation [54].

Chapter 1. Introduction

This study demonstrates the existence of a mesh orientation bias in smeared crack MPM results through the use of an elementary case study problem. Results show that accuracy of numerical solutions is only obtained when the orientations of cracks and grid element sides coincide. Further investigation reveals the reason for the preferential behavior to be the inherent compatibility of the deformation imposed by the spatial grid itself. This result presents a serious limitation of the method. In an attempt to remedy the bias in smeared crack MPM results, an embedded discontinuity representation of failure is implemented [41], [44]. However, this approach does not prove to be a useful alternative. Numerical results of embedded discontinuities in MPM share the same general grid orientation bias observed in smeared crack MPM results. Ultimately, use of smeared crack MPM as a computational failure method is cautioned.

Commonly used computational failure methods are discussed in the following chapter. Chapter 3 presents the governing continuum equations used to define the problem of a deformable solid and the specific representation used to model material failure. The numerical implementation of the governing equations is described in chapter 4. A study of computational failure results for smeared crack MPM is presented in chapter 5. Conclusions of the study and a discussion of potential future work are provided in chapter 6.

Preliminary findings of a different study are also presented in appendix C. The objective of this work is to simulate the experimentally observed size effect in mode I fracture energy for concrete using a modified multiple smeared crack material failure representation in MPM. Key differences between classical multiple smeared crack models and the modified multiple smeared crack approach are presented. A physical basis for the modification is postulated and the feasibility of the approach for simulating the size effect is demonstrated.

Chapter 2

A Review of Various Computational Material Failure Approaches

2.1 Quasi-brittle Material Failure

Many geological materials, including concrete, rock and sea ice, are characterized as quasi-brittle material due to the nature of their failure process. The process of quasi-brittle failure is different from that of brittle and ductile materials and is best described in terms of the widely accepted fracture process zone (FPZ) concept [9], [5]. Consider the simple case of mode I failure illustrated in figure 2.1 using a compact tension specimen (CTS) as an example. In general, the tip of a traction free crack is surrounded by a zone of material that behaves nonlinearly. Outside this nonlinear zone the material is considered to be elastic. The FPZ is the region within the nonlinear zone located immediately ahead of a traction free crack in which strain softening occurs. Strain softening is the decrease of stress accompanied by an increase in strain which precedes material failure. Strain softening is the result of localized deformations in the FPZ and is viewed as the direct result of the damage mechanism from which a crack can grow.

The relative size of the FPZ with respect to the structure in question is the key feature for characterizing fracture. Fracture of brittle materials can be characterized by linear elastic fracture mechanics (LEFM) because the nonlinear zone, much less the FPZ, is very small with respect to structure size. A relatively large zone of nonlinear deformation is observed for a ductile material that is almost entirely due to plastic hardening, while the FPZ remains small compared to the structure. Elastic-plastic fracture mechanics encompasses the failure of such materials and defines critical fracture quantities such as the crack tip opening displacement (CTOD) and the J integral. In contrast, the relatively large nonlinear zone observed in quasi-brittle material fracture is almost completely composed of the FPZ.

Experiments have demonstrated the strain softening nature of concrete in direct tension [22], [51], [52]. As a tensile test specimen is loaded using displacement

control the stress-strain response is elastic up to a limit stress. The strain localizes within the FPZ upon continued loading resulting in a gradual decrease of stress with increasing strain. Outside the FPZ elastic unloading occurs. Experimental observations support the commonly held view that the FPZ of concrete is composed of diffuse micro-cracks and crack bridging between matrix and aggregates in front of a traction free macro-crack which follows a tortuous path around aggregate [22], [33], [14], [51]. The gradual decrease in strain is a result of microcracking and the severing of bonds between the matrix and aggregates. The relatively large size of the FPZ in concrete prohibits the use of LEFM as a fracture criterion [26]. This result is supported by comparisons of data from concrete specimens with LEFM predictions [74], [9]. A proper model for quasi-brittle fracture must capture the process of strain softening in the fracture process zone.

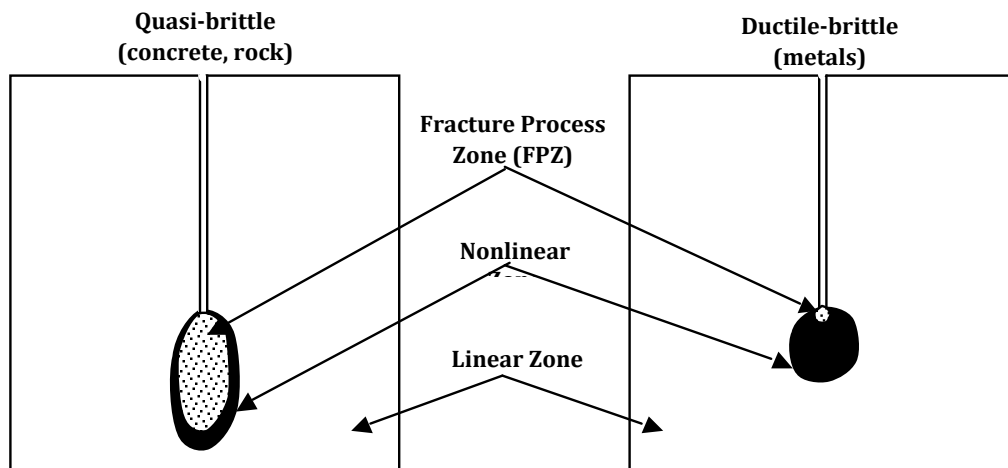


Figure 2.1: Illustration of FPZ for ductile (right) and quasi-brittle (left) materials

2.2 Modeling Strain Softening in a Continuum

Modeling of strain localization in solids is often performed by incorporating strain softening into constitutive models but important considerations for doing so must be accounted for in order to maintain a physically and mathematically meaningful description of the problem.

2.2.1 Physical Aspects of Strain Softening

The modeling of localization by incorporation of strain softening into local constitutive models (stress is purely a function of strain) has been criticized on a physical basis. Simple one-dimensional static analysis has shown that the use of strain softening leads to instability in the sense that work is always done by the structure for a localization zone with an arbitrarily small thickness [3]. Similar conclusions are drawn by examining the properties of the exact solution to one-dimensional wave propagation in a strain softening bar [8]; mainly that localization occurs in a zone of zero volume that absorbs zero energy. These analyses are used to support the claim that strain softening in a classical continuum can not represent real material response. Furthermore, since the results do not depend on the functional form of softening, softening can not be considered a material property of a classical continuum. However, these results are at odds with physical reality because strain softening is observed experimentally for concrete. It is a process that occurs in a localized zone of finite volume and consumes a finite amount of energy. Arguments against the use of strain softening as a material property have also been made on the basis that the experimentally observed strain softening in concrete is a structural effect [50].

The scale at which softening is observed may be material dependent. As mentioned before, the relative size of the strain localization zone (FPZ) with respect to the size of the test sample (such as a compact tension sample in figure 2.1) determines

Chapter 2. A Review of Various Computational Material Failure Approaches

the nature of the observed failure process which leads to different fracture criteria. From a material science point of view, the mechanisms driving localization generally occur on the scale of the material inhomogeneities. On this basis, the contrast in material behavior during failure observed on the scale of laboratory test specimens has led to the different fracture mechanics approaches for different materials. The size of the localization zone for metals is on the scale of millimeters. For geological materials such as concrete the size of the localization zone is on the order of 0.5 m for many applications [7]. Keeping along these same lines, if a concrete structure is very large with respect to the size of the localization zone, then LEFM would be an acceptable fracture criterion [9]. One might expect the opposite effect for very small metallic samples as noted by [59]. This effect of the relative sizes of structure to the FPZ is illustrated by Bazants size effect law [4], which roughly predicts the trend of increased brittleness with increasing structural size. The law, which relates nominal failure strength to structural size for geometrically similar structures for concrete and rock, accounts for the energy consumed in the localization zone. It demonstrates a gradual transition from a constant failure strength criterion for small structures to the LEFM failure criterion for large structures.

The scale of many structural applications of concrete, such as beams and slabs, demands that appropriate modeling techniques somehow incorporate softening behavior. Structural concrete design is not performed at the scale of the localization zone, but the scale of the problem is usually small enough so that the effect of the localization zone (softening) must be accounted for. The question is not whether or not strain softening behavior exists. At a certain scale determined by the material, it is observed. Observation of strain softening on a macroscopic scale is encountered in direct tensile tests for concrete [52]. In these tests the global load-displacement data recorded displays a post peak drop in load, from which a stress-strain curve is directly mapped in the usual engineering way (average stress is obtained by dividing the load by the original cross sectional area and the strain is obtained by dividing

the measured displacement by the original gauge length). The question has to do with whether or not the material can be considered a continuum at the scale of the localization zone. The answer is probably no, but this does not mean that strain softening is a physically meaningless concept for modeling heterogeneous materials (such as concrete) as a homogeneous continuum. The lateral dimension of the localization zone ahead of a crack is on the order of the maximum aggregate size, which is nearly the same size as the representative volume of concrete necessary for averaging micro-stresses over a volume of heterogeneous material to approximate a homogeneous material [9]. This characteristic dimension, which represents the width of the localization zone in which softening occurs, can be regarded as a material property. A physically meaningful context of a strain softening continuum is the modeling of localization in a heterogeneous material that is approximated as a homogeneous material through some representative volume, in which strain softening is permitted and associated with a characteristic width of the localization zone.

2.2.2 Mathematical Aspects of Strain Softening

A strain softening continuum must lead to a sound mathematical description of the problem. Implications of a straightforward incorporation of softening constitutive models into the classical continuum description are known to be associated with the loss of material stability, loss of ellipticity (or hyperbolicity) of the governing partial differential equation (PDE), the appearance of a discontinuity in strain rate (discontinuous bifurcation) or some combination of these things. A summary of the criteria for the appearance of aforementioned issues can be found in [36] and [11]. Stability refers to the continuous dependence of the solution on the problem data such as initial conditions and parameter values. Material stability specifically refers to how stability of the problem changes with respect to the material parameters (i.e. constitutive model). Violation of Hill's postulated local stability criterion, that

Chapter 2. A Review of Various Computational Material Failure Approaches

the second order work remain positive, requires the material tangent tensor to be positive definite [24]. Application of a more mathematically consistent definition of stability, namely that small perturbations of a system lead to small bounded solutions of a system [79], [60], has been shown to require positive definiteness of the acoustic tensor as the criterion for maintaining material stability. Hill's analysis of acceleration waves [25], following the developments of Hadamard in 1903, led to a criterion for the appearance of a discontinuous bifurcation of the strain rate field. A discontinuous bifurcation analysis assumes a kinematically admissible form of the jump in strain rate across a surface that acts as a boundary between material inside and outside a localization zone and continuity of traction across the surface. The resulting criterion for the appearance of a discontinuous bifurcation is that the acoustic tensor lose positive definiteness. This criterion also coincides with loss of ellipticity of the rate boundary value problem [53]. The loss of strong ellipticity was found to be the loss of positive definiteness of the symmetric part of the acoustic tensor [11]. It is generally argued in the literature that the loss of ellipticity (or hyperbolicity) is a critical point in the loading of a solid because the problem becomes ill-posed and ceases to be meaningful in a mathematical sense [65], [21], [60]. Loss of the form of the governing PDE is manifested in finite element simulations of strain softening solids by a lack of convergence of the solution with mesh refinement leading to physically meaningless numerical results [65], [60]. The mesh dependent results display a decrease in energy dissipation with decreasing mesh size because the volume of the localization zone decreases upon mesh refinement. These results support the analytical findings for the one dimensional strain softening case in which the localization zone reduces to a region of zero volume (a surface) that consumes no energy [8]. Much analysis has been performed for obtaining the critical values of softening parameters and orientations associated with discontinuous bifurcation (loss of ellipticity) for specific constitutive models in order to determine their range of applicability or to serve as an indication of material failure initiation [57], [46],

[11], [60], [61]. Loss of ellipticity has been used as a criterion for determining the initiation of localization or failure (discontinuity in displacement) and the orientation of the region of localization (failure surface) [63], [40].

2.3 Discrete Constitutive Models

The nonlinear fracture mechanics approach for capturing the softening associated with quasi-brittle material failure is to incorporate the fracture energy of the material through a cohesive crack model (also known as a discrete constitutive model). The idea of the cohesive crack model was introduced first by the original work of Hillerborg [28] who used the model successfully in finite element simulations.

Discrete constitutive models intend to model the process of localization and failure by idealizing the FPZ (strain localization zone of material softening) as a single plane of material failure, referred to as a failure surface, and defined by the unit normal vector \mathbf{n} . A discontinuity in the displacement field, denoted by $[[\mathbf{u}]]$, develops across the failure surface to model the formation of a crack. Figure 2.2 displays a two dimensional body containing an arbitrarily oriented cohesive crack surface defined by the unit normal and tangent basis vectors, $\{\mathbf{n}, \mathbf{t}\}$. The traction and crack opening displacement are represented in terms of $\{\mathbf{n}, \mathbf{t}\}$ as $\boldsymbol{\tau} = \tau_n \mathbf{n} + \tau_t \mathbf{t}$ and $[[\mathbf{u}]] = [[u_n]] \mathbf{n} + [[u_t]] \mathbf{t}$ respectively. Discrete constitutive models are generally associated with a failure initiation criterion, which predicts the orientation of the failure surface, and a softening law, which describes the process of failure over the failure surface.

For the case of mode I fracture the softening law relates the normal components of $\boldsymbol{\tau}$ and $[[\mathbf{u}]]$ on the cohesive crack surface such that τ_n is a decreasing function of $[[u_n]]$. As an example, a linear softening law is displayed in figure 2.3. Failure initiates on a given surface, defined by \mathbf{n} , when τ_n reaches the ultimate tensile strength of the

material τ_{nf} . Upon subsequent loading, τ_n decreases gradually as $[[u_n]]$ increases. The failure surface retains its traction carrying capability up to a critical value of separation, $[[u_n]] = u_0$, for which $\tau_n = 0$ and the failure surface is considered to be a traction free crack. The softening relationship incorporates the material properties that govern quasi-brittle failure which include the tensile strength, τ_{nf} , the shape of the softening curve and the fracture energy, G_f , which is defined as the area under the softening curve as follows:

$$G_f = \int_0^{u_0} \tau_n du_n \quad (2.3.1)$$

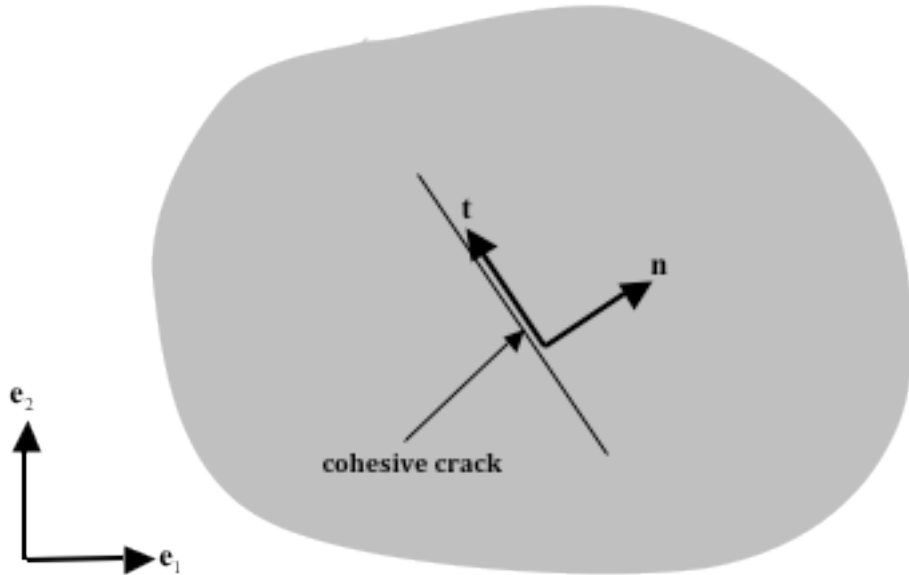


Figure 2.2: Discrete crack surface and associated local crack basis

The use of discrete constitutive models has proved to be a physically realistic method for modeling localization and fracture. Results of finite element analysis incorporating cohesive crack models, whether as a discrete crack or in a crack band, have compared very well to experimental mode I concrete fracture data [28], [9], [56], [54]. Numerical results not only match well to peak load and post peak behavior

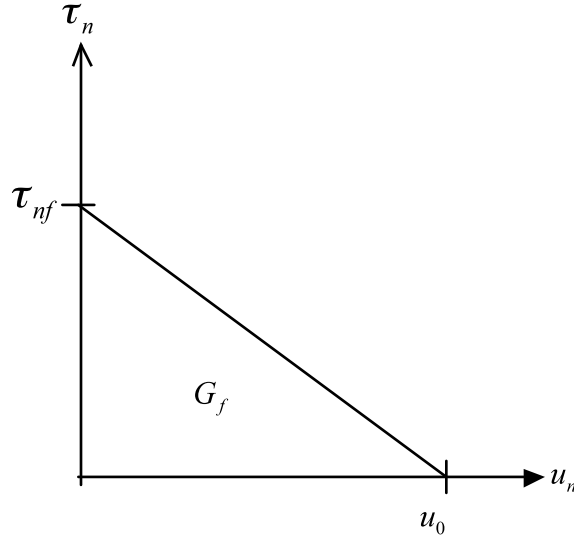


Figure 2.3: Linear softening law used for a discrete constitutive model

but capture the variation of nominal structural strength with the size of the test sample. One especially important consequence of using the fracture energy criterion is the obtainment of mesh independent results with regard to energy consumption. As Wells points out [75], discrete models are more physically realistic from an energy consumption standpoint than continuum softening constitutive models. In a continuum model, the energy dissipated in the localization zone is calculated as an integral over a volume which is zero because the volume of the localization zone in a classical softening continuum is zero. For the case of the discrete model a finite value of energy dissipated in the localization zone is calculated as a surface integral over a discrete failure surface. Thus the fracture energy of a material plays a key role in the appropriate physical model of localization and failure through discrete constitutive models and requires a precise quantification.

The key material properties of quasi-brittle fracture are obtained through experimental and computational means. The ultimate strength can be determined by direct tensile tests. The typical experimental method for obtaining the fracture energy is

Chapter 2. A Review of Various Computational Material Failure Approaches

the direct work of fracture method which initially utilized three-point bend tests of notched concrete beams [48], [49]. In this method G_f is measured to be the area under the load vs. displacement curve divided by the ligament area of the beam. A large comparative study of the work of fracture test method determined that the fracture energy does vary with the size of geometrically similar beams [27]. Similar findings using compact tension specimens indicate a trend of increasing fracture energy with increasing size of the test sample up to a certain size limit after which the value may be constant [78], [77]. This size effect with regard to G_f should be distinguished from the size effect observed in nominal structural strength of concrete (the peak load divided by the ligament area of the beam) [4], [6]. It has been demonstrated that the variation of fracture energy with size has a negligible effect on the calculations of nominal strength because the strength variation with fracture energy is generally less than data scatter observed in strength measurements [27]. This makes sense when considering the success of peak load predictions for geometrically similar samples of different size provided by finite element analysis that employ a single nominal fracture energy value. Wittmann et al. [77] postulate that the fracture energy size effect occurs because the specimen boundaries prevent full development of the FPZ. A similar claim is made by Rots et al. [56]. The shape of softening law is also considered a material property. The most commonly used forms of the softening curve are linear, bilinear or exponentially decaying functions. Numerical means have also been employed to obtain the correct bilinear softening curve parameters [78]. Parameter studies have shown that the form of the softening function has a significant effect on the global response (load vs. displacement) obtained from finite element simulations and merits attention when analyzing a problem [54]. It is appropriate to mention an additional fourth material parameter of crack band width or smearing length, L_c . This length parameter is a characteristic dimension of the softening zone that must be specified explicitly or inferred from the specific material failure representation used for modeling.

Discrete constitutive models take different forms but share the same two elements; a criterion for determining the normal, \mathbf{n} , to the potential failure surface and a criterion for the initiation of failure on that surface. For mode I failure of quasi-brittle materials the classical Rankine criterion is commonly used. The orientation of \mathbf{n} coincides with the direction of maximum principal stress and failure initiates on the failure surface once $\tau_n = \tau_{nf}$, the tensile failure-initiation stress. Other classical criteria include Tresca for mode II failure of ductile materials and Mohr-Columb for mixed mode failure of geological materials. Recently a discrete constitutive model for geological materials has been developed which can predict failure plane orientations for mixed mode failure under triaxial compression in agreement with experimental data for concrete [58]. Discrete models can also be induced from continuum softening models through the strong discontinuity analysis (SDA) [63]. Discrete models obtained using SDA include models of continuum plasticity and damage for applications to concrete structures [40], [41] and finite strain [42]. This approach is used extensively in the different computational failure modeling methods.

2.4 Continuous and Discontinuous Representation of Material Failure

The representation of problems of localization and failure generally fall into one of two categories; continuous or discontinuous. Here, continuous representations are associated with a continuous displacement field. They include the smeared crack approach and non-classical continuum descriptions. Discontinuous representations explicitly incorporate discontinuities (jumps) in the displacement field which represent physical cracks. They employ discrete constitutive models which relate the traction to displacement jump across a failure surface. The overwhelming majority of the numerical implementations of continuous and discontinuous representations

utilize the finite element method, so the computational advantages and disadvantages of the methods are discussed in the context of finite elements unless otherwise stated.

2.4.1 The Smeared Crack Approach

The smeared crack modeling approach utilizes a classical continuum description of the problem. The first successful smeared crack approach is the crack band model [9]. This model was inspired by Hillerborg’s cohesive crack model [28] but idealizes the fracture process zone as a band of a finite width as opposed to a discrete surface. The effect of localization within the band is represented by an inelastic strain contribution. In this approach the effect of failure is “smeared” across the width of the band. A thorough overview of smeared crack models is given by Rots [56], [54], [55]. The essential idea of the smeared crack model is the decomposition of total strain into the sum of material strain and crack strain. The material strain is typically considered to be only the elastic strain but it may also include other non-linear effects such as plasticity [17], [16]. The crack strain is an inelastic strain contribution that models the effect of cracks as failure surfaces with a specific orientation. The relationship between traction and crack strain is formulated in terms of the local failure plane basis, $\{\mathbf{n}, \mathbf{t}\}$ (see figure 2.2). A softening relationship between $\boldsymbol{\tau}$ and $[[\mathbf{u}]]$ is applied on this surface like a discrete constitutive model except $[[\mathbf{u}]]$ is smeared over a characteristic length, L_c (crack band width), as a crack strain. As mentioned before, the characteristic length used in smeared crack models is considered to be a material property, which for concrete, is on the order of the maximum aggregate size [9]. In reality cracks can open during loading and close during unloading. A crack that is in the process of opening or closing is said to be active. The smeared crack approach represents crack opening and closing as an increase and decrease of the crack strain respectively.

Chapter 2. A Review of Various Computational Material Failure Approaches

There are three types of smeared crack models; fixed, multiple and rotating. As the name implies, the fixed smeared crack model assumes a fixed orientation of the crack surface throughout loading. Once a crack has initiated, the axis of principal stress can rotate upon continued loading and the principal stress may exceed the mode I criterion for failure initiation for a different orientation. This drawback for the fixed smeared crack model can be remedied by allowing for multiple non-orthogonal cracks [19], [20], [54]. The multiple smeared crack model allows for more than one crack to initiate. The criterion for initiation of the first mode I crack is the usual Rankine criterion. Subsequent crack initiation is based on the Rankine criterion as well as a threshold angle. The threshold angle is the minimum allowable amount of rotation of the principal stress axis permitted before a new crack can initiate. Each crack surface contributes to the total crack strain. The rotating crack model is obtained in the limit of a zero threshold angle. The three smeared crack models have been evaluated for a combined loading of biaxial tension and shear up to failure and their stress-strain responses compared [54], [55]. As expected, the fixed crack model displays the stiffest response with no shear softening and the least amount of normal traction softening. The multiple smeared crack model was evaluated for several values of threshold angle. The stiffness of the response decreases as the threshold angle decreases. The rotating crack model displayed the least stiff response of all the models. These results demonstrate that the multiple and rotating crack models maintain control over the magnitude of the principal stress for combined loading situations where the axis of principal stress rotates.

Finite element codes commonly employ smeared crack approaches to simulate failure in structures. The computational aspects of the smeared crack representation are well documented [9], [17], [54]. The main issues of numerical analysis using smeared cracks are the lack of independence of results with respect to mesh size and orientation and the so called “stress locking” effect.

Chapter 2. A Review of Various Computational Material Failure Approaches

Numerical smeared crack results display a crack pattern from which a macro-crack path is deduced. These results are typically dependent on the finite element mesh orientation because the cracks prefer to align themselves with the lines of the mesh [56], [54], [35]. This is a very undesirable result from the standpoint of crack path prediction. If the crack path is aligned with the mesh lines, as in the case of uncurved crack paths for symmetrically loaded structures (i.e. three point beam bending, compact tension or direct tension), then there is no problem. For curved crack paths, the effect of the bias can be reduced by selecting specific mesh structures.

The smeared crack model incorporates strain softening in a classical continuum description by confining localization, and therefore energy dissipation, to a band of fixed width. This is critical for overcoming the mesh size dependence observed for classical strain softening constitutive models. It is generally recognized in the literature that the mesh size dependency of results are a manifestation of the ill-posedness of the underlying problem. Although use of the smeared crack representation generally remedies this problem from a computational point of view, the mathematical description is still considered to be ill-posed [65], [21], [18]. Furthermore, it is believed that the previously mentioned mesh orientation bias is also a result of ill-posedness of the governing problem [18]. This claim is probably overstated. Studies suggest that the preferential crack alignment with mesh lines is attributed to the nature of the finite element discretization [56], [54]. The mesh orientation bias was observed to disappear with mesh refinement of quadrilateral elements but not for triangular elements.

Numerical results of smeared crack models typically suffer from stress locking [54]. In many cases of fracture analysis a smeared crack pattern is meant to represent a traction free macro-crack. However, upon failure of the structure, stresses have been observed to build up across the failure surface represented by the smeared crack pattern. These locked in stresses in a supposedly failed structure are nonphysical

because they are inconsistent with traction free crack surface conditions. This problem, referred to as “stress locking” or spurious stiffening, is associated with curved crack paths in smeared crack analysis. Stress locking is caused by displacement compatibility between adjacent elements inside and outside of the localization zone. Solutions in which stress locking is encountered display stiff global load-displacement responses. Although the degree of problem varies with the type of smeared crack model used (fixed, multiple or rotating), the problem persists due to the fact that the kinematics of the failure surfaces are inadequately represented in the computational approach (finite elements). The issue of spurious stiffening is a serious limitation of smeared crack representation using finite elements and is a focus of the present research using MPM.

The smeared crack method has been successful for analyzing localization and failure for a number of problems but remains highly criticized. Implementation of the method is straightforward and can be done with minimal changes to existing codes. Use of the smeared crack approach eliminates the mesh size dependence of numerical results encountered for classical continuum softening models. The method has also been validated through good experimental data comparisons. Limitations based on mesh orientation bias and stress locking are clearly unacceptable computational disadvantages, but the dominant criticism is the potential ill-posedness of the underlying continuum problem. In an attempt to remedy this problem non-classical continuum theories have been developed for which the governing PDE form is maintained for strain softening.

2.4.2 Non-Classical Continuum Descriptions

The main goals of the development of non-classical continuum descriptions are to maintain the governing form of the partial differential equation (elliptic for the static case or hyperbolic for dynamic loading) in the presence of strain softening and model

Chapter 2. A Review of Various Computational Material Failure Approaches

zones of highly localized deformation. Several different models have been developed and essentially all models are a result of a change in the form of the constitutive model relating stress to strain based on phenomenological arguments of material behavior. Within each model a length parameter characterizing the width of the localization zone is introduced explicitly or implicitly. The specific non-classical continuum models described here are the non-local, gradient and Cosserat models. An overview of the models and their computational aspects are available [65], [21].

Non-local continuum models are based on constitutive models for which stress is not a function of the local strain but the spatial distribution of strain. The model is physically based on the premise that the interaction of microstructural defects that take place in a zone of localization is a non-local process. The internal variable (equivalent plastic strain, damage variable, etc.) is averaged as a weighted integral over the spatial domain in which a characteristic length is explicitly specified. This approach generally leads to governing equations that remain elliptic during softening for mode I or mode II type localization. Additional computational expenses are added for carrying out the proper evolution of the internal variable. Questions still remain regarding proper boundary conditions for the non-local approach. Recently a non-local continuum damage model has been used in an attempt to capture the fracture energy size effect trend observed in experiments [31]. Use of a non-local damage model for providing this effect is based on the postulate that the boundary of small specimens inhibits full development of the localization zone [77]. The idea is that non-local models will naturally take the proximity of the boundary into account due to the spatially averaged nature of the deformation. Numerical results of this study show that the trend of increasing fracture energy with increasing structure size can be simulated using a non-local damage model.

Gradient models, like non-local model, are physically based on the non-local microstructural argument of localization. However, the non-local effect is produced by

Chapter 2. A Review of Various Computational Material Failure Approaches

stress as a function of spatial gradients of strain. Additional spatial derivative terms enter into the governing equations which maintain elliptic and hyperbolic forms for static and dynamic problems respectively. The width of the localization zone is explicitly specified in the constitutive model. The resulting discrete system of equations incorporates the internal variable as a global unknown to be solved along with nodal displacements. Additional non-standard boundary conditions are also introduced. In general, gradient models are able to reproduce localization behavior in a continuum. The numerical results of one-dimensional bar problems illustrate their performance for static and dynamic cases [59], [65], [21]. Convergence of a solution with mesh refinement is observed and localization within the specified band is represented along with predefined stress-displacement curve. Results also display the increased brittleness in the structural response as the ratio of the localization zone width to structure size decreases.

The Cosserat (micro-polar) continuum model is physically based on the idea of microstructure interaction in a material [15]. The departure from classical continuum theory is the additional kinematic quantity of micro-rotation. A microelement of material is acted on by normal, shear and bending stresses that are related to normal, shear and curvature strains through an elasticity tensor. Two additional elastic constitutive parameters are introduced; a rotational shear modulus and a length parameter that relates couples and curvatures. The length parameter provides the internal length scale necessary for modeling localization. Inelastic constitutive models in Cosserat theory are applied much the same way as with classical continuum models. When strain softening models are used, loss of form of the governing equations generally depends on the loading [65]. By applying the proper kinematic restrictions for mode I loading, Sluys [65] shows that the governing dynamic equations reduce to the classical softening continuum description for which the form of the governing PDE is lost. Numerical simulations of a strain-softening Cosserat continuum for mode II loading do result in converged solutions that are able to capture localized

deformation indicating that the method is only adequate for modeling localization in shear.

For the most part, the non-classical continuum descriptions discussed have been successful for modeling localization while maintaining the form of the governing PDE but have definite shortcomings. The most apparent disadvantage compared to the smeared crack approach is the increased computational cost. All discrete non-classical continuum models introduce more degrees of freedom which incur a higher computational expense than smeared crack models. Additional cost is unavoidable because the appropriate modeling of localized deformation requires highly refined meshes in order to capture high strain gradients. The high computational cost alone can be prohibitive for practical use of the methods. Uncertainty of how to handle the additional boundary conditions introduced in non-local and gradient methods also brings up doubt as to the validity of results.

2.4.3 The Embedded Discontinuity Approach

A widely used method for representing localization and failure is that of embedded discontinuities. The embedded discontinuity model is intimately related to the finite element method, so much, that it is difficult to separate modeling and computational aspects. An overview and comparison of embedded discontinuity models is provided by Jirasek [30]. Generally speaking, the kinematic description of a standard finite element is enriched by an extra degree of freedom in order to represent a zone of localization or discontinuity (jump) in displacement. This degree of freedom is embedded in the element which is assumed to be crossed by a single band of localization (softening) or a plane of discontinuity (crack). The majority of embedded discontinuity models are based on the three-node constant strain triangle element or four-node bilinear elements (in two dimensions). Two basic forms of embedded discontinuity models are available; symmetric and unsymmetric, which refer to the

Chapter 2. A Review of Various Computational Material Failure Approaches

resulting symmetric and unsymmetric forms of the discrete system of equations for the finite element approximation. Different methods, consistent with standard finite element formulations, have been used to arrive at the various embedded discontinuity models. The weak form of the governing equations originates from variational principles such as the three-field (displacement, stress and strain) Hu-Washizu principle or the virtual work principle. The main differences between models lie in the different kinematic and traction continuity assumptions made at the element level of the formulation.

In symmetric approaches an enrichment of the standard element interpolation basis is made for either the strain [10] or displacement [41]. Either choice results in a different internal equilibrium condition and kinematic representation of the localization band or the discontinuity. The element equilibrium condition relates the traction within the localization band or over the discontinuity surface to the internal forces in the remaining element volume. If strain enrichment is chosen (statically optimal symmetric formulation) a suitable element equilibrium relation is obtained and equilibrium is guaranteed. However, the kinematics of the discontinuity is not properly represented because free relative motion of element pieces separated by a discontinuity is restricted. On the other hand, if displacement enrichment (kinematically optimal formulation) is used the resulting internal equilibrium conditions do not guarantee continuity of traction across a displacement jump or localization band, but the appropriate kinematic description of an element crossed by a discontinuity is maintained.

The nonsymmetric embedded discontinuity model (statically and kinematically optimal nonsymmetric formulation) remedies the problems encountered in both symmetric formulations. Simo and Oliver developed this method in the assumed enhanced strain (AES) framework [63], [41], [44], [64]. A discontinuity within an element is modeled by introducing an additional term into the standard finite element approx-

Chapter 2. A Review of Various Computational Material Failure Approaches

imation of displacement over a single element containing a Heaviside function (step function). The additional degree of freedom representing a jump in displacement (or high strain gradient) is introduced at the element level. The resulting strain in an enriched element is composed of a regular (continuous) component and a singular component. The singular part of strain is an incompatible mode that is interpreted in a distributional sense as a Dirac delta function acting over the surface of discontinuity. The admissible displacement variation is approximated by a function from a space that does not include a discontinuity. The Petrov-Galerkin approach is used since different basis functions are used for displacement and displacement variation. The resulting set of non-symmetric equations reflects satisfaction of the weak form of the internal equilibrium equation with boundary conditions and the strong form of traction continuity condition across the line of discontinuity or localization band. The best part of both symmetric embedded models is obtained because enrichment of the displacement allows for the relative motion between element pieces separated by a discontinuity while traction continuity across the discontinuity is enforced.

For any embedded discontinuity model certain aspects of implementation must be considered which affect performance. Discussions of important issues such as solution method, numerical integration and crack path continuity are available [41], [75]. An additional degree of freedom per element that represents localization or displacement jump is introduced into the formulation as an unknown. If the AES format is utilized then the additional degree of freedom can be solved at the element level and does not enter into the global set of equations. In this case static condensation of the global set of equations is used to solve for the continuous part of nodal displacements first. The additional degrees of freedom are then solved separately at the element level which saves computational cost if the crack path is confined to a relatively small number of elements. The information required for the set of cracked elements includes the orientation of the crack normal and the element sides crossed by the crack. A new element must be added to this set when the crack initiation criterion is met within

the element. The criteria for initiation and crack surface orientation are determined from the particular discrete constitutive model used. If crack path continuity across inter-element boundaries is desired, then an additional crack front tracking algorithm is necessary.

Embedded discontinuity approaches offer some improvement over the smeared crack representation of failure but retain some of the same numerical performance issues. Unlike smeared models, from which a macrocrack must be deduced from a smeared crack pattern, crack path continuity can be enforced via a crack front tracking algorithm [41]. However, crack path continuity is only possible in two dimensions and restricts the crack initiation to elements directly ahead of the crack tip. Consequently the failure initiation criteria can be violated in other elements away from the path resulting in a non-physical stress build up and the results can be sensitive to the mesh structure [75]. The stress locking (spurious stiffening) observed in smeared crack analysis of curved crack paths is overcome if the nonsymmetric embedded model is utilized [44]. The use of the statically optimal symmetric embedded model does result in stress locking due to an inappropriate kinematic representation of the discontinuity through an element. However, embedded models that maintain symmetry and reduce stress locking have been developed [44]. The result of mesh alignment bias of failure surfaces does persist for the embedded discontinuity model. In this respect the behavior of the nonsymmetric embedded model without crack continuity and the classical smeared crack model have been shown to behave almost identically [35].

2.4.4 Discontinuous Failure Representations

Discontinuous models of failure explicitly represent discontinuities in the displacement field. In general, they employ discrete constitutive models that relate traction to displacement jump across a failure surface. The difference between these models

Chapter 2. A Review of Various Computational Material Failure Approaches

resides in how the discontinuity is represented in the computational method, so it is more appropriate to talk about the different discontinuous computational failure methods. The appeal of discontinuous methods is their ability to represent the physical reality of a crack as a geometrical discontinuity in a solid. The three methods discussed are the use of interface elements, re-meshing, and the partition of unity method (PUM).

The first discontinuous approaches involved the use of zero thickness interface elements placed along inter-element boundaries [37], [23]. For concrete fracture the discrete constitutive model (traction vs. displacement) is applied across the interface element to model localization and fracture while regular elements in the mesh remain elastic. A cohesive crack model for concrete fracture was first successfully applied using interface elements [28]. A summary and comparison of continuous and lumped interface elements is provided by Rots [54]. For continuous interface elements the displacement over the surface separating two adjacent element faces (sides) varies as a continuous function over the faces. In contrast, the lumped interface element treats the displacement between two element faces as a constant vector quantity over the surface. In a comparison study of continuous and lumped approaches the response of an undamaged structure loaded in mode I is studied for various constant different dummy stiffness values for the interface elements. The lumped element is shown to behave better than its continuous counterpart because its response approached the completely rigid response of the structure (no interface elements) as the dummy stiffness increased. This was not the case for the continuous interface element and caution should be taken for relatively high stiffness values. The use of interface elements for modeling fracture has proved to be successful overall and is commonly used for fracture modeling at the macro scale [54] and micro scale [13]. Curved mode I fracture of concrete compares well to test data and does not exhibit the stress locking encountered in classical smeared methods since the discontinuity is modeled explicitly [54]. The downside of using interface elements is that the macro crack trajectory

Chapter 2. A Review of Various Computational Material Failure Approaches

is restricted to follow the element boundaries. Consequently the results are always mesh dependent. Theoretically a refined mesh (or at least locally refined mesh) is needed to accurately capture the crack path. For predetermined crack paths interface elements are only placed at the necessary locations. If the crack trajectory is unknown a priori, which is usually the case, interface elements can be placed between the shared edges of all elements. This can become computationally expensive as more global degrees of freedom are added to the discrete system of equations.

Discontinuous computational methods based on automatic mesh generation have also been utilized. Like the interface element method, cracks are confined to element boundaries but the mesh structure changes throughout the computation to accommodate the changing crack path. The discontinuity is the result of the changing mesh structure. The advance of a crack is accomplished by combining the prediction of the change in crack face orientation and crack length increment with a re-meshing procedure. The re-meshing only needs to be done locally near the crack tip. Ingraffea and Saouma [29] have successfully used this method to predict crack trajectories in concrete using LEFM. In this study the crack path discovered in the Fontana Dam was closely simulated. The large structural size of the dam allowed for the use of LEFM as a concrete fracture criteria and re-meshing near the crack tip required the use of singularity elements to properly capture the stress field. Ortiz and Pandolfi have also used similar approach to accurately reproduce crack trajectory results in a simulation of a drop-weight dynamic fracture test [45]. The drawback of the method is the complicated implementation of the automated meshing procedure and the potentially high computational cost of re-meshing many times throughout the course of the simulation.

Within the past decade a discontinuous fracture method known as the partition of unity method (PUM) or the extended finite element method (X-FEM) has been developed and applied successfully to fracture problems. The method exploits the

partition of unity property of interpolation polynomials used in finite element approximations by incorporating an enhancement to the underlying standard basis functions [1]. The enhancements are generally functions that provide desired properties to the approximate solution and are associated with additional degrees of freedom at the nodes. Since enrichment is provided at the nodes the enhancements to the solution takes place over the support of a node, thereby affecting the solution locally over elements overlapped by the support. The additional degrees of freedom are global unknowns and are added to a given node as needed throughout a computation. The solution enhancement to FEM for fracture problems is a discontinuous function (Heaviside function). The resulting PUM exhibits significant improvement over the mesh dependence shortcomings of the previously mentioned discontinuous computational methods. Not only can a discontinuity cross through elements and element boundaries but the displacement jump along the discontinuity is a continuous function of the same polynomial order as the finite element. The formulation of the discrete equations from the weak form of the governing equation and boundary conditions follows the standard FEM procedure. The difference is that the trial and test functions (displacement and its variation) contain a discontinuity. The strain is interpreted in a distributional sense as a Dirac delta function acting along the discontinuity so the weak form contains terms which are integrals over the discontinuity. The Galerkin method is applied to preserve symmetry for the cases of symmetric material tangent modulus. Details of the PUM formulation are provided by Wells and Sluys [76], [75]. Fracture prediction results that utilize the PUM have compared well to experimental observations and known analytical solutions. The method has been used to model elastic crack growth for which the solution contains additional enhancements of near-crack tip asymptotic solutions [34]. Discrete constitutive models have been applied to PUM fracture simulations for static and dynamic cases [76], [75]. In the latter study mesh independence of results are demonstrated with respect to mesh size and mesh line orientation.

Chapter 2. A Review of Various Computational Material Failure Approaches

The PUM does come with its own special computational aspects and disadvantages. Important issues regarding implementation include discontinuity propagation, tracking of the crack tip, the criteria for enhancing individual nodes and the proper computation of the crack orientation from the stress field [75]. One particularly important aspect is the integration of an element crossed by a discontinuity. Usually, the element is subdivided on both sides of the crack into sub-elements that are numerically integrated. Gauss points must also lie on the discontinuity in order to evaluate the surface or line integrals. Although the PUM has proved to be relatively superior with respect to mesh independence of results, it is necessary to use locally refined meshes in cracked areas in order to adequately predict crack trajectories. The two biggest drawbacks of the method are the complex implementation and the increased computational cost associated with the additional degrees of freedom.

Chapter 3

The Governing Equations

3.1 Introduction

The governing equations of a deformable solid continuum are presented. The kinematics of deformation is covered in section 3.2. Some preliminary mathematical considerations for forming conservation laws are discussed in section 3.3. The conservation of mass is derived in section 3.4. Section 3.5 provides derivations of the conservation of linear and angular momentum. Since material failure is of primary interest, the kinematic representation of discontinuities in a displacement field are given in section 3.5.2. The kinetic relationship presented in section 3.5.3 is the specific discrete constitutive model for material failure used for the present research. Section 3.5.4 discusses the representation of a discontinuous displacement field in a continuum for purposes of modeling failure. Section 3.6 summarizes the complete set of equations that define problem, from which the discrete equations are formed and solved numerically.

3.2 The Geometry of Deformation

The continuous deformation of a solid medium is considered. The two configurations of a deformable body displayed in figure 3.1 represent the same solid body of material points at two instances in time, denoted by $t \in \mathbb{R}^+$. The initial or reference configuration of the body, at which $t = 0$, is a set of points $\Omega_0 \in \mathbb{R}^3$. The position vector of a material point in the initial configuration is denoted by $\mathbf{X} \in \Omega_0$. At some time, $t > 0$, the body has deformed relative to its initial state. This deformed state is referred to as the current or spatial configuration of the body, and is represented by the set of points denoted as $\Omega \in \mathbb{R}^3$. The position vector of a material point in the current configuration is denoted by $\mathbf{x} \in \Omega$. The vectors, \mathbf{X} and \mathbf{x} , represent the position of material point at different times (see Figure 3.1). A one to one mapping exists between the material point positions such that $\mathbf{x} = \mathbf{x}(\mathbf{X}, t)$ and $\mathbf{X} = \mathbf{X}(\mathbf{x}, t)$. Initially

(at $t = 0$), $\mathbf{X} = \mathbf{X}(\mathbf{x}, 0)$. The sets of basis vectors, $\{\mathbf{E}_1, \mathbf{E}_2, \mathbf{E}_3\}$ and $\{\mathbf{e}_1, \mathbf{e}_2, \mathbf{e}_3\}$, are associated with the reference and deformed configuration respectively.

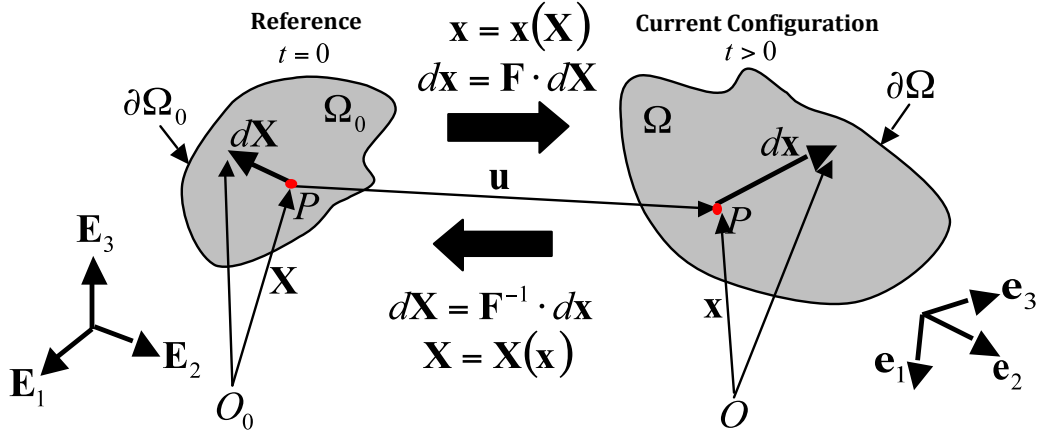


Figure 3.1: Illustration of a Deformation of a Solid Body

In terms of the their respective basis the initial and current positions of a material point are

$$\mathbf{X} = X_A \mathbf{E}_A \quad (3.2.1)$$

and

$$\mathbf{x} = x_i \mathbf{e}_i \quad (3.2.2)$$

where X_A represents the coordinates of \mathbf{X} with respect to the $\{\mathbf{E}_1, \mathbf{E}_2, \mathbf{E}_3\}$ basis, x_i represents the coordinates of \mathbf{x} with respect to the $\{\mathbf{e}_1, \mathbf{e}_2, \mathbf{e}_3\}$ basis and the summation convention is used for $A, i = 1, 2, 3$. When describing vectors in terms of coordinates and basis vectors, capitalized subscripts denote coordinates of the $\{\mathbf{E}_1, \mathbf{E}_2, \mathbf{E}_3\}$ basis and lower case subscripts denote coordinates with respect to the $\{\mathbf{e}_1, \mathbf{e}_2, \mathbf{e}_3\}$ basis. To emphasize the functional relationships of the vectors $\mathbf{x} = \mathbf{x}(\mathbf{X}, t)$ and $\mathbf{X} = \mathbf{X}(\mathbf{x}, t)$ equations (3.2.1) and (3.2.2) are expanded as follows:

$$\mathbf{X} = X_1(x_1, x_2, x_3, t) \mathbf{E}_1 + X_2(x_1, x_2, x_3, t) \mathbf{E}_2 + X_3(x_1, x_2, x_3, t) \mathbf{E}_3 \quad (3.2.3)$$

Chapter 3. The Governing Equations

$$\mathbf{x} = x_1(X_1X_2, X_3, t)\mathbf{e}_1 + x_2(X_1X_2, X_3, t)\mathbf{e}_2 + x_3(X_1X_2, X_3, t)\mathbf{e}_3 \quad (3.2.4)$$

Consider an infinitesimal material fiber segment in the reference configuration, denoted by the vector $d\mathbf{X}$, which deforms into the vector $d\mathbf{x}$ in the current configuration (see figure 3.1). The relationship between the differentials is

$$d\mathbf{x} = \nabla_0\mathbf{x} \cdot d\mathbf{X} \quad (3.2.5)$$

where the operation ∇_0 indicates a gradient of a quantity with respect to the components in the initial configuration X_A ($A = 1, 2, 3$). The deformation gradient is defined to be

$$\mathbf{F} = \nabla_0\mathbf{x} \quad (3.2.6)$$

Equation (3.2.4) is substituted into (3.2.6) to give \mathbf{F} in terms of its components. The result is

$$\mathbf{F} = \frac{\partial x_i}{\partial X_A} \mathbf{e}_i \otimes \mathbf{E}_A \quad (3.2.7)$$

where \otimes denotes the tensor product and $\mathbf{e}_i \otimes \mathbf{E}_A$ is the mixed second order tensor basis. Equation(3.2.5) is rewritten using (3.2.6) to obtain

$$d\mathbf{x} = \mathbf{F} \cdot d\mathbf{X} \quad (3.2.8)$$

The deformation gradient \mathbf{F} is a second order tensor that maps vectors embedded in the material from the reference configuration to the deformed configuration. A deformed material segment is mapped to the same reference segment as follows:

Chapter 3. The Governing Equations

$$d\mathbf{X} = \nabla\mathbf{X} \cdot d\mathbf{x} \quad (3.2.9)$$

In equation(3.2.9) the operation ∇ indicates the gradient of a quantity with respect to the spatial components of position in the current configuration x_i . It follows from equations (3.2.8) and (3.2.9) that

$$\mathbf{F}^{-1} = \nabla\mathbf{X} \quad (3.2.10)$$

and

$$\mathbf{F}^{-1} = \frac{\partial X_A}{\partial x_i} \mathbf{E}_A \otimes \mathbf{e}_i \quad (3.2.11)$$

Similarly, \mathbf{F}^{-1} maps material line segments from the current configuration to the reference configuration as follows:

$$d\mathbf{X} = \mathbf{F}^{-1} \cdot d\mathbf{x} \quad (3.2.12)$$

It is important to note that existence of the one-to-one mapping $\mathbf{x} = \mathbf{x}(\mathbf{X}, t)$ and $\mathbf{X} = \mathbf{X}(\mathbf{x}, t)$ requires that \mathbf{F}^{-1} exists. An equivalent requirement is

$$J = \det(\mathbf{F}) \neq 0 \quad (3.2.13)$$

Since $\det(\mathbf{F}) \neq 0$, we can assume without loss of generality that $\det(\mathbf{F}) > 0$.

Figure 3.2 illustrates the deformation of a differential volume element of material. In the reference configuration the volume element is a box defined by the line segments $d\mathbf{X}_1$, $d\mathbf{X}_2$ and $d\mathbf{X}_3$. The differential volume in the reference configuration dV_0 is computed as follows:

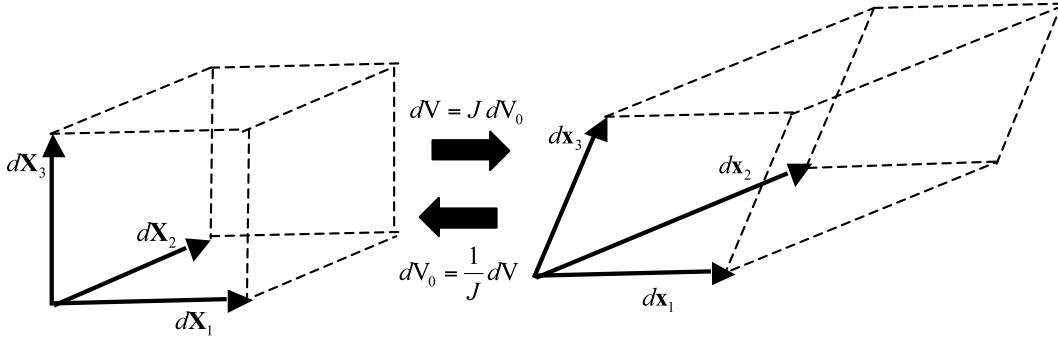


Figure 3.2: Illustration of a Deformation of a Volume Element

$$dV_0 = d\mathbf{X}_1 \cdot (d\mathbf{X}_2 \times d\mathbf{X}_3) \quad (3.2.14)$$

In the current configuration the box has deformed into a parallelepiped that is defined by the deformed line segments dx_1 , dx_2 and dx_3 . The volume of the deformed element dV is

$$dV = d\mathbf{x}_1 \cdot (d\mathbf{x}_2 \times d\mathbf{x}_3) \quad (3.2.15)$$

Equation (3.2.8) is substituted into equation (3.2.15). The result is

$$dV = \mathbf{F} \cdot d\mathbf{X}_1 \cdot (\mathbf{F} \cdot d\mathbf{X}_2 \times \mathbf{F} \cdot d\mathbf{X}_3) \quad (3.2.16)$$

For any second order tensor \mathbf{B} , and vectors \mathbf{u} , \mathbf{v} and \mathbf{w} the determinant of \mathbf{B} is defined by the following identity:

$$\det(\mathbf{B})\mathbf{u} \cdot (\mathbf{v} \times \mathbf{w}) = \mathbf{B} \cdot \mathbf{u} \cdot (\mathbf{B} \cdot \mathbf{v} \times \mathbf{B} \cdot \mathbf{w}) \quad \forall \mathbf{u}, \mathbf{v}, \mathbf{w} \quad (3.2.17)$$

Using the identity in equation (3.2.17) and equation (3.2.13), equation (3.2.16) becomes

Chapter 3. The Governing Equations

$$dV = JdV_0 \quad (3.2.18)$$

which states that the change in differential volume from the initial and current configurations is related by J . Since volume is always a positive quantity, J is also required to be positive. In the context of describing a deformation the restriction on J is

$$J = \det(\mathbf{F}) > 0 \quad (3.2.19)$$

The change in differential surface area is illustrated in 3.3. The surface area element in the reference configuration is a square defined by the material fiber segments $d\mathbf{X}_1$ and $d\mathbf{X}_2$. The differential area of the element in the initial configuration is considered to be a vector quantity $d\mathbf{A}_0$ defined as follows:

$$d\mathbf{A}_0 = \mathbf{N}_0 dA_0 = d\mathbf{X}_1 \times d\mathbf{X}_2 \quad (3.2.20)$$

In (3.2.20) \mathbf{N}_0 is a unit normal vector perpendicular to the area element and dA_0 is the magnitude of $d\mathbf{A}_0$. Alternatively, dA_0 is

$$dA_0 = \mathbf{N}_0 \cdot (d\mathbf{X}_1 \times d\mathbf{X}_2) \quad (3.2.21)$$

In the current configuration the area element deforms into a parallelogram defined by the deformed differential line segments $d\mathbf{x}_1$ and $d\mathbf{x}_2$. The deformed differential area element $d\mathbf{A}$ is expressed as follows:

$$d\mathbf{A} = \mathbf{n}dA = d\mathbf{x}_1 \times d\mathbf{x}_2 \quad (3.2.22)$$

Chapter 3. The Governing Equations

In (3.2.22), \mathbf{n} is the unit normal vector perpendicular to the area element and dA is the magnitude of $d\mathbf{A}$ which is expressed as follows:

$$dA = \mathbf{n} \cdot (d\mathbf{x}_1 \times d\mathbf{x}_2) \quad (3.2.23)$$

Substitution of (3.2.8) into (3.2.23) results in the following expression for $d\mathbf{A}$:

$$d\mathbf{A} = \mathbf{n}dA = (\mathbf{F} \cdot d\mathbf{X}_1) \times (\mathbf{F} \cdot d\mathbf{X}_2) \quad (3.2.24)$$

The inner product of the vector $\mathbf{F} \cdot \mathbf{N}_0$ with equation (3.2.24) is made and the following manipulations are performed:

$$\begin{aligned} (\mathbf{F} \cdot \mathbf{N}_0) \cdot \mathbf{n}dA &= (\mathbf{F} \cdot \mathbf{N}_0) \cdot (\mathbf{F} \cdot d\mathbf{X}_1) \times (\mathbf{F} \cdot d\mathbf{X}_2) \\ &= \det(\mathbf{F})\mathbf{N}_0 \cdot (d\mathbf{X}_1 \times d\mathbf{X}_2) \\ &= J\mathbf{N}_0 \cdot (d\mathbf{X}_1 \times d\mathbf{X}_2) \\ &= J\mathbf{N}_0 \cdot (\mathbf{N}_0 dA_0) \end{aligned} \quad (3.2.25)$$

The final result in (3.2.25) is restated to be

$$(\mathbf{N}_0 \cdot \mathbf{F}^T) \cdot d\mathbf{A} = J\mathbf{N}_0 \cdot d\mathbf{A}_0 \quad (3.2.26)$$

Since (3.2.26) holds for all \mathbf{N}_0 , the differential area elements in the reference and current configurations are related as follows:

$$d\mathbf{A} = J\mathbf{F}^{-T} \cdot d\mathbf{A}_0 \quad (3.2.27)$$

The expression in equation (3.2.27) is referred to as Nanson's relation, for which $\mathbf{F}^{-T} = (\mathbf{F}^T)^{-1}$.

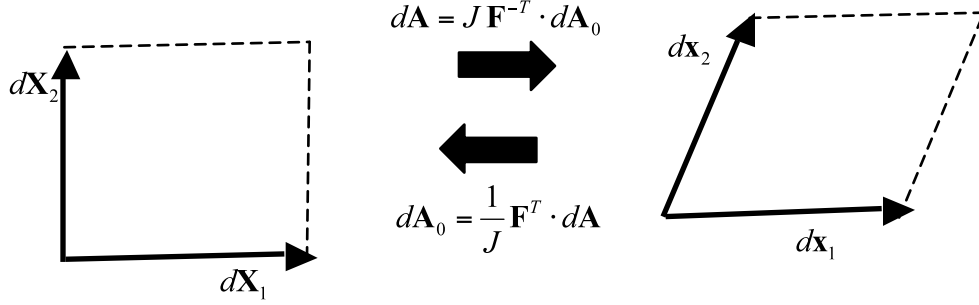


Figure 3.3: Illustration of a Deformation of an Area Element

Strain measures are generally expressed in terms of \mathbf{F} . Two common measures of strain are discussed here; the Lagrangian (or material) strain tensor, \mathbf{E} , and the Eulerian (or spatial) strain tensor, $\boldsymbol{\varepsilon}$. Consider only the lengths of the material fiber segments $dS_0 = |d\mathbf{X}|$ and $ds = |d\mathbf{x}|$ in the reference and current configurations respectively. The difference between the squares of dS_0 and ds serve as a measure of relative deformation and is expressed as the following:

$$ds^2 - dS_0^2 = d\mathbf{x} \cdot d\mathbf{x} - d\mathbf{X} \cdot d\mathbf{X} \quad (3.2.28)$$

When equation (3.2.28) is expressed in terms of the reference material segment $d\mathbf{X}$ using (3.2.8) the result is

$$\begin{aligned} ds^2 - dS_0^2 &= (\mathbf{F} \cdot d\mathbf{X}) \cdot (\mathbf{F} \cdot d\mathbf{X}) - d\mathbf{X} \cdot d\mathbf{X} \\ &= (d\mathbf{X} \cdot \mathbf{F}^T) \cdot (\mathbf{F} \cdot d\mathbf{X}) - d\mathbf{X} \cdot d\mathbf{X} \\ &= d\mathbf{X} \cdot [\mathbf{F}^T \cdot \mathbf{F} - \mathbf{I}] \cdot d\mathbf{X} \\ &= 2d\mathbf{X} \cdot \mathbf{E} \cdot d\mathbf{X} \end{aligned} \quad (3.2.29)$$

where the Lagrangian strain tensor \mathbf{E} is defined as follows:

Chapter 3. The Governing Equations

$$\mathbf{E} = \frac{1}{2}[\mathbf{F}^T \cdot \mathbf{F} - \mathbf{I}] \quad (3.2.30)$$

In terms of its components, \mathbf{E} is

$$\mathbf{E} = E_{AB}\mathbf{E}_A \otimes \mathbf{E}_B = \left[\frac{\partial x_i}{\partial X_A} \frac{\partial x_i}{\partial X_B} - \delta_{AB} \right] \mathbf{E}_A \otimes \mathbf{E}_A \quad (3.2.31)$$

If equation (3.2.28) is expressed in terms of the deformed material segment $d\mathbf{x}$ in the current configuration using (3.2.12), the result is

$$\begin{aligned} ds^2 - dS_0^2 &= d\mathbf{x} \cdot d\mathbf{x} - (\mathbf{F}^{-1} \cdot d\mathbf{x}) \cdot (\mathbf{F}^{-1} \cdot d\mathbf{x}) \\ &= d\mathbf{x} \cdot d\mathbf{x} - (d\mathbf{x} \cdot \mathbf{F}^{-T}) \cdot (\mathbf{F}^{-1} \cdot d\mathbf{x}) \\ &= d\mathbf{x} \cdot [\mathbf{I} - \mathbf{F}^{-T} \cdot \mathbf{F}^{-1}] \cdot d\mathbf{x} \\ &= 2d\mathbf{x} \cdot \boldsymbol{\varepsilon} \cdot d\mathbf{x} \end{aligned} \quad (3.2.32)$$

where the Eulerian strain tensor $\boldsymbol{\varepsilon}$ is defined as follows:

$$\boldsymbol{\varepsilon} = \frac{1}{2}[\mathbf{I} - \mathbf{F}^{-T} \cdot \mathbf{F}^{-1}] \quad (3.2.33)$$

In terms of its components, $\boldsymbol{\varepsilon}$ is

$$\boldsymbol{\varepsilon} = \varepsilon_{ij}\mathbf{e}_i \otimes \mathbf{e}_j = \left[\delta_{ij} - \frac{\partial X_A}{\partial x_i} \frac{\partial X_A}{\partial x_j} \right] \mathbf{e}_i \otimes \mathbf{e}_j \quad (3.2.34)$$

The strain tensors, \mathbf{E} and $\boldsymbol{\varepsilon}$, can also be expressed in terms of the displacement \mathbf{u} of a material point between initial and current configurations. Displacement is defined as a function of \mathbf{x} or \mathbf{X} as follows:

Chapter 3. The Governing Equations

$$\mathbf{u}(\mathbf{x}, t) = \mathbf{x} - \mathbf{X}(\mathbf{x}, t) \quad \text{or} \quad \mathbf{U}(\mathbf{X}, t) = \mathbf{x}(\mathbf{X}, t) - \mathbf{X} \quad (3.2.35)$$

The material displacement gradient $\nabla_0 \mathbf{U}$ is

$$\nabla_0 \mathbf{U} = \mathbf{F} - \mathbf{I} \quad (3.2.36)$$

The Lagrangian strain is expressed in terms of $\nabla_0 \mathbf{U}$ by substituting equation (3.2.36) into (3.2.30). The result is

$$\begin{aligned} \mathbf{E} &= \frac{1}{2} [(\nabla_0 \mathbf{U} + \mathbf{I})^T \cdot (\nabla_0 \mathbf{U} + \mathbf{I}) - \mathbf{I}] \\ &= [\nabla_0 \mathbf{U} + (\nabla_0 \mathbf{U})^T + (\nabla_0 \mathbf{U})^T \cdot (\nabla_0 \mathbf{U})] \end{aligned} \quad (3.2.37)$$

The spatial displacement gradient $\nabla \mathbf{u}$ is

$$\nabla \mathbf{u} = \mathbf{I} - \mathbf{F}^{-1} \quad (3.2.38)$$

The Eulerian strain is expressed in terms of $\nabla \mathbf{u}$ by substituting equation (3.2.38) into (3.2.33). The result is

$$\begin{aligned} \boldsymbol{\varepsilon} &= \frac{1}{2} [(\mathbf{I} - (\mathbf{I} - \nabla \mathbf{u})^T) \cdot (\mathbf{I} - \nabla \mathbf{u})] \\ &= [\nabla \mathbf{u} + (\nabla \mathbf{u})^T + (\nabla \mathbf{u})^T \cdot (\nabla \mathbf{u})] \end{aligned} \quad (3.2.39)$$

If the displacement gradients are assumed to be small with respect to the identity \mathbf{I} (i.e. $\|\nabla \mathbf{u}\| \ll 1$ and $\|\nabla_0 \mathbf{U}\| \ll 1$) then the multiplicative terms, $(\nabla_0 \mathbf{U})^T \cdot (\nabla_0 \mathbf{U})$ and $(\nabla \mathbf{u})^T \cdot (\nabla \mathbf{u})$, in (3.2.37) and (3.2.39) respectively can be ignored. In this case, equations (3.2.36) and (3.2.38) lead to the approximation of the deformation

Chapter 3. The Governing Equations

gradient as the identity. If $\mathbf{F} \approx \mathbf{I}$ there is no distinction between material and spatial gradients, and therefore $\nabla_0 \mathbf{U} \approx \nabla \mathbf{u}$. This small displacement gradient assumption leads to following small strain approximation:

$$\boldsymbol{\varepsilon} = (\nabla \mathbf{u})^S = \frac{1}{2}[\nabla \mathbf{u} + (\nabla \mathbf{u})^T] \quad (3.2.40)$$

The superscript, S , denotes the symmetric part of a second order tensor which is defined in equation (3.2.40) for $\nabla \mathbf{u}$. Only small strains are considered for the present study. From this point forward any reference to strain, $\boldsymbol{\varepsilon}$, is understood to be the small strain approximation in equation (3.2.40).

3.3 Representation of Quantities and their Time Derivatives

There are two ways to represent a continuum quantity. Consider an arbitrary scalar quantity, ϕ . One representation of ϕ is the material representation for which ϕ is expressed as a function of the position of a material point in the reference configuration and time as follows:

$$\phi = \phi(\mathbf{X}, t) \quad (3.3.1)$$

The interpretation of the material representation of any quantity, in this case $\phi(\mathbf{X}, t)$, is that the value of ϕ for a material point, \mathbf{X} that started at time t . The other representation of a continuum quantity is the spatial representation for which ϕ is expressed as a function of a point in space as follows:

$$\phi = \phi(\mathbf{X}(\mathbf{x}, t), t) \quad (3.3.2)$$

Chapter 3. The Governing Equations

The spatial representation, $\phi(\mathbf{x}, t)$, is interpreted as observing the value of ϕ for the material point that is currently at \mathbf{x} at time t .

The material representation can be thought of as the perspective of being attached to the material and observing the changes of quantities on that material in time. The spatial representation is the perspective of observing a fixed point in space and the changes of the quantities at that point as time goes by and material passes through the space.

The velocity $\mathbf{v}(\mathbf{x}, t)$ is the rate of change of position with respect to time at point \mathbf{x} at time t . This velocity is that of the material point currently located at \mathbf{x} at time t .

$$\mathbf{v}(\mathbf{x}, t) = \mathbf{v}(\mathbf{x}(\mathbf{X}, t), t) = \mathbf{V}(\mathbf{X}, t) \quad (3.3.3)$$

The velocity of a material point is the rate of change of that point's position with time as follows:

$$\mathbf{V}(\mathbf{X}, t) = \frac{\partial \mathbf{x}(\mathbf{X}, t)}{\partial t} \quad (3.3.4)$$

Substitution of equation (3.3.3) in equation (3.3.4) results in the following:

$$\frac{\partial \mathbf{x}(\mathbf{X}, t)}{\partial t} = \mathbf{v}(\mathbf{x}(\mathbf{X}, t), t) \quad (3.3.5)$$

Similarly, the acceleration of a material point is the time rate of change of the velocity as follows:

$$\mathbf{A}(\mathbf{X}, t) = \frac{\partial \mathbf{V}(\mathbf{X}, t)}{\partial t} \quad (3.3.6)$$

Chapter 3. The Governing Equations

Use of equation (3.3.3) and the chain rule, gives the following result for the acceleration:

$$\mathbf{A}(\mathbf{X}, t) = \frac{\partial \mathbf{V}(\mathbf{X}, t)}{\partial t} = \frac{\partial \mathbf{v}(\mathbf{x}, t)}{\partial t} + (\mathbf{v}(\mathbf{x}, t) \cdot \nabla) \mathbf{v}(\mathbf{x}, t) = \mathbf{a}(\mathbf{x}, t) \quad (3.3.7)$$

The final result in equation (3.3.7) is the material (or substantial) time derivative of the velocity. The material time derivative of the spatial representation of any quantity (\cdot) is defined by the following operator:

$$\frac{D(\cdot)}{Dt} = \frac{\partial(\cdot)}{\partial t} + (\mathbf{v} \cdot \nabla)(\cdot) \quad (3.3.8)$$

For the sake of convenience, a superimposed dot over a quantity will also be used to denote the material time derivative (e.g. $\dot{\phi} = d\phi/dt$).

The statement of conservation laws requires the total time derivative of an integral of some function $\psi = \psi(\mathbf{x}, t)$ over the volume V of the current configuration, Ω , as follows:

$$\frac{d}{dt} \int_{\Omega(t)} \psi dV \quad (3.3.9)$$

In equation (3.3.9) $\Omega = \Omega(t)$ is used to emphasize the fact that the current configuration volume is a function of time. In order to apply the material derivative to the integrand a change of variables to the original configuration Ω_0 is performed using equation (3.2.18) as follows:

Chapter 3. The Governing Equations

$$\begin{aligned}
 \frac{d}{dt} \int_{\Omega(t)} \psi dV &= \frac{d}{dt} \int_{\Omega_0} \psi J dV_0 \\
 &= \int_{\Omega_0} \frac{d(\psi J)}{dt} dV_0 \\
 &= \int_{\Omega_0} (\dot{\psi} J + \psi \dot{J}) dV_0
 \end{aligned} \tag{3.3.10}$$

It is apparent from equation (3.3.10) that an expression for the material time derivative \dot{J} is required. In order to obtain an expression for \dot{J} , it is necessary to express $J = \det \mathbf{F}$ in indicial notation as follows:

$$J = \det \mathbf{F} = \varepsilon_{ijk} F_{1i} F_{2j} F_{3k} = \varepsilon_{ijk} \frac{\partial x_1}{\partial X_i} \frac{\partial x_2}{\partial X_j} \frac{\partial x_3}{\partial X_k} \tag{3.3.11}$$

In (3.3.11) the third order alternating tensor ε_{ijk} is defined to be

$$\varepsilon_{ijk} = \begin{cases} 1 & \text{if } ijk = 123, \quad 231 \quad \text{or} \quad 312 \\ -1 & \text{if } ijk = 132, \quad 321 \quad \text{or} \quad 213 \\ 0 & \text{otherwise} \end{cases} \tag{3.3.12}$$

Using the chain rule, the material time derivative of (3.3.11) is

$$\dot{J} = \varepsilon_{ijk} \left[\frac{d}{dt} \left(\frac{\partial x_1}{\partial X_i} \right) \frac{\partial x_2}{\partial X_j} \frac{\partial x_3}{\partial X_k} + \frac{\partial x_1}{\partial X_i} \frac{d}{dt} \left(\frac{\partial x_2}{\partial X_j} \right) \frac{\partial x_3}{\partial X_k} + \frac{\partial x_1}{\partial X_i} \frac{\partial x_2}{\partial X_j} \frac{d}{dt} \left(\frac{\partial x_3}{\partial X_k} \right) \right] \tag{3.3.13}$$

The partial derivatives of x_p (for $p = 1, 2, 3$) with respect to space and time are assumed to be continuous and the following holds:

$$\frac{d}{dt} \left(\frac{\partial x_p}{\partial X_q} \right) = \frac{\partial}{\partial X_q} \left(\frac{dx_p}{dt} \right) = \frac{\partial}{\partial X_q} \left(\frac{\partial x_p}{\partial t} \right) = \frac{\partial v_p}{\partial X_q} \tag{3.3.14}$$

Chapter 3. The Governing Equations

Equation (3.3.13) is restated with the use of (3.3.14) to be

$$\dot{J} = \varepsilon_{ijk} \frac{\partial v_1}{\partial X_i} \frac{\partial x_2}{\partial X_j} \frac{\partial x_3}{\partial X_k} + \varepsilon_{ijk} \frac{\partial x_1}{\partial X_i} \frac{\partial v_2}{\partial X_j} \frac{\partial x_3}{\partial X_k} + \varepsilon_{ijk} \frac{\partial x_1}{\partial X_i} \frac{\partial x_2}{\partial X_j} \frac{\partial v_3}{\partial X_k} \quad (3.3.15)$$

The gradient of velocity components v_p ($p = 1, 2, 3$) with respect to the reference configuration in equation (3.3.15) can be expressed as a gradient with respect to the spatial configuration as follows:

$$\frac{\partial v_p}{\partial X_1} = \frac{\partial v_p}{\partial x_n} \frac{\partial x_n}{\partial X_1} \quad (3.3.16)$$

Using equation (3.3.16), equation (3.3.15) is restated to be

$$\dot{J} = \varepsilon_{ijk} \frac{\partial v_1}{\partial x_n} \frac{\partial x_n}{\partial X_i} \frac{\partial x_2}{\partial X_j} \frac{\partial x_3}{\partial X_k} + \varepsilon_{ijk} \frac{\partial x_1}{\partial X_i} \frac{\partial v_2}{\partial x_n} \frac{\partial x_n}{\partial X_j} \frac{\partial x_3}{\partial X_k} + \varepsilon_{ijk} \frac{\partial x_1}{\partial X_i} \frac{\partial x_2}{\partial X_j} \frac{\partial v_3}{\partial x_n} \frac{\partial x_n}{\partial X_k} \quad (3.3.17)$$

A non-zero result for each term in (3.3.17) is obtained only when the following restrictions are made to the dummy index, n :

$$\begin{aligned} \dot{J} &= \varepsilon_{ijk} \frac{\partial v_1}{\partial x_1} \frac{\partial x_1}{\partial X_i} \frac{\partial x_2}{\partial X_j} \frac{\partial x_3}{\partial X_k} + \varepsilon_{ijk} \frac{\partial x_1}{\partial X_i} \frac{\partial v_2}{\partial x_2} \frac{\partial x_2}{\partial X_j} \frac{\partial x_3}{\partial X_k} + \varepsilon_{ijk} \frac{\partial x_1}{\partial X_i} \frac{\partial x_2}{\partial X_j} \frac{\partial v_3}{\partial x_3} \frac{\partial x_3}{\partial X_k} \\ &= \left(\frac{\partial v_1}{\partial x_1} + \frac{\partial v_2}{\partial x_2} + \frac{\partial v_3}{\partial x_3} \right) \varepsilon_{ijk} \left(\frac{\partial x_1}{\partial X_i} \frac{\partial x_2}{\partial X_j} \frac{\partial x_3}{\partial X_k} \right) \end{aligned} \quad (3.3.18)$$

It can be shown that

$$J = \det(\mathbf{F}) = \varepsilon_{ijk} \left(\frac{\partial x_1}{\partial X_i} \frac{\partial x_2}{\partial X_j} \frac{\partial x_3}{\partial X_k} \right) \quad (3.3.19)$$

The final result in equation (3.3.18) is expressed in direct notation using equation (3.3.19) as follows:

$$\dot{J} = (\nabla \cdot \mathbf{v})J \quad (3.3.20)$$

Equation (3.3.20) is substituted into equation (3.3.10). The result is

$$\begin{aligned} \frac{d}{dt} \int_{\Omega(t)} \psi dV &= \int_{\Omega_0} \left(\dot{\psi} J + \psi (\nabla \cdot \mathbf{v}) J \right) dV_0 \\ &= \int_{\Omega_0} \left(\dot{\psi} + \psi (\nabla \cdot \mathbf{v}) \right) J dV_0 \end{aligned} \quad (3.3.21)$$

A change of variables from the reference configuration to the current configuration is made for the final result in equation(3.3.21). The result is

$$\frac{d}{dt} \int_{\Omega(t)} \psi dV = \int_{\Omega(t)} \left(\dot{\psi} + \psi (\nabla \cdot \mathbf{v}) \right) dV \quad (3.3.22)$$

The relationship in equation (3.3.22) is used frequently in the derivation of conservation laws in the following sections because the governing equations are formed in terms of the spatial configuration.

3.4 Conservation of Mass

Mass is a positive scalar quantity that refers to an amount of physical matter. The conservation of mass states that the total mass of a body, denoted by m , remains constant with time. Consider an arbitrary subdomain of the current configuration, $B(t) \subset \Omega(t)$, that has volume, ΔV , and mass, Δm . In a continuum the mass density function, denoted by $\rho = \rho(\mathbf{x}, t)$, is defined everywhere in B to be

$$\rho(\mathbf{x}, t) = \lim_{\Delta V \rightarrow 0} \frac{\Delta m}{\Delta V} \quad (3.4.1)$$

Chapter 3. The Governing Equations

for which $\rho(\mathbf{x}, t) > 0$.

Conservation of mass in B is stated to be

$$m = \int_B \rho(\mathbf{x}, t) dV = \text{constant} \quad (3.4.2)$$

An equivalent statement of conservation of mass is that the material time derivative of mass is equal to zero as follows:

$$\frac{dm}{dt} = \frac{d}{dt} \int_B \rho(\mathbf{x}, t) dV = 0 \quad (3.4.3)$$

Equation (3.3.22) is used in equation (3.4.3) to give the following result:

$$\frac{d}{dt} \int_B \rho(\mathbf{x}, t) dV = \int_B (\dot{\rho} + \rho(\nabla \cdot \mathbf{v})) dV = 0 \quad (3.4.4)$$

Now consider any scalar, vector or tensor valued function $\psi(\mathbf{x})$ that is defined everywhere in $B \subset \Omega$. If the subregion B is arbitrary and $\psi(\mathbf{x})$ is continuous the localization theorem states that

$$\int_B \psi(\mathbf{x}) dV = 0 \quad \implies \quad \psi(\mathbf{x}) = 0 \quad (3.4.5)$$

Using the localization theorem in equation (3.4.4) the local form of conservation of mass (continuity) is

$$\dot{\rho} + \rho(\nabla \cdot \mathbf{v}) = 0 \quad (3.4.6)$$

3.5 Conservation of Momentum

The total linear momentum in $B(t) \subset \Omega(t)$ is denoted by \mathbf{P} , and defined to be

$$\mathbf{P} = \int_B \rho \mathbf{v} dV \quad (3.5.1)$$

The time rate change of linear momentum is obtained by use of equation (3.3.22) as follows:

$$\begin{aligned} \dot{\mathbf{P}} &= \int_B \left(\frac{d(\rho \mathbf{v})}{dt} + \rho(\nabla \cdot \mathbf{v}) \mathbf{v} dV \right) \\ &= \int_B (\dot{\rho} \mathbf{v} + \rho \dot{\mathbf{v}} + \rho(\nabla \cdot \mathbf{v}) \mathbf{v}) dV \\ &= \int_B (\mathbf{v}(\dot{\rho} + \rho(\nabla \cdot \mathbf{v})) + \rho \dot{\mathbf{v}}) dV \end{aligned} \quad (3.5.2)$$

The final result in equation (3.5.2) is simplified using the conservation of mass in equation(3.4.6) to be

$$\dot{\mathbf{P}} = \int_B \rho \dot{\mathbf{v}} dV \quad (3.5.3)$$

Newton's second law states that the time rate change of linear momentum is equal to the sum of external forces, \mathbf{f} , as follows:

$$\dot{\mathbf{P}} = \mathbf{f} \quad (3.5.4)$$

The sum of external forces is assumed to have two contributions; forces from tractions that act over the surface of B and body forces that act over the volume of B (such as gravitational or magnetic forces). The traction vector (or stress vector) function, $\boldsymbol{\tau} = \boldsymbol{\tau}(\mathbf{x}, t)$, is defined as the force per unit area that acts over the surface of the

Chapter 3. The Governing Equations

arbitrary subdomain $B(t) \subset \Omega(t)$. Recall that the surface of B , denoted by ∂B , is defined by the normal vector \mathbf{n} to that surface. The traction vector is defined by the following linear transformation of \mathbf{n} :

$$\boldsymbol{\tau} = \boldsymbol{\sigma} \cdot \mathbf{n} \quad (3.5.5)$$

In equation (3.5.5) $\boldsymbol{\sigma} = \boldsymbol{\sigma}(\mathbf{x}, t)$ is the second order Cauchy stress tensor. The total body force per unit mass is denoted as $\mathbf{b} = \mathbf{b}(\mathbf{x}, t)$. The sum of external forces on B is stated in terms of its volume and surface contributions to be

$$\mathbf{f} = \int_{\partial B} \boldsymbol{\tau} dA + \int_B \rho \mathbf{b} dV \quad (3.5.6)$$

Where the surface integral in equation (3.5.6) is restated using equation (3.5.5) to be

$$\int_{\partial B} \boldsymbol{\tau} dA = \int_{\partial B} \boldsymbol{\sigma} \cdot \mathbf{n} dA \quad (3.5.7)$$

By use of the divergence theorem, equation (3.5.7) becomes

$$\int_{\partial B} \boldsymbol{\sigma} \cdot \mathbf{n} dA = \int_B \nabla \cdot \boldsymbol{\sigma} dV \quad (3.5.8)$$

Equations (3.5.4), (3.5.6) and (3.5.8) are combined to give the following integral form of the conservation of momentum:

$$\int_B (\rho \dot{\mathbf{v}} - \nabla \cdot \boldsymbol{\sigma} - \rho \mathbf{b}) dV = \mathbf{0} \quad (3.5.9)$$

It follows from equation (3.4.5) that the local form of the conservation of linear momentum is

Chapter 3. The Governing Equations

$$\rho \dot{\mathbf{v}} = \nabla \cdot \boldsymbol{\sigma} + \rho \mathbf{b} \quad (3.5.10)$$

Equation (3.5.10) is restated in indicial notation for later reference to be

$$\rho \dot{v}_k = \frac{\partial \sigma_{kl}}{\partial x_l} + \rho b_k \quad (3.5.11)$$

The total angular momentum, \mathbf{L} , in $B(t) \subset \Omega(t)$ is defined to be

$$\mathbf{L} = \int_B (\mathbf{x} \times \rho \mathbf{v}) dV \quad (3.5.12)$$

The time rate change of angular momentum is obtained by the use of equation (3.3.22) as follows:

$$\begin{aligned} \dot{\mathbf{L}} &= \int_B \left(\frac{d}{dt} (\mathbf{x} \times \rho \mathbf{v}) + (\nabla \cdot \mathbf{v})(\mathbf{x} \times \rho \mathbf{v}) \right) dV \\ &= \int_B (\dot{\mathbf{x}} \times \rho \mathbf{v} + \mathbf{x} \times (\dot{\rho} \mathbf{v} + \rho \dot{\mathbf{v}}) + (\nabla \cdot \mathbf{v})(\mathbf{x} \times \rho \mathbf{v})) dV \\ &= \int_B ((\mathbf{v} \times \rho \mathbf{v}) + \mathbf{x} \times (\dot{\rho} + \rho(\nabla \cdot \mathbf{v}))\mathbf{v} + \mathbf{x} \times \rho \dot{\mathbf{v}}) dV \end{aligned} \quad (3.5.13)$$

The final result in equation (3.5.13) is simplified by using the conservation of mass in equation (3.4.6) and the fact that the cross product of any vector with itself is the zero vector. The result is

$$\dot{\mathbf{L}} = \int_B \mathbf{x} \times \rho \dot{\mathbf{v}} dV \quad (3.5.14)$$

The balance of angular momentum states that the material time derivative of angular momentum is equal to the sum of all moments (with respect to the origin) produced

Chapter 3. The Governing Equations

by the traction, $\boldsymbol{\tau} = \boldsymbol{\tau}(\mathbf{x}, t)$, acting over the surface of B and body force, $\mathbf{b} = \mathbf{b}(\mathbf{x}, t)$, acting over the volume of B . The balance of angular momentum is

$$\int_B \mathbf{x} \times \rho \dot{\mathbf{v}} dV = \int_{\partial B} \mathbf{x} \times \boldsymbol{\tau} dA + \int_B \mathbf{x} \times \rho \mathbf{b} dV \quad (3.5.15)$$

Equation (3.5.7) and the divergence theorem are employed to simplify equation (3.5.15) to the following form:

$$\int_B (\mathbf{x} \times \rho \dot{\mathbf{v}} - \nabla \cdot (\mathbf{x} \times \boldsymbol{\sigma}) - \mathbf{x} \times \rho \mathbf{b}) dV = \mathbf{0} \quad (3.5.16)$$

In order to simplify further manipulations, equation (3.5.16) is restated in indicial notation as follows:

$$\int_B \left(\varepsilon_{ijk} x_j \rho \dot{v}_k - \frac{\partial}{\partial x_l} (\varepsilon_{ijk} x_j \sigma_{kl}) - \varepsilon_{ijk} x_j \rho b_k \right) dV = 0 \quad (3.5.17)$$

Equation (3.5.17) is restated by the following series of steps:

$$\begin{aligned} 0 &= \int_B \left(\varepsilon_{ijk} x_j \rho \dot{v}_k - \left(\varepsilon_{ijk} \frac{\partial x_j}{\partial x_l} \sigma_{kl} + \varepsilon_{ijk} x_j \frac{\partial \sigma_{kl}}{\partial x_l} \right) - \varepsilon_{ijk} x_j \rho b_k \right) dV \\ &= \int_B \left(\varepsilon_{ijk} x_j \rho \dot{v}_k - \left(\varepsilon_{ijk} \delta_{jl} \sigma_{kl} + \varepsilon_{ijk} x_j \frac{\partial \sigma_{kl}}{\partial x_l} \right) - \varepsilon_{ijk} x_j \rho b_k \right) dV \\ &= \int_B \left(\varepsilon_{ijk} x_j \rho \dot{v}_k - \left(\varepsilon_{ijk} \sigma_{kj} + \varepsilon_{ijk} x_j \frac{\partial \sigma_{kl}}{\partial x_l} \right) - \varepsilon_{ijk} x_j \rho b_k \right) dV \\ &= \int_B \left(\varepsilon_{ijk} x_j \left(\rho \dot{v}_k - \frac{\partial \sigma_{kl}}{\partial x_l} - \rho b_k \right) - \varepsilon_{ijk} \sigma_{kj} \right) dV \end{aligned} \quad (3.5.18)$$

The steps leading to the final result in (3.5.18) utilize the fact that $\partial x_i / \partial x_j = \delta_{ij}$ where the Kronecker delta function is defined to be

$$\delta_{ij} = \begin{pmatrix} 1 & \text{for } j = i \\ 0 & \text{for } j \neq i \end{pmatrix} \quad (3.5.19)$$

The final result in equation (3.5.18) is simplified further using the conservation of linear momentum in equation (3.5.10). The result is

$$\int_B \varepsilon_{ijk} \sigma_{kj} dV = 0 \quad (3.5.20)$$

Equation (3.5.20) requires that the following symmetry condition holds:

$$\sigma_{kj} = \sigma_{jk} \quad (3.5.21)$$

In direct notation equation (3.5.21) is

$$\boldsymbol{\sigma} = \boldsymbol{\sigma}^T \quad (3.5.22)$$

Equation (3.5.22) is the final consequence of the balance of angular momentum which requires symmetry of the Cauchy stress tensor.

3.5.1 Weak Form of the Linear Momentum Balance

The weak form, or variational form, of the linear momentum balance is obtained for future use in computational developments. Equation (3.5.10) is also known as the strong form of the linear momentum balance. The weak form is obtained by integrating the product of equation (3.5.10) with an admissible variation of the solution, denoted by $\mathbf{w} = \mathbf{w}(\mathbf{x}, t)$, over the volume of Ω as follows:

$$\int_{\Omega} \mathbf{w} \cdot (\rho \dot{\mathbf{v}} - \nabla \cdot \boldsymbol{\sigma} - \rho \mathbf{b}) dV = 0 \quad (3.5.23)$$

Chapter 3. The Governing Equations

In equation (3.5.23) the function, $\mathbf{w} = \mathbf{w}(\mathbf{x}, t)$ (also known as the test function), is required to be zero on the portion of the boundary, $\partial\Omega$ (see figure 3.1), where the displacement is prescribed.

By the product rule, the following holds:

$$\int_{\Omega} \nabla \cdot (\mathbf{w} \cdot \boldsymbol{\sigma}) dV = \int_{\Omega} \nabla \mathbf{w} : \boldsymbol{\sigma} + \mathbf{w}(\nabla \cdot \boldsymbol{\sigma}) dV \quad (3.5.24)$$

Equation (3.5.24) is expressed alternatively using the divergence theorem and equation (3.5.5) to be

$$\int_{\Omega} \nabla \cdot (\mathbf{w} \cdot \boldsymbol{\sigma}) dV = \int_{\partial\Omega} \mathbf{w} \cdot \boldsymbol{\sigma} \cdot \mathbf{n} dA = \int_{\partial\Omega} \mathbf{w} \cdot \boldsymbol{\tau} dA \quad (3.5.25)$$

Equations (3.5.24) and (3.5.25) are combined and substituted into (3.5.23) to give the following weak form of the conservation of linear momentum:

$$\int_{\Omega} \rho \mathbf{w} \cdot \dot{\mathbf{v}} dV = - \int_{\Omega} \nabla \mathbf{w} : \boldsymbol{\sigma} dV + \int_{\partial\Omega} \mathbf{w} \cdot \boldsymbol{\tau} dA + \int_{\Omega} \rho \mathbf{w} \cdot \mathbf{b} dV \quad (3.5.26)$$

3.5.2 Strong Discontinuity Kinematics

Discrete constitutive models can be applied to problems of fracture in the context of strong discontinuities. The discussion of strong discontinuity kinematics follows from [40, 43] and references therein for the case of infinitesimal strain. Consider a discontinuity in the body Ω denoted by the surface Γ with normal vector \mathbf{n} and tangential vector \mathbf{t} depicted in figure 3.4. The two regions Ω^+ , and Ω^- , are separated by Γ . The displacement field, $\mathbf{u}(\mathbf{x}, t)$, in Ω is written in terms of a continuous and a discontinuous part as follows:

Chapter 3. The Governing Equations

$$\mathbf{u}(\mathbf{x}, t) = \underbrace{\bar{\mathbf{u}}(\mathbf{x}, t)}_{\text{continuous part}} + \underbrace{H_\Gamma[[\mathbf{u}]](\mathbf{x}, t)}_{\text{discontinuous part}} \quad (3.5.27)$$

In equation (3.5.27), $\bar{\mathbf{u}}(\mathbf{x}, t)$ represents the regular continuous part of the displacement field, $[[\mathbf{u}]](\mathbf{x}, t)$ is the jump in the displacement field and $H_\Gamma(\mathbf{x})$ is the Heaviside function defined as follows:

$$H_\Gamma(\mathbf{x}) = \begin{pmatrix} 0 & \text{for } \mathbf{x} \in \Omega^- \\ 1 & \text{for } \mathbf{x} \in \Omega^+ \end{pmatrix} \quad (3.5.28)$$

The small strain tensor, $\boldsymbol{\varepsilon}(\mathbf{x}, t)$, is computed from equation (3.2.40) to be

$$\boldsymbol{\varepsilon}(\mathbf{x}, t) = (\nabla \mathbf{u})^S = (\nabla \bar{\mathbf{u}})^S + \nabla H_\Gamma \otimes [[\mathbf{u}]] + H_\Gamma (\nabla [[\mathbf{u}]])^S \quad (3.5.29)$$

The gradient of the Heaviside function in equation (3.5.29) is defined in the sense of distributions to be $\nabla H_\Gamma = \delta_\Gamma(\mathbf{x})\mathbf{n}$ where $\delta_\Gamma(\mathbf{x})$ is the Dirac delta function, defined in terms of any smooth function $\phi(\mathbf{x}, t)$ with compact support as follows:

$$\int_\Omega \phi(\mathbf{x}, t) \delta_\Gamma(\mathbf{x}) dV = \int_\Gamma \phi(\mathbf{x}, t) dA \quad (3.5.30)$$

It follows that the expression for strain in equation (3.5.29) becomes

$$\boldsymbol{\varepsilon}(\mathbf{x}, t) = (\nabla \bar{\mathbf{u}})^S + H_\Gamma (\nabla [[\mathbf{u}]])^S + \delta_\Gamma ([[\mathbf{u}]]) \otimes \mathbf{n}^S \quad (3.5.31)$$

The regular part of the small strain tensor, defined as $\bar{\boldsymbol{\varepsilon}}(\mathbf{x}, t) = (\nabla \bar{\mathbf{u}})^S + H_\Gamma (\nabla [[\mathbf{u}]])^S$, is bounded. The singular and unbounded part of the strain is $\delta_\Gamma ([[\mathbf{u}]]) \otimes \mathbf{n}^S$. In terms of its regular and singular contributions the strain tensor is

$$\boldsymbol{\varepsilon}(\mathbf{x}, t) = \underbrace{\bar{\boldsymbol{\varepsilon}}(\mathbf{x}, t)}_{\text{regular and bounded part}} + \underbrace{\delta_{\Gamma}([\mathbf{u}] \otimes \mathbf{n})^S}_{\text{singular and unbounded part}} \quad (3.5.32)$$

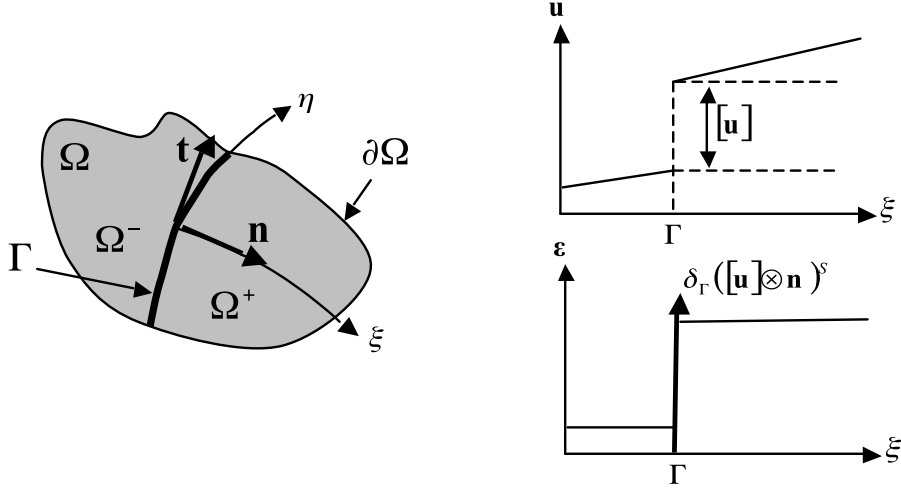


Figure 3.4: Illustration of strong discontinuity kinematics concept

For practical purposes a regularization of the kinematics in equation (3.5.32) is used in order to keep the singular part of the strain bounded. A regularized Dirac delta function is defined to be

$$\delta_{\Gamma}^L = \frac{1}{L_c} \mu_{\Gamma}(\mathbf{x}) \quad (3.5.33)$$

where L_c is the smearing length (or band width) and $\mu_{\Gamma}(\mathbf{x})$ is a collocation function defined as follows:

$$\mu_{\Gamma}(\mathbf{x}) = \begin{pmatrix} 0 & \text{for } \mathbf{x} \in \Omega/\Gamma \\ 1 & \text{for } \mathbf{x} \in \Gamma \end{pmatrix} \quad (3.5.34)$$

The regularized strain field is

$$\boldsymbol{\varepsilon}(\mathbf{x}, t) = \bar{\boldsymbol{\varepsilon}}(\mathbf{x}, t) + \frac{1}{L_c} \mu_\Gamma([\![\mathbf{u}]\!] \otimes \mathbf{n})^S \quad (3.5.35)$$

where the regularized term becomes unbounded as $L_c \rightarrow 0$.

3.5.3 Elastic De-cohesive Constitutive Model for Geological Materials

The relationship between stress and strain is called the constitutive equation and is denoted generally as $\boldsymbol{\sigma} = \boldsymbol{\sigma}(\boldsymbol{\varepsilon})$. In a classical continuum $\boldsymbol{\sigma} = \boldsymbol{\sigma}(\boldsymbol{\varepsilon})$ is defined everywhere in Ω . However, in the presence of a discontinuity, represented by the surface Γ with normal vector \mathbf{n} in figure 3.4, a discrete constitutive model is imposed on Γ which relates the traction, $\boldsymbol{\tau} = \boldsymbol{\sigma} \cdot \mathbf{n}$, on Γ to the displacement discontinuity across Γ . The traction-displacement discontinuity relationship associated with the discrete constitutive model is denoted generally as $\boldsymbol{\tau} = \boldsymbol{\tau}([\![\mathbf{u}]\!])$. In general terms, the application of the constitutive model to a body Ω that has a discontinuity across a surface Γ is stated as the following:

$$\boldsymbol{\sigma} = \boldsymbol{\sigma}(\boldsymbol{\varepsilon}) \quad x \in \Omega/\Gamma \quad (3.5.36)$$

$$\boldsymbol{\sigma} \cdot \mathbf{n} = \boldsymbol{\tau} = \boldsymbol{\tau}([\![\mathbf{u}]\!]) \quad \mathbf{x} \in \Gamma \quad (3.5.37)$$

The discrete constitutive model used for this study is presented. The model is a modification to the elastic de-cohesive model for geological materials [58]. Prior to the initiation of failure the material is considered to be linear elastic for which stress $\boldsymbol{\sigma}$ and strain $\boldsymbol{\varepsilon}$ are related through the fourth order isotropic elasticity tensor \mathbf{C} as follows:

$$\boldsymbol{\sigma} = \mathbf{C} : \boldsymbol{\varepsilon}^e \quad (3.5.38)$$

In equation (3.5.38) the superscript e is used on the strain tensor to emphasize that the deformation is purely elastic. Elastic deformation of the material continues until the initiation of failure.

The material failure process initiates on a discrete surface, defined by the unit normal vector \mathbf{n} and referred to as the failure surface. The determination of \mathbf{n} depends on the local stress $\boldsymbol{\sigma}$ at a point in the deformable body. The traction on a potential failure surface defined by \mathbf{n} is $\boldsymbol{\tau} = \boldsymbol{\sigma} \cdot \mathbf{n}$. A de-cohesion function of $\boldsymbol{\tau}$, denoted by $F_n = F_n(\boldsymbol{\tau})$, is also defined. Material failure initiates on the surface defined by \mathbf{n} if the following criterion is met:

$$F = \max_{\forall \mathbf{n}} F_n(\boldsymbol{\tau}) = 0 \quad (3.5.39)$$

Equation (3.5.39) states that the potential failure surface orientation corresponds to the normal vector \mathbf{n} that maximizes $F_n = F_n(\boldsymbol{\tau})$. Classical failure criteria associated with specific forms of F_n include the Rankine, Tresca, and Mohr-Coulomb criteria. Each criterion predicts the failure stress as well as the failure plane orientation. The Rankine failure criterion is typically used for tensile stress states of brittle materials and incorporates the normal component of traction on a failure surface, denoted by $\tau_n = \boldsymbol{\tau} \cdot \mathbf{n}$. The failure planes predicted by the Rankine criteria correspond to the direction of the maximum principal stress. The de-cohesion function associated with Rankine failure is

$$F_n = \frac{\tau_n}{\tau_{nf}} - 1 \quad (\text{Rankine}) \quad (3.5.40)$$

where τ_{nf} is the ultimate tensile strength of the material. From equation (3.5.40) it is obvious that the failure surface initiation occurs when $\tau_n = \tau_{nf}$.

Chapter 3. The Governing Equations

The Tresca criterion predicts failure planes corresponding to the maximum shear stress on a potential failure surface, and is used for ductile materials such as metals.

The shear stress on a surface with normal \mathbf{n} is

$$\tau_s = \left(\|\boldsymbol{\tau}\|^2 - \tau_n^2 \right)^{\frac{1}{2}} \quad (3.5.41)$$

The form of F_n associated with Tresca is

$$F_n = \frac{\tau_s}{\tau_{sf}} - 1 \quad (Tresca) \quad (3.5.42)$$

where τ_{sf} is the shear strength of the material. The failure surface initiation criterion for Tresca is $\tau_s = \tau_{sf}$ on a plane with normal \mathbf{n} that is oriented 45° from the plane of maximum principal stress.

Geological material failure is often predicted by the Mohr-Coulomb criterion, which predicts failure planes at a fixed angle relative to the direction of maximum principal stress. The de-cohesion function associated with Mohr-Coulomb incorporates both the normal and shear traction components as follows:

$$F_n = \frac{\tau_s}{\tau_{sf}} + \frac{\tau_n}{\tau_{nf}} - 1 \quad (Mohr - Coulomb) \quad (3.5.43)$$

All three classical models are useful for certain materials and loadings but none of them are able to reproduce realistic predictions of failure planes for all stress states of a given material.

The failure criteria that results from the specific form of the de-cohesion function F_n used for this study predicts the value of failure initiation stress and the failure surface orientation (crack orientation) for all states of stress, which are in good agreement with experimental failure data for geological materials such as concrete and sea ice [58]. A specific advantage over classical failure criteria is the ability of the

Chapter 3. The Governing Equations

model to correctly predict failure plane orientations for triaxial compression stress states, including axial splitting. However, before presenting the specific form of F_n it is necessary to discuss how the failure process is modeled by discrete constitutive models once a failure surface has initiated.

Discrete constitutive models are associated with a traction-displacement relationship, $\boldsymbol{\tau} = \boldsymbol{\tau} ([[\mathbf{u}]])$, that is applied on the failure surface defined by \mathbf{n} . The function $\boldsymbol{\tau} = \boldsymbol{\tau} ([[\mathbf{u}]])$ incorporates the effect of softening into the model that is observed during the material failure process. This relationship is often referred to as the softening law because the magnitude of traction decreases as the displacement discontinuity magnitude increases. The model of interest utilizes a linear softening law which relates the normal components of traction and displacement, defined as $\tau_n = \mathbf{n} \cdot \boldsymbol{\sigma} \cdot \mathbf{n} = \boldsymbol{\tau} \cdot \mathbf{n}$ and $[[u_n]] = [[\mathbf{u}]] \cdot \mathbf{n}$ respectively. The function, $\tau_n = \tau_n ([[u_n]])$, illustrated in figure 2.3, is associated with mode I type failures. The material properties governing failure are incorporated into the softening law and include the ultimate tensile strength τ_{nf} and the mode I fracture energy G_f , which is the area under the traction-displacement function. The quantity, u_0 , is referred to as the critical crack opening and is defined as the value of $[[u_n]]$ for which $\tau_n = 0$. Complete failure is reached once $[[u_n]] = u_0$, and the failure surface is interpreted to be a crack with two traction free surfaces that are unable to sustain tensile load. For a linear softening law, the critical crack opening is computed to be

$$u_0 = \frac{2G_f}{\tau_{nf}} \quad (3.5.44)$$

The specific form of the de-cohesion function F_n is expressed in terms of stress components in the local orthonormal failure plane basis $\{\mathbf{n}, \mathbf{t}, \mathbf{p}\}$ where \mathbf{n} is the unit normal vector to the failure surface, \mathbf{t} is a unit vector in the failure plane that is chosen to be perpendicular to \mathbf{n} and $\mathbf{p} = \mathbf{n} \times \mathbf{t}$. In terms of a standard orthonormal global vector basis $\{\mathbf{e}_1, \mathbf{e}_2, \mathbf{e}_3\}$, $\mathbf{n} = n_1\mathbf{e}_1 + n_2\mathbf{e}_2 + n_3\mathbf{e}_3$, $\mathbf{t} = t_1\mathbf{e}_1 + t_2\mathbf{e}_2 + t_3\mathbf{e}_3$ and

Chapter 3. The Governing Equations

$\mathbf{p} = p_1\mathbf{e}_1 + p_2\mathbf{e}_2 + p_3\mathbf{e}_3$. A second-order orthogonal transformation tensor \mathbf{A} is defined as follows:

$$\mathbf{A} = \begin{pmatrix} n_1 & t_1 & p_1 \\ n_2 & t_2 & p_2 \\ n_3 & t_3 & p_3 \end{pmatrix} \quad (3.5.45)$$

In terms of the local failure plane basis, the stress is

$$\boldsymbol{\sigma}^l = \mathbf{A}^T \cdot \boldsymbol{\sigma}^g \cdot \mathbf{A} \quad (3.5.46)$$

where $\boldsymbol{\sigma}^g$ contains the components of stress in the global $\{\mathbf{e}_1, \mathbf{e}_2, \mathbf{e}_3\}$ basis and $\boldsymbol{\sigma}^l$ contains the stress components in the local $\{\mathbf{n}, \mathbf{t}, \mathbf{p}\}$ basis. The components of $\boldsymbol{\sigma}^l$ are

$$\boldsymbol{\sigma}^l = \begin{pmatrix} \sigma_{nn} & \sigma_{nt} & \sigma_{np} \\ \sigma_{nt} & \sigma_{tt} & \sigma_{tp} \\ \sigma_{np} & \sigma_{tp} & \sigma_{pp} \end{pmatrix} \quad (3.5.47)$$

For simplicity the following convention is adopted:

$$\tau_n = \sigma_{nn}, \quad \tau_t = \sigma_{nt}, \quad \tau_p = \sigma_{pn} \quad (3.5.48)$$

The form of the de-cohesion function is

$$F_n(\boldsymbol{\sigma}, [[\mathbf{u}]]) = \bar{\tau}_s^2 - \frac{1}{C_{f/m}} \tanh[\psi(1 + C_\psi\psi)] \quad (3.5.49)$$

where

Chapter 3. The Governing Equations

$$\psi = -C_{f/m} \frac{B_n}{(1 + C_s \bar{\sigma}_f^2)} \quad (3.5.50)$$

$$B_n = \bar{\tau}_n (1 + C_n \bar{\sigma}_f^2) + \bar{\sigma}_f^2 \left(1 + \frac{\bar{\tau}_n}{\bar{P}_{sm}}\right) - f_n \quad (3.5.51)$$

$$\bar{\sigma}_f^2 = f_n \bar{\sigma}^2 \quad (3.5.52)$$

$$\bar{P}_{sm} = 2 - \frac{(\tau_n + \sigma_{tt} + \sigma_{pp})}{3\tau_{nf}} \quad (3.5.53)$$

$$f_n = 1 - \frac{[[u_n]]}{u_0} \quad (3.5.54)$$

$$\chi = \left(\frac{f'_c}{f'_b}\right)^2 - 2 \quad (3.5.55)$$

$$\bar{\sigma}^2 = \frac{1}{(f'_c)^2} [\sigma_{tt}^2 + \chi \sigma_{tt} \sigma_{pp} + \sigma_{pp}^2 + (2 - \chi) \sigma_{tp}^2] \quad (3.5.56)$$

$$\bar{\tau}_n = \frac{\tau_n}{\tau_{nf}} \quad \bar{\tau}_s = \frac{\tau_s}{\tau_{sf}} \quad C_{f/m} = \frac{\tau_{sf}^2}{\tau_{sm}^2} \quad (3.5.57)$$

The function f_n , referred to as the softening function, incorporates softening into the de-cohesion function by introducing the normal component of displacement discontinuity $[[u_n]]$ which evolves with loading. The quantity τ_s is the magnitude of the shear stress in the failure plane. The material parameters in equations (3.5.49) - (3.5.57) include the ultimate tensile stress τ_{nf} , the uniaxial compressive strength f'_c , the biaxial compressive failure stress f'_b , shear strength τ_{sf} , shear strength with large

Chapter 3. The Governing Equations

mean pressure τ_{sm} , coupling parameters C_ψ , C_n , C_s and the critical crack opening u_0 .

The preceding form of F_n was developed to predict failure of geological materials for all stress states, but for the purposes of this study only brittle mode I failure is considered. In this case, the critical orientation, \mathbf{n} , is only associated with a positive traction τ_n , requiring that $\bar{\tau}_s = 0$, $\sigma_{tt} = \sigma_{pp} = \sigma_{tp} = 0$ and $\bar{\sigma} = 0$. This simplification results in the following forms of ψ and F_n in equations (3.5.50) and (3.5.49) respectively:

$$\psi = -C_{f/m} (\bar{\tau}_n - f_n) \quad (3.5.58)$$

$$F_n = -\frac{1}{C_{f/m}} \tanh \left[-C_{f/m} (\bar{\tau}_n - f_n) - C_\psi C_{f/m}^2 (\bar{\tau}_n - f_n)^2 \right] \quad (3.5.59)$$

The shear strength ratio is always chosen so that $C_{f/m} = \tau_{sf}^2 / \tau_{sm}^2 \ll 1$. In this case the second order term in $C_{f/m}$ of (3.5.59) is neglected. Equation (3.5.59) becomes

$$F_n = -\frac{1}{C_{f/m}} \tanh \left[-C_{f/m} (\bar{\tau}_n - f_n) \right] \quad (3.5.60)$$

Since the argument of the hyperbolic tangent function is small, the following approximation is made:

$$F_n = \bar{\tau}_n - f_n \quad (3.5.61)$$

If failure has not initiated, $[[u_n]] = 0$, $f_n = 1$, and equation (3.5.61) reduces to the form of F_n associated with the Rankine criteria for brittle failure in tension (equation

Chapter 3. The Governing Equations

(3.5.40)). Substitution of the expressions for $\bar{\tau}_n$ and f_n in equations (3.5.57) and (3.5.54) into equation (3.5.61) results in the following form of F_n :

$$F_n = \frac{\tau_n}{\tau_{nf}} + \frac{[[u_n]]}{u_0} - 1 \quad (3.5.62)$$

By applying the failure initiation criterion, $F_n = 0$, equation (3.5.62) yields the linear relationship for $\tau_n = \tau_n ([[u_n]])$, depicted in figure 2.3 as follows:

$$\tau_n = \tau_{nf} \left(1 - \frac{[[u_n]]}{u_0} \right) \quad (3.5.63)$$

The linear form of $\tau_n = \tau_n ([[u_n]])$ in (3.5.63) is selected for simplicity but other forms are commonly used [54].

In the present model a failure state is defined by $\boldsymbol{\sigma}$ and $[[\mathbf{u}]]$. The failure model is formulated as a direct analogy to rate independent plasticity models [62] for which the de-cohesion function, $F_n(\boldsymbol{\sigma}, [[\mathbf{u}]])$, plays the role of a yield function and the displacement discontinuity, $[[\mathbf{u}]]$, is treated as an internal variable. During the material failure process $[[\mathbf{u}]]$ is assumed to evolve according to following associated flow rule:

$$[[\dot{\mathbf{u}}]] = \dot{\omega} \frac{\partial F_n}{\partial \boldsymbol{\tau}} \quad (3.5.64)$$

In equation (3.5.64) the parameter, $\dot{\omega}$, is required to be positive and is obtained by enforcing the consistency condition as follows:

$$\dot{F}_n = 0 \quad (3.5.65)$$

The components of $[[\dot{\mathbf{u}}]]$ are assumed to follow an associative evolution equation:

Chapter 3. The Governing Equations

$$\dot{u}_n = \dot{\omega} \frac{\partial F_n}{\partial \tau_n}, \quad \dot{u}_t = \dot{\omega} \frac{\partial F_n}{\partial \tau_t}, \quad \dot{u}_p = \dot{\omega} \frac{\partial F_n}{\partial \tau_p} \quad (3.5.66)$$

The particular forms of the partial derivatives, $\partial F_n / \partial \tau_n$, $\partial F_n / \partial \tau_t$ and $\partial F_n / \partial \tau_p$, in equation (3.5.66) are derived. In doing so, the expression for \dot{F}_n is obtained, which will prove to be useful later for numerical implementation of the constitutive model. The expression for \dot{F}_n is obtained by taking the time derivative of equation (3.5.49). The result is

$$\dot{F}_n = \frac{\partial}{\partial t} (\bar{\tau}_s^2) - D_\psi \dot{\psi} \quad (3.5.67)$$

where

$$D_\psi = \frac{(1 + 2C_\psi \psi)}{C_{f/m}} [1 - \tanh^2 [\psi (1 + C_\psi \psi)]] \quad (3.5.68)$$

$$\dot{\psi} = -C_{f/m} \frac{\dot{B}_n}{(1 + C_s \bar{\sigma}_f^2)} + \frac{C_{f/m} B_n}{(1 + C_s \bar{\sigma}_f^2)^2} C_s \frac{\partial}{\partial t} (\bar{\sigma}_f^2) \quad (3.5.69)$$

$$\dot{B}_n = \dot{\bar{\tau}}_n (1 + C_n \bar{\sigma}_f^2) + \bar{\tau}_n C_n \frac{\partial}{\partial t} (\bar{\sigma}_f^2) + \frac{\partial}{\partial t} (\bar{\sigma}_f^2) \left(1 + \frac{\bar{\tau}_n}{\bar{P}_{sm}}\right) + \bar{\sigma}_f^2 \frac{\dot{\bar{\tau}}_n}{\bar{P}_{sm}} - \bar{\sigma}_f^2 \frac{\bar{\tau}_n}{\bar{P}_{sm}^2} \dot{\bar{P}}_{sm} - \dot{f}_n \quad (3.5.70)$$

The time derivative of \bar{P}_{sm} is

$$\dot{\bar{P}}_{sm} = -\frac{1}{3} \dot{\bar{\tau}}_n - \frac{(\dot{\sigma}_{tt} + \dot{\sigma}_{pp})}{3\tau_{nf}} \quad (3.5.71)$$

Substitution of equation (3.5.71) into the expressions for \dot{B}_n and $\dot{\psi}$ in equations (3.5.70) and (3.5.69) respectively results in the following:

Chapter 3. The Governing Equations

$$\begin{aligned} \dot{B}_n = & \dot{\bar{\tau}}_n \left(1 + C_n \bar{\sigma}_f^2 + \frac{\bar{\sigma}_f^2}{\bar{P}_{sm}} + \frac{1}{3} \frac{\bar{\tau}_n \bar{\sigma}_f^2}{\bar{P}_{sm}^2} \right) + \frac{\partial}{\partial t} (\bar{\sigma}_f^2) \left(1 + \bar{\tau}_n C_n + \frac{\bar{\tau}_n}{\bar{P}_{sm}} \right) \\ & + \frac{1}{3} \frac{\bar{\tau}_n \bar{\sigma}_f^2}{\bar{P}_{sm}^2} \frac{(\dot{\sigma}_{tt} + \dot{\sigma}_{pp})}{\tau_{nf}} - \dot{f}_n \end{aligned} \quad (3.5.72)$$

$$\begin{aligned} \dot{\psi} = & - \frac{C_{f/m}}{(1 + C_s \bar{\sigma}_f^2)} \left[\dot{\bar{\tau}}_n \left(1 + C_n \bar{\sigma}_f^2 + \frac{\bar{\sigma}_f^2}{\bar{P}_{sm}} + \frac{1}{3} \frac{\bar{\tau}_n \bar{\sigma}_f^2}{\bar{P}_{sm}^2} \right) \right. \\ & + \frac{\partial}{\partial t} (\bar{\sigma}_f^2) \left(1 + \bar{\tau}_n C_n + \frac{\bar{\tau}_n}{\bar{P}_{sm}} - \frac{C_s B_n}{(1 + C_s \bar{\sigma}_f^2)} \right) \\ & \left. + \frac{1}{3} \frac{\bar{\tau}_n \bar{\sigma}_f^2}{\bar{P}_{sm}^2} \frac{(\dot{\sigma}_{tt} + \dot{\sigma}_{pp})}{\tau_{nf}} - \dot{f}_n \right] \end{aligned} \quad (3.5.73)$$

For the purposes of compactness, the following quantities are defined:

$$D_{\psi\sigma} = \frac{C_{f/m}}{(1 + C_s \bar{\sigma}_f^2)} D_\psi = \frac{(1 + 2C_\psi \psi)}{(1 + C_s \bar{\sigma}_f^2)} [1 - \tanh^2 [\psi (1 + C_\psi \psi)]] \quad (3.5.74)$$

$$D_{\tau n} = 1 + \frac{\bar{\sigma}_f^2}{\bar{P}_{sm}} \left(1 + C_n \bar{P}_{sm} + \frac{\bar{\tau}_n}{3\bar{P}_{sm}} \right) \quad (3.5.75)$$

$$D_{\bar{\sigma}} = 1 + \frac{\bar{\tau}_n}{\bar{P}_{sm}} (1 + C_n \bar{P}_{sm}) - \frac{C_s B_n}{(1 + C_s \bar{\sigma}_f^2)} \quad (3.5.76)$$

$$D_{ttpp} = \frac{1}{3} \frac{\bar{\tau}_n \bar{\sigma}_f^2 f_c}{\bar{P}_{sm}^2 \tau_{nf}} \quad (3.5.77)$$

$$\bar{\sigma}_{tt} = \frac{\sigma_{tt}}{f_c} \quad \bar{\sigma}_{pp} = \frac{\sigma_{pp}}{f_c} \quad (3.5.78)$$

Substitution of equations (3.5.74) - (3.5.78) into (3.5.73) yield the following result for $\dot{\psi}$:

Chapter 3. The Governing Equations

$$\dot{\psi} = -\frac{C_{f/m}}{(1 + C_s \bar{\sigma}_f^2)} \left[D_{\tau n} \dot{\bar{r}}_n + D_{\bar{\sigma}} \frac{\partial}{\partial t} (\bar{\sigma}_f^2) + D_{ttpp} (\dot{\bar{\sigma}}_{tt} + \dot{\bar{\sigma}}_{pp}) - \dot{f}_n \right] \quad (3.5.79)$$

The quantity, $\partial \bar{\sigma}_f^2 / \partial t$, in equation (3.5.79) is obtained from the material time derivative of equation (3.5.56) as follows:

$$\frac{\partial}{\partial t} (\bar{\sigma}_f^2) = \dot{f}_n \bar{\sigma}^2 + f_n \frac{\partial}{\partial t} (\bar{\sigma}^2) \quad (3.5.80)$$

Equation (3.5.80) is substituted into equation (3.5.79). The result is

$$\dot{\psi} = -\frac{C_{f/m}}{(1 + C_s \bar{\sigma}_f^2)} \left[D_{\tau n} \dot{\bar{r}}_n + D_{\bar{\sigma}} \frac{\partial}{\partial t} (\bar{\sigma}^2) f_n + D_{ttpp} (\dot{\bar{\sigma}}_{tt} + \dot{\bar{\sigma}}_{pp}) - (1 - D_{\bar{\sigma}} \bar{\sigma}^2) \dot{f}_n \right] \quad (3.5.81)$$

The material time derivative of $\bar{\sigma}^2$ is

$$\frac{\partial (\bar{\sigma}^2)}{\partial t} = \frac{1}{(f'_c)^2} [\dot{\sigma}_{tt} (2\sigma_{tt} + \chi \sigma_{pp}) + \dot{\sigma}_{pp} (2\sigma_{pp} + \chi \sigma_{tt}) + 2(2 - \chi) \dot{\sigma}_{tp} \sigma_{tp}] \quad (3.5.82)$$

Equation (3.5.82) is substituted into (3.5.81) to give the following result for $\dot{\psi}$:

$$\dot{\psi} = -\frac{C_{f/m}}{(1 + C_s \bar{\sigma}_f^2)} \left[\begin{aligned} & D_{\tau n} \dot{\bar{r}}_n + \left(\frac{D_{\bar{\sigma}}}{(f'_c)^2} (2\sigma_{tt} + \chi \sigma_{pp}) f_n + \frac{D_{ttpp}}{f'_c} \right) \dot{\sigma}_{tt} \\ & + \left(\frac{D_{\bar{\sigma}}}{(f'_c)^2} (2\sigma_{pp} + \chi \sigma_{tt}) f_n + \frac{D_{ttpp}}{f'_c} \right) \dot{\sigma}_{pp} \\ & + \frac{D_{\bar{\sigma}}}{(f'_c)^2} 2(2 - \chi) \sigma_{tp} \dot{\sigma}_{tp} \\ & - (1 - D_{\bar{\sigma}} \bar{\sigma}^2) \dot{f}_n \end{aligned} \right] \quad (3.5.83)$$

Chapter 3. The Governing Equations

An alternative expression for $\bar{\tau}_s^2$ is

$$\bar{\tau}_s^2 = \frac{1}{\tau_{sf}^2} (\tau_t^2 + \tau_p^2) \quad (3.5.84)$$

The time derivative of equation (3.5.84) is

$$\frac{\partial}{\partial t} (\bar{\tau}_s^2) = \frac{2}{\tau_{sf}^2} (\tau_t \dot{\tau}_t + \tau_p \dot{\tau}_p) \quad (3.5.85)$$

Equation (3.5.83) and (3.5.85) are substituted into the expression for \dot{F}_n in equation (3.5.67). The result is.

$$\dot{F}_n = \frac{2}{\tau_{sf}^2} \tau_t \dot{\tau}_t + \frac{2}{\tau_{sf}^2} \tau_p \dot{\tau}_p + D_{\psi\sigma} \left[\begin{array}{l} \frac{D_{\tau n}}{\tau_{nf}} \dot{\tau}_n + \left(\frac{D_{\bar{\sigma}}}{(f'_c)^2} (2\sigma_{tt} + \chi\sigma_{pp}) f_n + \frac{D_{ttpp}}{f'_c} \right) \dot{\sigma}_{tt} \\ + \left(\frac{D_{\bar{\sigma}}}{(f'_c)^2} (2\sigma_{pp} + \chi\sigma_{tt}) f_n + \frac{D_{ttpp}}{f'_c} \right) \dot{\sigma}_{pp} \\ + \frac{D_{\bar{\sigma}}}{(f'_c)^2} 2(2 - \chi) \sigma_{tp} \dot{\sigma}_{tp} \\ - (1 - D_{\bar{\sigma}} \bar{\sigma}^2) \dot{f}_n \end{array} \right] \quad (3.5.86)$$

A time derivative of F_n is also expressed in general terms by use of the chain rule, as follows:

$$\dot{F}_n = \frac{\partial F_n}{\partial \tau_t} \dot{\tau}_t + \frac{\partial F_n}{\partial \tau_p} \dot{\tau}_p + \frac{\partial F_n}{\partial \tau_n} \dot{\tau}_n + \frac{\partial F_n}{\partial \sigma_{tt}} \dot{\sigma}_{tt} + \frac{\partial F_n}{\partial \sigma_{pp}} \dot{\sigma}_{pp} + \frac{\partial F_n}{\partial \sigma_{tp}} \dot{\sigma}_{tp} + \frac{\partial F_n}{\partial f_n} \dot{f}_n \quad (3.5.87)$$

The expressions in equations (3.5.86) and (3.5.87) are equated, and by inspection, the partial derivatives in equation (3.5.86) are deduced to be

Chapter 3. The Governing Equations

$$\frac{\partial F_n}{\partial \tau_n} = \frac{D_{\psi\sigma} D_{\tau n}}{\tau_{nf}}, \quad \frac{\partial F_n}{\partial \tau_t} = \frac{2}{\tau_{sf}^2} \tau_t, \quad \frac{\partial F_n}{\partial \tau_p} = \frac{2}{\tau_{sf}^2} \tau_p \quad (3.5.88)$$

$$\frac{\partial F_n}{\partial \sigma_{tt}} = \frac{D_{\psi\sigma}}{(f'_c)^2} \left(D_{\bar{\sigma}} (2\sigma_{tt} + \chi\sigma_{pp}) f_n + f'_c D_{ttpp} \right) \quad (3.5.89)$$

$$\frac{\partial F_n}{\partial \sigma_{pp}} = \frac{D_{\psi\sigma}}{(f'_c)^2} \left(D_{\bar{\sigma}} (2\sigma_{pp} + \chi\sigma_{tt}) f_n + f'_c D_{ttpp} \right) \quad (3.5.90)$$

$$\frac{\partial F_n}{\partial \sigma_{tp}} = \frac{D_{\psi\sigma} D_{\bar{\sigma}}}{(f'_c)^2} 2(2 - \chi) \sigma_{tp} \quad (3.5.91)$$

$$\frac{\partial F_n}{\partial f_n} = -D_{\psi\sigma} (1 - D_{\bar{\sigma}} \bar{\sigma}^2) \quad (3.5.92)$$

Equations (3.5.88) - (3.5.92) are substituted into the equations in (3.5.66) to give the following result for the evolution of the components of $[[\dot{\mathbf{u}}]]$:

$$\dot{u}_n = \dot{\omega} \frac{D_{\psi\sigma} D_{\tau n}}{\tau_{nf}}, \quad \dot{u}_t = \dot{\omega} \frac{2}{\tau_{sf}^2} \tau_t, \quad \dot{u}_p = \dot{\omega} \frac{2}{\tau_{sf}^2} \tau_p \quad (3.5.93)$$

The discrete constitutive model for geological materials is summarized. The traction on a surface with normal \mathbf{n} is defined to be $\boldsymbol{\tau} = \boldsymbol{\sigma} \cdot \mathbf{n}$. A de-cohesion function of stress $F_n(\boldsymbol{\sigma})$ is defined in equations (3.5.49) - (3.5.57) such that initiation of a failure plane with normal \mathbf{n} coincides with a zero value for $F_n(\boldsymbol{\sigma})$ when maximized over all possible orientations. A traction-displacement relationship in equation (3.2.28) is used to relate $\boldsymbol{\tau}$ to $[[\mathbf{u}]]$ on the failure surface defined by \mathbf{n} . The displacement discontinuity $[[\mathbf{u}]]$ evolves according to the associative flow rule in (3.5.64) while the consistency condition is maintained. In general, the complete set of equations is as follows:

$$\begin{aligned}
 F &= \max_{\forall \mathbf{n}} F_n(\boldsymbol{\sigma}) = 0 \quad (\text{failure initiation criterion}) \\
 \boldsymbol{\tau} &= \boldsymbol{\tau}([\![\mathbf{u}]\!]) \quad (\text{traction – separation law}) \\
 [\![\dot{\mathbf{u}}]\!] &= \dot{\omega} \frac{\partial F_n}{\partial \boldsymbol{\tau}} \quad (\text{evolution of displacement jump}) \\
 \dot{F}_n(\boldsymbol{\sigma}, [\![\mathbf{u}]\!]) &= 0 \quad (\text{consistency condition})
 \end{aligned} \tag{3.5.94}$$

3.5.4 A Continuum Representation of Material Failure

Although the set of equations in (3.5.94) only apply to a discrete failure surface of material defined by \mathbf{n} , discrete constitutive models can be applied to continuum problems of material failure within the framework of strong discontinuity kinematics (see section 3.5.2). Recall the composition of strain in the presence of a displacement discontinuity across the failure region, $\Gamma \in \Omega$ (see figure 3.4), stated in equation (3.5.35) and repeated below for convenience.

$$\boldsymbol{\varepsilon}(\mathbf{x}, t) = \bar{\boldsymbol{\varepsilon}}(\mathbf{x}, t) + \frac{1}{L_c} \mu_\Gamma([\![\mathbf{u}]\!] \otimes \mathbf{n})^S$$

The strain field in Ω is

$$\begin{aligned}
 \boldsymbol{\varepsilon} &= \bar{\boldsymbol{\varepsilon}} & \forall \mathbf{x} \in \Omega/\Gamma \\
 \boldsymbol{\varepsilon} &= \bar{\boldsymbol{\varepsilon}} + \frac{1}{L_c}([\![\dot{\mathbf{u}}]\!] \otimes \mathbf{n})^S & \forall \mathbf{x} \in \Gamma
 \end{aligned} \tag{3.5.95}$$

The effect of material failure is incorporated into a continuum problem through the use of an inelastic strain. In analogy to small deformation inelasticity, an additive decomposition of elastic and inelastic strain contributions is assumed as follows:

Chapter 3. The Governing Equations

$$\boldsymbol{\varepsilon} = \boldsymbol{\varepsilon}^e + \boldsymbol{\varepsilon}^{dc} \quad (3.5.96)$$

The inelastic strain component, $\boldsymbol{\varepsilon}^{dc}$, referred to as the de-cohesion strain, represents the deformation due to failure in Γ . The strain contributions within Ω are as follows:

$$\begin{aligned} \boldsymbol{\varepsilon} &= \boldsymbol{\varepsilon}^e & \forall \mathbf{x} \in \Omega/\Gamma \\ \boldsymbol{\varepsilon} &= \boldsymbol{\varepsilon}^e + \boldsymbol{\varepsilon}^{dc} & \forall \mathbf{x} \in \Gamma \end{aligned} \quad (3.5.97)$$

Compatibility of the continuum strain representation of failure in equation (3.5.97) with the strong discontinuity kinematics in equation (3.5.95) requires the following relationship for the de-cohesion strain:

$$\boldsymbol{\varepsilon}^{dc} = \frac{1}{L_c} ([[\mathbf{u}]]) \otimes \mathbf{n})^S \quad (3.5.98)$$

Stress is computed from linear elasticity everywhere in Ω to be

$$\boldsymbol{\sigma} = \mathbf{C} : (\boldsymbol{\varepsilon} - \boldsymbol{\varepsilon}^{dc}) \quad (3.5.99)$$

The evolution of the displacement discontinuity, $[[\dot{\mathbf{u}}]]$, is governed by equation (3.5.64) as follows:

$$[[\dot{\mathbf{u}}]]) = \dot{\omega} \frac{\partial F_n}{\partial \boldsymbol{\tau}}$$

It follows from equation (3.5.98) that the rate of de-cohesion strain, $\dot{\boldsymbol{\varepsilon}}^{dc}$, is

$$\dot{\boldsymbol{\varepsilon}}^{dc} = \frac{1}{L_c} ([[\dot{\mathbf{u}}]]) \otimes \mathbf{n})^S \quad (3.5.100)$$

Chapter 3. The Governing Equations

while the consistency condition of equation (3.5.65) is enforced for the de-cohesion function $F_n(\boldsymbol{\sigma})$ as follows:

$$\dot{F}_n(\boldsymbol{\sigma}) = 0$$

Equations (3.5.99), (3.5.64), (3.5.100) and (3.5.65) comprise the complete set of equations governing the continuum representation of the elastic de-cohesive constitutive model of section 3.5.3.

3.6 The Initial Boundary Value Problem

The complete set of equations for the initial boundary value problem are presented for the deformable solid body Ω with boundary $\partial\Omega$ depicted in figure 3.1. The local form of the conservation of linear momentum from equation (3.5.10) is restated as follows:

$$\rho \dot{\mathbf{v}} = \nabla \cdot \boldsymbol{\sigma} + \rho \mathbf{b} \quad \forall \quad \mathbf{x} \in \Omega, \quad t \geq 0 \quad (3.6.1)$$

Initial and boundary conditions must be specified for a well-posed problem. At $t = 0$, $\mathbf{x} = \mathbf{X}$ and the following initial conditions are prescribed for the displacement \mathbf{u} and velocity \mathbf{v} :

$$\begin{aligned} \mathbf{u}(\mathbf{x}, 0) &= \mathbf{u}_0(\mathbf{X}) \quad \forall \quad \mathbf{X} \in \Omega_0 \\ \mathbf{v}(\mathbf{x}, 0) &= \mathbf{v}_0(\mathbf{X}) \quad \forall \quad \mathbf{X} \in \Omega_0 \end{aligned} \quad (3.6.2)$$

The boundary is divided into two sets of points such that, $\partial\Omega = \partial\Omega^u \cup \partial\Omega^t$. The displacement (or essential) boundary conditions are applied to $\partial\Omega^u$ and the traction

Chapter 3. The Governing Equations

boundary conditions are applied to $\partial\Omega^t$ as follows:

$$\begin{aligned}\mathbf{u}(\mathbf{x}, t) &= \mathbf{g}(t) \quad \forall \mathbf{x} \in \partial\Omega^u, \quad t \geq 0 \\ \boldsymbol{\tau}(\mathbf{x}, t) &= \mathbf{h}(t) \quad \forall \mathbf{x} \in \partial\Omega^t, \quad t \geq 0\end{aligned}\tag{3.6.3}$$

The constitutive model (or kinetic relations) completes the set of equations for the initial boundary value problem by relating stress $\boldsymbol{\sigma}$ to strain $\boldsymbol{\varepsilon}$. In order to incorporate the failure region $\Gamma \subset \Omega$ (see figure 3.4), the elastic de-cohesive constitutive model of section 3.5.3 is applied to the continuum problem within the framework of strong discontinuity kinematics as discussed in section 3.5.4. The constitutive model is summarized in rate form as follows:

$$\begin{aligned}\dot{\boldsymbol{\sigma}} &= \mathbf{C} : \dot{\boldsymbol{\varepsilon}} && \forall \mathbf{x} \in \Omega/\Gamma \\ \left. \begin{aligned}\dot{\boldsymbol{\sigma}} &= \mathbf{C} : (\dot{\boldsymbol{\varepsilon}} - \dot{\boldsymbol{\varepsilon}}^{dc}) \\ [[\dot{\mathbf{u}}]] &= \dot{\omega} \frac{\partial F_n}{\partial \boldsymbol{\tau}} \\ \dot{\boldsymbol{\varepsilon}}^{dc} &= \frac{1}{L_c} ([[\dot{\mathbf{u}}]] \otimes \mathbf{n})^S \\ \dot{F}_n(\boldsymbol{\sigma}, [[\mathbf{u}]]) &= 0\end{aligned}\right\} && \forall \mathbf{x} \in \Gamma\end{aligned}\tag{3.6.4}$$

The specific form of the de-cohesion function $F_n(\boldsymbol{\sigma})$ in equation (3.6.4) is taken from equations (3.5.49) - (3.5.57).

Equations (3.6.1) - (3.6.4) complete the closed set of equations that form the initial boundary value problem. The numerical solution method to the initial boundary value problem is presented next.

Chapter 4

Numerical Modeling with the Material-point Method

4.1 Introduction

The material-point method (MPM) is a computational particle-in-cell based method of solving solid mechanics problems that uses both material and spatial representations of the problem. MPM was developed at the University of New Mexico [67], [71], [68] as an extension of the FLIP method, developed and used at Los Alamos National Laboratory to simulate fluid flow [12]. A solid body is represented by discrete material points that move relative to a computational grid that represents space. Material quantities are carried by the material points and are transferred between material points and grid nodes throughout the computation. The grid does not retain any information, but provides an updated material reference frame that is used to update the motion of the material points and compute spatial gradients.

MPM extends the range of application of computational solid mechanics to encompass large deformation dynamic problems that can pose difficulty to purely Lagrangian computational solid mechanics methods. An advantage is gained from the use of both Lagrangian and Eulerian representations. The use of a Lagrangian description to solve the momentum equation eliminates the nonlinear convective acceleration terms that arise in Eulerian methods. The Eulerian grid serves only as an updated Lagrangian frame for updating the material point quantities. Interpenetration of material points is precluded. These advantages allow for robust simulations of large deformation processes encountered in problems of penetration and impact [71], [68], contact between multiple deformable bodies [2] and manufacturing problems such as metal forming and upsetting [66] that cause severe mesh tangling in purely Lagrangian methods.

Particular attributes of MPM make the method attractive for simulating material separation. There is no connectivity imposed between material points, so the separation of material can be handled naturally by the method. Since interpenetration of

material points is not allowed, the method would not require additional algorithms for treating contact between already failed material surfaces. Successful explicit MPM simulations of dynamic material failure has been demonstrated using both smeared crack representations of failure [69] and explicit crack representation [38]. Recently implicit dynamic MPM has been used to simulate the process of lead formation (cracks) associated with the motion of sea ice [70], [47] using a smeared crack failure representation. This work has motivated the present study of the smeared crack approach to computational failure in MPM.

The computational method is presented in this chapter. The discrete MPM momentum equations are derived in section 4.2. A general MPM implementation is described in section 4.3. Specific considerations for a 2D and an axisymmetric MPM implementation are provided in section 4.4. Section 4.5 presents the implementation of the discrete constitutive model for failure.

4.2 The Discrete MPM Equations

MPM involves the discretization of space, denoted by $\mathbf{x} \in \mathbb{R}^3$, and the body of solid material $\Omega \subset \mathbb{R}^3$. Space is discretized by a set of grid cells connected by the set of N_n grid node positions $\{\mathbf{x}_i\}_{i=1}^{N_n}$. The solid body is discretized by the set of N_p material points $\{\mathbf{X}_p\}_{p=1}^{N_p} \subset \Omega$. The subscripts i and p will be used to denote quantities associated with grid nodes and material points respectively.

Each material point is associated with a discrete mass M_p that remains constant through time, t . The total mass, m , of the body Ω is simply $m = \sum_{p=1}^{N_p} M_p$. In MPM the mass density, $\rho(\mathbf{x}, t)$, is represented as a distribution of discrete material point masses using the Dirac delta distribution $\delta(\mathbf{x})$ as follows:

$$\rho(\mathbf{x}, t) = \sum_{p=1}^{N_p} M_p \delta(\mathbf{x} - \mathbf{X}_p) \quad (4.2.1)$$

The total mass, m , of the body Ω is obtained by the integration of the mass density over the volume V of the body Ω . By use of the integration property of $\delta(\mathbf{x})$, m is obtained by integration of (4.2.1) as follows:

$$\begin{aligned} \int_{\Omega} \rho(\mathbf{x}, t) dV &= \int_{\Omega} \sum_{p=1}^{N_p} M_p \delta(\mathbf{x} - \mathbf{X}_p) dV \\ &= \sum_{p=1}^{N_p} M_p \int_{\Omega} \delta(\mathbf{x} - \mathbf{X}_p) dV \\ &= \sum_{p=1}^{N_p} M_p \\ &= m \end{aligned} \quad (4.2.2)$$

The discrete set of MPM equations are obtained from the weak form of the conservation of momentum in equation (3.5.26). The weak form of momentum is restated below to be

$$\int_{\Omega} \rho \mathbf{w} \cdot \dot{\mathbf{v}} dV = - \int_{\Omega} \rho \nabla \mathbf{w} : \boldsymbol{\sigma}^s dV + \int_{\partial\Omega} \mathbf{w} \cdot \boldsymbol{\tau} dA + \int_{\Omega} \rho \mathbf{w} \cdot \mathbf{b} dV \quad (4.2.3)$$

where the specific stress $\boldsymbol{\sigma}_s$ is defined to be $\boldsymbol{\sigma}_s = \boldsymbol{\sigma}/\rho$.

Substitution of (4.2.1) into (4.2.3) replaces the integrals in (4.2.3) with sums of material quantities evaluated at the material point positions \mathbf{X}_p at any time t as follows:

$$\begin{aligned}
 \sum_{p=1}^{N_p} M_p \mathbf{w}(\mathbf{X}_p, t) \cdot \dot{\mathbf{v}}(\mathbf{X}_p, t) &= - \sum_{p=1}^{N_p} M_p \boldsymbol{\sigma}^s(\mathbf{X}_p, t) : \nabla \mathbf{w}(\mathbf{X}_p, t) \\
 &+ \int_{\partial\Omega} \mathbf{w}(\mathbf{x}, t) \cdot \boldsymbol{\tau}(\mathbf{x}, t) dA \\
 &+ \sum_{p=1}^{N_p} M_p \mathbf{w}(\mathbf{X}_p, t) \cdot \mathbf{b}(\mathbf{X}_p, t) \quad (4.2.4)
 \end{aligned}$$

Some quantities in equation (4.2.4) are approximated with standard finite element nodal basis functions, $N_i(\mathbf{x})$, $i = 1, 2, \dots, N_n$ which satisfy the partition of unity property, $\sum_{i=1}^{N_n} N_i(\mathbf{x}) = 1$. The velocity \mathbf{v} , acceleration $\dot{\mathbf{v}}$ and the test function \mathbf{w} approximations are

$$\mathbf{v}(\mathbf{x}, t) = \sum_{i=1}^{N_n} \mathbf{v}_i(t) N_i(\mathbf{x}) \quad (4.2.5)$$

$$\dot{\mathbf{v}}(\mathbf{x}, t) = \sum_{i=1}^{N_n} \dot{\mathbf{v}}_i(t) N_i(\mathbf{x}) \quad (4.2.6)$$

$$\mathbf{w}(\mathbf{x}, t) = \sum_{i=1}^{N_n} \mathbf{w}_i(t) N_i(\mathbf{x}) \quad (4.2.7)$$

The approximations in equations (4.2.5) - (4.2.7) are substituted into (4.2.4). The result is

$$\begin{aligned}
 \sum_{i=1}^{N_n} \sum_{j=1}^{N_n} \sum_{p=1}^{N_p} M_p \mathbf{w}_i \cdot \dot{\mathbf{v}}_j N_i(\mathbf{X}_p) N_j(\mathbf{X}_p) &= - \sum_{i=1}^{N_n} \sum_{p=1}^{N_p} M_p \boldsymbol{\sigma}_p^s : (\mathbf{w}_i \otimes \nabla N_i(\mathbf{X}_p)) \\
 &+ \sum_{i=1}^{N_n} \int_{\partial\Omega} \mathbf{w}_i \cdot \boldsymbol{\tau}(\mathbf{x}, t) N_i(\mathbf{x}) dA \\
 &+ \sum_{i=1}^{N_n} \sum_{p=1}^{N_p} M_p \mathbf{w}_i \cdot \mathbf{b}(\mathbf{X}_p, t) N_i(\mathbf{X}_p) \quad (4.2.8)
 \end{aligned}$$

Further simplification of (4.2.8) results in the following:

$$\begin{aligned}
 \sum_{i=1}^{N_n} \mathbf{w}_i \cdot \sum_{j=1}^{N_n} \sum_{p=1}^{N_p} M_p \dot{\mathbf{v}}_j N_i(\mathbf{X}_p) N_j(\mathbf{X}_p) &= - \sum_{i=1}^{N_n} \mathbf{w}_i \cdot \sum_{p=1}^{N_p} M_p \boldsymbol{\sigma}_p^s \cdot \nabla N_i(\mathbf{X}_p) \\
 &+ \sum_{i=1}^{N_n} \mathbf{w}_i \cdot \int_{\partial\Omega} \boldsymbol{\tau}(\mathbf{x}, t) N_i(\mathbf{x}) dA \\
 &+ \sum_{i=1}^{N_n} \mathbf{w}_i \cdot \sum_{p=1}^{N_p} M_p \mathbf{b}(\mathbf{X}_p, t) N_i(\mathbf{X}_p) \quad (4.2.9)
 \end{aligned}$$

Since (4.2.9) holds for all \mathbf{w}_i , discrete MPM equations reduce to the following:

$$\begin{aligned}
 \sum_{j=1}^{N_n} \sum_{p=1}^{N_p} M_p \dot{\mathbf{v}}_j N_i(\mathbf{X}_p) N_j(\mathbf{X}_p) &= - \sum_{p=1}^{N_p} M_p \boldsymbol{\sigma}_p^s \cdot \nabla N_i(\mathbf{X}_p) \\
 &+ \int_{\partial\Omega} \boldsymbol{\tau}(\mathbf{x}, t) N_i(\mathbf{x}) dA \\
 &+ \sum_{p=1}^{N_p} M_p \mathbf{b}(\mathbf{X}_p, t) N_i(\mathbf{X}_p) \quad (4.2.10)
 \end{aligned}$$

The mass matrix, m_{ij} , is defined to be

$$m_{ij} = \sum_{p=1}^{N_p} M_p N_i(\mathbf{X}_p) N_j(\mathbf{X}_p) \quad (4.2.11)$$

The internal forces at the nodes are defined as follows:

$$\mathbf{f}_i^{int} = - \sum_{p=1}^{N_p} M_p \boldsymbol{\sigma}_p^s \cdot \nabla N_i(\mathbf{X}_p) \quad (4.2.12)$$

The external forces at the nodes are

$$\mathbf{f}_i^{ext} = \mathbf{b}_i + \hat{\boldsymbol{\tau}}_i \quad (4.2.13)$$

where $\hat{\boldsymbol{\tau}}_i$ represents the external force contribution from the traction applied on the boundary and is computed to be

$$\hat{\boldsymbol{\tau}}_i = \int_{\partial\Omega} \boldsymbol{\tau}(\mathbf{x}, t) N_i(\mathbf{x}) dA \quad (4.2.14)$$

and \mathbf{b}_i is the external force contribution from body forces computed to be

$$\mathbf{b}_i = \sum_{p=1}^{N_p} M_p \mathbf{b}(\mathbf{X}_p, t) N_i(\mathbf{X}_p) \quad (4.2.15)$$

Equation (4.2.10) is simplified using (4.2.11) – (4.2.15). The resulting grid node equation is

$$\sum_{j=1}^{N_n} m_{ij} \dot{\mathbf{v}}_j = \mathbf{f}_i^{int} + \mathbf{f}_i^{ext} \quad (4.2.16)$$

A simplification is made to the mass matrix m_{ij} by using a mass lumping technique. Using row sums of m_{ij} and the partition of unity property of the basis functions $N_i(\mathbf{X}_p)$, a simpler diagonalized mass matrix m_i is obtained. This simplification leads to the following:

$$m_i = \sum_{p=1}^{N_p} M_p N_i(\mathbf{X}_p) \quad (4.2.17)$$

The mass lumping approximation in equation (4.2.17), is used to simplify equation (4.2.16) to the following:

$$m_i \dot{\mathbf{v}}_i = \mathbf{f}_i^{int} + \mathbf{f}_i^{ext} \quad (4.2.18)$$

Equation (4.2.18) can also be rewritten in terms of momentum as the following:

$$\dot{\mathbf{p}}_i = \mathbf{f}_i^{int} + \mathbf{f}_i^{ext} \quad (4.2.19)$$

The system of MPM grid node equations represented by equations (4.2.18) and (4.2.19) must be discretized temporally in order to obtain solutions at discrete times. A discrete time is denoted by t^k ($k = 1, 2, \dots$), and the time step is computed to be $\Delta t = t^{k+1} - t^k$. Quantities associated with a discrete time t^k are denoted with the superscript k . Each discrete time, t^k , corresponds to a discrete configuration, $\Omega(t^k)$, of the solid body.

MPM is an updated Lagrangian numerical method. In this type of approach the grid solution to (4.2.18) or (4.2.19) at the current time step is computed with respect to an updated Lagrangian (material) reference frame. Quantities associated with the current time step are denoted by the superscript L . The material quantities associated with $\Omega(t^L)$ are functions of material positions in the previous discrete configuration, $\mathbf{X}^k \in \Omega(t^k)$. For this reason the method is considered to be updated.

Formulation of the discrete MPM equations in terms of momentum is preferable over a velocity formulation because it leads to a more robust computational method [71]. Consequently, equation (4.2.19) is utilized for time discretization. The following time integration scheme, taken from Sulsky and Kaul [66], is applied to equation (4.2.19):

$$\dot{\mathbf{p}}_i^L \cong \frac{\mathbf{p}_i^L - \mathbf{p}_i^k}{\Delta t} = (\mu \mathbf{f}_i^L + (1 - \mu) \mathbf{f}_i^k) \quad (4.2.20)$$

In equation (4.2.20) \mathbf{f}_i^L and \mathbf{f}_i^k are defined to be

$$\mathbf{f}_i^L = \mathbf{f}_i^{int L} + \mathbf{f}_i^{ext L}, \quad \mathbf{f}_i^k = \mathbf{f}_i^{int k} + \mathbf{f}_i^{ext k} \quad (4.2.21)$$

The quantity μ in equation (4.2.20) is a weighting factor for which $0 \leq \mu \leq 1$. If $\mu = 0$ then the integration scheme is purely explicit. If $\mu = 1$ then the time integration scheme is purely implicit.

4.3 General Implementation of MPM

Numerical implementation of the MPM algorithm is summarized. A single MPM computational cycle (time step) incorporates three phases; the initialization phase, the Lagrangian phase and the convective phase. The material point quantities available from the previous (k th) time step are \mathbf{X}_p^k , \mathbf{V}_p^k , $\boldsymbol{\varepsilon}_p^k$ and $\boldsymbol{\sigma}_p^{s,k}$. Solution to these quantities at the next $k+1$ time step are obtained at the end of the computational cycle.

During the initialization phase the grid node quantities \mathbf{p}_i^k , $\mathbf{f}_i^{int,k}$ and $\mathbf{f}_i^{ext,k}$ are computed for time t^k . The grid momentum, \mathbf{p}_i^k , is obtained by mapping the momentum from the material points to the grid. The mapping is based on the following mass weighted least squares relationship between the material points and nodal velocities:

$$m_i^k \mathbf{v}_i^k = \sum_{p=1}^{N_p} M_p \mathbf{V}_p^k N_i(\mathbf{X}_p^k) \quad (4.3.1)$$

The grid momentum, \mathbf{p}_i^k , is taken to be the left hand side of equation (4.3.1) as follows:

$$\mathbf{p}_i^k = m_i^k \mathbf{v}_i^k \quad (4.3.2)$$

The material point momentum, \mathbf{P}_p^k , is

$$\mathbf{P}_p^k = M_p \mathbf{V}_p^k \quad (4.3.3)$$

Upon substitution of (4.3.2) and (4.3.3) into (4.3.1), the grid momentum is computed to be

$$\mathbf{p}_i^k = \sum_{p=1}^{N_p} \mathbf{P}_p^k N_i(\mathbf{X}_p^k) \quad (4.3.4)$$

The internal and external forces on the grid, $\mathbf{f}_i^{int\ k}$ and $\mathbf{f}_i^{ext\ k}$, are computed from equations (4.2.12) and (4.2.13) respectively. The nodal lumped mass matrix, m_i^k , is computed from equation (4.2.17).

During the Lagrangian phase of the computational cycle equation (4.2.20) is solved for \mathbf{p}_i^L . The updated Lagrangian grid solution is then used to update the material point positions and velocities. Since the momentum of points within the grid cells can be represented by the nodal momentum and element basis functions the material point positions are updated as follows:

$$\mathbf{X}_p^L = \mathbf{X}_p^k + \Delta t \sum_{i=1}^{N_n} \frac{1}{m_i^k} \mathbf{p}_i^L N_i(\mathbf{X}_p^k) \quad (4.3.5)$$

The material point velocity is updated in a similar manner by using the time rate of change of momentum (total force) as follows:

$$\mathbf{V}_p^L = \mathbf{V}_p^k + \Delta t \sum_{i=1}^{N_n} \frac{1}{m_i^k} \dot{\mathbf{p}}_i^L N_i(\mathbf{X}_p^k) \quad (4.3.6)$$

The material point position and velocity updates in equations (4.3.5) and (4.3.6) are computed within single-valued continuous velocity and acceleration fields provided by the nodal solutions. This type of update precludes interpenetration of material

points and ensures that the material points move in proportion to the motion of the grid cells.

Increments of material point strain are computed from gradients of the updated Lagrangian velocity field. The nodal values of the updated velocity field, denoted by \mathbf{v}_i^L , are obtained by mapping the updated velocity on material points, \mathbf{V}_p^L , to grid nodes using equation (4.3.1) as follows:

$$\mathbf{v}_i^L = \frac{1}{m_i^k} \sum_{p=1}^{N_p} M_p \mathbf{V}_p^L N_i(\mathbf{X}_p^k) \quad (4.3.7)$$

The strain increment is computed by multiplying the symmetric gradient of the Lagrangian velocity solution in equation (4.2.5) by the time step. The result is

$$\Delta \boldsymbol{\varepsilon}_p = \frac{\Delta t}{2} \sum_{i=1}^{N_n} \left[\nabla N_i(\mathbf{X}_p^k) \otimes \mathbf{v}_i^L + (\nabla N_i(\mathbf{X}_p^k) \otimes \mathbf{v}_i^L)^T \right] \quad (4.3.8)$$

The material point strain is updated as follows:

$$\boldsymbol{\varepsilon}_p^L = \boldsymbol{\varepsilon}_p^k + \Delta \boldsymbol{\varepsilon}_p \quad (4.3.9)$$

The increment in stress is computed by evaluation of the constitutive model. This computation is presented in the following section but for now the stress increment computation is expressed symbolically as the following:

$$\Delta \boldsymbol{\sigma}_p^s = \Delta \boldsymbol{\sigma}_p^s(\Delta \boldsymbol{\varepsilon}_p) \quad (4.3.10)$$

The updated stress is

$$\boldsymbol{\sigma}_p^{s,L} = \boldsymbol{\sigma}_p^{s,k} + \Delta \boldsymbol{\sigma}_p^s \quad (4.3.11)$$

For this study the solution to the discrete set MPM equations in (4.2.20) is obtained using methods of implicit dynamics in MPM [66]. In general equation (4.2.20) is non-linear in \mathbf{p}_i^L and requires an iterative solution involving equations (4.3.6) - (4.3.11). The details of the solution method and procedure are provided in Appendix A.

The convective phase of the computational step is when the material points are held fixed and the grid nodes move relative to the material. During this phase, the grid is redefined. Typically the nodal positions are moved back to their original position. The material point quantities at the $k+1$ time step are equal to the updated material point quantities at the end of the Lagrangian step. The result is

$$\mathbf{X}_p^{k+1} = \mathbf{X}_p^L, \quad \mathbf{V}_p^{k+1} = \mathbf{V}_p^L, \quad \boldsymbol{\varepsilon}_p^{k+1} = \boldsymbol{\varepsilon}_p^L, \quad \boldsymbol{\sigma}_p^{s,k+1} = \boldsymbol{\sigma}_p^{s,L} \quad (4.3.12)$$

4.4 Two Dimensional & Axisymmetric Implementation of MPM

Two-dimensional and axisymmetric MPM implementations are based on a logically rectangular background grid containing four-node elements. In two dimensions the rectangular Cartesian coordinates, (x, y) define a plane. Many three dimensional problems in cylindrical coordinates (r, θ, z) are reduced to plane problems due to the symmetrical nature of the geometry and loading about the axis of symmetry z , for which the solution is identical for all θ . As a result, only the axisymmetric plane (r, z) is considered. Throughout the developments of the present section, the two-dimensional coordinates (x, y) are used but can be replaced by the axisymmetric coordinates (r, z) without loss of generality. For certain quantities, the out of plane θ components enter into the formulation, and are treated explicitly in cylindrical coordinates.

The master element for the four node quad elements are shown in figure 4.1 in terms of the local element coordinates, (ξ, η) , for which $-1 \leq \xi \leq 1$, $-1 \leq \eta \leq 1$.

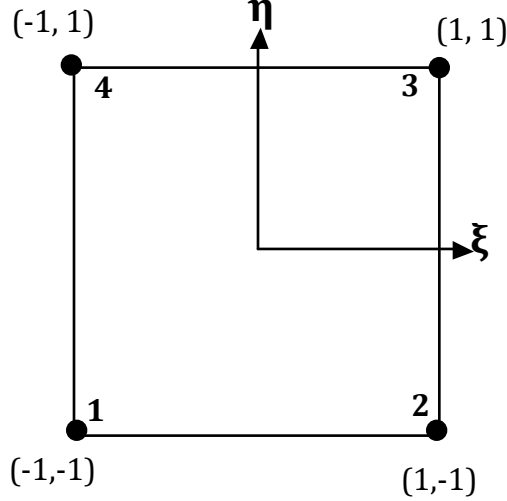


Figure 4.1: 2-D Master Element

The nodal basis functions corresponding to the node numbering in figure 4.1 are

$$\begin{aligned}
 N_1(\xi, \eta) &= \frac{1}{4}(1 - \xi)(1 - \eta) \\
 N_2(\xi, \eta) &= \frac{1}{4}(1 + \xi)(1 - \eta) \\
 N_3(\xi, \eta) &= \frac{1}{4}(1 + \xi)(1 + \eta) \\
 N_4(\xi, \eta) &= \frac{1}{4}(1 - \xi)(1 + \eta)
 \end{aligned} \tag{4.4.1}$$

During the convective phase of the computation, elements in which material points reside must be updated. The domain of a home element for a given material point \mathbf{X}_p at the k^{th} time step is denoted by Ω_e^k . If the updated material point position at the current time $k + 1$ does not lie within the domain of the its home element at the previous time Ω_e^k (i.e. $(\xi(\mathbf{X}_p^{k+1}), \eta(\mathbf{X}_p^{k+1}))_p^{k+1} \notin \Omega_e^k = \{-1 \leq \xi \leq 1 \quad -1 \leq \eta \leq 1\}_e^k$), then a neighboring element is searched for the updated coordinate. The choice of which neighbor element to search is based on the

position (in natural coordinates (ξ, η)) of the material point with respect to the element center of Ω_e^k . The neighbor search process continues until Ω_e^{k+1} is located, for which $(\xi(\mathbf{X}_p^{k+1}), \eta(\mathbf{X}_p^{k+1}))_p^{k+1} \in \Omega_e^{k+1} = \{-1 \leq \xi \leq 1 \quad -1 \leq \eta \leq 1\}_e^{k+1}$ is satisfied. Once the residing elements have been located for all material points the convective phase of the computation is concluded.

The element search algorithm requires element neighbor data for each element. The necessary information is stored in two arrays. One array contains integers identifying the home element number of each material point at the previous time step. This array is updated at the end of the convective phase of each time step. The other array stores the element neighbor numbers for each element. In the 2-D (or axisymmetric) and four node quadrilateral element case this element neighbor array contains a set of four integers for each possible element neighbor for each element (there are fewer than four neighbors for elements on the computational grid boundary). The element neighbor array does not change at any point in the computation and it must be generated during preprocessing. An element search based on knowledge of the neighboring elements incurs a much lower computational cost compared to an element by element search for material points. The use of an element neighbor array allows for a robust search algorithm that does not depend on how the background mesh is generated. The use of a neighbor element array is essential for problems that utilize meshes with areas of local refinement.

Other considerations for the numerical implementation include the evaluation of basis functions and their gradients. Evaluation of nodal basis functions at \mathbf{X}_p^k is required for much of the computations. Since the basis functions are evaluated in terms of local element coordinates, the material point coordinates must be mapped to the local coordinates. The corresponding local coordinates are computed as $\xi_p = \xi(\mathbf{X}_p^k) = \xi(x_p, y_p)$ and $\eta_p = \eta(\mathbf{X}_p^k) = \eta(x_p, y_p)$.

Newton's method is used to obtain the local element coordinates of material points.

Chapter 4. Numerical Modeling with the Material-point Method

For the sake of brevity, the subscript p and superscript k are dropped from the material point coordinates. An isoparametric formulation is assumed for which the global material point coordinates, (x, y) , are expressed in terms of the element basis functions as follows:

$$x = \sum_{i=1}^{N_n} x_i N_i(\xi, \eta), \quad y = \sum_{i=1}^{N_n} y_i N_i(\xi, \eta) \quad (4.4.2)$$

A Taylor expansion of x_p about a point (ξ_0, η_0) is performed. The function is first expanded about ξ_0 , resulting in the following:

$$x(\xi_0 + \Delta\xi, \eta_0 + \Delta\eta) = x(\xi_0, \eta_0 + \Delta\eta) + \frac{\partial x}{\partial \xi}(\xi_0, \eta_0 + \Delta\eta) \Delta\xi + \dots \quad (4.4.3)$$

where \dots denotes higher order terms. Next, equation (4.4.3) is expanded about η_0 to give the following result:

$$\begin{aligned} x(\xi_0 + \Delta\xi, \eta_0 + \Delta\eta) = & \left[x(\xi_0, \eta_0) + \frac{\partial x}{\partial \eta}(\xi_0, \eta_0) \Delta\eta + \dots \right] \\ & + \left[\frac{\partial x}{\partial \xi}(\xi_0, \eta_0) \Delta\xi + \frac{\partial^2 x}{\partial \xi \partial \eta}(\xi_0, \eta_0) \Delta\xi \Delta\eta + \dots \right] \end{aligned} \quad (4.4.4)$$

The same procedure for the y coordinate gives the following:

$$\begin{aligned} y(\xi_0 + \Delta\xi, \eta_0 + \Delta\eta) = & \left[y(\xi_0, \eta_0) + \frac{\partial y}{\partial \eta}(\xi_0, \eta_0) \Delta\eta + \dots \right] \\ & + \left[\frac{\partial y}{\partial \xi}(\xi_0, \eta_0) \Delta\xi + \frac{\partial^2 y}{\partial \xi \partial \eta}(\xi_0, \eta_0) \Delta\xi \Delta\eta + \dots \right] \end{aligned} \quad (4.4.5)$$

If only first order terms are retained in (4.4.4) and (4.4.5), the following system of equations remains

$$x(\xi_0 + \Delta\xi, \eta_0 + \Delta\eta) - x(\xi_0, \eta_0) \approx \frac{\partial x}{\partial \xi}(\xi_0, \eta_0) \Delta\xi + \frac{\partial x}{\partial \eta}(\xi_0, \eta_0) \Delta\eta \quad (4.4.6)$$

$$y(\xi_0 + \Delta\xi, \eta_0 + \Delta\eta) - y(\xi_0, \eta_0) \approx \frac{\partial y}{\partial \xi}(\xi_0, \eta_0) \Delta\xi + \frac{\partial y}{\partial \eta}(\xi_0, \eta_0) \Delta\eta \quad (4.4.7)$$

In order to locate ξ_p and η_p for a given $\mathbf{X}_p^k = (x_p^k, y_p^k)$, the following system of equations are solved iteratively via Newton's method.

$$\begin{bmatrix} x_p - x(\xi_0, \eta_0) \\ y_p - y(\xi_0, \eta_0) \end{bmatrix} = \begin{bmatrix} \sum_{i=1}^4 x_i \frac{\partial N_i}{\partial \xi}(\xi_0, \eta_0) & \sum_{i=1}^4 x_i \frac{\partial N_i}{\partial \eta}(\xi_0, \eta_0) \\ \sum_{i=1}^4 y_i \frac{\partial N_i}{\partial \xi}(\xi_0, \eta_0) & \sum_{i=1}^4 y_i \frac{\partial N_i}{\partial \eta}(\xi_0, \eta_0) \end{bmatrix} \begin{bmatrix} \Delta\xi \\ \Delta\eta \end{bmatrix} \quad (4.4.8)$$

$$\xi = \xi_0 + \Delta\xi, \quad \eta = \eta_0 + \Delta\eta \quad (4.4.9)$$

A solution to equations (4.4.8) and (4.4.9) is obtained when the norm of the LHS of (4.4.8) is within an acceptably small tolerance.

The basis function gradients are evaluated for computation of internal grid forces and strain increments. Using the chain rule, partial derivative of the basis functions with respect to the local element coordinates are expressed as the following:

$$\begin{aligned} \frac{\partial N_i}{\partial \xi} &= \frac{\partial N_i}{\partial x} \frac{\partial x}{\partial \xi} + \frac{\partial N_i}{\partial y} \frac{\partial y}{\partial \xi} \\ \frac{\partial N_i}{\partial \eta} &= \frac{\partial N_i}{\partial x} \frac{\partial x}{\partial \eta} + \frac{\partial N_i}{\partial y} \frac{\partial y}{\partial \eta} \end{aligned} \quad (4.4.10)$$

From (4.4.10) the basis function gradient ∇N_i can be expressed in matrix form as follows:

$$\nabla N_i = \begin{bmatrix} \frac{\partial N_i}{\partial x} \\ \frac{\partial N_i}{\partial y} \end{bmatrix} = \mathbf{J}^{-1} \begin{bmatrix} \frac{\partial N_i}{\partial \xi} \\ \frac{\partial N_i}{\partial \eta} \end{bmatrix} \quad (4.4.11)$$

The Jacobian matrix \mathbf{J} in (4.4.11) is

$$\mathbf{J} = \begin{bmatrix} \sum_{i=1}^4 x_i \frac{\partial N_i}{\partial \xi}(\xi_p, \eta_p) & \sum_{i=1}^4 y_i \frac{\partial N_i}{\partial \xi}(\xi_p, \eta_p) \\ \sum_{i=1}^4 x_i \frac{\partial N_i}{\partial \eta}(\xi_p, \eta_p) & \sum_{i=1}^4 y_i \frac{\partial N_i}{\partial \eta}(\xi_p, \eta_p) \end{bmatrix} \quad (4.4.12)$$

For ease of implementation, several of the computations are expressed in matrix form. The internal forces on the grid nodes are computed as follows:

$$\mathbf{f}_i^k = \begin{bmatrix} f_x \\ f_y \end{bmatrix}_i^k = - \sum_{p=1}^{N_p} M_p \begin{bmatrix} \frac{\partial N_i}{\partial x} & 0 & \frac{\partial N_i}{\partial y} \\ 0 & \frac{\partial N_i}{\partial y} & \frac{\partial N_i}{\partial x} \end{bmatrix}_p^k \begin{bmatrix} \sigma_{xx}^s \\ \sigma_{yy}^s \\ \sigma_{xy}^s \end{bmatrix}_p \quad (\text{plane}) \quad (4.4.13)$$

$$\mathbf{f}_i^k = \begin{bmatrix} f_r \\ f_z \end{bmatrix}_i^k = - \sum_{p=1}^{N_p} M_p \begin{bmatrix} \frac{\partial N_i}{\partial r} & 0 & \frac{N_i}{r} & \frac{\partial N_i}{\partial z} \\ 0 & \frac{\partial N_i}{\partial z} & 0 & \frac{\partial N_i}{\partial r} \end{bmatrix}_p^k \begin{bmatrix} \sigma_{rr}^s \\ \sigma_{zz}^s \\ \sigma_{\theta\theta}^s \\ \sigma_{rz}^s \end{bmatrix}_p \quad (\text{axisymmetric}) \quad (4.4.14)$$

The strain increment evaluation on the material points is expressed as follows:

$$\Delta \boldsymbol{\varepsilon}_p = \begin{bmatrix} \Delta \varepsilon_{xx} \\ \Delta \varepsilon_{yy} \\ 2\Delta \varepsilon_{xy} \end{bmatrix}_p = \Delta t \sum_{i=1}^{N_n} \begin{bmatrix} \frac{\partial N_i}{\partial x} & 0 \\ 0 & \frac{\partial N_i}{\partial y} \\ \frac{\partial N_i}{\partial y} & \frac{\partial N_i}{\partial x} \end{bmatrix}_p^k \begin{bmatrix} v_x \\ v_y \end{bmatrix}_i^L \quad (\text{plane}) \quad (4.4.15)$$

$$\Delta \boldsymbol{\varepsilon}_p = \begin{bmatrix} \Delta \varepsilon_{rr} \\ \Delta \varepsilon_{zz} \\ \Delta \varepsilon_{\theta\theta} \\ \Delta \varepsilon_{rz} \end{bmatrix}_p = \Delta t \sum_{i=1}^{N_n} \begin{bmatrix} \frac{\partial N_i}{\partial r} & 0 \\ 0 & \frac{\partial N_i}{\partial z} \\ \frac{N_i}{r} & 0 \\ \frac{\partial N_i}{\partial z} & \frac{\partial N_i}{\partial r} \end{bmatrix}_p^k \begin{bmatrix} v_r \\ v_z \end{bmatrix}_i^L \quad (\text{axisymmetric}) \quad (4.4.16)$$

The specific stress increment $\Delta \boldsymbol{\sigma}_p^s$ for isotropic linear elastic materials is computed as follows:

$$\Delta \boldsymbol{\sigma}_p^s = \begin{bmatrix} \Delta \sigma_{xx}^s \\ \Delta \sigma_{yy}^s \\ \Delta \sigma_{xy}^s \end{bmatrix}_p = \frac{\mathbf{C}}{\rho} \begin{bmatrix} \Delta \varepsilon_{xx} \\ \Delta \varepsilon_{yy} \\ 2\Delta \varepsilon_{xy} \end{bmatrix}_p \quad (\text{plane}) \quad (4.4.17)$$

$$\Delta \boldsymbol{\sigma}_p^s = \begin{bmatrix} \Delta \sigma_{rr}^s \\ \Delta \sigma_{zz}^s \\ \Delta \sigma_{\theta\theta}^s \\ \Delta \sigma_{rz}^s \end{bmatrix}_p = \frac{\mathbf{C}}{\rho} \begin{bmatrix} \Delta \varepsilon_{rr} \\ \Delta \varepsilon_{zz} \\ \Delta \varepsilon_{\theta\theta} \\ \Delta \varepsilon_{rz} \end{bmatrix}_p \quad (\text{axisymmetric}) \quad (4.4.18)$$

The elastic modulus Y and Poisson's ratio ν are used to form the of isotropic elasticity matrix \mathbf{C} . For two dimensional problems \mathbf{C} has the following form:

$$\mathbf{C} = \frac{Y}{(1+\nu)(1-2\nu)} \begin{bmatrix} 1-\nu & \nu & 0 \\ \nu & 1-\nu & 0 \\ 0 & 0 & \frac{1-2\nu}{2} \end{bmatrix} \quad (\text{plane strain}) \quad (4.4.19)$$

$$\mathbf{C} = \frac{Y}{(1-\nu^2)} \begin{bmatrix} 1 & \nu & 0 \\ \nu & 1 & 0 \\ 0 & 0 & \frac{1-\nu^2}{2(1+\nu)} \end{bmatrix} \quad (\text{plane stress}) \quad (4.4.20)$$

For axisymmetric problems \mathbf{C} is

$$\mathbf{C} = \frac{Y}{(1+\nu)(1-2\nu)} \begin{bmatrix} 1-\nu & \nu & \nu & 0 \\ \nu & 1-\nu & \nu & 0 \\ \nu & \nu & 1-\nu & 0 \\ 0 & 0 & 0 & \frac{1-2\nu}{2} \end{bmatrix} \quad (\text{axisymmetric}) \quad (4.4.21)$$

4.5 Numerical Implementation of the Elastic De-cohesive Constitutive Model

The numerical evaluation of the elastic de-cohesive constitutive model of section 3.5.3 is presented. The computation of stress as a function of strain, $\boldsymbol{\sigma}_p^k = \boldsymbol{\sigma}_p^k(\boldsymbol{\varepsilon}_p^k)$, is made for a discrete time t^k on a material point \mathbf{X}_p . For the sake of brevity, the subscript p and superscript k are dropped from material point quantities from this point forward with the understanding that the constitutive model is computed locally at a material point at a discrete time.

The continuum representation of the discrete elastic de-cohesion model presented in section 3.5.4 is implemented into MPM. This type of representation, also known as a smeared crack representation, is based on the strong discontinuity kinematics (see section 3.5.2) for which the strain field $\boldsymbol{\varepsilon}(\mathbf{x}, t)$ in a deformable body Ω is composed of regular and singular parts that account for a jump in the displacement field, $[[\mathbf{u}]]$, across a failure surface $\Gamma \subset \Omega$ with normal vector \mathbf{n} (see figure 3.4). The strain field given by equation (3.5.95) is below for convenience.

$$\begin{aligned} \boldsymbol{\varepsilon} &= \bar{\boldsymbol{\varepsilon}} & \forall \mathbf{x} \in \Omega/\Gamma \\ \boldsymbol{\varepsilon} &= \bar{\boldsymbol{\varepsilon}} + \frac{1}{L_c} ([[\dot{\mathbf{u}}]] \otimes \mathbf{n})^S & \forall \mathbf{x} \in \Gamma \end{aligned}$$

The regular bounded strain contribution in equation (3.5.95) is $\bar{\boldsymbol{\varepsilon}} = (\nabla \bar{\mathbf{u}})^S + H_\Gamma (\nabla [[\mathbf{u}]])^S$. The implementation of the model assumes that the displacement discontinuity $[[\mathbf{u}]]$ is constant over grid cells. Consequently, $\nabla [[\mathbf{u}]] = \mathbf{0}$, and $\bar{\boldsymbol{\varepsilon}} = (\nabla \bar{\mathbf{u}})^S$ in Ω/Γ .

The smeared crack treatment of the elastic de-cohesive model is analogous to any rate independent inelastic constitutive model for which the total strain is composed of the sum of elastic and inelastic contributions. In this case the inelastic strain is

the de-cohesion strain $\boldsymbol{\epsilon}^{dc}$. The rate of the total strain is obtained from equation (3.5.96) to be

$$\dot{\boldsymbol{\epsilon}} = \dot{\boldsymbol{\epsilon}}^e + \dot{\boldsymbol{\epsilon}}^{dc} \quad (4.5.1)$$

The continuum representation (smeared crack representation) of the discrete elastic de-cohesive constitutive model is summarized in equation (3.6.4) and repeated below for convenience.

$$\dot{\boldsymbol{\sigma}} = \mathbf{C} : (\dot{\boldsymbol{\epsilon}} - \dot{\boldsymbol{\epsilon}}^{dc}) \quad (\text{elasticity})$$

$$[[\dot{\mathbf{u}}]] = \dot{\omega} \frac{\partial F_n}{\partial \boldsymbol{\tau}} \quad (\text{evolution of displacement jump})$$

$$\dot{\boldsymbol{\epsilon}}^{dc} = \frac{1}{L_c} ([[\dot{\mathbf{u}}]] \otimes \mathbf{n})^S \quad (\text{evolution of de - cohesion strain})$$

$$\dot{F}_n(\boldsymbol{\sigma}, [[\mathbf{u}]]) = 0 \quad (\text{consistency condition})$$

A general numerical algorithm for evaluation of a non-linear constitutive model is presented. The procedure described is similar to that for rate independent plasticity [62]. The displacement discontinuity $[[\mathbf{u}]]$ across a failure surface with normal \mathbf{n} , and consequently the de-cohesion strain $\boldsymbol{\epsilon}^{dc}$, is allowed to evolve so that the consistency condition in equation (3.6.4) is maintained. In practice the consistency condition is maintained by enforcing the following conditions:

$$\begin{aligned} F_n < 0 & \quad \text{elastic behavior} \\ F_n = 0 & \quad [[\mathbf{u}]] \text{ is evolving} \\ F_n > 0 & \quad \text{not allowed} \end{aligned} \quad (4.5.2)$$

When $F_n < 0$ elastic deformation occurs and $[[\mathbf{u}]]$ does not evolve. Loading continues

until the initiation of failure on a discrete failure surface with normal \mathbf{n} . Continued loading on a failure plane requires evolution of the displacement discontinuity while maintaining the condition, $F_n = 0$. In actuality a trial elastic state of deformation is assumed for which $F_n > 0$, and then $[[\mathbf{u}]]$ evolves in order to satisfy the $F_n = 0$ condition. The solution to $F_n(\boldsymbol{\sigma}, [[\mathbf{u}]]) = 0$ is obtained iteratively using the Newton-Raphson algorithm. Recall that ω is required to be a monotonically increasing parameter (i.e. $\dot{\omega} \geq 0$). The parameter ω is allowed to evolve throughout the iteration. The general procedure is executed by the following steps:

1. Let $k \in \mathbb{N}^+$ represent the Newton iteration, set $k = 0$ and choose a small tolerance value, ε . The value of the de-cohesion function for the trial elastic state is $F_n^k = F_n^0 > \varepsilon$.
2. Evaluate

$$\frac{\partial F_n^k}{\partial \omega}$$

3. Compute the increment in ω to be

$$\Delta\omega = -\frac{F_n^k}{\frac{\partial F_n^k}{\partial \omega}}$$

4. Increment ω as follows:

$$\omega^{k+1} = \omega^k + \Delta\omega$$

5. Evaluate $F_n^{k+1} = F_n(\omega^{k+1})$.
6. If $F_n^{k+1} > \varepsilon$ increase the iteration by overwriting $k \rightarrow k + 1$ and return to step 2. If $|F_n^{k+1}| < \varepsilon$ then a solution has been obtained and the procedure is terminated.

The preceding algorithm is referred to as a general procedure because the specific form of the de-cohesion function F_n and its partial derivative $\partial F_n/\partial\omega$ are not explicit functions of ω . In the case of the elastic de-cohesive model algorithm, only the increment $\Delta\omega$ is computed. The parameter ω is never explicitly updated during the iteration, but is reflected in the evolution of the displacement discontinuity $[[\mathbf{u}]]$ and de-cohesive strain $\boldsymbol{\varepsilon}^{dc}$. Within the iteration, the de-cohesion function F_n is evaluated using the updated displacement discontinuity and stress. However, the algorithm requires that the function $\partial F_n/\partial\omega$ be evaluated.

Recall the form of \dot{F}_n in equation (3.5.86), displayed below for convenience.

$$\dot{F}_n = \frac{2}{\tau_{sf}^2} \tau_t \dot{\tau}_t + \frac{2}{\tau_{sf}^2} \tau_p \dot{\tau}_p + D_{\psi\sigma} \left[\begin{array}{l} \frac{D_{\tau n}}{\tau_{nf}} \dot{\tau}_n + \left(\frac{D_{\bar{\sigma}}}{(f'_c)^2} (2\sigma_{tt} + \chi\sigma_{pp}) f_n + \frac{D_{ttpp}}{f'_c} \right) \dot{\sigma}_{tt} \\ + \left(\frac{D_{\bar{\sigma}}}{(f'_c)^2} (2\sigma_{pp} + \chi\sigma_{tt}) f_n + \frac{D_{ttpp}}{f'_c} \right) \dot{\sigma}_{pp} \\ + \frac{D_{\bar{\sigma}}}{(f'_c)^2} 2(2 - \chi) \sigma_{tp} \dot{\sigma}_{tp} \\ - (1 - D_{\bar{\sigma}} \bar{\sigma}^2) \dot{f}_n \end{array} \right]$$

During the evolution of $[[\mathbf{u}]]$ the total strain is assumed to remain constant and the following condition holds:

$$\dot{\boldsymbol{\varepsilon}} = 0 \quad (\text{while } [[\mathbf{u}]] \text{ is evolving}) \quad (4.5.3)$$

As $[[\mathbf{u}]]$ evolves, it follows from the elastic stress-strain relationship in (3.6.4) that the stress rate is

$$\dot{\boldsymbol{\sigma}} = -\mathbf{C} : \dot{\boldsymbol{\varepsilon}}^{dc} \quad (\text{while } [[\mathbf{u}]] \text{ is evolving}) \quad (4.5.4)$$

Equation (4.5.4) is expressed alternatively in indicial notation as follows:

$$\dot{\sigma}_{ij} = -\frac{Y}{(1+\nu)(1-2\nu)} [(1-2\nu)\dot{\epsilon}_{ij}^{dc} + \nu\dot{\epsilon}_{kk}^{dc}\delta_{ij}] \quad (i, j = n, t, p) \quad (4.5.5)$$

The non-zero components of $\dot{\epsilon}^{dc}$ in equation (4.5.5) are

$$\dot{\epsilon}_{nn}^{dc} = \frac{\dot{\omega}}{L_c} \frac{D\psi_\sigma D\tau_n}{\tau_{nf}}, \quad \dot{\epsilon}_{nt}^{dc} = \frac{\dot{\omega}}{L_c} \frac{\tau_t}{\tau_{sf}^2}, \quad \dot{\epsilon}_{pn}^{dc} = \dot{\omega} \frac{\tau_p}{\tau_{sf}} \quad (4.5.6)$$

Equations (4.5.5) and (4.5.6) are combined to obtain the components of $\dot{\sigma}$ as $[[\mathbf{u}]]$ evolves. The result is

$$\begin{aligned} \dot{\sigma}_{nn} &= -\dot{\omega} \frac{E_1}{L_c} \frac{D\psi_\sigma D\tau_n}{\tau_{nf}}, & \dot{\sigma}_{tt} &= -\dot{\omega} \frac{E_2}{L_c} \frac{D\psi_\sigma D\tau_n}{\tau_{nf}}, & \dot{\sigma}_{pp} &= -\dot{\omega} \frac{E_2}{L_c} \frac{D\psi_\sigma D\tau_n}{\tau} \\ \dot{\sigma}_{nt} &= -\dot{\omega} \frac{2G}{L_c} \frac{\tau_t}{\tau_{sf}^2}, & \dot{\sigma}_{tp} &= 0, & \dot{\sigma}_{pn} &= -\dot{\omega} \frac{2G}{L_c} \frac{\tau_p}{\tau_{sf}^2} \end{aligned} \quad (4.5.7)$$

where the elastic constants in equation (4.5.7) are defined as follows:

$$E_1 = \frac{Y(1-\nu)}{(1+\nu)(1-2\nu)}, \quad E_2 = \frac{Y\nu}{(1+\nu)(1-2\nu)}, \quad 2G = \frac{Y}{(1+\nu)} \quad (4.5.8)$$

The components of $\dot{\sigma}$ in equation (4.5.7) are substituted into equation (3.5.86). The result is

$$\begin{aligned} \dot{F}_n &= -\dot{\omega} \frac{2}{\tau_{sf}^2} \tau_t \frac{2G}{L_c} \frac{\tau_t}{\tau_{sf}^2} - \dot{\omega} \frac{2}{\tau_{sf}^2} \tau_p \frac{2G}{L_c} \frac{\tau_p}{\tau_{sf}^2} \\ &+ D_{\psi\sigma} \left[\begin{array}{l} -\dot{\omega} \frac{D_{\tau n}}{\tau_{nf}} \left(\frac{E_1}{L_c} \frac{D_{\psi\sigma} D_{\tau n}}{\tau_{nf}} \right) \\ -\dot{\omega} \left(\frac{D_{\bar{\sigma}}}{(f'_c)^2} (2\sigma_{tt} + \chi\sigma_{pp}) f_n + \frac{D_{ttpp}}{f'_c} \right) \frac{E_2}{L_c} \frac{D_{\psi\sigma} D_{\tau n}}{\tau_{nf}} \\ -\dot{\omega} \left(\frac{D_{\bar{\sigma}}}{(f'_c)^2} (2\sigma_{pp} + \chi\sigma_{tt}) f_n + \frac{D_{ttpp}}{f'_c} \right) \frac{E_2}{L_c} \frac{D_{\psi\sigma} D_{\tau n}}{\tau_{nf}} \\ +\dot{\omega} (1 - D_{\bar{\sigma}} \bar{\sigma}^2) \frac{1}{u_0} \frac{D_{\psi\sigma} D_{\tau n}}{\tau_{nf}} \end{array} \right] \end{aligned} \quad (4.5.9)$$

An alternative expression for \dot{F}_n is

$$\dot{F}_n = \frac{\partial F_n}{\partial \omega} \dot{\omega} \quad (4.5.10)$$

Equations (4.5.9) and (4.5.10) are combined and the factor $\dot{\omega}$ can be eliminated. The following expression for $\partial F_n / \partial \omega$ is induced:

$$\frac{\partial F_n}{\partial \omega} = -\frac{4G}{\tau_{sf}^4 L_c} (\tau_t^2 + \tau_p^2) + D_{\psi\sigma}^2 D_{\tau n} \left[\begin{array}{l} -\frac{D_{\tau n} E_1}{\tau_{nf}^2 L_c} - \frac{D_{\bar{\sigma}} f_n E_2}{(f'_c)^2 L_c \tau_{nf}} (2 + \chi) (\sigma_{tt} + \sigma_{pp}) \\ -\frac{2D_{ttpp} E_2}{f'_c L_c \tau_{nf}} + (1 - D_{\bar{\sigma}} \bar{\sigma}^2) \frac{1}{u_0 \tau_{nf}} \end{array} \right] \quad (4.5.11)$$

The following material parameters are defined:

$$C_{TG} = \frac{2G}{\tau_{sf}^2 L_c}, \quad C_{E1} = \frac{E_1}{\tau_{nf}^2 L_c}, \quad C_{E2} = \frac{E_2}{f'_c \tau_{nf} L_c} \quad (4.5.12)$$

Equation (4.5.11) is simplified to the following form with the use of equation (4.5.12):

$$\frac{\partial F_n}{\partial \omega} = -\frac{2C_{TG}}{\tau_{sf}^2} (\tau_t^2 + \tau_p^2) + D_{\psi\sigma}^2 D_{\tau n} \left[\begin{array}{l} -C_{E1} D_{\tau n} - \frac{C_{E2} D_{\bar{\sigma}} f_n}{f'_c} (2 + \chi) (\sigma_{tt} + \sigma_{pp}) \\ -2C_{E2} D_{ttpp} + (1 - D_{\bar{\sigma}} \bar{\sigma}^2) \frac{1}{u_0 \tau_{nf}} \end{array} \right] \quad (4.5.13)$$

The specific constitutive model algorithm used to evaluate stress at material point is presented. The smeared crack implementation of the elastic de-cohesion model treats multiple failure surfaces at a material point. Each failure surface is handled individually and it is assumed that the failure surfaces do not interact with each other. The multiple smeared crack concept is illustrated in figure 4.2. Failure of a representative volume of heterogeneous material, such as concrete, is considered to have contributions from multiple failure surfaces that may evolve simultaneously. The representative volume is idealized by a homogeneous sub-volume of material represented by a material point. Within each discrete sub-volume of material multiple discrete failure surfaces are permitted to initiate. The displacement discontinuity across each failure surface evolves according to the prescribed loading up to the point of complete failure. Evolution of the displacement discontinuities provides the softening behavior associated with localized deformation of material and failure.

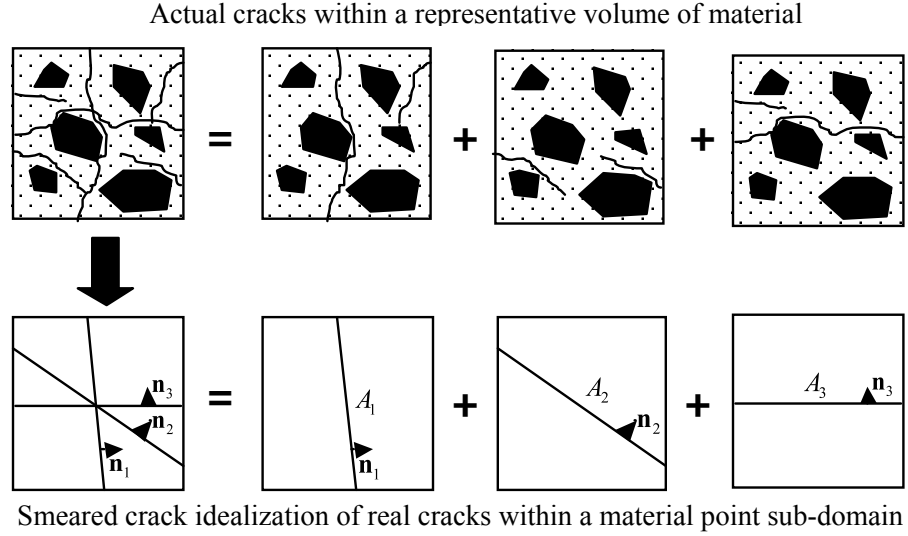


Figure 4.2: Multiple smeared crack concept

The effect of material failure on multiple failure surfaces is captured through the inelastic de-cohesive strain $\boldsymbol{\varepsilon}^{dc}$. If J failure surfaces have initiated over a material point sub-volume ($J = 3$ for the case in figure 4.2), then $\{ [[\mathbf{u}_j]] , \mathbf{n}_j j = 1, \dots, J \}$ represents the set of failure surface normal vectors \mathbf{n}_j and associated displacement discontinuity vectors $[[\mathbf{u}_j]]$. The de-cohesive strain associated with the j^{th} failure surface is computed from equation (3.5.98) as follows:

$$\boldsymbol{\varepsilon}_j^{dc} = \frac{1}{L_c} ([[\mathbf{u}_j]] \otimes \mathbf{n}_j)^S \quad (4.5.14)$$

The total de-cohesive strain $\boldsymbol{\varepsilon}^{dc}$ is the sum of the de-cohesive strain contributions from all J failure surfaces. It follows that $\boldsymbol{\varepsilon}^{dc}$ is

$$\boldsymbol{\varepsilon}^{dc} = \sum_{j=1}^J \boldsymbol{\varepsilon}_j^{dc} = \sum_{j=1}^J \frac{1}{L_c} ([[\mathbf{u}_j]] \otimes \mathbf{n}_j)^S \quad (4.5.15)$$

It is important to note that the value of the smearing length L_c in equation (4.5.14) plays a critical role in the computation of $\boldsymbol{\varepsilon}^{dc}$. The criterion for choosing a value

for L_c varies. The quantity L_c is sometimes viewed as a material parameter [9] with a definite value that can be measured. Consistent methods for computing L_c have also been established and are widely used [39], [69]. Neither view is advocated here. However, the value of L_c is required to satisfy certain theoretical considerations.

An upper bound on the value of L_c is established on a simple theoretical basis. Recall that the parameter ω is required to be a monotonically increasing quantity. It follows that increment $\Delta\omega$ computed in the general algorithm must also be positive. Since F_n is always positive during the iteration, it is required that $\partial F_n/\partial\omega < 0$. Consider the simple loading situation of uniaxial tension for which the only non-zero stress component is σ_{nn} . In this case, $\tau_t = \tau_p = \sigma_{tt} = \sigma_{pp} = 0$, $\bar{\sigma}^2 = 0$, $D_{tpp} = 0$ and $D_{\tau n} = 1$. If $\partial F_n/\partial\omega < 0$ is enforced for uniaxial tension, then equation (4.5.13) becomes

$$-C_{E1} + \frac{1}{u_0\tau_{nf}} < 0 \quad (4.5.16)$$

Recall from equations (4.5.12) and (3.5.44) that $C_{E1} = E_1/(\tau_{nf}^2 L_c)$ and $u_0 = 2G_f/\tau_{nf}$. The inequality in equation (4.5.16) is manipulated to establish an upper bound on the value of L_c in terms of the other independent material parameters as follows:

$$L_c < \frac{2G_f E_1}{\tau_{nf}^2} \quad (4.5.17)$$

Equation (4.5.17) is the well known criteria necessary for maintaining a negative softening modulus for σ_{nn} that precludes local stress reversal.

The following procedure for evaluation of the elastic de-cohesion constitutive model applies to the initiation and evolution of cracking on multiple failure surfaces up to the point of complete failure (loss of traction carrying capability). The infor-

mation available for each material point from the previous computational cycle includes the stress $\boldsymbol{\sigma}^0$, total strain $\boldsymbol{\varepsilon}^0$ and the set of de-cohesion history variables $\{ [[\mathbf{u}_j^0]] , \mathbf{n}_j \quad j = 1, \dots, J \}$ for J failure surfaces that have already initiated. A total strain increment $\Delta\boldsymbol{\varepsilon}$ is available. The procedure for computing a solution for the stress $\boldsymbol{\sigma}^L$ at the current computational cycle (time step) is given by the following steps:

1. Compute a stress increment $\Delta\boldsymbol{\sigma}$ to be $\Delta\boldsymbol{\sigma} = \mathbf{C} : \Delta\boldsymbol{\varepsilon}$.
2. Compute the trial stress to be $\boldsymbol{\sigma}^{tr} = \boldsymbol{\sigma}^0 + \Delta\boldsymbol{\sigma}$.
3. Let $j \in \mathbb{N}^+$ denote the discrete failure surface. If $J = 0$ proceed to step 4. If $J > 0$ perform the following steps for $j = 1, \dots, J$ only if $[[\mathbf{u}_j^0]] \cdot \mathbf{n}_j < u_0$:
 - (a) Construct \mathbf{t}_j such that $\mathbf{t}_j \cdot \mathbf{n}_j = 0$ and compute $\mathbf{p}_j = \mathbf{n}_j \times \mathbf{t}_j$.
 - (b) Construct the transformation tensor \mathbf{A}_j using equation (3.5.45).
 - (c) Transform the components of the trail stress from the global basis $\{\mathbf{e}_1, \mathbf{e}_2, \mathbf{e}_3\}$ to the local failure surface basis $\{\mathbf{n}_j, \mathbf{t}_j, \mathbf{p}_j\}$ by computing $\boldsymbol{\sigma}_j^{trl} = \mathbf{A}_j^T \cdot \boldsymbol{\sigma}_j^{trg} \cdot \mathbf{A}_j$ as follows:

$$\sigma_{nn} = n_1 n_1 \sigma_{11} + n_2 n_2 \sigma_{22} + n_3 n_3 \sigma_{33} + 2n_1 n_2 \sigma_{12} + 2n_2 n_3 \sigma_{23} + 2n_3 n_1 \sigma_{31}$$

$$\sigma_{tt} = t_1 t_1 \sigma_{11} + t_2 t_2 \sigma_{22} + t_3 t_3 \sigma_{33} + 2t_1 t_2 \sigma_{12} + 2t_2 t_3 \sigma_{23} + 2t_3 t_1 \sigma_{31}$$

$$\sigma_{pp} = p_1 p_1 \sigma_{11} + p_2 p_2 \sigma_{22} + p_3 p_3 \sigma_{33} + 2p_1 p_2 \sigma_{12} + 2p_2 p_3 \sigma_{23} + 2p_3 p_1 \sigma_{31}$$

$$\begin{aligned} \sigma_{nt} = n_1 t_1 \sigma_{11} + n_2 t_2 \sigma_{22} + n_3 t_3 \sigma_{33} + (n_1 t_2 + n_2 t_1) \sigma_{12} + (n_2 t_3 + n_3 t_2) \sigma_{23} \\ + (n_3 t_1 + n_1 t_3) \sigma_{31} \end{aligned}$$

$$\begin{aligned} \sigma_{tp} = t_1 p_1 \sigma_{11} + t_2 p_2 \sigma_{22} + t_3 p_3 \sigma_{33} + (t_1 p_2 + t_2 p_1) \sigma_{12} + (t_2 p_3 + t_3 p_2) \sigma_{23} \\ + (t_3 p_1 + t_1 p_3) \sigma_{31} \end{aligned}$$

$$\begin{aligned} \sigma_{pn} = p_1 n_1 \sigma_{11} + p_2 n_2 \sigma_{22} + p_3 n_3 \sigma_{33} + (p_1 n_2 + p_2 n_1) \sigma_{12} + (p_2 n_3 + p_3 n_2) \sigma_{23} \\ + (p_3 n_1 + p_1 n_3) \sigma_{31} \end{aligned}$$

Evaluate $F_n(\boldsymbol{\sigma}_j^{tr}, [[\mathbf{u}_j^0]])$ using the expressions in equations (3.5.49) - (3.5.57).

- (d) If $F_n(\boldsymbol{\sigma}_j^{tr}, [[\mathbf{u}_j^0]]) < 0$ then the intermediate stress solution for crack j , $\boldsymbol{\sigma}_j = \boldsymbol{\sigma}_j^{tr}$ has been obtained. If $j \leq J$, overwrite $j \rightarrow j + 1$ and return to step 3. If $j = J$, a solution for the material point stress $\boldsymbol{\sigma}^L = \boldsymbol{\sigma}_J$ has been obtained and the procedure is terminated.
- (e) If $F_n(\boldsymbol{\sigma}_j^{tr}, [[\mathbf{u}_j^0]]) > 0$ perform the Newton Raphson algorithm to find $\boldsymbol{\sigma}_j$ and $[[\mathbf{u}_j^L]]$ that satisfy $F_n(\boldsymbol{\sigma}_j, [[\mathbf{u}_j^L]]) = 0$. Let the index $k \in \mathbb{N}^+$ represent the Newton iteration. Initiate the procedure by setting $k = 0$, $\boldsymbol{\sigma}_j^{tr k} = \boldsymbol{\sigma}_j^{tr}$, $[[\mathbf{u}_j]]^k = [[\mathbf{u}_j^0]]$, $F_n^k = F_n(\boldsymbol{\sigma}_j^{tr k}, [[\mathbf{u}_j]]^k)$, and selecting a small tolerance value ε . In the following steps the superscript k is placed on a function to denote the evaluation of that function at the k^{th} Newton iterate of trail stress $\boldsymbol{\sigma}_j^{tr k}$ and displacement discontinuity $[[\mathbf{u}_j]]^k$ associated with failure surface j .
- (f) For $k = 1, 2, \dots$ perform the following steps:

Chapter 4. Numerical Modeling with the Material-point Method

- i. Evaluate $\frac{\partial F_n^k}{\partial \omega} = \frac{\partial F_n}{\partial \omega} (\boldsymbol{\sigma}_j^{trk})$ using the expressions in equations (4.5.13), (3.5.74) - (3.5.77) and (3.5.50) - (3.5.57).
- ii. Compute the increment in the parameter ω to be

$$\Delta \omega = - \frac{F_n^k}{\frac{\partial F_n^k}{\partial \omega}}$$

- iii. Compute the increment in the components of $\Delta [[\mathbf{u}_j]]$ using equations (3.5.74) and (3.5.75) as follows:

$$\Delta [[u_n]] = \Delta \omega \frac{D_{\psi\sigma}^k D_{\tau n}^k}{\tau_{nf}}, \quad \Delta [[u_t]] = \Delta \omega \frac{2}{\tau_{sf}^2} \tau_t^{trk}, \quad \Delta [[u_p]] = \Delta \omega \frac{2}{\tau_{sf}^2} \tau_p^{trk}$$

- iv. Increment the displacement discontinuity $[[\mathbf{u}_j]]$ as follows:

$$[[\mathbf{u}_j]]^{k+1} = [[\mathbf{u}_j]]^k + \Delta [[\mathbf{u}_j]]$$

- v. Compute the increment in the components of $\Delta \boldsymbol{\varepsilon}_j^{dc}$ using equations (3.5.74) and (3.5.75) as follows:

$$\Delta \varepsilon_{nnj}^{dc} = \frac{\Delta \omega}{L_c} \frac{D_{\psi\sigma}^k D_{\tau n}^k}{\tau_{nf}}, \quad \Delta \varepsilon_{ntj}^{dc} = \frac{\Delta \omega}{L_c} \frac{\tau_t^{trk}}{\tau_{sf}^2}, \quad \Delta \varepsilon_{pnj}^{dc} = \Delta \omega \frac{\tau_p^{trk}}{\tau_{sf}^2}$$

- vi. Compute the increment of the components of the trial stress $\Delta \boldsymbol{\sigma}_j^{tr} = -\mathbf{C} : \Delta \boldsymbol{\varepsilon}_j^{dc}$ using equations (4.5.7) and (4.5.8) as follows:

$$\begin{aligned} \Delta \sigma_{nnj}^{tr} &= -E_1 \Delta \varepsilon_{nnj}^{dc}, & \Delta \sigma_{ttj}^{tr} &= -E_2 \Delta \varepsilon_{nnj}^{dc}, & \Delta \sigma_{ppj}^{tr} &= -E_2 \Delta \varepsilon_{nnj}^{dc} \\ \Delta \sigma_{ntj}^{tr} &= -2G \Delta \varepsilon_{ntj}^{dc}, & \Delta \sigma_{tpj}^{tr} &= 0, & \Delta \sigma_{pnj}^{tr} &= -2G \Delta \varepsilon_{pnj}^{dc} \end{aligned}$$

vii. Update the $(k + 1)^{th}$ trial stress iterate as follows:

$$\boldsymbol{\sigma}_j^{tr\ k+1} = \boldsymbol{\sigma}_j^{tr\ k} + \Delta\boldsymbol{\sigma}$$

viii. Evaluate $F_n^{k+1} = F_n\left(\boldsymbol{\sigma}_j^{tr\ k+1}, [[\mathbf{u}_j]]^{k+1}\right)$ using the expressions in equations (3.5.49) - (3.5.57).

ix. If $F_n^{k+1} > \varepsilon$, increase the iteration by overwriting $k \rightarrow k+1$ and return to step i. If $|F_n^{k+1}| < \varepsilon$ then the solution for $[[\mathbf{u}_j^L]] = [[\mathbf{u}_j]]^{k+1}$ and an intermediate stress solution for crack j , $\boldsymbol{\sigma}_j = \boldsymbol{\sigma}_j^{tr\ k+1}$, have been obtained and the procedure is terminated.

x. Transform the components of $\boldsymbol{\sigma}_j$ from the local failure surface basis $\{\mathbf{n}_j, \mathbf{t}_j, \mathbf{p}_j\}$ to the global basis $\{\mathbf{e}_1, \mathbf{e}_2, \mathbf{e}_3\}$ by computing $\boldsymbol{\sigma}_j^g = \mathbf{A}_j \cdot \boldsymbol{\sigma}_j^l \cdot \mathbf{A}_j^T$ as follows:

$$\sigma_{11} = n_1 n_1 \sigma_{nn} + t_1 t_1 \sigma_{tt} + p_1 p_1 \sigma_{pp} + 2n_1 t_1 \sigma_{nt} + 2t_1 p_1 \sigma_{tp} + 2p_1 n_1 \sigma_{pn}$$

$$\sigma_{22} = n_2 n_2 \sigma_{nn} + t_2 t_2 \sigma_{tt} + p_2 p_2 \sigma_{pp} + 2n_2 t_2 \sigma_{nt} + 2t_2 p_2 \sigma_{tp} + 2p_2 n_2 \sigma_{pn}$$

$$\sigma_{33} = n_3 n_3 \sigma_{nn} + t_3 t_3 \sigma_{tt} + p_3 p_3 \sigma_{pp} + 2n_3 t_3 \sigma_{nt} + 2t_3 p_3 \sigma_{tp} + 2p_3 n_3 \sigma_{pn}$$

$$\begin{aligned} \sigma_{12} = & n_1 n_2 \sigma_{nn} + t_1 t_2 \sigma_{tt} + p_1 p_2 \sigma_{pp} + (n_1 t_2 + n_2 t_1) \sigma_{nt} + (t_1 p_2 + t_2 p_1) \sigma_{tp} \\ & + (p_1 n_2 + p_2 n_1) \sigma_{pn} \end{aligned}$$

$$\begin{aligned} \sigma_{23} = & n_2 n_3 \sigma_{nn} + t_2 t_3 \sigma_{tt} + p_2 p_3 \sigma_{pp} + (n_2 t_3 + n_3 t_2) \sigma_{nt} + (t_2 p_3 + t_3 p_2) \sigma_{tp} \\ & + (p_2 n_3 + p_3 n_2) \sigma_{pn} \end{aligned}$$

$$\begin{aligned} \sigma_{31} = & n_3 n_1 \sigma_{nn} + t_3 t_1 \sigma_{tt} + p_3 p_1 \sigma_{pp} + (n_3 t_1 + n_1 t_3) \sigma_{nt} + (t_3 p_1 + t_1 p_3) \sigma_{tp} \\ & + (p_3 n_1 + p_1 n_3) \sigma_{pn} \end{aligned}$$

(g) If $j \leq J$, overwrite $j \rightarrow j + 1$, set $\boldsymbol{\sigma}^{tr} = \boldsymbol{\sigma}_j^g$ and return to step (a). If $j = J$, a solution for the material point stress $\boldsymbol{\sigma}^L = \boldsymbol{\sigma}_j$ has been obtained

and the procedure is terminated.

4. Determine if another failure surface has initiated by evaluating the failure surface initiation criteria in equation (3.5.39)

(a) Solve for F and \mathbf{n} such that $F = \max_{\forall \mathbf{n}} F_n$.

(b) If $F > 0$ then overwrite $J \rightarrow J + 1$. Set $\mathbf{n}_J = \mathbf{n}$ and $[[\mathbf{u}_J]] = \mathbf{0}$.

The preceding constitutive algorithm only considers the failure process for a given \mathbf{n} for which $[[u_n]] < u_0$. Post failure treatment of the motion and loading of failure surfaces addresses cases for which $[[u_n]] \geq u_0$ and $\tau_n \leq 0$ for a given \mathbf{n} . A post failure value of $\tau_n = 0$ for \mathbf{n} indicates crack opening. In this case, $[[u_n]]$ increases and $\Delta[[\mathbf{u}]]$ is computed by assuming that $\Delta\boldsymbol{\epsilon}^{dc} = \Delta\boldsymbol{\epsilon}$. A post failure value of $\tau_n < 0$ indicates compressive traction between the surfaces of a closed crack. In this case $[[u_n]] = u_0$ is enforced while adjusting $\boldsymbol{\tau}$ on the failure surface according to a Columb friction law.

The determination of the failure surface initiation criteria requires the numerical evaluation of $F = \max_{\forall \mathbf{n}} F_n$. In general, this is done by assuming that failure surface normal, \mathbf{n} , lies in the plane defined by the principal stress directions corresponding to the maximum and minimum principal stress. This assumption is based on observations that \mathbf{n} is defined by a linear combination of the two eigenvectors of $\boldsymbol{\sigma}$ corresponding to the minimum and maximum eigenvalues for many different stress states. The actual algorithm is a bisection method that computes the angle between \mathbf{n} and the maximum principal stress direction which satisfies the failure surface initiation criteria.

Chapter 5

Evaluation of the Smearred Crack Approach in MPM

5.1 Introduction

The results of this study are presented in this chapter. The overall objective of this research is to study the grid dependence of computational fracture results using a smeared crack approach in MPM. The specific aims are to determine how the numerical results vary with the orientation of the grid, what are the causes of the grid orientation bias of results and what, if any, simple approaches are available to remedy the problem. The simple 2D problem of a bar in uniaxial tension, used to study the behavior of the numerical method, is discussed in section 5.2. A preliminary study of mesh orientation bias in MPM results is presented in section 5.3 for an elastic constitutive model. A baseline failure simulation of the tensile bar is established in section 5.4. Section 5.5 presents findings of the grid dependence investigation for smeared crack MPM. The causes of the problems are provided and potential remedies are also explored.

5.2 Case Study Problem: 2-D Elastic De-cohesive Bar in Tension

A simple problem is chosen for the purposes of studying the behavior of numerical results using a smeared crack representation of fracture in MPM. A 2D elastic de-cohesive bar in tension is utilized as the case study. The advantage of such a problem is the prior knowledge of the global response and stress state. When a problem's solution is well known, it is usually easier to identify the effects in the numerical solution caused by the computational method itself. An exact solution for the global response of the bar is derived in section 5.2.1. The preprocessing of the problem in MPM is discussed in section 5.2.2.

5.2.1 The Analytical Solution

Consider the two dimensional bar in tension depicted in figure 5.1. The bar is subject to an axial tensile force P at the right end while the left end remains fixed. The displacement of the point of load application, designated as δ , is the total elongation of the bar. At some point during the loading of the bar a failure surface initiates which has a normal vector \mathbf{n} . As the material separates accross the surface the magnitude of the displacement discontinuity $[[\mathbf{u}]]$ increases . The vector basis $\{\mathbf{n}, \mathbf{t}\}$ is attached to the bar and does not necessarily coincide with the global unit vector basis $\{\mathbf{e}_x, \mathbf{e}_y\}$. In two dimensions \mathbf{n} is defined in terms of the parameter α as follows:

$$\mathbf{n} = \cos \alpha \mathbf{e}_x + \sin \alpha \mathbf{e}_y \quad (5.2.1)$$

The material of the bar is described by an elastic de-cohesive constitutive model. The goal of the present analysis is to obtain the analytical expression, $P = P(\delta)$, for the elastic de-cohesive bar in tension. The P vs. δ response of the bar is illustrated in figure 5.1

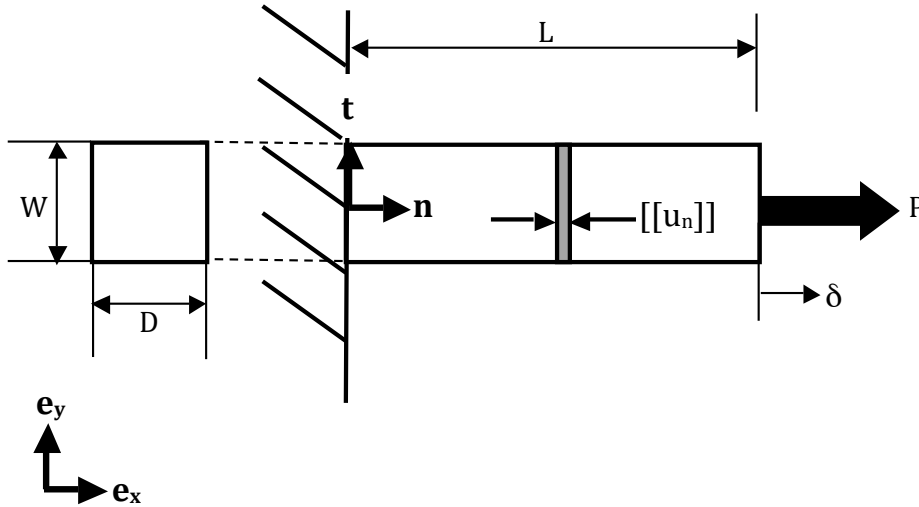


Figure 5.1: Illustration of the elastic de-cohesive tensile bar problem

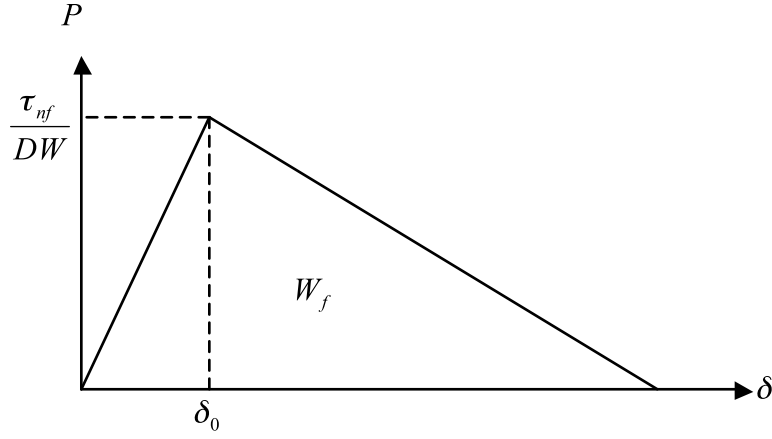


Figure 5.2: Illustration of $P-\delta$ response of the elastic de-cohesive tensile bar problem

For a smeared crack representation of failure the total strain, $\boldsymbol{\varepsilon}$, in the bar is composed of elastic and inelastic (de-cohesive) contributions as follows:

$$\boldsymbol{\varepsilon} = \boldsymbol{\varepsilon}^e + \boldsymbol{\varepsilon}^{dc} \quad (5.2.2)$$

The stress is related to the elastic strain as follows:

$$\boldsymbol{\sigma} = \mathbf{C} : \boldsymbol{\varepsilon}^e \quad (5.2.3)$$

In (5.2.3) \mathbf{C} is the fourth order isotropic elasticity tensor. Plane strain is assumed for which the stress and strain components are related as follows:

$$\begin{aligned} \sigma_{nn} &= \frac{Y}{(1+\nu)(1-2\nu)} [(1-\nu)\varepsilon_{nn} + \nu\varepsilon_{tt}] \\ \sigma_{tt} &= \frac{Y}{(1+\nu)(1-2\nu)} [(1-\nu)\varepsilon_{tt} + \nu\varepsilon_{nn}] \\ \sigma_{nt} &= \frac{Y}{(1+\nu)}\varepsilon_{nt} \end{aligned} \quad (5.2.4)$$

Since the bar is in uniaxial tension the following conditions must hold:

$$\begin{aligned}\sigma_{tt} &= 0 \\ \varepsilon_{nt} &= 0\end{aligned}\tag{5.2.5}$$

The conditions in (5.2.5) are used and the stress strain relationship becomes

$$\sigma_{nn} = E^* \varepsilon_{nn}^e\tag{5.2.6}$$

where

$$E^* = \frac{Y}{(1 - \nu^2)}\tag{5.2.7}$$

During the initial elastic loading the total strain is equal to the elastic strain contribution and the axial stress is related to the elongation as follows:

$$\sigma_{nn} = \frac{E^*}{L} \delta \quad (\text{elastic loading})\tag{5.2.8}$$

The axial stress σ_{nn} increases linearly up to a peak value that coincides with the ultimate tensile strength τ_{nf} . Upon continued loading softening occurs due to crack opening across a discrete failure surface with unit vector normal \mathbf{n} (see figure 5.1). Since pure mode I fracture is occurring in the bar the displacement discontinuity across the failure surface is $[[\mathbf{u}]] = [[u_n]] \mathbf{n}$. The normal component of $[[\mathbf{u}]]$, $[[u_n]]$, is related to the axial stress by the following linear softening relationship:

$$\sigma_{nn} = \tau_{nf} \left(1 - \frac{[[u_n]]}{u_0} \right)\tag{5.2.9}$$

Chapter 5. Evaluation of the Smeared Crack Approach in MPM

The development of inelastic de-cohesive strains ϵ^{dc} is due to the evolution of u_n . The axial component of the de-cohesive strain contribution is

$$\epsilon_{nn}^{dc} = \frac{[[u_n]]}{L} \quad (5.2.10)$$

The total axial strain component in the bar is

$$\epsilon_{nn} = \frac{\delta}{L} = \epsilon_{nn}^e + \epsilon_{nn}^{dc} \quad (5.2.11)$$

Equations (5.2.6), (5.2.10) and (5.2.11) are combined to give the following:

$$\frac{\delta}{L} = \frac{\sigma_{nn}}{E^*} + \frac{[[u_n]]}{L} \quad (5.2.12)$$

Equation (5.2.12) is rearranged as follows:

$$[[u_n]] = u_0 \left(1 - \frac{\sigma_{nn}}{\tau_{nf}} \right) \quad (5.2.13)$$

The function $\sigma_{nn}(\delta)$ is obtained by substituting (5.2.13) into (5.2.12) and rearranging terms. The final result is

$$\sigma_{nn} = \frac{E^*}{\left(L - \frac{E^* u_0}{\tau_{nf}} \right)} (\delta - u_0) \quad (\textit{softening}) \quad (5.2.14)$$

Equation (5.2.14) describes the softening relationship between axial stress in the bar and the total elongation for loading past the peak stress. It is important to note that in order to maintain softening behavior in (5.2.14) the following condition must hold:

$$L < \frac{E^* u_0}{\tau_{nf}} \quad (5.2.15)$$

In general the stress is

$$\sigma_{nn} = \frac{E^*}{L} \delta [1 - H(\delta - \delta_0)] + \frac{E^*}{\left(L - \frac{E^* u_0}{\tau_{nf}}\right)} (\delta - u_0) H(\delta - \delta_0) \quad (5.2.16)$$

where

$$\delta_0 = \frac{\tau_{nf} L}{E^*} \quad (5.2.17)$$

and $\sigma_{nn}(\delta_0) = \tau_{nf}$ is satisfied. The Heaviside function $H(\delta - \delta_0)$ in (5.2.16) is defined as follows:

$$H(\delta - \delta_0) = \begin{cases} 1 & \delta \geq \delta_0 \\ 0 & \delta < \delta_0 \end{cases} \quad (5.2.18)$$

It is desired to obtain the analytical expression, $P = P(\delta)$, for the elastic de-cohesive bar in tension. The P vs. δ response of the bar is illustrated in 5.2. The load P is computed to be the axial stress multiplied by the cross sectional area of the bar WD . It follows that the $P = P(\delta)$ relationship for the elastic de-cohesive bar is

$$P = \frac{WDE^*}{L} \delta [1 - H(\delta - \delta_0)] + \frac{WDE^*}{\left(L - \frac{E^* u_0}{\tau_{nf}}\right)} (\delta - u_0) H(\delta - \delta_0) \quad (5.2.19)$$

The work of fracture W_f is defined to be

$$W_f = \int_0^\delta P(\delta) d\delta \quad (5.2.20)$$

Chapter 5. Evaluation of the Smeared Crack Approach in MPM

Substitution of (5.2.19) into (5.2.20) gives

$$\begin{aligned}
 W_f = & \frac{WDE^*}{L} \left[\int_0^\delta \delta d\delta - \int_0^\delta \delta H(\delta - \delta_0) d\delta \right] \\
 & + \frac{WDE^*}{\left(L - \frac{E^*u_0}{\tau_{nf}} \right)} \left[\int_0^\delta \delta H(\delta - \delta_0) d\delta - \int_0^\delta u_0 H(\delta - \delta_0) d\delta \right]
 \end{aligned} \tag{5.2.21}$$

The following change of variables is made:

$$s = \delta - \delta_0, \quad -\delta_0 \leq s \leq \delta - \delta_0 \tag{5.2.22}$$

The expression in (5.2.21) becomes

$$\begin{aligned}
 W_f = & \frac{WDE^*}{L} \left[\int_0^\delta \delta d\delta - \int_{-\delta_0}^{\delta-\delta_0} (s + \delta_0) H(s) ds \right] \\
 & + \frac{WDE^*}{\left(L - \frac{E^*u_0}{\tau_{nf}} \right)} \left[\int_{-\delta_0}^{\delta-\delta_0} (s + \delta_0) H(s) ds - \int_{-\delta_0}^{\delta-\delta_0} u_0 H(s) ds \right]
 \end{aligned} \tag{5.2.23}$$

By definition of the Heaviside function, (5.2.23) becomes

$$\begin{aligned}
 W_f = & \frac{WDE^*}{L} \left[\int_0^\delta \delta d\delta - H(s) \int_0^{\delta-\delta_0} (s + \delta_0) ds \right] \\
 & + \frac{WDE^*}{\left(L - \frac{E^*u_0}{\tau_{nf}} \right)} H(s) \left[\int_0^{\delta-\delta_0} (s + \delta_0) ds - \int_0^{\delta-\delta_0} u_0 ds \right]
 \end{aligned} \tag{5.2.24}$$

The integrals in (5.2.24) are evaluated to give the following result:

$$\begin{aligned}
 W_f = & \frac{WDE^*}{2L} \delta^2 + \frac{WDE^*}{L} \left[\frac{(\delta - \delta_0)^2}{2} + \delta_0 (\delta - \delta_0) \right] H(\delta - \delta_0) \\
 & + \frac{WDE^*}{\left(L - \frac{E^* u_0}{\tau_{nf}} \right)} \left[\frac{(\delta - \delta_0)^2}{2} + (\delta_0 - u_0) (\delta - \delta_0) \right] H(\delta - \delta_0) \quad (5.2.25)
 \end{aligned}$$

After some simplification of (5.2.25) the work of fracture relationship becomes

$$\begin{aligned}
 W_f = & \frac{WDE^*}{2L} \delta^2 + \frac{WDE^*}{2L} [\delta^2 - \delta_0^2] H(\delta - \delta_0) \\
 & + \frac{WDE^*}{\left(L - \frac{E^* u_0}{\tau_{nf}} \right)} \left[\frac{1}{2} (\delta^2 - \delta_0^2) - u_0 (\delta - \delta_0) \right] H(\delta - \delta_0) \quad (5.2.26)
 \end{aligned}$$

The analytical results of the preceding analysis (equations (5.2.19) & (5.2.26)) are used in the following computational studies of the elastic de-cohesion tensile bar problem for the purposes of determining numerical solution accuracy.

5.2.2 Problem Setup and Other Computational Considerations

MPM discretizations of the tensile bar problem are displayed in figure 5.3 and figure 5.4 for cases of $\alpha = 0$ and $\alpha \neq 0$ respectively. For all the computations performed the global basis, $\{\mathbf{e}_x, \mathbf{e}_y\}$, is taken to coincide with the grid lines while the unit vector basis, $\{\mathbf{n}, \mathbf{t}\}$, is fixed to the bar. The case of $\alpha = 0$ is referred to as the baseline case. For the baseline case the material points are uniformly distributed within the square cells using four material points per cell (see figure 5.3). The $\alpha \neq 0$ configuration in figure 5.4 is generated by simply applying a rotation to the the material points of the baseline case about the center of bar. The red material points represent deformable material and the green points represent rigid material points.

The velocity boundary conditions are applied to the bar through the use of the rigid material points. The velocity of the rigid points must be transferred to the nodes of the grid because the discrete equations of motion are solved on the grid. During the MPM computational cycle the velocity of a grid node is overwritten with the velocity of a rigid material point if the rigid point resides in the support of that particular grid node. Because the velocity (or displacement) boundary conditions are applied in such a manner in MPM, the boundary of a body of material points is considered to be a set of grid nodes that surround the deformable material points. It is important to note that these points are not defined explicitly, but rather deduced from the position of the rigid material points. Therefore, the correct positioning of rigid material points becomes an important consideration which will be addressed later. The velocity of the rigid material points are prescribed. For this problem a zero velocity is applied to the rigid points at the left end of the bar and a constant velocity of $\mathbf{V}_p = v_L \mathbf{n}$ is applied to the rigid points at the right end of the bar.

Values of material parameters for concrete are selected for the tensile bar simulation.

Chapter 5. Evaluation of the Smeared Crack Approach in MPM

The material parameters associated with the elastic de-cohesion constitutive model and their values are listed in table 5.1 along with other relevant problem data.

The bar problem is set up to initiate the ideal macroscopic failure surface with normal, \mathbf{n} , depicted in 5.1. This is accomplished by prescribing different material regions in the bar as illustrated by the configuration of material points in figure 5.5. Elastic material, represented by red material points, surrounds a region of elastic de-cohesive material in the central region of the bar, which are represented by blue material points. Within this potential failure region, lies a subregion of weakened material represented by yellow material points. This weak material serves as the intended failure initiation region. The macroscopic failure surface (crack) that forms across the bar is deduced from the pattern of failed material points. Because the bar geometry is uniform, a weak region of failure initiation must be specified in order to avoid uniform failure over all material in the failure region, and consequently an inaccurate representation of the failure of the tensile bar. The tensile strength of the weakened material points is 90% of the τ_{nf} of the surrounding material. A single failure surface with normal \mathbf{n} is prescribed to all material points within the failure region and only one failure surface is allowed to initiate throughout loading. Formation of the correct macroscopic crack surface across the bar depends on the size and placement of the weakened material region. The effects of varying the weakened region is addressed in later sections.

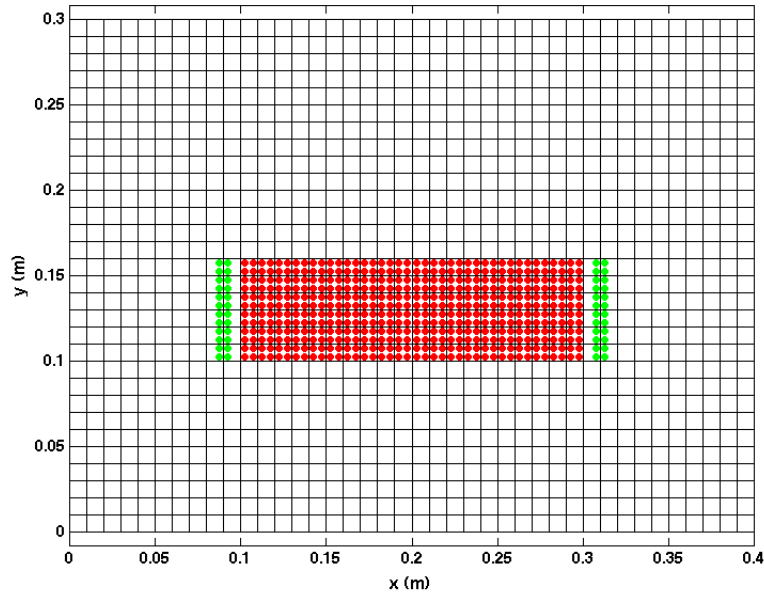


Figure 5.3: Baseline ($\alpha = 0^\circ$) MPM configurations of tensile bar problem

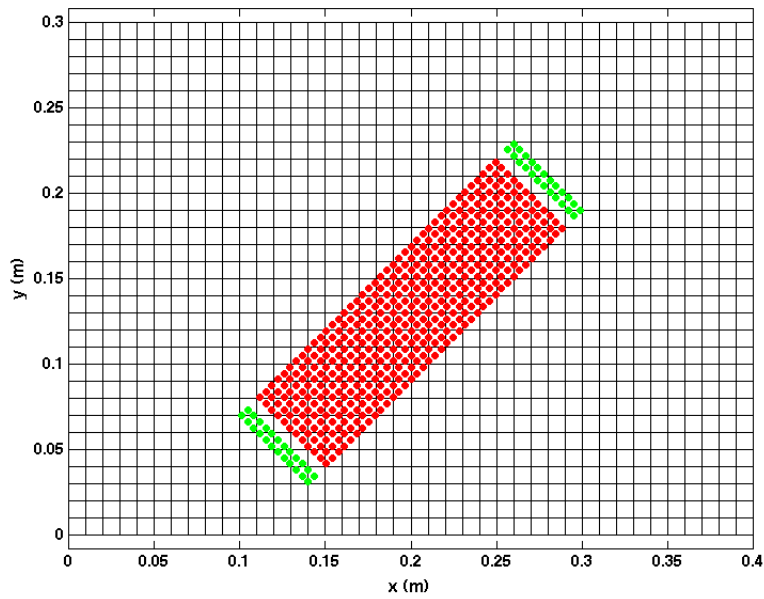


Figure 5.4: MPM configurations of bar problem for $\alpha = 45^\circ$

Table 5.1: Bar problem data

problem data	Symbol	Value	Unit
mass density	ρ	2350	kg/m^3
Young's modulus	E	24.9	GPa
Poisson's ratio	ν	0.18	dimensionless
ultimate tensile strength	τ_{nf}	2.7	MPa
shear strength	τ_{sf}	14.9	MPa
shear strength for large mean pressure	τ_{sm}	90.0	MPa
compressive strength	f'_c	42.7	MPa
fracture energy	G_f	61.35	N/m
coupling parameter	C_n	0.2	dimensionless
coupling parameter	C_s	0.1	dimensionless
coupling parameter	C_ψ	5.0	dimensionless
bar length	L	20	cm
bar width	W	6	cm
bar depth	D	6	cm
load velocity	v_L	0.01	m/s
material points per cell	N/A	4	N/A

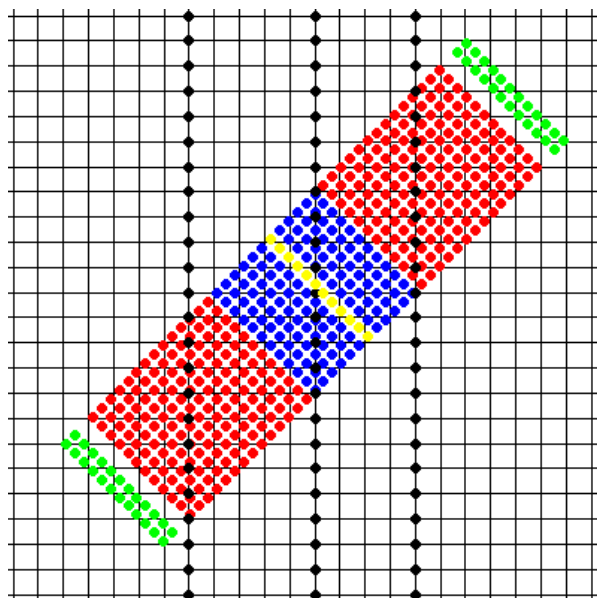


Figure 5.5: MPM configuration key

Chapter 5. Evaluation of the Smeared Crack Approach in MPM

Several important quantities are computed throughout the simulation which include the load point elongation δ , the axial load in the bar P , the elastic strain energy, U , the energy dissipated by mode I fracture, E_f and the work of fracture W_f .

The discrete load point displacement (elongation) of the bar at the $k + 1$ time step is computed to be

$$\delta^{k+1} = \delta^k + \Delta t v_L \quad (5.2.27)$$

The axial load computed at the k^{th} time step, denoted as P^k , is obtained from the reaction forces at a set of grid nodes that cuts through the bar. Consider the cutting plane that is coincident with a set of grid nodes located at $x_i = \text{constant}$ depicted by the vertical lines of black grid nodes in figure 5.5. The set of cutting plane grid nodes indices is designated as $\{i_x\} = \{i \mid x_i = \text{constant}\}$. Equilibrium of internal forces in the bar requires that $\mathbf{f}_i^{int k} = \mathbf{0}$ for all i . It follows that the sum of internal force contributions from all grid nodes, $i \in \{i_x\}$, also be equal to zero as follows:

$$\sum_{i \in \{i_x\}} \mathbf{f}_i^{int k} = \mathbf{0} \quad (5.2.28)$$

In equation (5.2.28), $\mathbf{f}_i^{int k}$ is the internal force at a grid node $i \in \{i_x\}$. Recall that the entire set of material points is $\{\mathbf{X}_p\}_{p=1}^{N_p}$. A subset of material points in $\{\mathbf{X}_p\}_{p=1}^{N_p}$ for which $X_p > x_i = \text{constant}$ is designated as $\{p_x\} = \{p \mid X_p > x_i = \text{constant}\}$. Since $\{\mathbf{X}_p\}_{p=1}^{N_p} = \{p_x\} \cup C\{p_x\}$, where $C\{p_x\}$ is the complement of $\{p_x\}$, the expression for $\mathbf{f}_i^{int k}$ in equation (5.2.28) is rewritten using equation (4.2.12) as follows:

$$\mathbf{f}_i^{int k} = - \sum_{p \in \{p_x\}} M_p \boldsymbol{\sigma}_p^{s k} \cdot \nabla N_i(\mathbf{X}_p^k) - \sum_{p \in C\{p_x\}} M_p \boldsymbol{\sigma}_p^{s k} \cdot \nabla N_i(\mathbf{X}_p^k) \quad (5.2.29)$$

Equation (5.2.29) is substituted into (5.2.28). The result is

$$- \sum_{i \in \{i_x\}} \left[\sum_{p \in \{p_x\}} M_p \boldsymbol{\sigma}_p^{s k} \cdot \nabla N_i(\mathbf{X}_p^k) \right] - \sum_{i \in \{i_x\}} \left[\sum_{p \in C\{p_x\}} M_p \boldsymbol{\sigma}_p^{s k} \cdot \nabla N_i(\mathbf{X}_p^k) \right] = \mathbf{0} \quad (5.2.30)$$

The two terms in equation (5.2.30) are equal and opposite forces that act over the line of grid nodes defined by $i \in \{i_x\}$. Define the reaction force \mathbf{f}^R over the grid nodes $i \in \{i_x\}$ to be

$$\mathbf{f}^R = - \sum_{i \in \{i_x\}} \left[\sum_{p \in \{p_x\}} M_p \boldsymbol{\sigma}_p^{s k} \cdot \nabla N_i(\mathbf{X}_p^k) \right] \quad (5.2.31)$$

The axial force in the bar P^k is simply the component of \mathbf{f}^R resolved in the \mathbf{n} direction as follows:

$$P^k = \mathbf{f}^R \cdot \mathbf{n} \quad (5.2.32)$$

The elastic strain energy U in the body Ω is defined to be

$$U = \frac{1}{2} \int_{\Omega} \boldsymbol{\sigma} : \boldsymbol{\varepsilon}^e dV \quad (5.2.33)$$

In indicial notation equation (5.2.33) is

$$U = \frac{1}{2} \int_{\Omega} \sigma_{ij} : \varepsilon_{ij}^e dV \quad (5.2.34)$$

The relationship for isotropic elasticity is

$$\sigma_{ij} = - \frac{Y}{(1 + \nu)(1 - 2\nu)} \left[(1 - 2\nu) \varepsilon_{ij}^e + \nu \varepsilon_{kk}^e \delta_{ij} \right] \quad (5.2.35)$$

Chapter 5. Evaluation of the Smearred Crack Approach in MPM

Equations (5.2.34) and (5.2.35) are combined. The 2D result in terms of the $\{\mathbf{e}_x, \mathbf{e}_y\}$ global basis components is

$$U = \frac{1}{2} \int_{\Omega} \left[\frac{1}{2E} (\sigma_{xx}^2 + \sigma_{yy}^2) - \frac{\nu}{E} \sigma_{xx} \sigma_{yy} + \frac{1}{2G} \sigma_{xy}^2 \right] dV \quad (5.2.36)$$

In MPM the computation of U^k approximates the integral in (5.2.36) as a discrete sum over all material points p with discrete volumes $V_p = M_p/\rho$ at time t^k as follows:

$$U = \frac{1}{2} \sum_{p=1}^{N_p} \frac{M_p}{\rho} \left[\frac{1}{2E} (\sigma_{xx}^2 + \sigma_{yy}^2) - \frac{\nu}{E} \sigma_{xx} \sigma_{yy} + \frac{1}{2G} \sigma_{xy}^2 \right]_p^k \quad (5.2.37)$$

Let A_{Γ} be the failure surface associated with the region of discontinuity Γ in the body Ω (as depicted in figure 3.4). The energy dissipated by mode I fracture in Γ is

$$E_f = \int_{A_{\Gamma}} \left[\int_0^{[[u_n]]} \tau_n ([[u_n]]) d[[u_n]] \right] dA_{\Gamma} \quad (\text{for } [[u_n]] \leq u_0) \quad (5.2.38)$$

Recall the linear softening relationship of equation (3.5.63) rewritten below.

$$\tau_n = \tau_{nf} \left(1 - \frac{[[u_n]]}{u_0} \right)$$

Equation (3.5.63) is substituted into (5.2.38) and the inner integral is evaluated. The result is

$$E_f = \int_{A_{\Gamma}} \tau_{nf} [[u_n]] \left(1 - \frac{[[u_n]]}{2u_0} \right) dA_{\Gamma} \quad (\text{for } [[u_n]]^k \leq u_0) \quad (5.2.39)$$

Chapter 5. Evaluation of the Smeared Crack Approach in MPM

Let the discrete failure surfaces across a material point be approximated as DL_c . The integral in (5.2.39) is approximated as a finite sum over material points p to be

$$E_f^k = DL_c \sum_{p=1}^{N_p} \tau_{nf} [[u_n]]_p^k \left(1 - \frac{[[u_n]]_p^k}{2u_0} \right) \quad \left(\text{for } [[u_n]]_p^k \leq u_0 \right) \quad (5.2.40)$$

In equation (5.2.40) the characteristic length is computed to be

$$L_c = \frac{h}{2} \quad (5.2.41)$$

where h is the side length of a square grid cell. The value of L_c is dependent on the spatial discretization with the following restriction from equation (5.2.15) which precludes local stress reversal:

$$L_c < \frac{2E^*G_f}{\tau_{nf}^2}$$

The amount of available energy that can be dissipated from complete failure of a single crack on a single material point is reached once $[[u_n]]_p = u_0$. It follows from equations (5.2.40) and (3.5.44) that the energy dissipated by complete failure of a crack per material point is

$$E_{fp} = DL_c \frac{\tau_{nf} u_0}{2} = DL_c G_f \quad (5.2.42)$$

Not surprisingly, the energy required for mode I failure of one crack over one material point is just the product of the discrete failure surface area (DL_c) and the fracture energy G_f . The total energy dissipated by complete failure of the bar across the idealized failure surface in figure 5.1 is simply DWG_f .

The integral definition of the work of fracture, W_f , in equation (5.2.20) is approximated numerically to compute W_f^k at time t^k as follows:

$$W_f^k = \sum_k P^k (\delta^k - \delta^{k-1}) \quad (5.2.43)$$

The quantity DWG_f is the exact solution for the work of fracture energy required for complete failure of the bar and is used for comparisons against numerical solutions of W_f^k .

The numerical solution error of the computed load P^k with respect to the exact solution $P(\delta)$ in equation (5.2.19) is computed as follows

$$E_p = \frac{|P^k - P(\delta^k)|}{|P(\delta^k)|} \quad (5.2.44)$$

The error computed from equation (5.2.44) is used for the convergence studies in the following section.

The error is computed from a solution obtained on the grid rather than material points because the discrete MPM equations are solved on the grid nodes. For this reason grid quantity error is considered to be the more appropriate error measure. Other measures of solution error were considered during the course of this study which include error in the elastic strain energy computed on material points U^k and the error in the velocity solution computed on the grid nodes.

Although measuring grid quantity error is appropriate for MPM computations, measuring nodal velocity error presented problems for non-baseline cases for which $\alpha \neq 0$. The velocity solution error was measured with respect to the corresponding baseline solution at grid nodes, which was demonstrated to converge with mesh refinement. Measuring error for $\alpha \neq 0$ cases was problematic due to the incompatibility of node sets between the $\alpha = 0$ and $\alpha \neq 0$ cases. To remedy the incompatibility problem the

Chapter 5. Evaluation of the Smeared Crack Approach in MPM

material point configurations of the $\alpha \neq 0$ cases were rotated back to the baseline solution, the material point velocity was mapped to the corresponding baseline grid configuration and the grid velocity error was computed. A measure of grid velocity error was obtained for which solution convergence was generally observed. However, the axial load computation error was selected over the velocity solution error as the best error measure because it is computed directly and represents a solution that is computed on the actual grid whereas the velocity error requires a significant amount of post processing as well as other questionable assumptions.

Solution error based on the elastic energy, U^k , computed on material points, was ultimately abandoned because the MPM solution is not computed on the material points. Use of solution errors in U^k presented other problems as well. The computation of error in U^k is straightforward. The error is measured with respect to an exact solution $U(\delta)$. However, this error measure seems to magnify the inherent MPM error associated with material points crossing grid cell boundaries or being located very close to grid cell boundaries. As a result, the convergence behavior was severely affected by the position of material points. This problem was compounded by the placement of rigid material points used to apply velocity boundary conditions.

Recall the application of essential boundary conditions for which the velocity of a grid node is taken to be the velocity of a rigid material point that resides in the support of that particular grid node. Figure 5.6 displays two different placements of rigid material points for loading the right end of the bar. The arrows placed at grid nodes indicate the direction of the boundary velocity applied to that node by the rigid material points. As the pictures indicate, the placement of the rigid points produces different velocity boundary conditions at the nodes. The top figure depicts the placement of rigid points at the visible boundary of the bar. The consequence is that the boundary velocity is applied to grid nodes that reside within the deformable domain of the body of material points. In this case some cells near the boundary

will have the same boundary velocity prescribed at all their nodes. Any deformable material points within such cells are located within a constant velocity field that does not produce any strain, and therefore have zero stress. Obviously, the zero stress material points have a definite adverse affect on the solution error in U^k , strengthening the case to discard this error measurement for MPM results.

Placement of rigid material points at the visible boundary does not properly represent the tensile bar problem. Convergence studies were performed using this boundary condition representation and the grid solution error measure, E_p . In general, solution accuracy in E_p does not decrease with increasing grid resolution because the boundary conditions of the bar problem are not correctly represented.

The bottom plot in figure 5.6 displays an appropriate placement of rigid material points for the bar problem. The velocity boundary conditions are correctly applied only to nodes that lie outside the deformable material domain by placing the rigid points slightly offset from the right end of the bar. Offsetting the rigid points from the end of the bar prevents the occurrence of zero stress material points near the boundary where velocity is prescribed. As a result, the problem is represented correctly and an increase in numerical solution accuracy with increasing grid resolution is obtained and is shown in the following section.

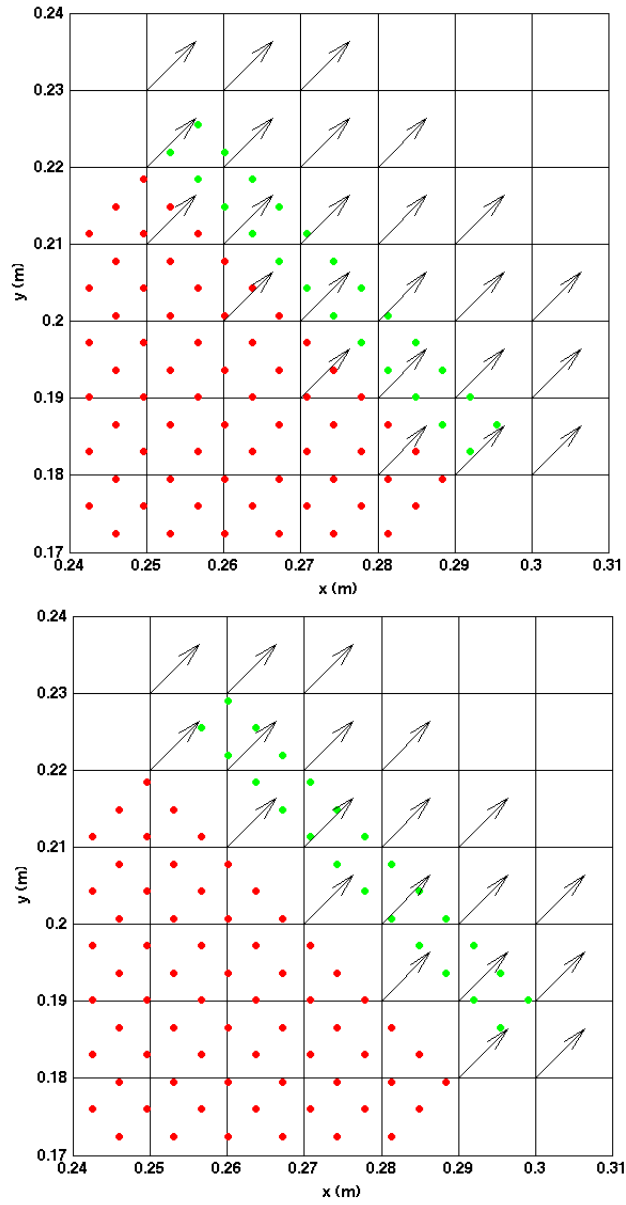


Figure 5.6: Comparison of the placement of rigid material points for applying velocity boundary conditions

5.3 A Preliminary Study of Mesh Orientation Bias in MPM Results

A preliminary study of mesh orientation bias of MPM results was performed using an isotropic elastic material for the tensile bar. The object of this part of the investigation is to obtain a general idea of how the orientation of the grid relative to the body of material points affects the convergence rate of the numerical solution with mesh refinement.

Figure 5.7 displays baseline configurations of the problem for the four grid resolutions used in the convergence study. The solution error in axial load is measured using equation (5.2.44). The exact solution to $P(\delta)$ for the elastic problem is obtained from (5.2.19) for an infinitely strong material ($\tau_{nf} \rightarrow \infty$) to be

$$P(\delta) = \frac{WDE^*}{L}\delta \tag{5.3.1}$$

Convergence results for the baseline case are displayed in figure 5.8. The plot on the left displays the solution error percentage vs. the inverse side length of a square grid cell, denoted by h^{-1} . Convergence of the numerical solution for the baseline case is observed with mesh refinement because E_p decreases with decreasing h (increasing h^{-1}). The plot on the right of figure 5.8 is of $\log E_p$ vs. h^{-1} . The rate of convergence denoted by, m_p , is estimated by a least squares fit to the $\log E_p$ vs. h^{-1} data. For the baseline case a convergence rate value of $m_p = 1.44$ is computed.

Error results for $\alpha = 15^\circ, 30^\circ, 45^\circ$ are plotted in figure 5.9. In general, the numerical solution error is observed to increase with increasing value of α for a given grid resolution. Estimated values of convergence rates are displayed in table 5.2. Convergence is observed for all $\alpha \neq 0$ cases. However a significant decrease in convergence rate relative to the baseline simulation is also observed.

Chapter 5. Evaluation of the Smearred Crack Approach in MPM

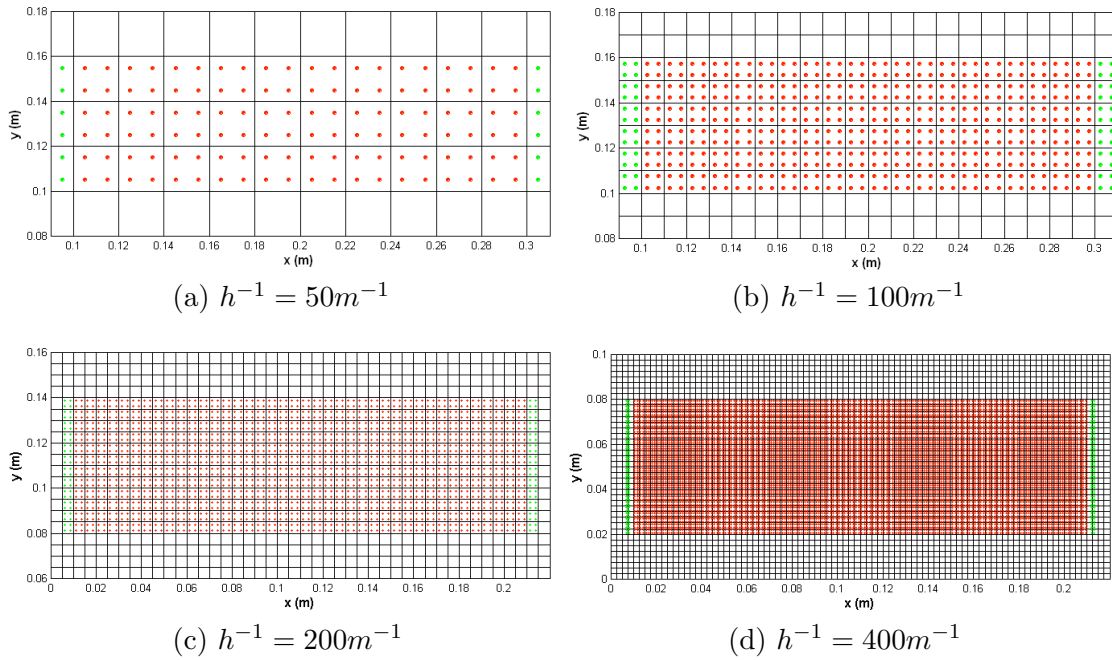


Figure 5.7: MPM configurations of baseline elastic bar in tension problem

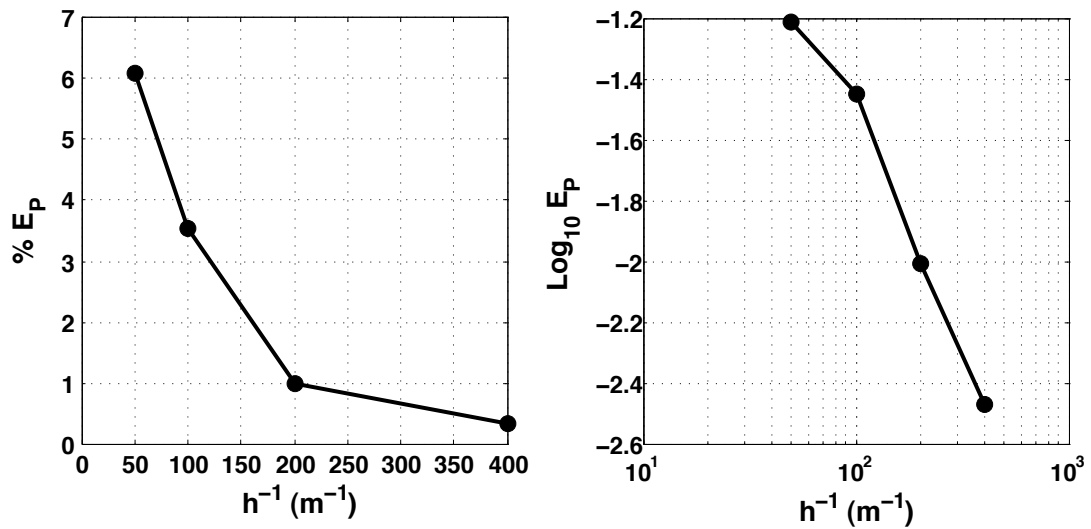


Figure 5.8: MPM convergence study for the baseline configuration elastic bar

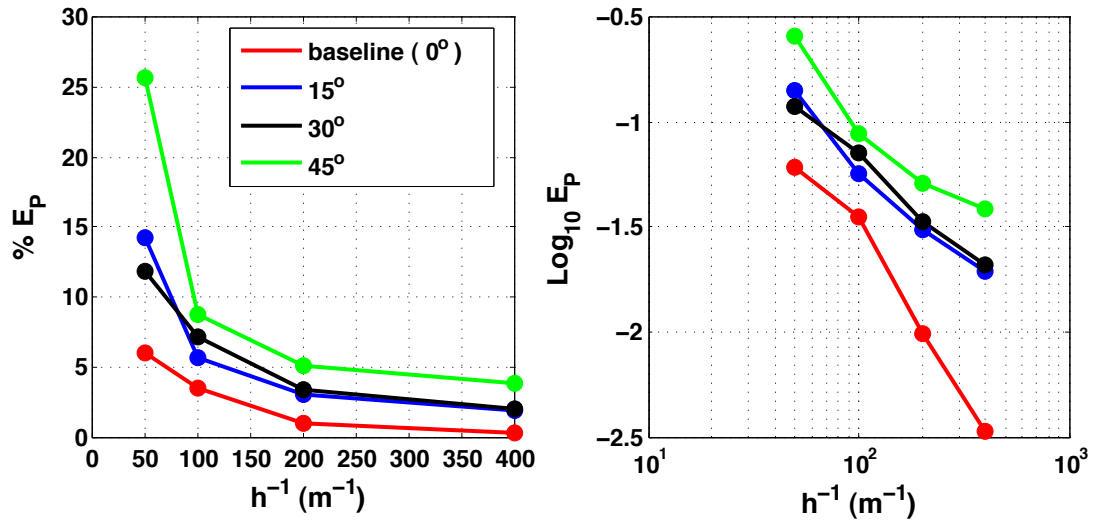


Figure 5.9: Convergence behavior comparison of elastic bar problem in MPM with different α

Table 5.2: Convergence rate results for elastic tensile bar problem

α	m_p
0°	-1.4354
15°	-0.9482
30°	-0.8573
45°	-0.8982

5.4 The Baseline Failure Simulation

Baseline case results for the MPM failure simulation of an elastic de-cohesive bar in tension are presented. A general idea of the accuracy of the simulations is provided by visual comparisons of numerical results with the analytical solutions for axial load, $P(\delta)$, and work of fracture, $W_f(\delta)$ (equations (5.2.19) and (5.2.26)). Results are obtained for four different grid resolutions, h . When considering problems of material failure, accurate numerical solutions capture not only the correct global response, but the correct global failure surface. In the case of the bar problem the failure surface is idealized by a transverse plane with surface normal, \mathbf{n} (see figure 5.1). Three different configurations of weakened material are utilized as failure initiation locations in order to determine which configurations lead to failure patterns resembling correct results for the global failure surface. Patterns of weak material points include material points within a square of fixed area, a transverse line of material points and a single material point. Material points within a weakened region of material have a value of τ_{nf} that is 10% lower than the surrounding material.

Figure 5.10 displays baseline configurations of the tensile bar problem with a fixed square area of weakened material points. Upon complete failure of the bar, the failure pattern is visualized by the contour plots of normalized displacement discontinuity, $[[u_n]]/u_0$ in figure 5.11. Completely failed material is associated with $[[u_n]]/u_0 \geq 1$. The global failure pattern resulting from each grid resolution not only initiates within the weakened region of material, but represents the correct global failure surface expected from the exact solution. As h increases the failure pattern localizes into a narrow band resembling a macro-crack. Figure 5.12 displays comparisons of numerical and analytical global response results. Three numerical results for P vs. δ , corresponding to the three node sets where the reaction force is computed (see figure 5.5), are plotted along with the exact solution. For each grid resolution, all three computed P vs. δ response curves fall on top of each other and match very closely to

the analytical solution. The plots of energy also display closely matched comparisons of numerical and analytical results of W_f vs. δ responses. These responses consist of contributions of elastic potential energy, U , and energy dissipated by fracture, E_f , that are also computed and displayed in the energy plots. During the initial elastic loading of the bar U increases and $E_f = 0$ as expected. Softening of the material occurs for loading beyond the peak load. Post peak loading is characterized by a gradual drop in U and an increase in E_f . Upon complete failure $U = 0$ and $W_f = E_f = WDG_f$ which corresponds to the expected energy that is dissipated from complete failure of the bar, and is plotted as a constant value of energy.

Favorable results are also obtained for the MPM configurations of the tensile bar problem with a transverse line of weakened material points displayed in figure 5.13. Contour plots of $[[u_n]]/u_0$ in figure 5.14 display failure patterns that also initiate from the weakened region of material and reproduce the correct global failure surface. As the grid is refined the failure pattern resembles the ideal global macro-crack surface. The analytical and numerical solutions of the P vs. δ and W_f vs. δ responses, displayed in figure 5.15, compare very well. Initiating the problem with a weakened transverse line of material points is essentially imposing the idealized failure surface for the bar displayed in figure 5.1. Failure initiation of the weak material occurs simultaneously on the failure surface at a slightly lower ultimate tensile stress than that of the surrounding material. This can be seen in the P vs. δ responses for each value of h because the numerically computed peak load is slightly lower than the peak load predicted by the analytical solution.

Mixed results are observed for material point configurations of the bar problem with a single weak material point serving as an intended failure initiation location (figure 5.16). Figure 5.17 shows that the failure patterns for simulations with low grid resolution initiate from the weakened material point while those of high grid resolution initiate at the boundary of the de-cohesion and elastic material regions. Figure 5.18

displays the corresponding numerical and analytical comparisons of the P vs. δ and W_f vs. δ responses. Very good comparisons are observed for the $h^{-1} = 50 m^{-1}$ and $h^{-1} = 100 m^{-1}$ cases in figures 5.18a and 5.18b respectively. However, the numerically computed global responses for the $h^{-1} = 200 m^{-1}$ and $h^{-1} = 400 m^{-1}$ cases, displayed in figures 5.18c and 5.18d respectively, clearly deviate from the exact solution.

In summary, the baseline MPM simulation of the elastic de-cohesive bar in tension is performed for three different regions of initially weakened material. Very good agreement is observed between analytical and numerical results of both global response and failure pattern for cases where material weakness is imposed within a fixed square area of material points or a transverse line of material points. Use of a single weak material point does not guarantee failure initiation at the location of the weak material point. The MPM configuration associated with a transverse line of material points is the most ideal representation of the elastic de-cohesive bar problem because the global failure surface is predetermined. For this reason, this case is selected to perform the grid orientation bias study presented in the following section.

Chapter 5. Evaluation of the Smearred Crack Approach in MPM

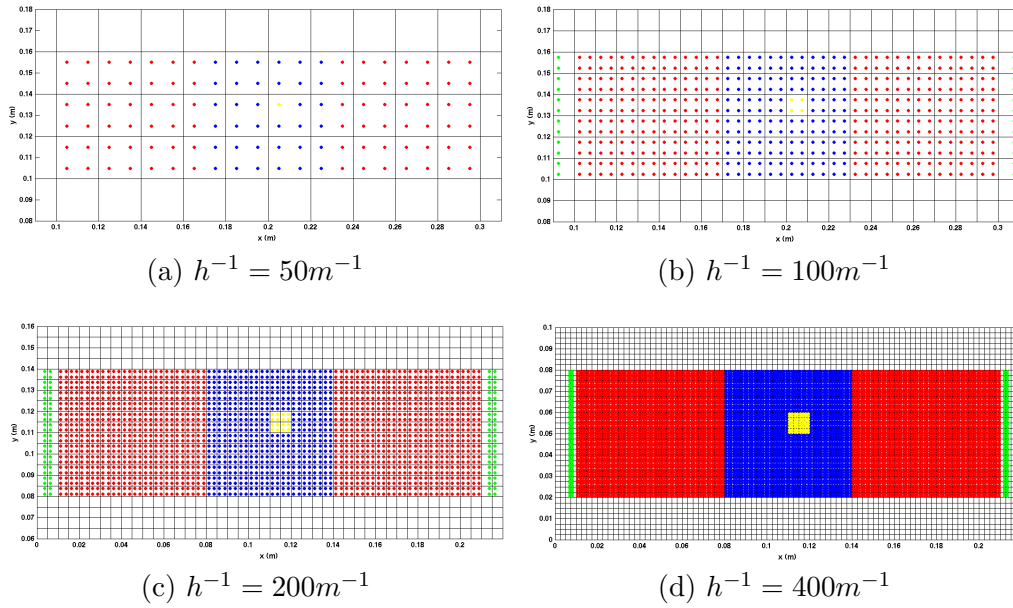


Figure 5.10: Baseline MPM configurations of tensile bar with area of weakness

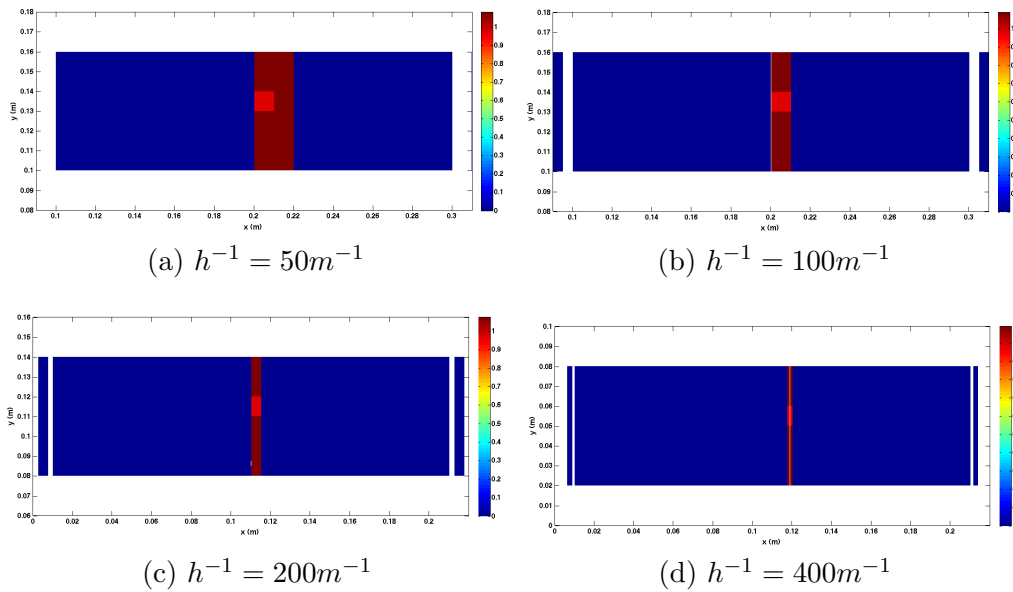


Figure 5.11: Post failure $[[u]]_n/u_0$ plots of tensile bar with area of weakness

Chapter 5. Evaluation of the Smearred Crack Approach in MPM

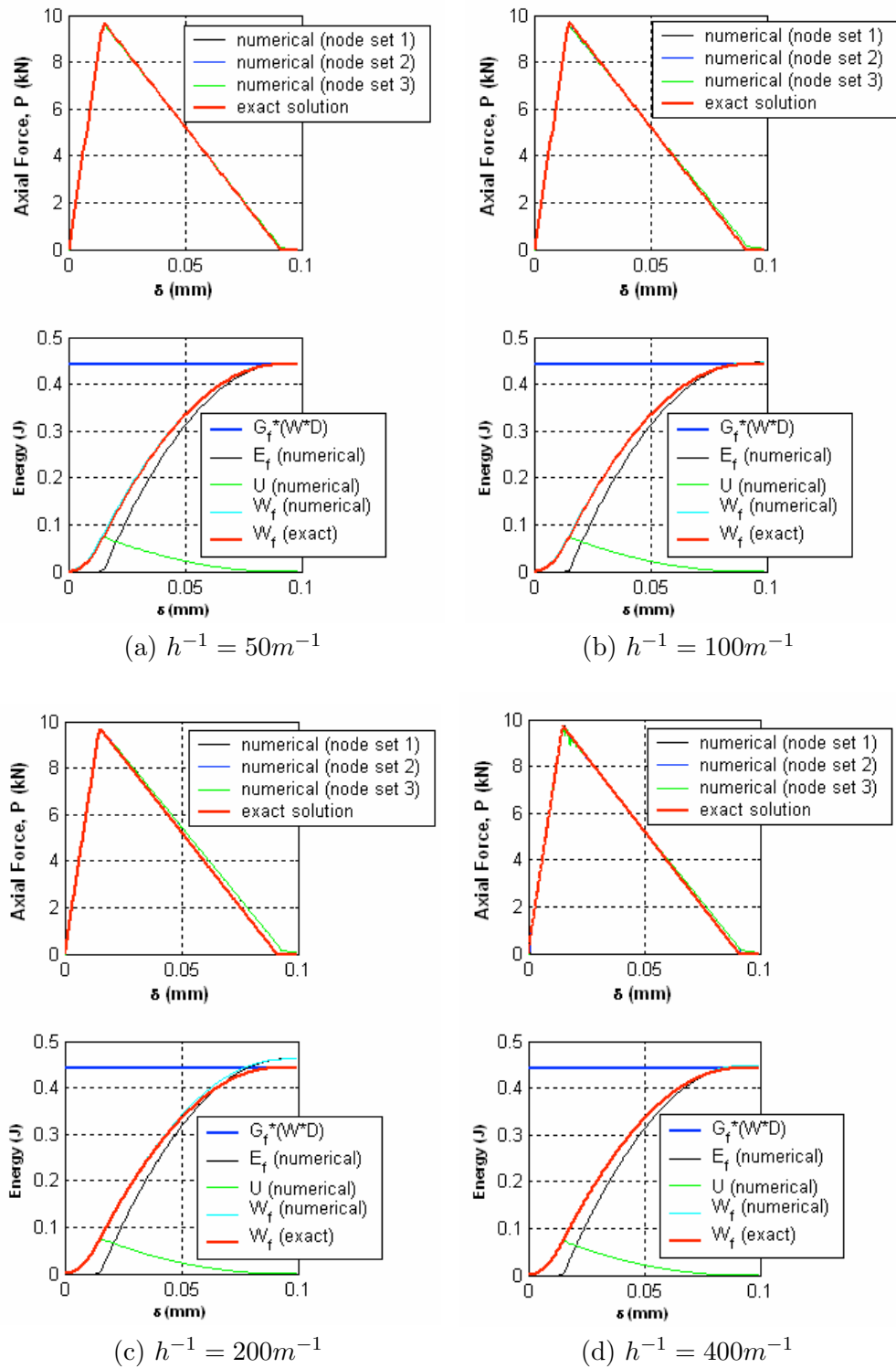


Figure 5.12: MPM solutions of baseline tensile bar problem with area of weakness

Chapter 5. Evaluation of the Smeard Crack Approach in MPM

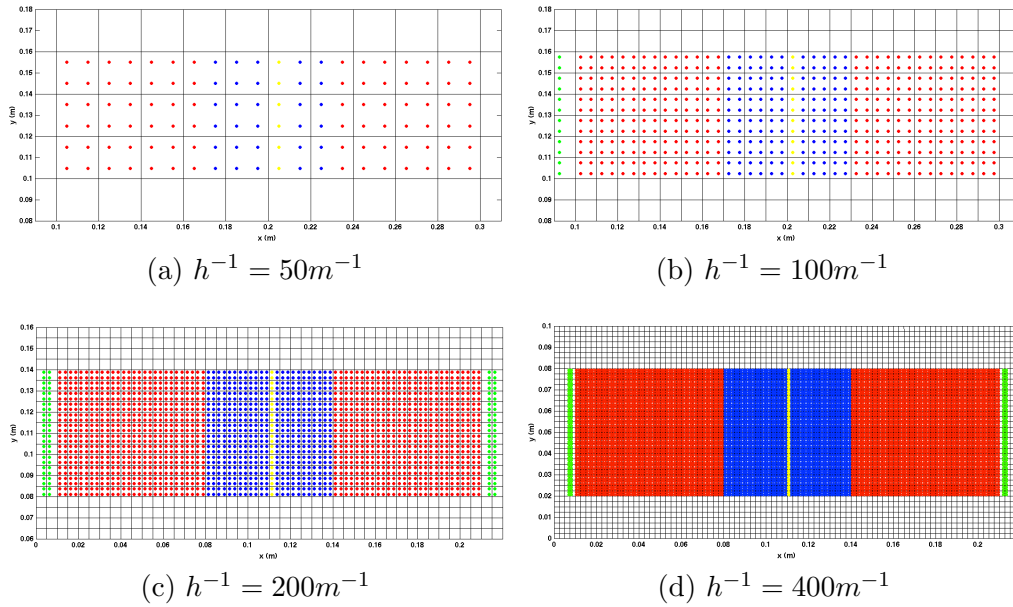


Figure 5.13: Baseline MPM configurations of tensile bar with plane of weakness

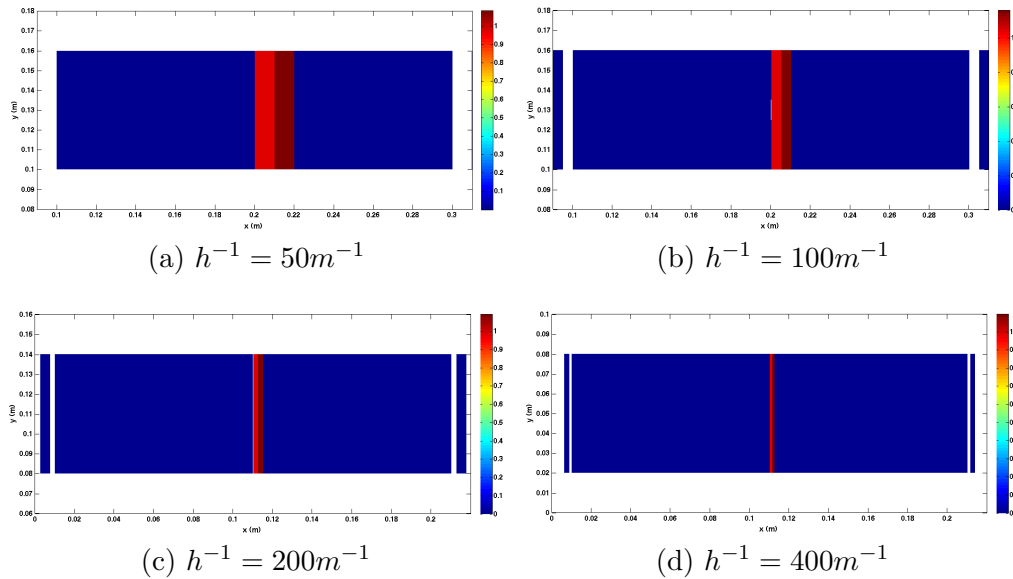


Figure 5.14: Post failure $[[u]]_n/u_0$ plots of tensile bar with plane of weakness

Chapter 5. Evaluation of the Smearred Crack Approach in MPM

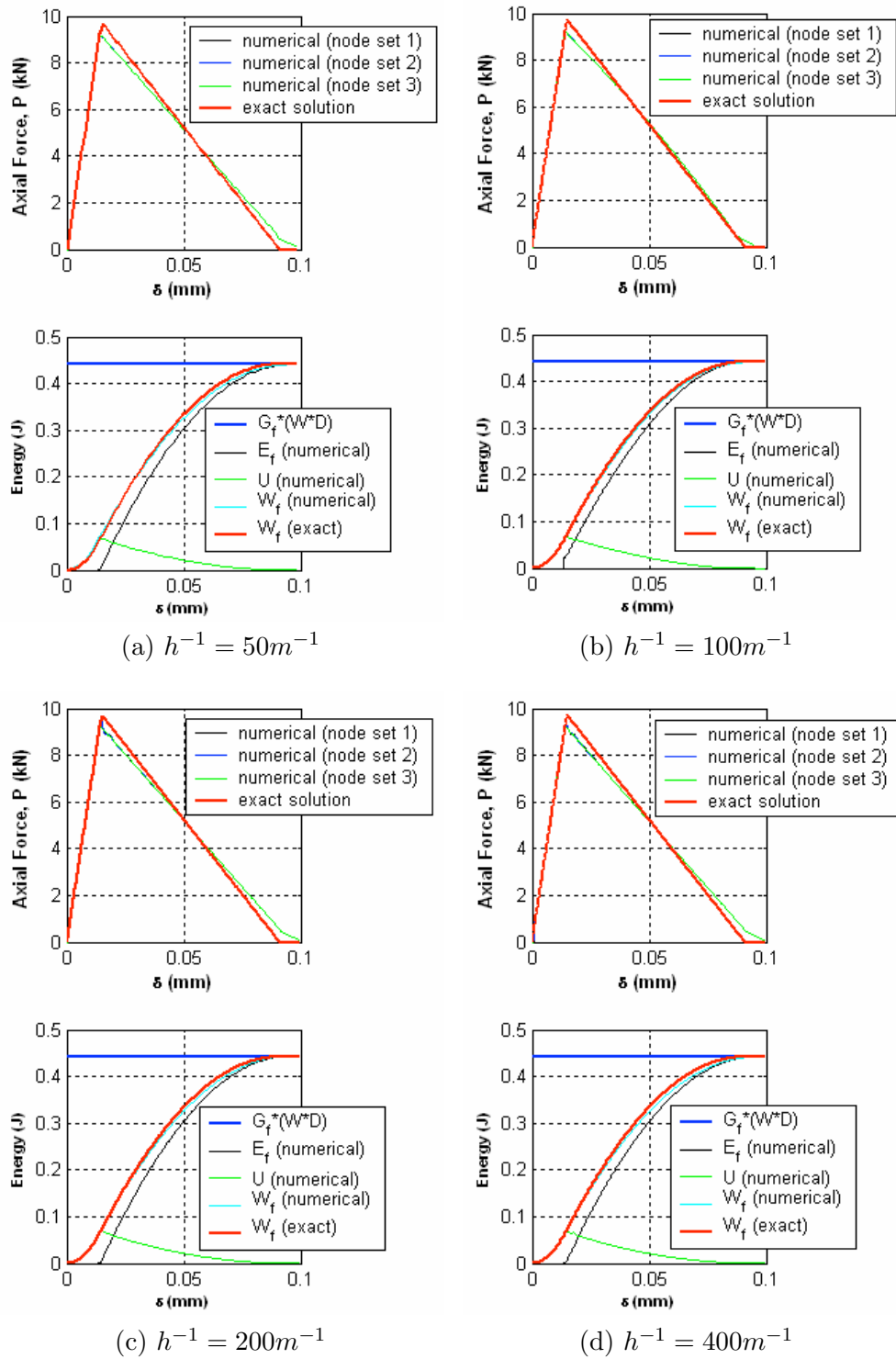


Figure 5.15: MPM solutions for baseline tensile bar problem with plane of weakness

Chapter 5. Evaluation of the Smeared Crack Approach in MPM

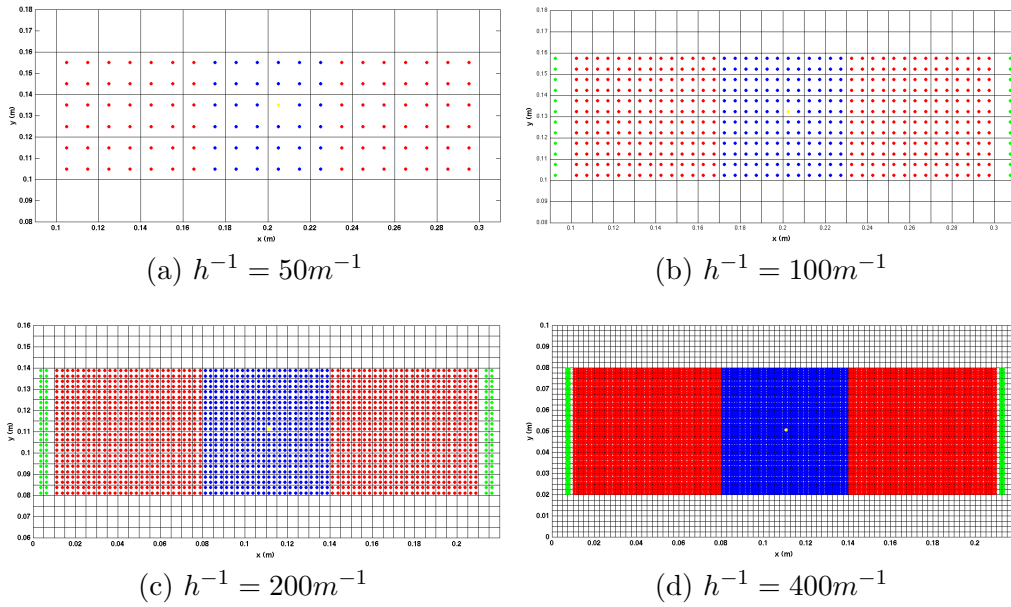


Figure 5.16: Baseline MPM configurations of tensile bar with one weak point

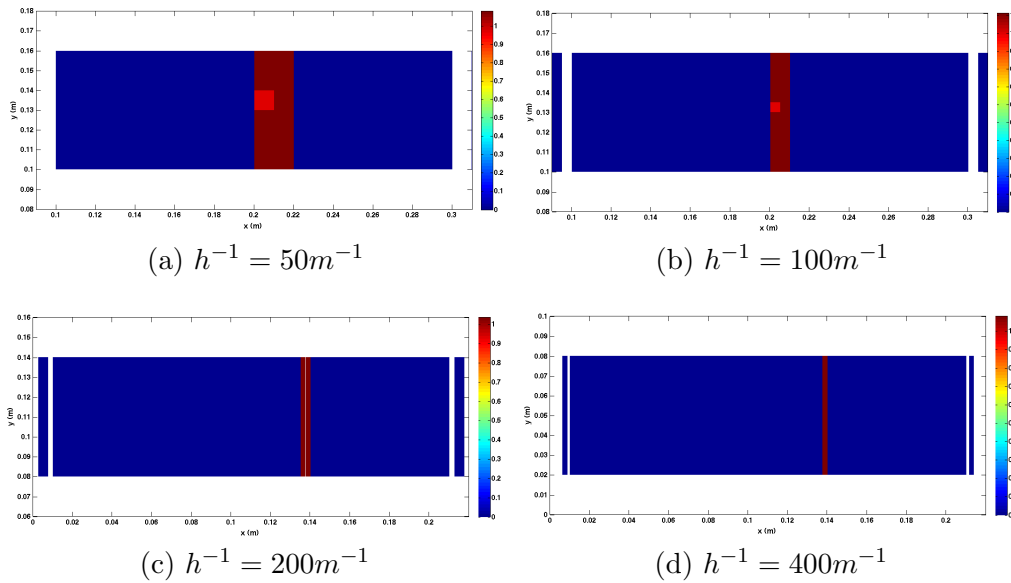


Figure 5.17: Post failure $[[u]]_n/u_0$ plots of tensile bar with one weak point

Chapter 5. Evaluation of the Smearred Crack Approach in MPM

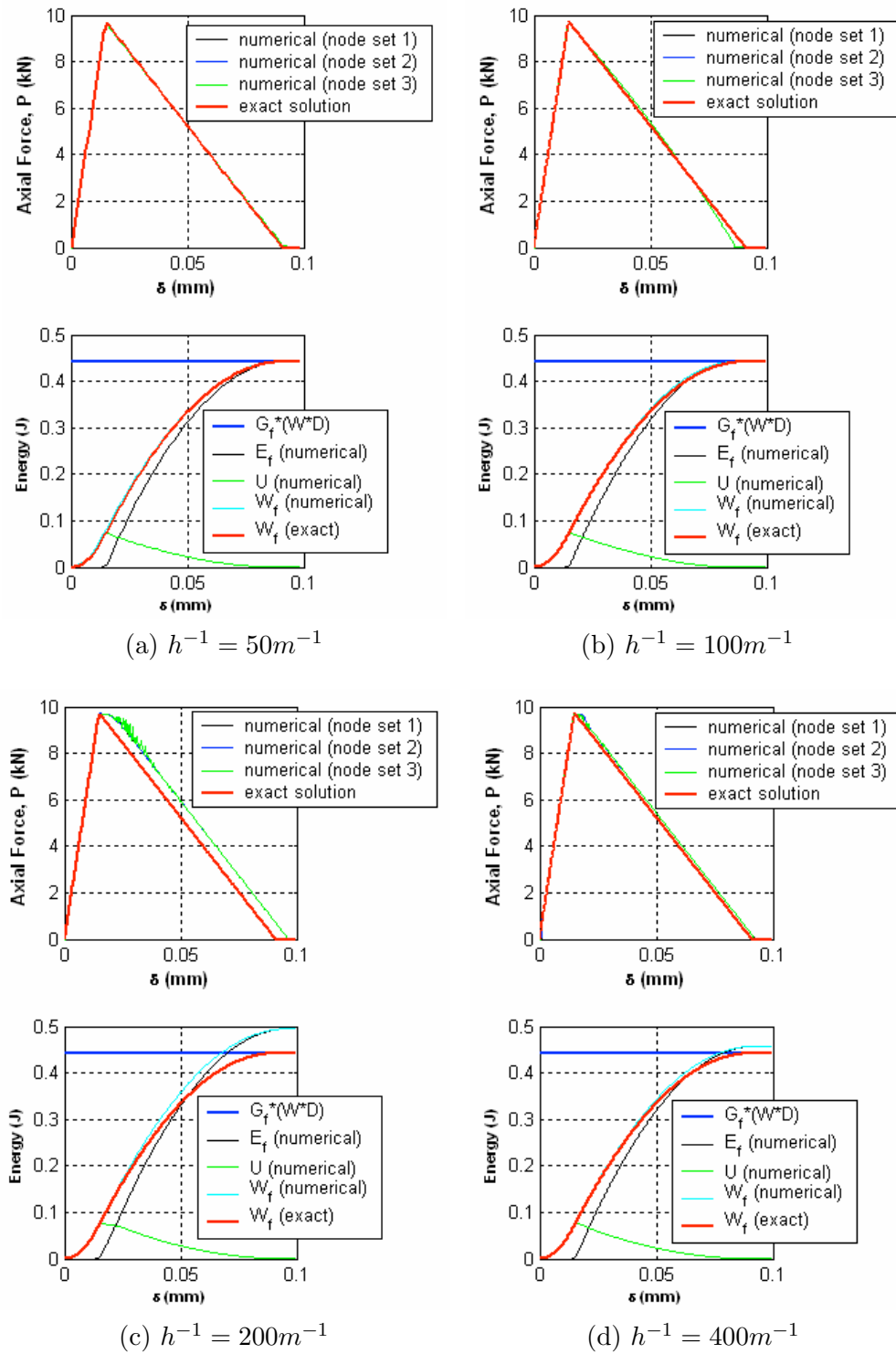


Figure 5.18: MPM solutions for baseline tensile bar problem with one weak point

5.5 Mesh Dependency in Smearred Crack MPM Results

Any robust computational method must demonstrate solution convergence as the spatial discretization of the problem is resolved, regardless the discretization structure. This capability has been demonstrated for an isotropic linear elastic body in MPM with regard to the effect of relative orientation between the grid and the body of material points (see section 5.3). The existence of some type of mesh orientation bias in smearred crack MPM results is hypothesized based on past findings for smearred crack analysis in FEM [54]. How does the orientation of the computational grid effect material failure simulation results in MPM using the smearred crack approach? Are the effects significant, and if so, what are their causes? Is there a simple remedy to the problem? Obtaining answers to the aforementioned questions lies at the heart of this research and is the focus of this section.

5.5.1 The Mesh Orientation Bias

The bias due to grid orientation in computational fracture results using a smearred crack approach in MPM is demonstrated using the two configurations of the bar problem displayed in figures 5.19 and 5.20. Only the $h^{-1} = 400 m^{-1}$ grid resolution is used for the baseline ($\alpha = 0^\circ$) and $\alpha = 45^\circ$ cases. The correct global failure surface is imposed by prescribing a weakened transverse line of material points across the width of the bar that have a reduced value of τ_{nf} from the surrounding material.

The global responses for P vs. δ and W_f vs. δ are displayed in figures 5.21 and 5.22 for the baseline and $\alpha = 45^\circ$ cases respectively. The difference between results for the two grid orientations is immediately apparent. Numerical results for the baseline case agree well with the exact solution. An extreme stiffening of the P vs. δ response

is observed for the $\alpha = 45^\circ$ case during post peak loading. Consequently, the W_f vs. δ response differs significantly from the exact solution. Although some softening is occurs, the elastic energy, U , does not decrease after the peak load is reached and the energy dissipated from fracture, E_f , continues to increase.

The various plots of energy in figure 5.22 provide two pieces of information that could explain the cause of the troubling result of the stiff P vs. δ response for the $\alpha = 45^\circ$ case. These clues are the continuously increasing value of E_f and constant value of U throughout loading.

In order to gain further insight to the cause of the continuous increase in E_f , the failure patterns for the final configurations are examined. Contour plots of $[[u_n]]/u_0$ are displayed in figures 5.23 and 5.24 for the baseline and $\alpha = 45^\circ$ cases respectively. Complete failure is observed for the baseline case. The failure is confined to a very narrow region that resembles the ideal global failure surface consistent with the exact solution. In the case of $\alpha = 45^\circ$, complete failure does not occur anywhere. The failure region develops at the center of the bar and is spread several element widths along the length of the bar. Although no material points completely fail, the diffusion of the failure pattern in the $\alpha = 45^\circ$ case is enough to significantly increase the global energy dissipated by fracture, E_f .

The constant value of elastic potential energy, U , observed for the $\alpha = 45^\circ$ case (figure 5.22) suggests that a constant state of stress remains in the bar during softening. For this reason, stress component contours are examined for the baseline and $\alpha = 45^\circ$ cases at both pre and post load peak loading states. Figures 5.25 - 5.30 display normalized stress contours of the σ_{nn} , σ_{tt} and σ_{nt} components of $\boldsymbol{\sigma}$ for baseline and $\alpha = 45^\circ$ cases at a point during the initial elastic loading just prior to the peak load. For the most part the stress components are uniform throughout the bar for the baseline case and represent a nearly uniaxial stress state. Some non-uniformity of the stress field is observed near the ends of the bar and are attributed to the stress

concentrations caused by no-slip boundary conditions imposed. The value of σ_{xx}/τ_{nf} is nearly equal to 1 everywhere in the bar as expected (see figure 5.25). The values of σ_{yy}/τ_{nf} (figure 5.27) and σ_{xy}/τ_{nf} (figure 5.29) are zero everywhere except near the no-slip boundary. The contours of stress components for $\alpha = 45^\circ$ are not uniform across the bar, but can be described as having a distinct uniform grid pattern. The plot of σ_{nn}/τ_{nf} in figure 5.26 shows that the extreme values of tension are located on the lines of the grid pattern, while material points between the lines have a slightly lower value. Figures 5.28 and 5.30 display a similar trend for the σ_{tt}/τ_{nf} and σ_{nt}/τ_{nf} stress components respectively. It can be argued that σ_{tt}/τ_{nf} and σ_{nt}/τ_{nf} are zero throughout the bar in an average sense. The overall behavior of the $\alpha = 45^\circ$ case is uniaxial tension for elastic loading; a result confirmed by the convergence studies performed in section 5.3. The specific cause of the patterns observed in the stress field for $\alpha = 45^\circ$ is addressed in a later section.

Figures 5.31 - 5.36 display contours plots of σ_{nn}/τ_{nf} , σ_{tt}/τ_{nf} and σ_{nt}/τ_{nf} for baseline and $\alpha = 45^\circ$ cases at a point during the softening portion of loading. As expected, a nearly uniaxial state of stress is maintained in the bar for the baseline case throughout failure. The value of σ_{xx}/τ_{nf} displayed in figure 5.31 has dropped to a value lower than 1. The values of σ_{yy}/τ_{nf} (figure 5.33) and σ_{xy}/τ_{nf} (figure 5.35) remain nearly zero throughout the bar with small variations near the failure region. The contour plot of σ_{nn}/τ_{nf} for $\alpha = 45^\circ$ retains the same uniform grid pattern (figure 5.32). Some softening has occurred but the decrease in σ_{nn}/τ_{nf} is obviously not uniform over the bar. A distinct difference in the values of stress are observed for the elastic and de-cohesion material regions. Although material is failing, values of $\sigma_{nn}/\tau_{nf} = 1$ still persist in the elastic region. A generally lower value of σ_{nn}/τ_{nf} is observed in the de-cohesive material region with the lowest values located inside the diffuse band of failure. While values of σ_{tt}/τ_{nf} remain nearly zero in the elastic material region, the magnitude of σ_{tt}/τ_{nf} increase to values greater than one in the de-cohesion region (see figure 5.34). However, the most notable result for the $\alpha = 45^\circ$ case is the shear

stress component, σ_{nt} , displayed in figure 5.36 which increases to magnitudes of more than twice the value of τ_{nf} near the failure region.

Comparison of the baseline ($\alpha = 0^\circ$) and $\alpha = 45^\circ$ cases reveal a definite grid orientation bias in results for smeared crack analysis in MPM. A close look at $[[u_n]]/u_0$ and the components of $\boldsymbol{\sigma}$ in the bar provide some insight into the unfavorable global response results for $\alpha = 45^\circ$ (see figure 5.22). The continuous increase in E_f is due to a spreading of the failure pattern (see figure 5.24). The reason that the elastic potential energy, U , is maintained at a constant value during post-peak loading seems to be the nature of the non-uniform development in stress over the bar during softening. In general, all stress components remain unchanged within the elastic region while σ_{nn} decreases and the σ_{tt} and σ_{nt} components increase within the de-cohesive material. This non-physical stiffening of material surrounding the failure region is ultimately the reason for the stiffening in the P vs. δ response for the $\alpha = 45^\circ$ case, and could be the cause of the observed spreading of the failure pattern. The following analysis of the MPM stress computation in the presence of failure is intended to provide an explanation for the difference in stress results observed for baseline and non-baseline simulations.

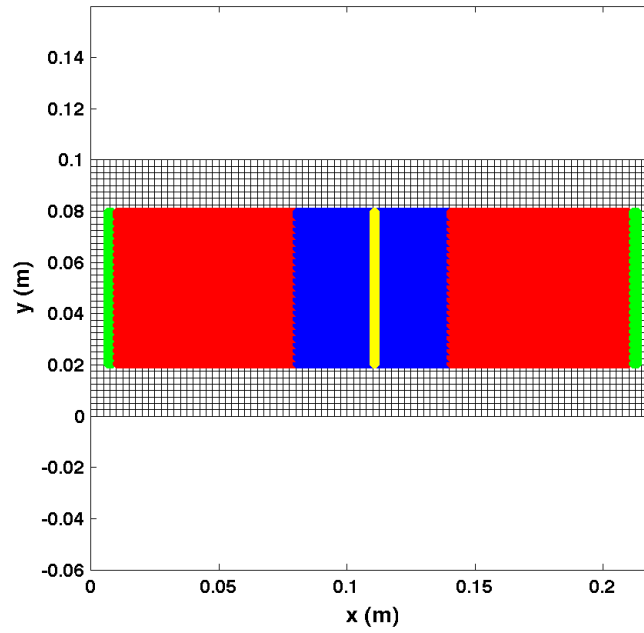


Figure 5.19: Baseline configuration of tensile bar

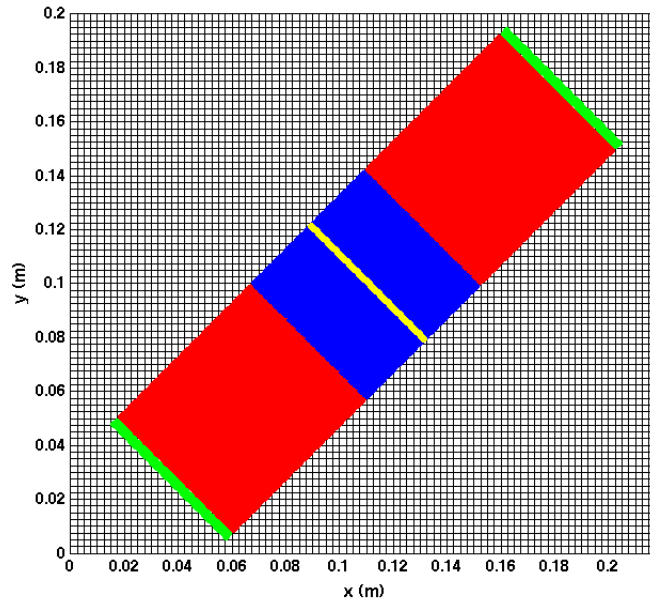


Figure 5.20: $\alpha = 45^\circ$ configuration of tensile bar

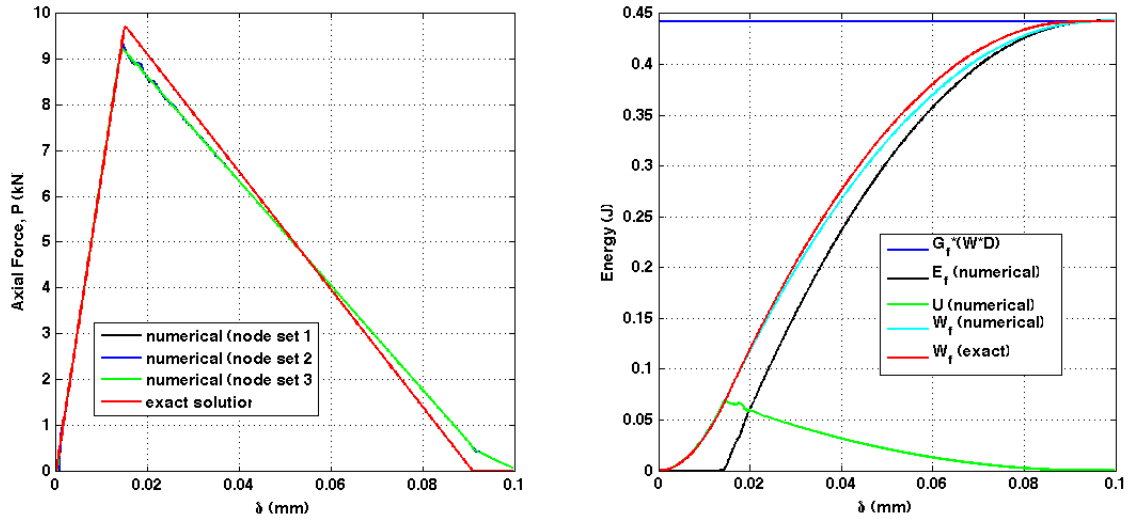


Figure 5.21: P and W_f vs. δ response for baseline tensile bar case

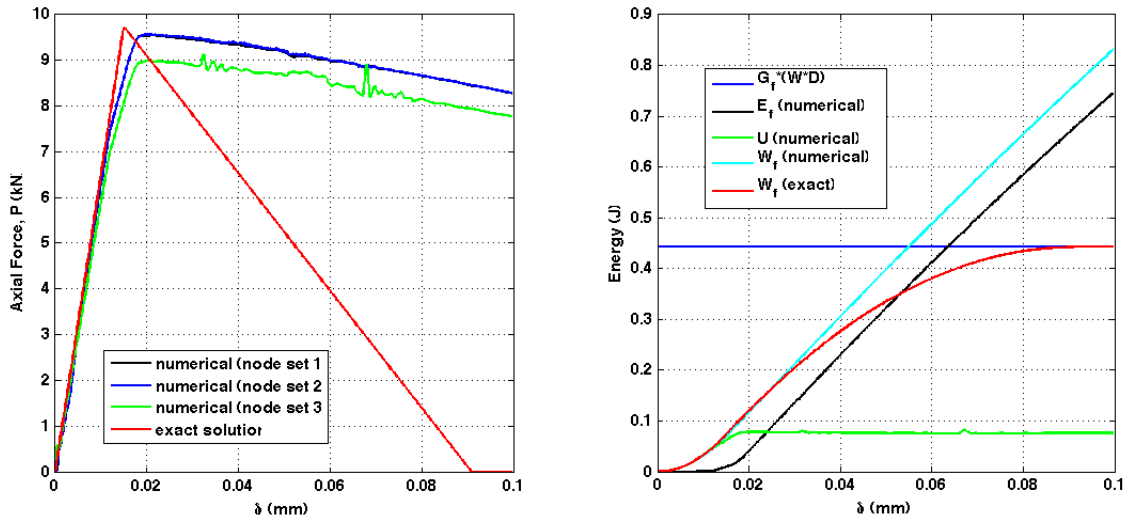


Figure 5.22: P and W_f vs. δ response for $\alpha = 45^\circ$ tensile bar case

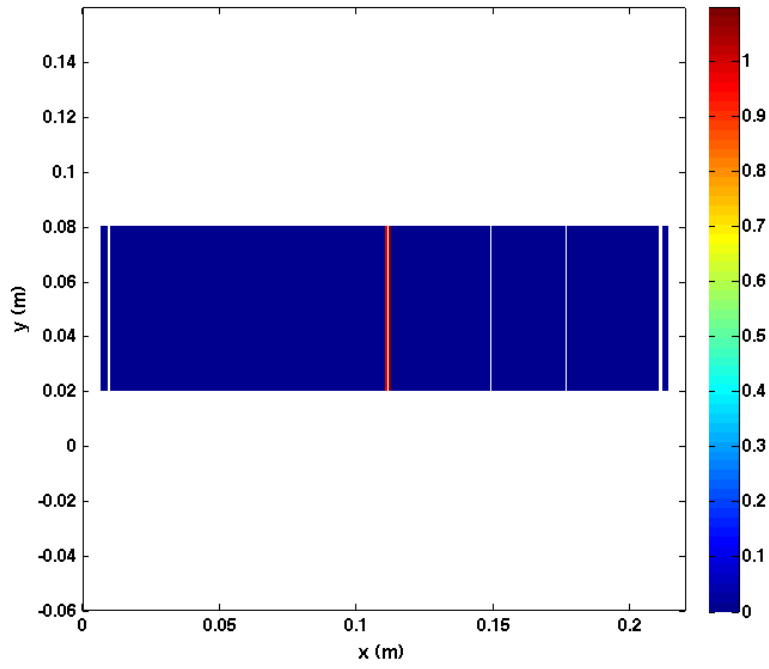


Figure 5.23: $[[u_n]]/u_0$ for baseline tensile bar case at failure

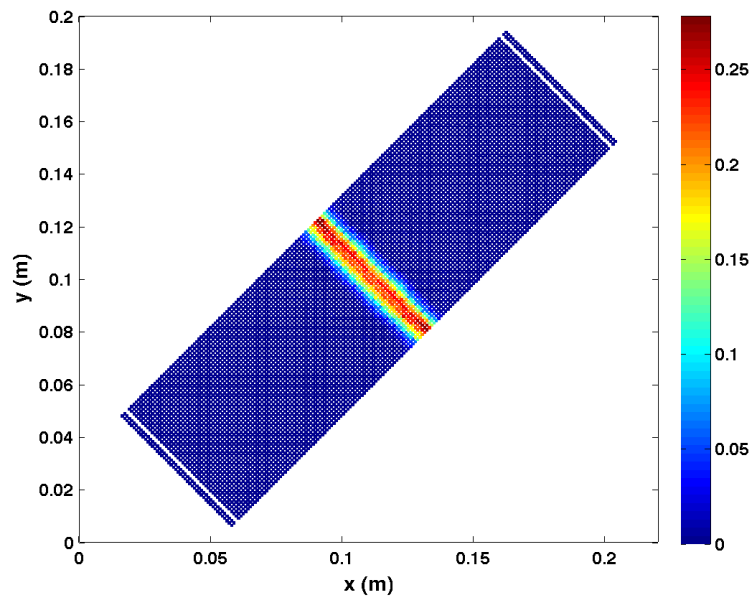


Figure 5.24: $[[u_n]]/u_0$ for $\alpha = 45^\circ$ tensile bar case at failure

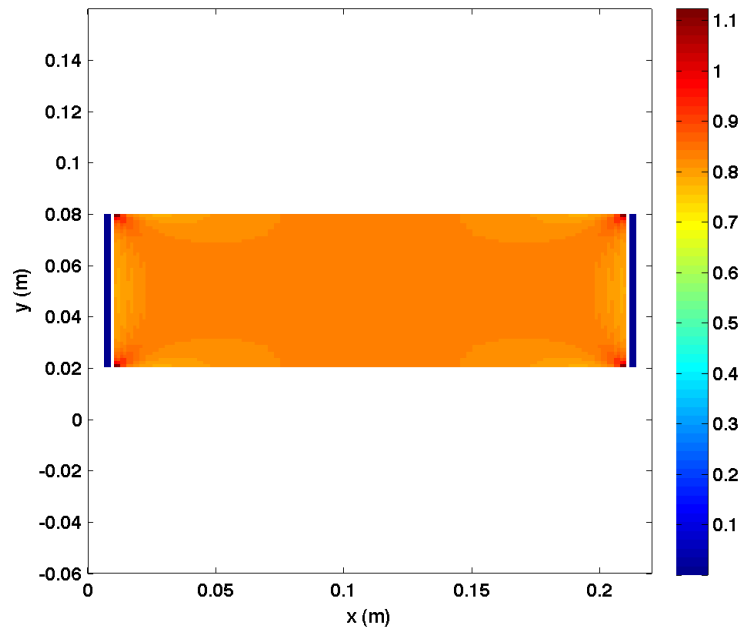


Figure 5.25: σ_{xx}/τ_{nf} for baseline tensile bar case during elastic deformation

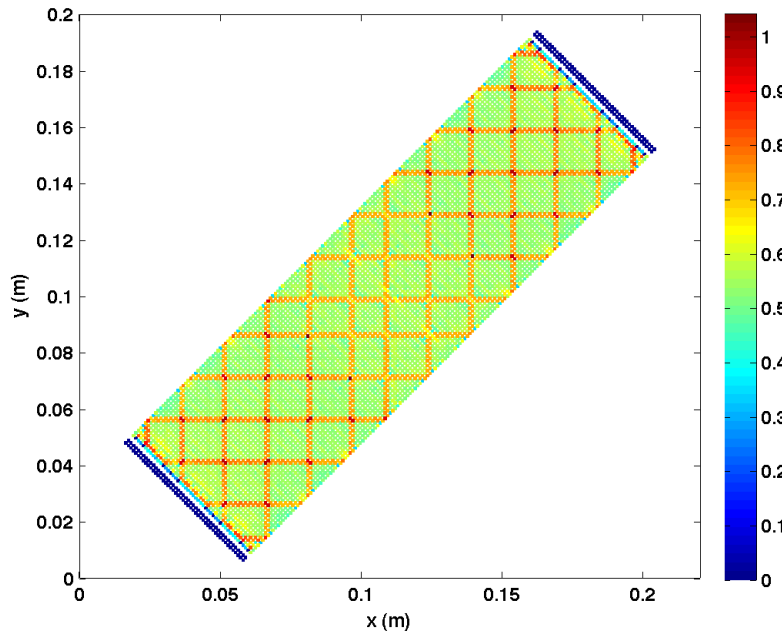


Figure 5.26: σ_{nn}/τ_{nf} for $\alpha = 45^\circ$ tensile bar case during elastic deformation

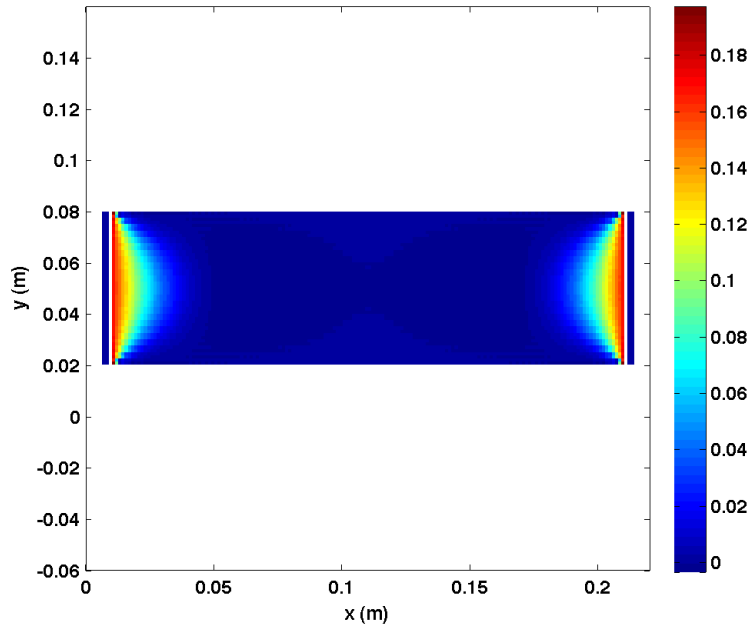


Figure 5.27: σ_{yy}/τ_{nf} for baseline tensile bar case during elastic deformation

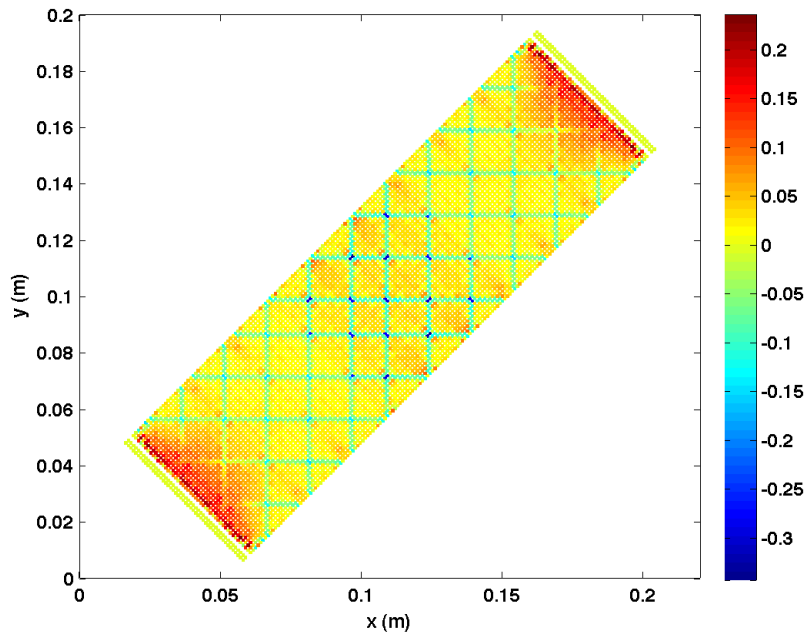


Figure 5.28: σ_{tt}/τ_{nf} for $\alpha = 45^\circ$ tensile bar case during elastic deformation

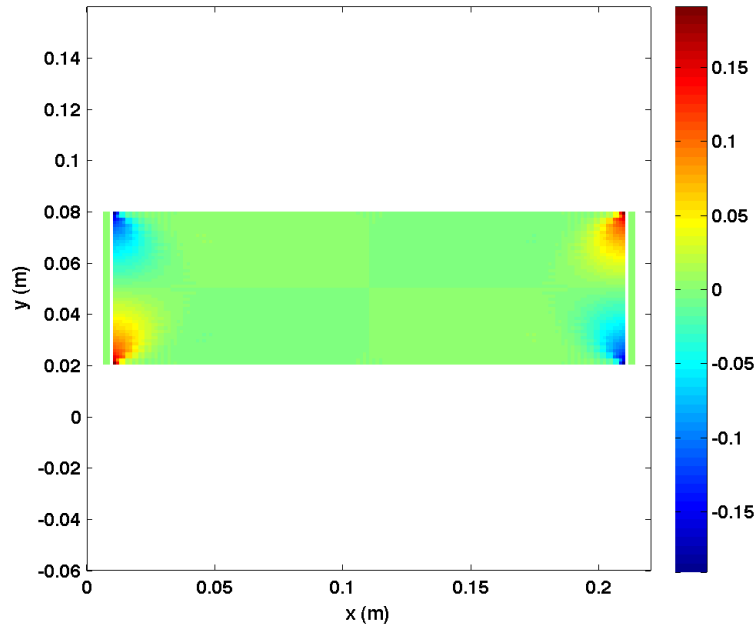


Figure 5.29: σ_{xy}/τ_{nf} for baseline tensile bar case during elastic deformation

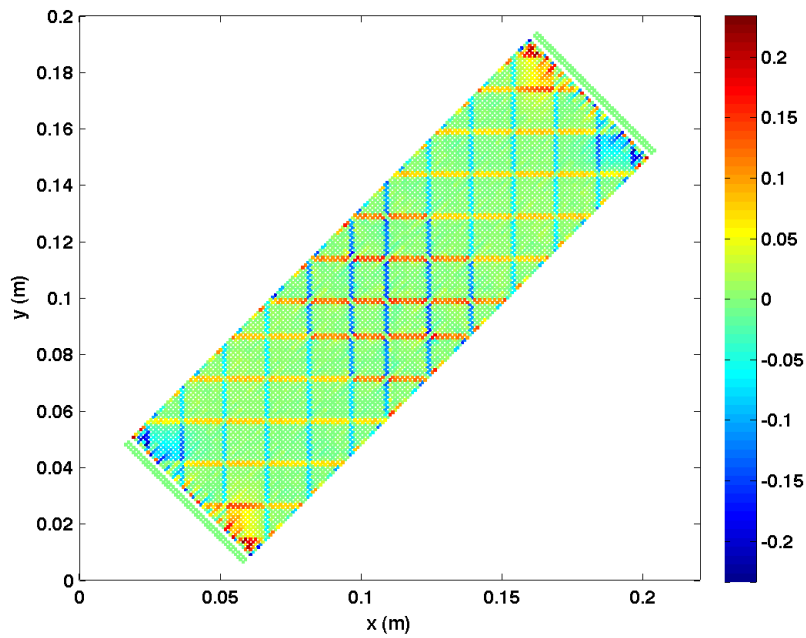


Figure 5.30: σ_{nt}/τ_{nf} for $\alpha = 45^\circ$ tensile bar case during elastic deformation

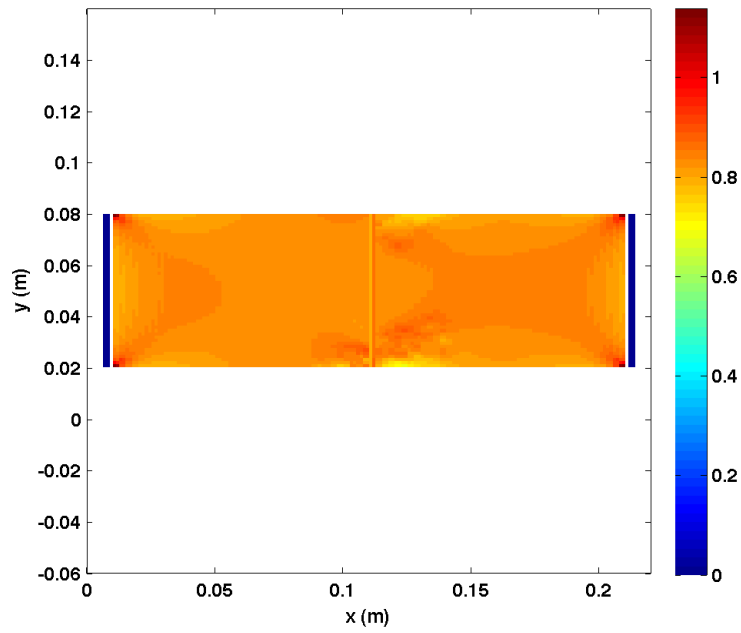


Figure 5.31: σ_{xx}/τ_{nf} for baseline tensile bar case during softening

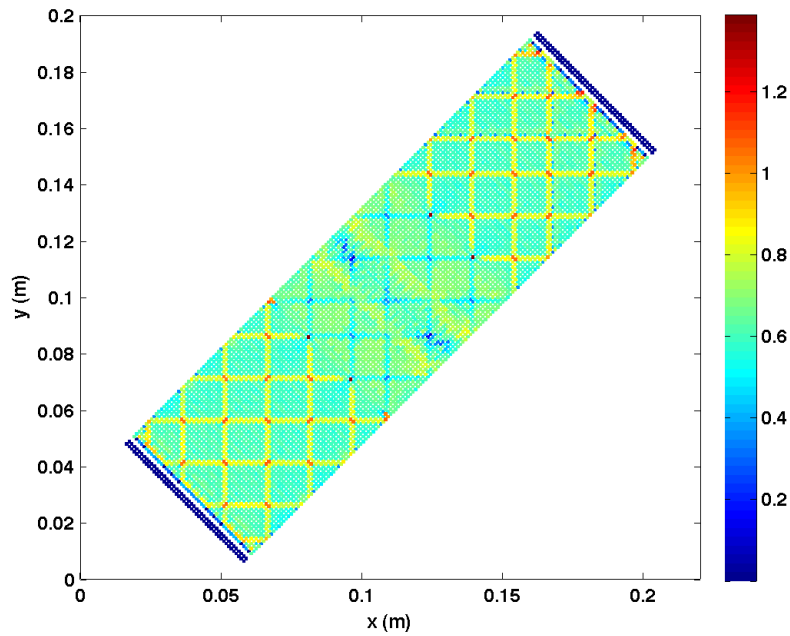


Figure 5.32: σ_{nn}/τ_{nf} for $\alpha = 45^\circ$ tensile bar case during softening

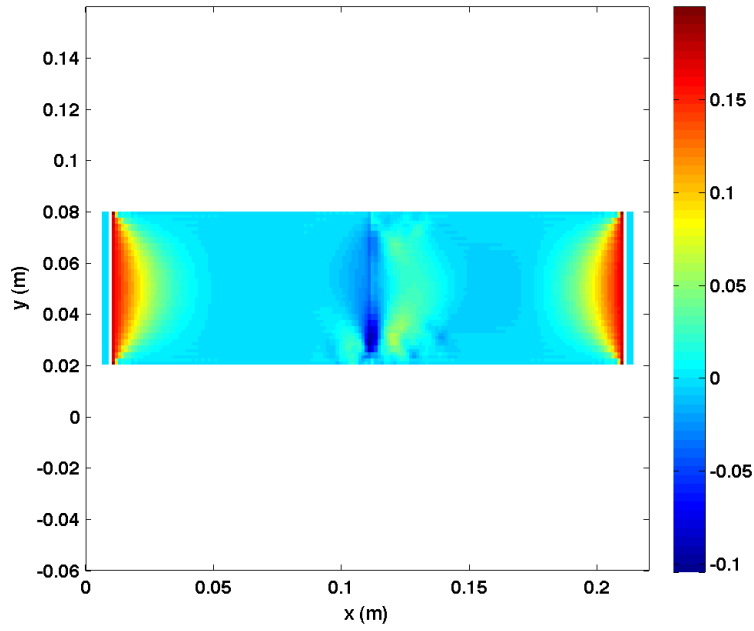


Figure 5.33: σ_{yy}/τ_{nf} for baseline tensile bar case during softening

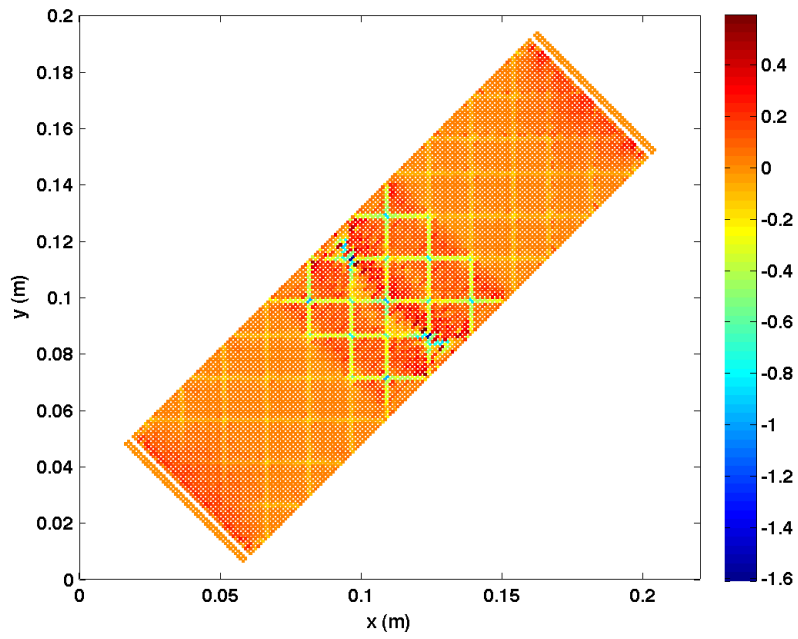


Figure 5.34: σ_{tt}/τ_{nf} for $\alpha = 45^\circ$ tensile bar case during softening

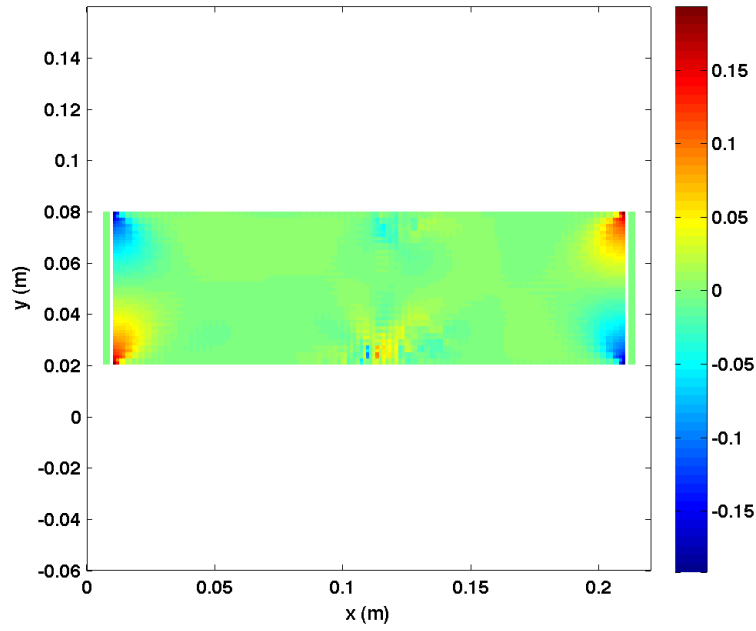


Figure 5.35: σ_{xy}/τ_{nf} for baseline tensile bar case during softening

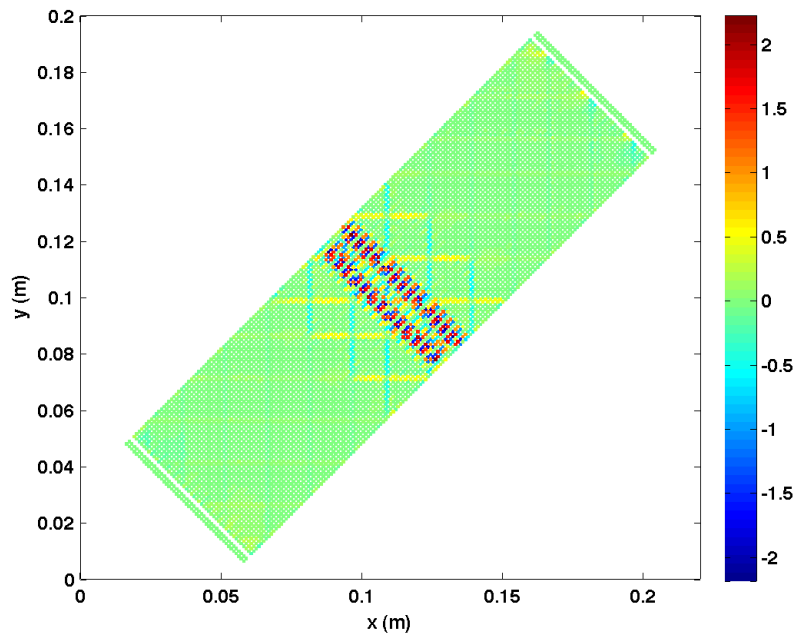


Figure 5.36: σ_{nt}/τ_{nf} for $\alpha = 45^\circ$ tensile bar case during softening

5.5.2 Analysis of the Stress Computation

In the preceding section it was observed that very different stress states are obtained for baseline and non-baseline grid orientations using smeared crack MPM for even the simple case of mode I failure of a bar in tension. A non-physical increase in stress around the failure region occurs for the $\alpha \neq 0$ case, leading to a very stiff global response. However, the baseline simulation produces results consistent with analytical predictions for failure of the bar in uniaxial stress. The purpose of the analysis in this section is to provide an explanation for the difference in stress results observed for baseline and non-baseline simulations at the local level of a material point. A simplified analysis of a material point stress computation in the presence of mode I failure is performed. The hope is that the analysis can provide a simple remedy to the problem.

Consider the single four node square element displayed in figure 5.37 that comprises the spatial 2-D MPM mesh. The local element coordinates of the element are (ξ, η) for which $-1 \leq \xi \leq 1$ and $-1 \leq \eta \leq 1$. Each node position is denoted by \mathbf{x}_i ($i = 1, 2, 3, 4$). The element sides are aligned with the global unit vector basis $\{\mathbf{e}_x, \mathbf{e}_y\}$ and the length of the element side is h . The velocity of each node is denoted as \mathbf{v}_i . A material point, denoted as $\mathbf{X}_p = (X_p, Y_p)$, lies within the element and is represented by a discrete square sub-volume within the element. The set (ξ_p, η_p) in (4.4.2) denotes the local element coordinates of \mathbf{X}_p . The global coordinates (X_p, Y_p) of \mathbf{X}_p are expressed in terms of the nodal basis functions N_i as follows from equation (4.4.2):

$$X_p = \sum_{i=1}^{N_n} x_i N_i(\xi_p, \eta_p), \quad Y_p = \sum_{i=1}^{N_n} y_i N_i(\xi_p, \eta_p)$$

Figure 5.37 depicts a general mode I fracture scenario of a material point in MPM. A single failure plane has formed over the material point with surface normal \mathbf{n} .

A discontinuity, denoted by $[[\mathbf{u}]] = [[u_n]] \mathbf{n}$, is evolving over the sub-volume. For simplicity it is assumed that the nodal velocities are $\mathbf{v}_i = v_i \mathbf{n}$ ($i = 1, 2, 3, 4$) where v_i denotes the magnitude of the velocity at node i . This simplification represents pure mode I fracture on the failure surface because the motion of the failure plane is assumed to correspond exactly to the motion produced by the velocity field provided by the nodes.

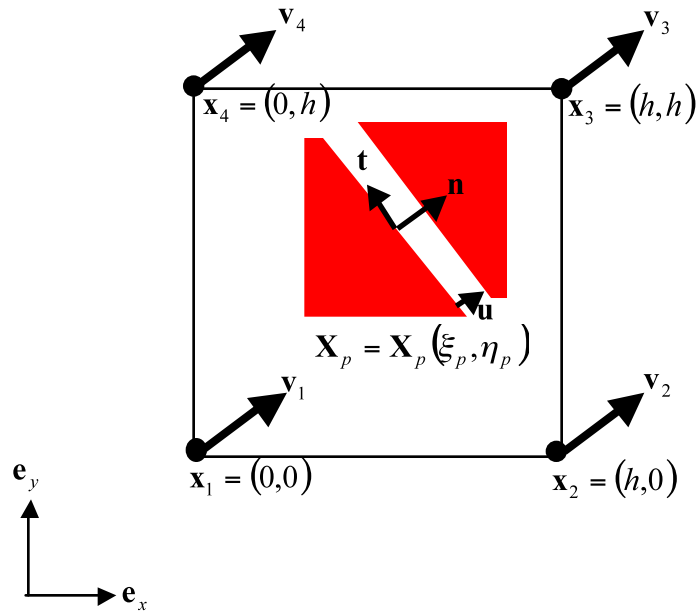


Figure 5.37: Illustration of a general pure mode I failure for a single material point in 2-D

Recall that the mode I fracture is parameterized by the angle, α , such that the failure plane normal vector from equation (5.2.1) is

$$\mathbf{n} = \cos \alpha \mathbf{e}_x + \sin \alpha \mathbf{e}_y$$

An additional constraint is imposed on the velocity field in order to achieve the approximate motion in the 2-D MPM tensile bar simulation. The requirement is

that the directional derivative of the velocity field in the transverse \mathbf{t} direction must be zero as follows:

$$\frac{d\mathbf{v}}{dt} = \nabla\mathbf{v} \cdot \mathbf{t} = 0 \quad (5.5.1)$$

The spatial velocity gradient in equation (5.5.1) $\nabla\mathbf{v}$ is

$$[\nabla\mathbf{v}] = \begin{bmatrix} \frac{\partial v_x}{\partial x} & \frac{\partial v_x}{\partial y} \\ \frac{\partial v_y}{\partial x} & \frac{\partial v_y}{\partial y} \end{bmatrix} \quad (5.5.2)$$

and

$$\mathbf{t} = -\sin\alpha \mathbf{e}_x + \cos\alpha \mathbf{e}_y \quad (5.5.3)$$

In MPM the spatial velocity gradient is computed from equation (4.2.5) as follows:

$$\nabla\mathbf{v} = \sum_{i=1}^4 [\mathbf{v}_i \otimes \nabla N_i(\mathbf{X}_p)] \quad (5.5.4)$$

where ∇N_i is the spatial gradient of the nodal basis function N_i ($i = 1, 2, 3, 4$) computed from equation (4.4.11) to be

$$\nabla N_i = \begin{bmatrix} \frac{\partial N_i}{\partial x} \\ \frac{\partial N_i}{\partial y} \end{bmatrix} = \mathbf{J}^{-1} \begin{bmatrix} \frac{\partial N_i}{\partial \xi} \\ \frac{\partial N_i}{\partial \eta} \end{bmatrix}$$

The Jacobian matrix in equation (4.4.11) is taken from equation (4.4.12) to be

$$\mathbf{J} = \begin{bmatrix} \sum_{i=1}^4 x_i \frac{\partial N_i}{\partial \xi}(\xi_p, \eta_p) & \sum_{i=1}^4 y_i \frac{\partial N_i}{\partial \xi}(\xi_p, \eta_p) \\ \sum_{i=1}^4 x_i \frac{\partial N_i}{\partial \eta}(\xi_p, \eta_p) & \sum_{i=1}^4 y_i \frac{\partial N_i}{\partial \eta}(\xi_p, \eta_p) \end{bmatrix}$$

Equation (4.4.2) is used to evaluate the partial derivatives of global coordinates with respect to local element coordinates. The basis functions are restated from equation (4.4.1) as follows:

$$\begin{aligned} N_1(\xi, \eta) &= \frac{1}{4}(1 - \xi)(1 - \eta) \\ N_2(\xi, \eta) &= \frac{1}{4}(1 + \xi)(1 - \eta) \\ N_3(\xi, \eta) &= \frac{1}{4}(1 + \xi)(1 + \eta) \\ N_4(\xi, \eta) &= \frac{1}{4}(1 - \xi)(1 + \eta) \end{aligned}$$

The partial derivatives of the basis functions with respect to the local element coordinates are

$$\begin{aligned} \frac{\partial N_1}{\partial \xi} &= \frac{1}{4}(\eta - 1) & \frac{\partial N_1}{\partial \eta} &= \frac{1}{4}(\xi - 1) \\ \frac{\partial N_2}{\partial \xi} &= \frac{1}{4}(1 - \eta) & \frac{\partial N_2}{\partial \eta} &= -\frac{1}{4}(1 + \xi) \\ \frac{\partial N_3}{\partial \xi} &= \frac{1}{4}(1 + \eta) & \frac{\partial N_3}{\partial \eta} &= \frac{1}{4}(1 + \xi) \\ \frac{\partial N_4}{\partial \xi} &= -\frac{1}{4}(1 + \eta) & \frac{\partial N_4}{\partial \eta} &= \frac{1}{4}(1 - \xi) \end{aligned} \tag{5.5.5}$$

Equation (5.5.5) are used to evaluate the components of \mathbf{J} in (4.4.11). The result is

$$\begin{aligned}
 \frac{\partial X_p}{\partial \xi} &= \sum_{i=1}^4 x_i \frac{\partial N_i}{\partial \xi}(\xi_p, \eta_p) = \frac{h}{4}(1 - \eta) + \frac{h}{4}(1 + \eta) = \frac{h}{2} \\
 \frac{\partial X_p}{\partial \eta} &= \sum_{i=1}^4 x_i \frac{\partial N_i}{\partial \eta}(\xi_p, \eta_p) = -\frac{h}{4}(1 + \xi) + \frac{h}{4}(1 + \xi) = 0 \\
 \frac{\partial Y_p}{\partial \xi} &= \sum_{i=1}^4 y_i \frac{\partial N_i}{\partial \xi}(\xi_p, \eta_p) = \frac{h}{4}(1 + \eta) - \frac{h}{4}(1 + \eta) = 0 \\
 \frac{\partial Y_p}{\partial \eta} &= \sum_{i=1}^4 y_i \frac{\partial N_i}{\partial \eta}(\xi_p, \eta_p) = \frac{h}{4}(1 + \xi) + \frac{h}{4}(1 - \xi) = \frac{h}{2}
 \end{aligned} \tag{5.5.6}$$

It follows from equation (4.4.12) that \mathbf{J}^{-1} is computed for an arbitrary material point position (ξ, η) to be

$$\mathbf{J}^{-1}(\xi, \eta) = \frac{2}{h} \begin{bmatrix} 1 & 0 \\ 0 & 1 \end{bmatrix} \tag{5.5.7}$$

Since the nodal velocities are $\mathbf{v}_i = v_i \mathbf{n}$ ($i = 1, 2, 3, 4$), the velocity gradient in equation (5.5.4) is expressed as follows:

$$\nabla \mathbf{v} = \sum_{i=1}^4 [v_i \mathbf{n} \otimes \nabla N_i(\mathbf{X}_p)] \tag{5.5.8}$$

Equation (5.5.8) is expressed in matrix form for $\mathbf{v}_i = v_i \mathbf{n} = v_i (\cos \alpha \mathbf{e}_x + \sin \alpha \mathbf{e}_y)$.

The result is

$$[\nabla v] = \sum_{i=1}^4 v_i \begin{bmatrix} \cos \alpha \frac{\partial N_i}{\partial x} & \cos \alpha \frac{\partial N_i}{\partial y} \\ \sin \alpha \frac{\partial N_i}{\partial x} & \sin \alpha \frac{\partial N_i}{\partial y} \end{bmatrix} \tag{5.5.9}$$

The terms of the sum in (5.5.9) are evaluated by using equations (4.4.11), (5.5.5) and (5.5.7) as follows:

$$\begin{aligned}
 [\nabla \mathbf{v}] &= \frac{2v_1}{h} \begin{bmatrix} \cos \alpha (\eta - 1) & \cos \alpha (\xi - 1) \\ \sin \alpha (\eta - 1) & \sin \alpha (\xi - 1) \end{bmatrix} \\
 &+ \frac{2v_2}{h} \begin{bmatrix} \cos \alpha (1 - \eta) & -\cos \alpha (1 + \xi) \\ \sin \alpha (1 - \eta) & -\sin \alpha (1 + \xi) \end{bmatrix} \\
 &+ \frac{2v_3}{h} \begin{bmatrix} \cos \alpha (1 + \eta) & \cos \alpha (1 + \xi) \\ \sin \alpha (1 + \eta) & \sin \alpha (1 + \xi) \end{bmatrix} \\
 &+ \frac{2v_4}{h} \begin{bmatrix} -\cos \alpha (1 + \eta) & \cos \alpha (1 - \xi) \\ -\sin \alpha (1 + \eta) & \sin \alpha (1 - \xi) \end{bmatrix}
 \end{aligned} \tag{5.5.10}$$

The components of $\nabla \mathbf{v}$ are

$$\begin{aligned}
 \frac{\partial v_x}{\partial x} &= \frac{2}{h} \cos \alpha [(1 - \eta)(v_2 - v_1) + (1 + \eta)(v_3 - v_4)] \\
 \frac{\partial v_y}{\partial y} &= \frac{2}{h} \sin \alpha [(1 - \xi)(v_4 - v_1) + (1 + \xi)(v_3 - v_2)] \\
 \frac{\partial v_x}{\partial y} &= \frac{2}{h} \cos \alpha [(1 - \xi)(v_4 - v_1) + (1 + \xi)(v_3 - v_2)] \\
 \frac{\partial v_y}{\partial x} &= \frac{2}{h} \sin \alpha [(1 - \eta)(v_2 - v_1) + (1 + \eta)(v_3 - v_4)]
 \end{aligned} \tag{5.5.11}$$

For compactness the following parameters are defined:

$$\begin{aligned}
 A &= [(1 - \eta)(v_2 - v_1) + (1 + \eta)(v_3 - v_4)] \\
 B &= [(1 - \xi)(v_4 - v_1) + (1 + \xi)(v_3 - v_2)]
 \end{aligned} \tag{5.5.12}$$

Using (5.5.11) and (5.5.12), $\nabla \mathbf{v}$ is expressed in matrix form to be

$$[\nabla v] = \frac{2}{h} \begin{bmatrix} \cos \alpha A & \cos \alpha B \\ \sin \alpha A & \sin \alpha B \end{bmatrix} \quad (5.5.13)$$

The directional derivative in equation (5.5.1) is computed to be

$$\left[\frac{dv}{dt} \right] = \frac{2}{h} \begin{bmatrix} \cos \alpha (-\sin \alpha A + \cos \alpha B) \\ \sin \alpha (-\sin \alpha A + \cos \alpha B) \end{bmatrix} \quad (5.5.14)$$

From (5.5.14) it is apparent that a pure mode I motion requires the following constraint on the velocity field:

$$\sin \alpha A = \cos \alpha B \quad (5.5.15)$$

The strain increment on a material point is computed from equation (4.3.8) to be

$$\Delta \boldsymbol{\varepsilon}_p = \frac{\Delta t}{2} \sum_{i=1}^4 \left[\nabla N_i(\mathbf{X}_p) \otimes \mathbf{v}_i + (\nabla N_i(\mathbf{X}_p) \otimes \mathbf{v}_i)^T \right] \quad (5.5.16)$$

Equation (5.5.16) is constructed from the symmetric part of $\nabla \mathbf{v}$ in equation (5.5.10) as follows:

$$\begin{aligned}
 & \Delta [\boldsymbol{\varepsilon}_p] \\
 &= \Delta t \frac{2v_1}{h} \left[\begin{array}{cc} \cos \alpha (\eta - 1) & \frac{1}{2} (\cos \alpha (\xi - 1) + \sin \alpha (\eta - 1)) \\ \frac{1}{2} (\cos \alpha (\xi - 1) + \sin \alpha (\eta - 1)) & \sin \alpha (\xi - 1) \end{array} \right] \\
 &+ \Delta t \frac{2v_2}{h} \left[\begin{array}{cc} \cos \alpha (1 - \eta) & \frac{1}{2} (\sin \alpha (1 - \eta) - \cos \alpha (1 + \xi)) \\ \frac{1}{2} (\sin \alpha (1 - \eta) - \cos \alpha (1 + \xi)) & -\sin \alpha (1 + \xi) \end{array} \right] \\
 &+ \Delta t \frac{2v_3}{h} \left[\begin{array}{cc} \cos \alpha (1 + \eta) & \frac{1}{2} (\cos \alpha (1 + \xi) + \sin \alpha (1 + \eta)) \\ \frac{1}{2} (\cos \alpha (1 + \xi) + \sin \alpha (1 + \eta)) & \sin \alpha (1 + \xi) \end{array} \right] \\
 &+ \Delta t \frac{2v_4}{h} \left[\begin{array}{cc} -\cos \alpha (1 + \eta) & \frac{1}{2} (\cos \alpha (1 - \xi) - \sin \alpha (1 + \eta)) \\ \frac{1}{2} (\cos \alpha (1 - \xi) - \sin \alpha (1 + \eta)) & \sin \alpha (1 - \xi) \end{array} \right]
 \end{aligned} \tag{5.5.17}$$

In terms of the $\{\mathbf{e}_x, \mathbf{e}_y\}$ basis the components of the strain increment are

$$\Delta \varepsilon_{xx} = \frac{2 \Delta t}{h} \cos \alpha [(1 - \eta) (v_2 - v_1) + (1 + \eta) (v_3 - v_4)] \tag{5.5.18}$$

$$\Delta \varepsilon_{yy} = \frac{2 \Delta t}{h} \sin \alpha [(1 - \xi) (v_4 - v_1) + (1 + \xi) (v_3 - v_2)] \tag{5.5.19}$$

$$\begin{aligned}
 \Delta \varepsilon_{xy} &= \frac{\Delta t}{h} \cos \alpha [(1 - \xi) (v_4 - v_1) + (1 + \xi) (v_3 - v_2)] \\
 &+ \frac{\Delta t}{h} \sin \alpha [(1 - \eta) (v_2 - v_1) + (1 + \eta) (v_3 - v_4)]
 \end{aligned} \tag{5.5.20}$$

Using equation (5.5.12), equations (5.5.18) - (5.5.20) are expressed in compact form as follows:

$$\Delta\varepsilon_{xx} = \frac{2\Delta t}{h} \cos\alpha A \quad (5.5.21)$$

$$\Delta\varepsilon_{yy} = \frac{2\Delta t}{h} \sin\alpha B \quad (5.5.22)$$

$$\Delta\varepsilon_{xy} = \frac{\Delta t}{h} \cos\alpha B + \frac{\Delta t}{h} \sin\alpha A \quad (5.5.23)$$

It will prove to be useful to express the strain increment in terms of the failure surface basis vectors $\{\mathbf{n}, \mathbf{t}\}$ by using the following transformation relationships:

$$\begin{aligned} \Delta\varepsilon_{nn} &= \cos^2\alpha \Delta\varepsilon_{xx} + 2\cos\alpha \sin\alpha \Delta\varepsilon_{xy} + \sin^2\alpha \Delta\varepsilon_{yy} \\ \Delta\varepsilon_{tt} &= \sin^2\alpha \Delta\varepsilon_{xx} - 2\cos\alpha \sin\alpha \Delta\varepsilon_{xy} + \cos^2\alpha \Delta\varepsilon_{yy} \\ \Delta\varepsilon_{nt} &= (\Delta\varepsilon_{yy} - \Delta\varepsilon_{xx}) \cos\alpha \sin\alpha + \Delta\varepsilon_{xy} (\cos^2\alpha - \sin^2\alpha) \end{aligned} \quad (5.5.24)$$

Equations (5.5.23) and (5.5.24) are combined to give the following result:

$$\Delta\varepsilon_{nm} = \frac{2\Delta t}{h} [\cos\alpha A + \sin\alpha B] \quad (5.5.25)$$

$$\Delta\varepsilon_{tt} = 0 \quad (5.5.26)$$

$$\Delta\varepsilon_{nt} = \frac{\Delta t}{h} [\cos\alpha B - \sin\alpha A] \quad (5.5.27)$$

The mode I velocity field constraint in equation (5.5.15) is imposed on the strain increment components in equations (5.5.25) - (5.5.27). After some manipulations the final result is

$$\Delta\varepsilon_{nn} = \frac{2\Delta t}{h \cos \alpha} A \quad (5.5.28)$$

$$\Delta\varepsilon_{tt} = 0 \quad (5.5.29)$$

$$\Delta\varepsilon_{nt} = 0 \quad (5.5.30)$$

It should be noted that mode I velocity field constraint in equation (5.5.15) is identical to requiring that $\Delta\varepsilon_{nt} = 0$ in equation (5.5.27).

The total strain increment on a material point, $\Delta\varepsilon$, is composed of elastic and de-cohesive contributions as follows:

$$\Delta\varepsilon = \Delta\varepsilon^e + \Delta\varepsilon^{dc} \quad (5.5.31)$$

The de-cohesion strain increment $\Delta\varepsilon^{dc}$ in equation (5.5.31) represents opening of the failure surface and is evaluated from equation (3.5.98) to be

$$\Delta\varepsilon^{dc} = \frac{1}{2L_c} [\Delta [[\mathbf{u}]] \otimes \mathbf{n} + \mathbf{n} \otimes \Delta [[\mathbf{u}]]] \quad (5.5.32)$$

A characteristic length of $L_c = h/2$ is used in (5.5.32) for a single material point. In terms of the $\{\mathbf{n}, \mathbf{t}\}$ basis, the components of $\Delta\varepsilon^{dc}$ are

$$\Delta\varepsilon_{nn}^{dc} = \frac{2}{h} \Delta [[u_n]] \quad (5.5.33)$$

$$\Delta\varepsilon_{tt}^{dc} = 0 \quad (5.5.34)$$

$$\Delta \varepsilon_{nt}^{dc} = 0 \quad (5.5.35)$$

The stress increment on a material point, $\Delta \boldsymbol{\sigma}$, is computed from isotropic linear elasticity as follows:

$$\Delta \boldsymbol{\sigma} = \mathbf{C} : \Delta \boldsymbol{\varepsilon}^e \quad (5.5.36)$$

The stress increment components in the $\{\mathbf{n}, \mathbf{t}\}$ basis are obtained by combining equations (5.5.28)-(5.5.31) and (5.5.33)-(5.5.36) with the matrix relationships in equations (4.4.17) and (4.4.21). The final result is

$$\Delta \sigma_{nn} = \frac{2}{h} \frac{E(1-\nu)}{(1+\nu)(1-2\nu)} \left[\frac{\Delta t A}{\cos \alpha} - \Delta [[u_n]] \right] \quad (5.5.37)$$

$$\Delta \sigma_{tt} = \frac{2}{h} \frac{E\nu}{(1+\nu)(1-2\nu)} \left[\frac{\Delta t A}{\cos \alpha} - \Delta [[u_n]] \right] \quad (5.5.38)$$

$$\Delta \sigma_{nt} = 0 \quad (5.5.39)$$

The increment in the normal component of displacement discontinuity, $\Delta [[u_n]]$, is obtained from softening relationship in (3.5.63) to be

$$\Delta [[u_n]] = u_0 \left(1 - \frac{\Delta \sigma_{nn}}{\tau_{nf}} \right) \quad (5.5.40)$$

Equation (5.5.40) and the relationships for u_0 and E_1 in equations (3.5.44) and (4.5.8) respectively are substituted into (5.5.37). The result is

$$\Delta \sigma_{nn} = \frac{2 E_1}{h} \left[\frac{\Delta t A}{\cos \alpha} - \frac{2 G_f}{\tau_{nf}} \left(1 - \frac{\Delta \sigma_{nn}}{\tau_{nf}} \right) \right] \quad (5.5.41)$$

Equation (5.5.41) is rearranged to obtain the following result for $\Delta\sigma_{nn}$:

$$\Delta\sigma_{nn} = 2E_1 \left(h - \frac{4E_1 G_f}{\tau_{nf}^2} \right)^{-1} \left(\frac{\Delta t A}{\cos \alpha} - \frac{2G_f}{\tau_{nf}} \right) \quad (5.5.42)$$

The expression for A in (5.5.12) is substituted into (5.5.42), which leads to the following result:

$$\Delta\sigma_{nn} = 2E_1 \left(h - \frac{4E_1 G_f}{\tau_{nf}^2} \right)^{-1} \left(\frac{\Delta t}{\cos \alpha} [(1 - \eta)(v_2 - v_1) + (1 + \eta)(v_3 - v_4)] - \frac{2G_f}{\tau_{nf}} \right) \quad (5.5.43)$$

Equation (5.5.43) is the general form of the stress increment at a material point for the simple mode I failure depicted in figure 5.37. In general, $\Delta\sigma_{nn}$ is a function of the local position of the material point within the element and the orientation angle of the failure plane normal, α .

The baseline MPM simulation of the elastic de-cohesion bar in tension corresponds to $\alpha = 0$, which is illustrated in figure 5.38 for a single material point in a cell. Since $\cos \alpha = 1$ and $\sin \alpha = 0$ for this case, the pure mode I motion restriction in equation (5.5.15) requires that $B = 0$. It is also assumed that the material point lies within the bounds of the element such that $-1 < \xi < 1$ and $-1 < \eta < 1$. As a consequence the following restrictions apply for the nodal velocity magnitude when $\alpha = 0$:

$$v_4 = v_1, \quad v_3 = v_2 \quad (5.5.44)$$

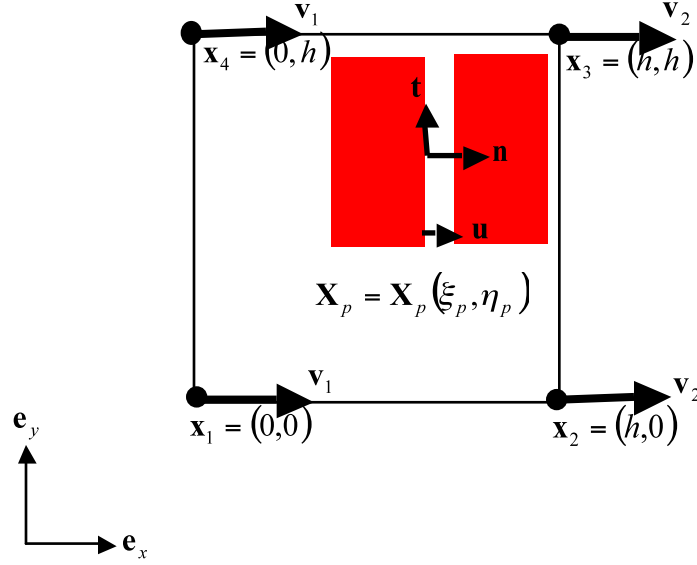


Figure 5.38: Illustration of a pure mode I failure for a single material point in 2-D for $\alpha = 0$

It follows from equation (5.5.43) that the form of the stress increment for the baseline case of $\alpha = 0$ is

$$\Delta\sigma_{nn} = 2E_1 \left(h - \frac{4E_1 G_f}{\tau_{nf}^2} \right)^{-1} \left(2\Delta t (v_2 - v_1) - \frac{2G_f}{\tau_{nf}} \right) \quad (5.5.45)$$

The magnitude of the displacement increment of node i is taken to be

$$\Delta u_i = \Delta t v_i \quad (5.5.46)$$

Substitution of (5.5.46) into (5.5.45) results in the following:

$$\Delta\sigma_{nn} = 2E_1 \left(h - \frac{4E_1 G_f}{\tau_{nf}^2} \right)^{-1} \left(2(\Delta u_2 - \Delta u_1) - \frac{2G_f}{\tau_{nf}} \right) \quad (5.5.47)$$

The relative displacement increment $\Delta u_2 - \Delta u_1$ in equation (5.5.47) is the increment

in elongation of the element in the \mathbf{n} direction (or \mathbf{e}_x in this case), and is defined as follows:

$$\Delta\delta_{elem} = \Delta u_2 - \Delta u_1 \quad (5.5.48)$$

By using (5.5.48) and recalling the expression for u_0 in equation (3.5.44), equation (5.5.47) can be expressed as the following:

$$\Delta\sigma_{nn} = E_1 \left(\frac{h}{2} - \frac{E_1 u_0}{\tau_{nf}} \right)^{-1} (2\Delta\delta_{elem} - u_0) \quad (5.5.49)$$

Equation (5.5.49) is the increment of the normal stress component for a single material point that is softening due to a pure mode I failure for the case of $\alpha = 0$. This is a special case because $\Delta\sigma_{nn}$ is independent of the material point location within the element. Equation (5.5.49) is compared to the exact solution of axial stress in the elastic de-cohesive tensile bar during softening in (5.2.14) restated below for convenience.

$$\sigma_{nn} = E^* \left(L - \frac{E^* u_0}{\tau_{nf}} \right)^{-1} (\delta - u_0)$$

The forms of equations (5.2.14) and (5.5.49) are very similar. In light of this comparison, it is no surprise that the baseline ($\alpha = 0$) case accurately reproduces the exact solution for the elastic de-cohesion bar in tension.

For a non-baseline case where $\alpha \neq 0$ the issue is not so clear. Obviously, accuracy of the numerical MPM solution is lost. As previously discussed, there are two observations regarding the mesh dependence of smeared crack computational fracture simulation results in MPM based on this simple problem. The first is a stiffening of the global $P = P(\delta)$ ($\sigma_{nn}(\delta)$) response and the second is a dispersion of the fail-

ure (de-cohesion) pattern. Can these issues be explained by simply analyzing $\Delta\sigma_{nn}$ locally for $\alpha \neq 0$?

The general expression for $\Delta\sigma_{nn}$ on a material point that is softening due to a mode I failure is

$$\Delta\sigma_{nn} = \bar{H} \left(\frac{1}{\cos \alpha} [(1 - \eta) (\Delta u_2 - \Delta u_1) + (1 + \eta) (\Delta u_3 - \Delta u_4)] - \frac{2G_f}{\tau_{nf}} \right) \quad (5.5.50)$$

where \bar{H} is the softening modulus defined to be

$$\bar{H} = E_1 \left(\frac{h}{2} - \frac{2E_1 G_f}{\tau_{nf}^2} \right)^{-1} \quad (5.5.51)$$

The criterion or ensuring softening in equation (5.2.15) is applied to the case in (5.5.50) . The length restriction on h becomes

$$\frac{h}{2} < \frac{2E_1 G_f}{\tau_{nf}^2} \quad (5.5.52)$$

The dependence of $\Delta\sigma_{nn}$ on α in equation (5.5.50) is examined. The softening modulus is essentially divided by a factor of $\cos \alpha$. Since increasing α from a value of zero (the baseline case) decreases $\cos \alpha$, division by $\cos \alpha$ should decrease the softening modulus (because it is always negative). Keeping along these lines, the expected global response should be associated with a steeper softening slope. However this is not the case. The expected behavior predicted by the local functional dependence of stress on α directly contradicts the observed stiffening behavior of the global response upon increasing α from a value of zero.

There is a chance that elimination of the α dependence of stress altogether could remedy the bias of results. Although this type of thinking is completely counter-intuitive to the preceding analysis, it requires only a simple numerical experiment.

Chapter 5. Evaluation of the Smeared Crack Approach in MPM

By inspection of (5.5.50), division of h and G_f by $\cos \alpha$, will eliminate α from the expression for $\Delta\sigma_{nn}$ in equation (5.5.50). This experiment does not work (results not shown). The stiffened global response of the bar for $\alpha \neq 0$ persists as well as the dispersion of the failure pattern. Adjustment of other parameters such as the smearing length L_c or the fracture energy G_f have no effect on the stiffening behavior or spreading of the failure pattern.

In conclusion, a local analysis of stress for a pure mode I failure at a material point leads to some insight but fails to provide a simple remedy to the mesh orientation bias observed in results of smeared crack fracture computations in MPM. The similarity between the exact solution for the elastic de-cohesion bar in tension and the axial stress component computation is clear and demonstrates analytically the reason for the high accuracy of MPM results for the baseline case. However, analytical results of local stress computations do not explain the stiffening of the global response with increased values of α , but lead one to believe that a softer global response would be obtained by increasing α from the baseline value. As a result the analysis does not provide a basis for simply adjusting fracture parameters which would lead to more favorable results. An adjustment of material parameters based on the analysis in order to eliminate α proves to not help the matter either.

5.5.3 Stiffening and Crack Pattern Dispersion Effects

In this section, potential global effects leading to the problems of stiffening and failure pattern dispersion observed in smeared crack MPM results are considered. An even closer examination of the stress field in the presence of material failure is performed in order to determine the causes of these problems.

Prior to exploring the details of the stress field in the bar during material failure, it is necessary to revisit the issue of the general non-uniformity of stress observed over the bar for $\alpha \neq 0$ (see section 5.5.1). Recall the stress contours displayed for elastic loading in figures 5.25 - 5.30. The uniaxial stress condition of the bar is reproduced for $\alpha = 0$ with a uniform stress field across the bar. Although the global response of an elastic bar in uniaxial stress is reproduced for $\alpha \neq 0$, the stress fields are not uniform over the bar. In the case of $\alpha = 45^\circ$, the contours of stress components resemble a uniform grid pattern. This result presents an added difficulty to the analysis of stress results and a more accurate representation of the stress field result is desired.

Uniformity of the stress field within the bar is obtained from an initial configuration of material points that are uniformly distributed within grid cells. Figure 5.39 displays a close up view in the potential failure zone for the $\alpha = 45^\circ$ configuration of the tensile bar with a non-uniform in-cell material point distribution. This configuration is produced by rotating the baseline configuration of the bar by α . Note that the position of some material points coincide with the lines of the grid. The $\alpha = 45^\circ$ configuration of the bar displayed in figure 5.40 is discretized by material points that are uniformly distributed within grid cells. This configuration is generated directly from a grid that is completely filled with material points that are uniformly distributed within the cells.

A comparison between the stress fields resulting from uniform and non-uniform in-

cell material point distributions is displayed in figures 5.41 - 5.46 for $\alpha = 45^\circ$ at the same point during elastic loading. A dramatic improvement in stress field uniformity is realized when material points are distributed uniformly within grid cells. A clear state of uniaxial stress is observed for which the value of $\sigma_{nn}/\tau_{nf} < 1$ is nearly uniform throughout the bar (see figure 5.41). The values of σ_{tt}/τ_{nf} and σ_{nt}/τ_{nf} , displayed in figures 5.44 and 5.46 respectively, are essentially zero. As mentioned before, some non-uniformity in stress is present due to stress concentrations near the near no-slip boundaries. However, a uniaxial stress state is simulated in the interior of the bar where material failure occurs.

A close-up view of the σ_{nn}/τ_{nf} contour resulting from a non-uniform in-cell distribution of material points is displayed in figure 5.47. The non-uniformity of σ_{nn} is attributed to the close proximity of material points to cell boundaries. It is observed that material points of high stress that form the lines of the pattern lie within grid cells whose borders coincide with material point positions. When the in-cell distribution of material points is uniform, a more accurate stress field is computed because errors due to material points crossing grid cells is eliminated. In fact, the preliminary study of the elastic bar performed in section 5.3 not only demonstrates independence of MPM results with respect to by grid orientation, but the in-cell distribution of material points as well (see figure 5.9). By electing a uniform in-cell distribution for the simulation, the effect of grid orientation is isolated. For this reason, such a distribution is used to study smeared crack MPM results of the stress field for $\alpha \neq 0$.

Figure 5.48 displays a comparison of convergence behavior between cases of different α for the elastic bar problem with a uniform in-cell distribution of material points. The same comparison for a non-uniform in-cell material point distribution is displayed in figure 5.9 and repeated again in figure 5.49 for the sake of convenience. Obviously, a uniform in-cell material point distribution results in a more accurate

numerical solution for any given $\alpha \neq 0$ and grid resolution h . Unlike the case of non-uniform in-cell material point distributions, the error values for $\alpha \neq 0$ cases do not differ much from those of the baseline case. Comparison between the behavior of the two material point distributions leads to the conclusion that the observed difference in error between the different $\alpha \neq 0$ cases in figure 5.49 is due mostly to the cell crossing error associated with the non-uniform distribution of material points, and not the difference in orientation angle α .

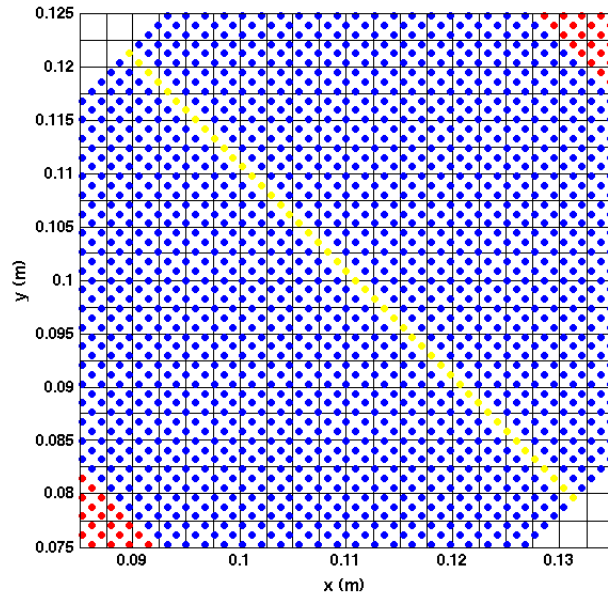


Figure 5.39: $\alpha = 45^\circ$ configuration of tensile bar with a non-uniform in-cell material point distribution

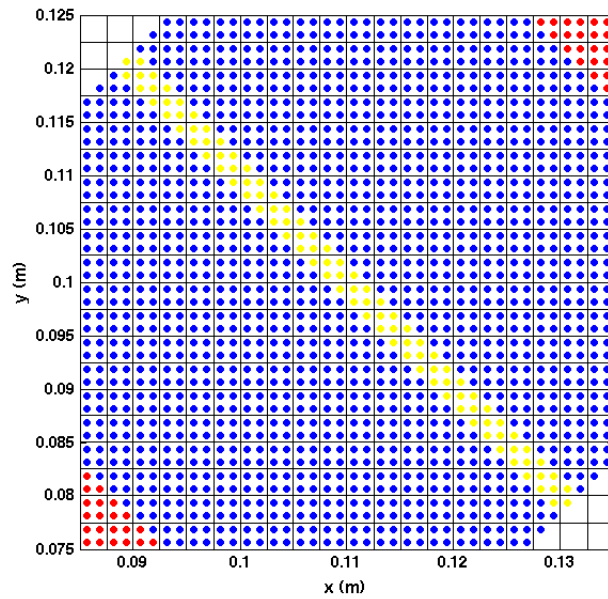


Figure 5.40: $\alpha = 45^\circ$ configuration of tensile bar with a uniform in-cell material point distribution

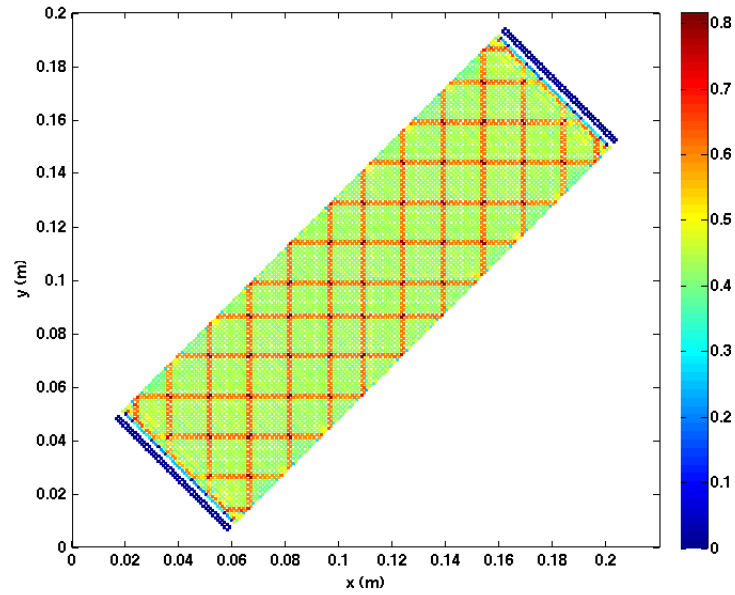


Figure 5.41: σ_{nn}/τ_{nf} for $\alpha = 45^\circ$ configuration with a non-uniform in-cell material point distribution during elastic deformation

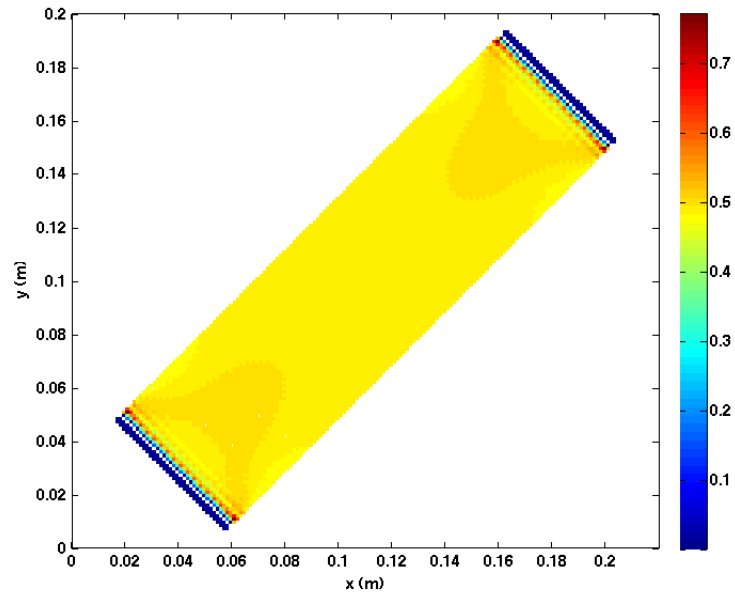


Figure 5.42: σ_{nn}/τ_{nf} for $\alpha = 45^\circ$ configuration with a uniform in-cell material point distribution during elastic deformation

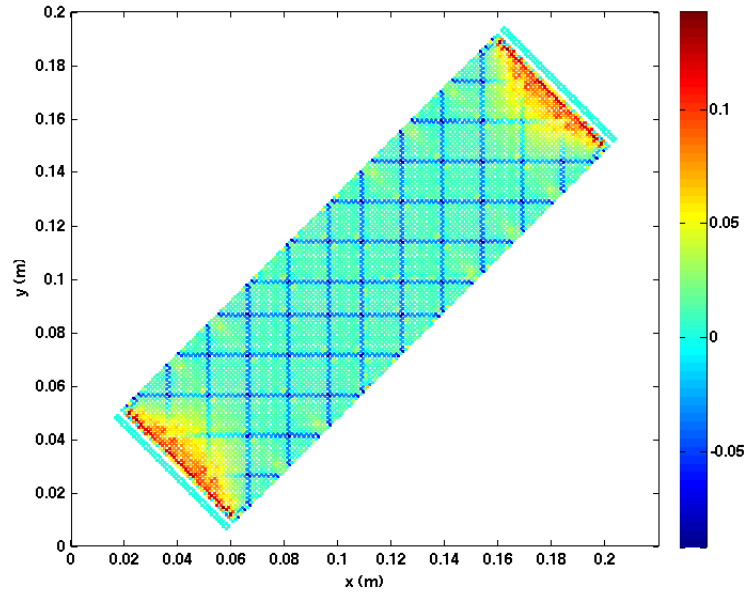


Figure 5.43: σ_{tt}/τ_{nf} for $\alpha = 45^\circ$ configuration with a non-uniform in-cell material point distribution during elastic deformation

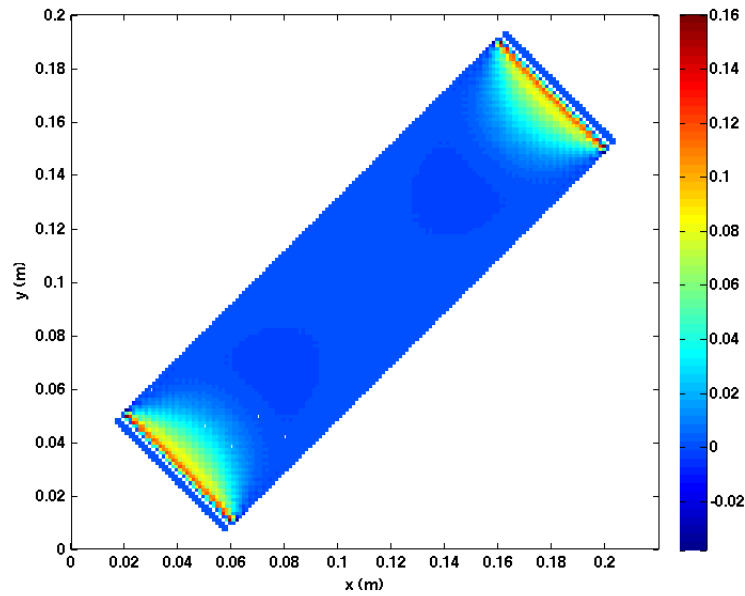


Figure 5.44: σ_{tt}/τ_{nf} for $\alpha = 45^\circ$ configuration with a uniform in-cell material point distribution during elastic deformation

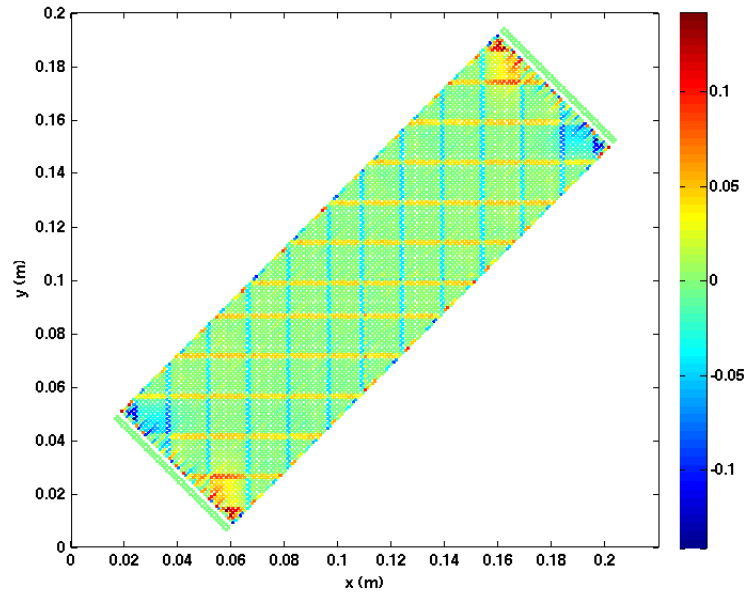


Figure 5.45: σ_{nt}/τ_{nf} for $\alpha = 45^\circ$ configuration with a non-uniform in-cell material point distribution during elastic deformation

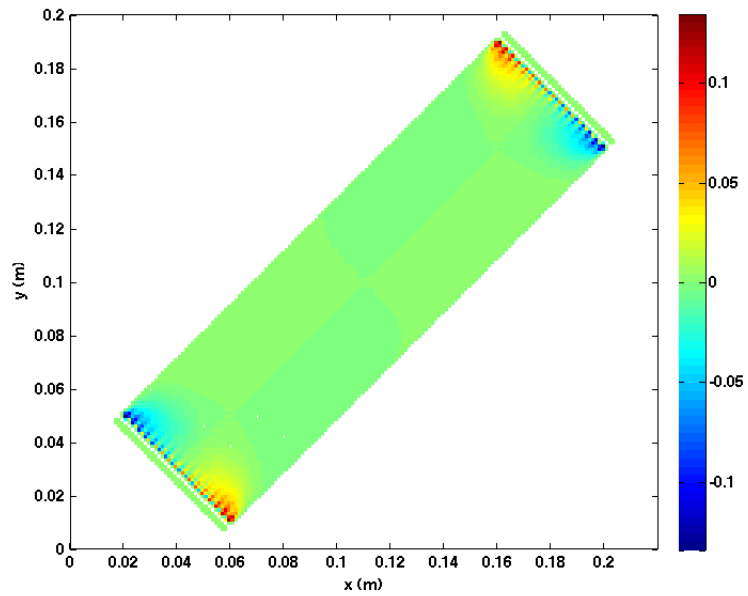


Figure 5.46: σ_{nt}/τ_{nf} for $\alpha = 45^\circ$ configuration with a uniform in-cell material point distribution during elastic deformation

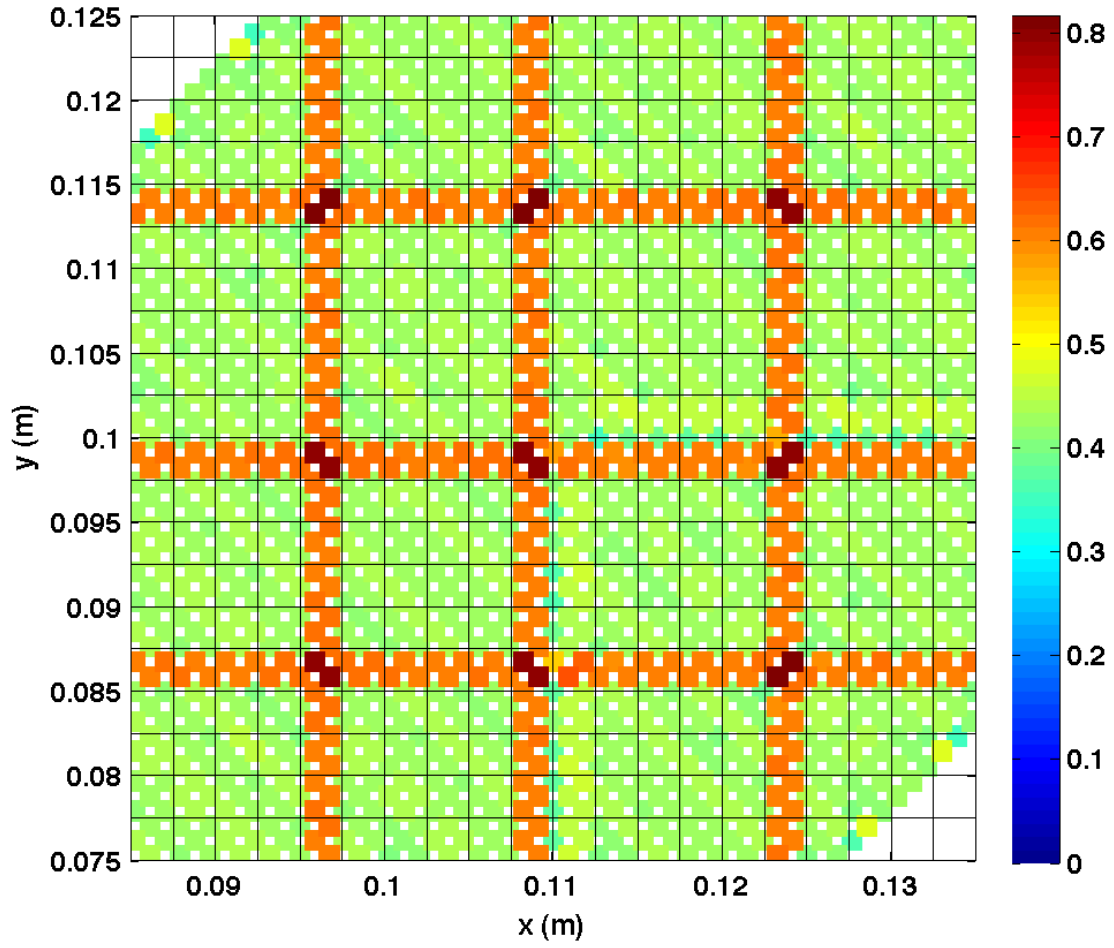


Figure 5.47: σ_{nn}/τ_{nf} for $\alpha = 45^\circ$ configuration with a non-uniform in-cell material point distribution during elastic deformation

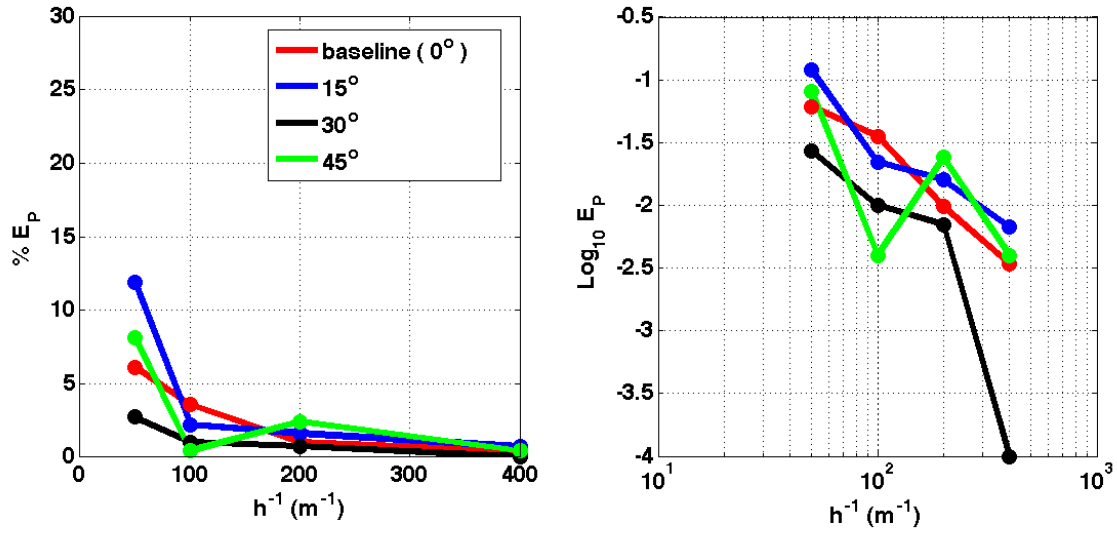


Figure 5.48: Convergence behavior comparison of elastic bar problem in MPM with a uniform in-cell material point distribution for different α

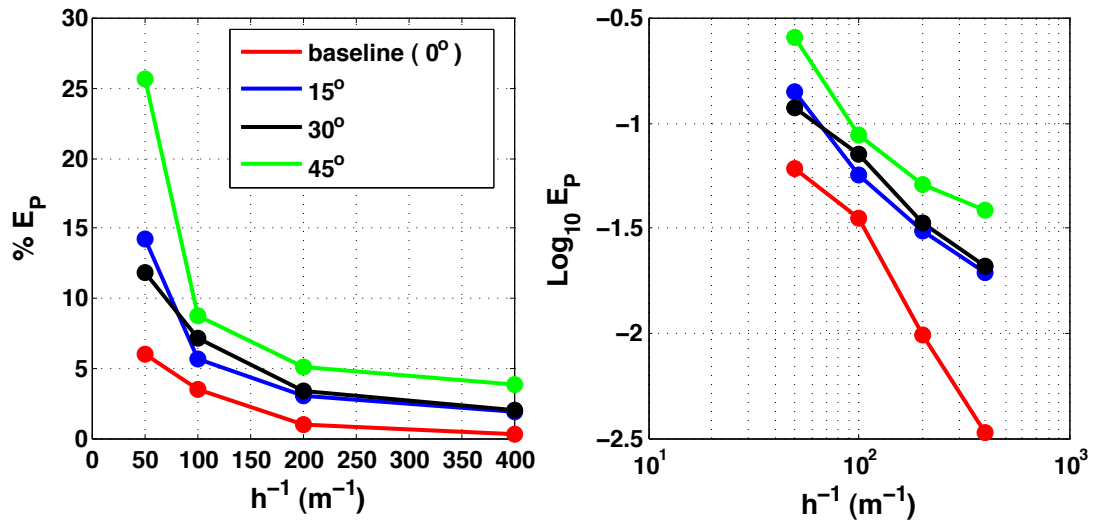


Figure 5.49: Convergence behavior comparison of elastic bar problem in MPM with a non-uniform in-cell material point distribution for different α

The global responses for the elastic de-cohesive tensile bar for $\alpha = 45^\circ$ are displayed in figures 5.50 and 5.51 for non-uniform and uniform in-cell material point distributions respectively. There are some minor differences but the same general behavior is observed. Results for the uniform in-cell grid distribution appear to be more accurate with respect to the exact solution for the initial elastic portion of the loading. Both simulations exhibit the same stiff post-peak loading response. Figure 5.52 displays the same dispersion of the failure pattern that occurs for simulations with non-uniform in-cell material point distributions. The use of a uniform in-cell material point distribution offers no improvement to failure simulation results of the tensile bar for the $\alpha = 45^\circ$ case. The utility of the uniform in-cell material point distribution for this research is the clear picture of stress that it provides for investigating potential causes of the grid orientation bias of results.

Figures 5.53 - 5.55 display contours of stress components in the $\alpha = 45^\circ$ bar configuration with a uniform in-cell material point distribution during post peak loading. The development of stress during failure is generally non-uniform across the bar. The value of σ_{nn}/τ_{nf} is uniform everywhere in the bar except within the narrow band of weakened material where some softening takes place (figure 5.53). Despite some softening, the value of σ_{nn}/τ_{nf} within material points that surround the narrow band remains nearly one. The stress appears to be "locked in" near the failure region which explains the level post peak P vs. δ response in figure 5.51. A small variation in σ_{tt}/τ_{nf} from a value of zero is also observed within the failure region (figure 5.54). Extreme stiffening in the material surrounding the narrow band of weak material is apparent in the σ_{nt}/τ_{nf} contour displayed in figure 5.55. The value of σ_{nt} is zero everywhere including the weakened band of material where σ_{nn} is decreasing due to failure. Bands of high failure surface shear stress, σ_{nt} , form around the softening zone. This effect will be referred to as shear stiffening.

The cause of global stiffening and the dispersion of the failure region associated with

smeared crack MPM results for $\alpha \neq 0$ configurations of the bar is postulated to be the compatibility of deformation enforced by the grid cells themselves. Proof of this claim is provided by a heuristic argument. Consider the square group of four elements within the failure zone indicated by the bold outline in figure 5.56. Material points in the upper right element belong to the weak band of material points for which failure initiates on a failure surface defined by \mathbf{n} . Softening is occurring on these points which lead to a decrease in σ_{nn} . Consider the illustration of an incremental deformation of the same group of four elements pictured in figure 5.57. The general motion of the nodes in the \mathbf{n} direction is depicted by the arrows. The element deformation resulting from this motion is essentially shear. If only material in the upper right element is softening, then a decrease in the stress of that element is realized. Connectivity of the grid nodes requires the other three elastic elements to deform in a compatible manner to the element that is softening. The elastic elements deform in shear, but since they are undamaged the elastic deformation actually leads to an increase in the shear stress, σ_{nt} . This effect is observed in the close up view of σ_{nt} results displayed in figure 5.58. Since failure initiates in the upper right element, σ_{nt} remains zero on the failure surface. As it deforms and softens, an unphysical increase in σ_{nt} is induced in the elastic (undamaged) elements by the compatibility of the deformation imposed by the grid. The shear stiffening also spreads away from the weak material band of initial failure forming a wide zone. An increase in σ_{nt} within the shear stiffening zone causes unphysical material failure to initiate and develop, leading to the dispersion of the material failure zone. Note that the size of the entire shear stiffening zone is comparable to that of the failure zone displayed in figure 5.56. The effect of unphysical shear stiffening and subsequent spreading of failure seems to be a self sustaining process caused primarily by the compatibility of deformation imposed by the grid.

The same effect was discovered by Rots over twenty years ago for smeared crack analysis in FEM [54]. In his studies, he used the term "stress locking" to describe

the unphysical increase in stress that occurs around material failure regions that are supposed to represent traction free crack surfaces. The stress locking effect ultimately leads to stiff global responses in smeared crack FEM results. Although a number of disadvantages were identified for smeared crack analysis in FEM, the problem of stiffening due to "stress locking" seems to be the most serious. A literature review by the author reveals that smeared crack FEM was ultimately abandoned as a computational fracture method in pursuit of better ways for representing material failure in FEM. Other more successful fracture simulation methods in FEM have been developed over the past twenty years and include the method of embedded discontinuities [41, 30, 44] and the extended finite element method (XFEM) [76]. In general, each method improved on the representation of fracture in the smeared crack approach by using a more accurate representation of the kinematics of the discontinuity in displacement in the numerical method.

If a smeared crack failure representation is used in either FEM or MPM, the result is unphysical stiffening as a result of the inherent compatibility in deformation enforced by the computational grid. Mesh independent results can not be obtained using smeared crack MPM due to the stiffening associated with material failure simulations for which the orientations of failure surfaces do not coincide with the orientation of grid cell lines. This conclusion is reached even for the elementary case study problem provided by this research. It is also important to note that the accurate results obtained in previous smeared-crack MPM studies using explicit dynamics only reflect the favorable case of failure surface and grid cell alignment [69]. The mesh orientation bias observed in smeared crack MPM results represents a serious limitation of its use as a computational fracture method in general. For the method to be considered a valid approach for solving material failure problems, a remedy to the grid dependence must be developed. A simple remedy has not presented itself through the analysis performed for this study.

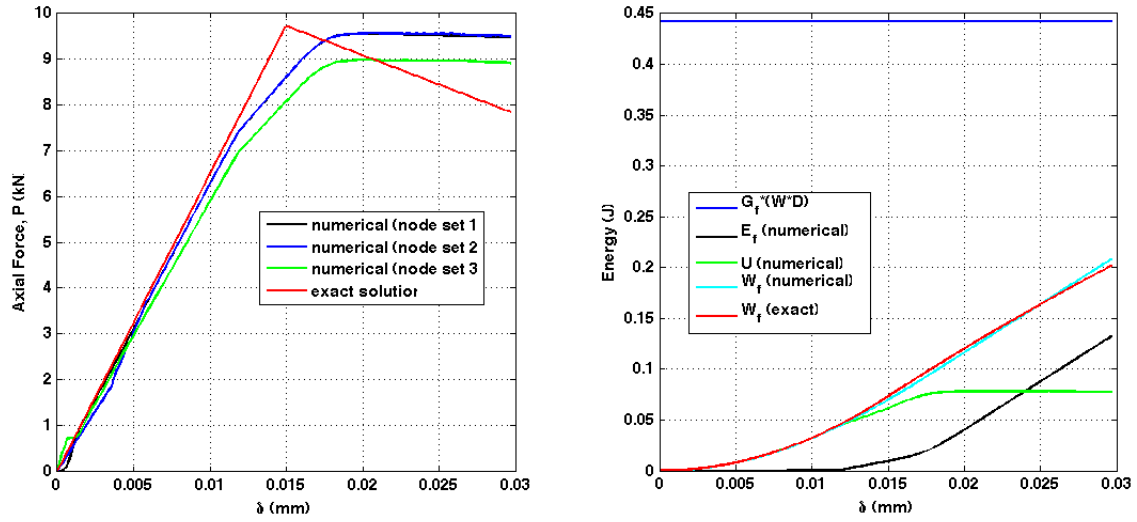


Figure 5.50: P and W_f vs. δ response for $\alpha = 45^\circ$ tensile bar case with a non-uniform in-cell material point distribution

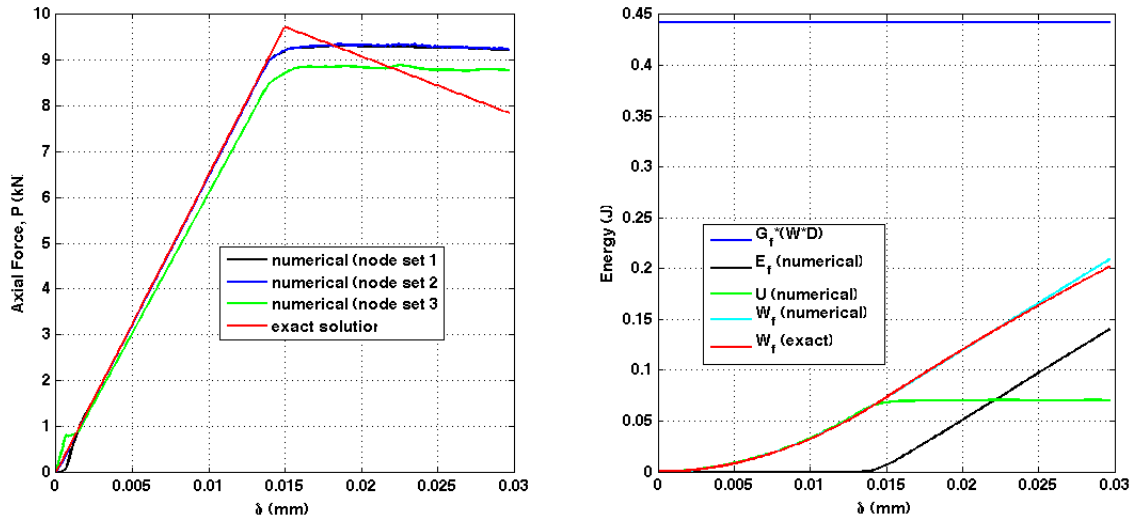


Figure 5.51: P and W_f vs. δ response for $\alpha = 45^\circ$ tensile bar case with a uniform in-cell material point distribution

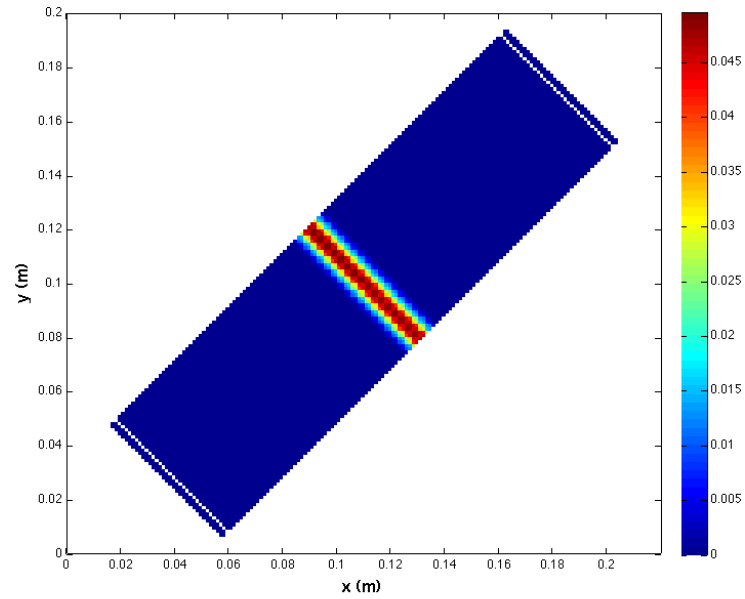


Figure 5.52: $[[u_n]]/u_0$ for $\alpha = 45^\circ$ configuration with a uniform in-cell material point distribution during softening

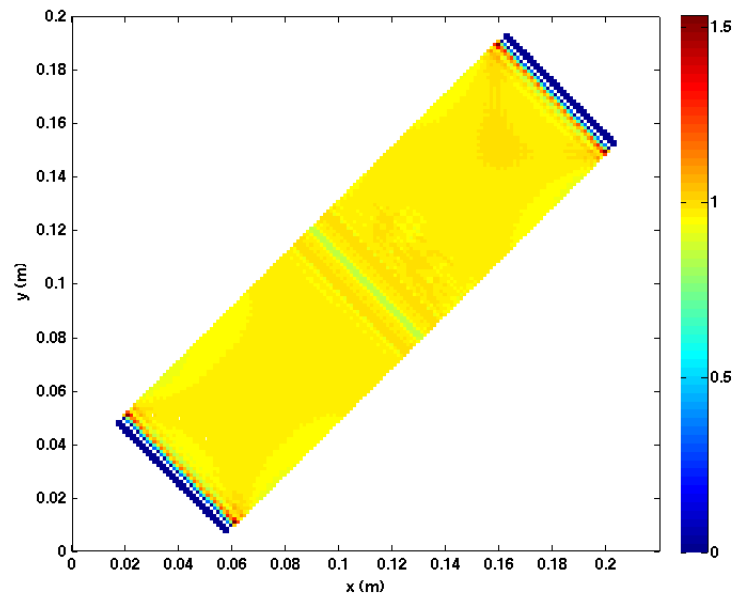


Figure 5.53: σ_{nn}/τ_{nf} for $\alpha = 45^\circ$ configuration with a uniform in-cell material point distribution during softening

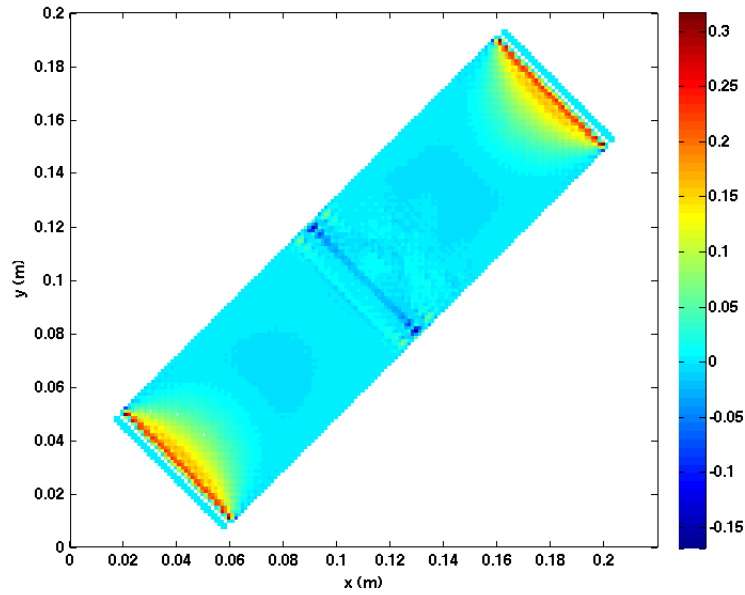


Figure 5.54: σ_{tt}/τ_{nf} for $\alpha = 45^\circ$ configuration with a uniform in-cell material point distribution during softening

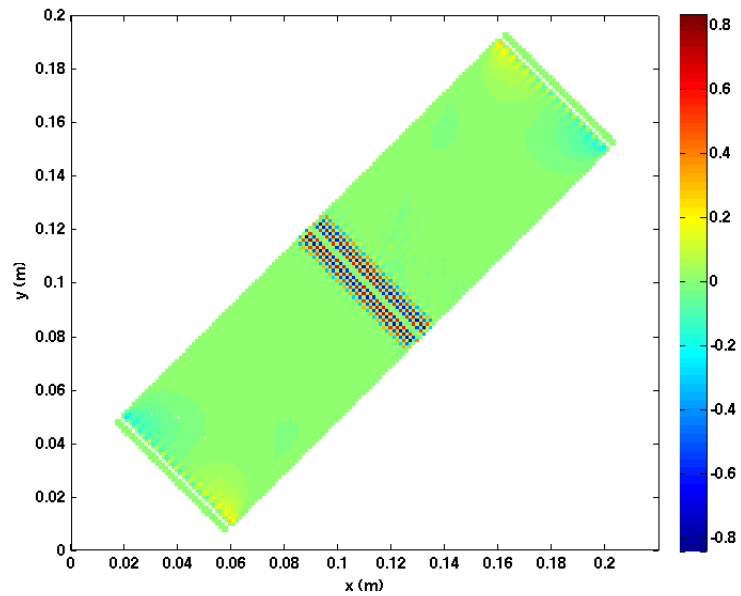


Figure 5.55: σ_{nt}/τ_{nf} for $\alpha = 45^\circ$ configuration with a uniform in-cell material point distribution during softening

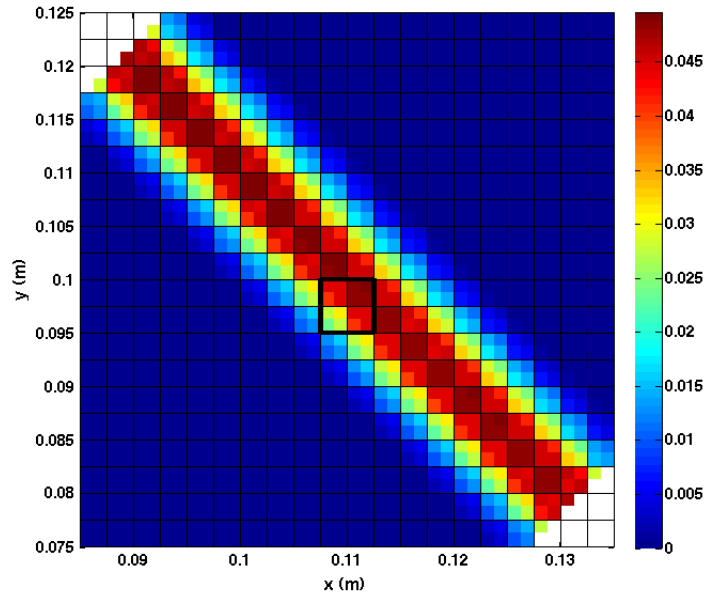


Figure 5.56: Close up of $[[u_n]]/u_0$ for $\alpha = 45^\circ$ configuration during softening

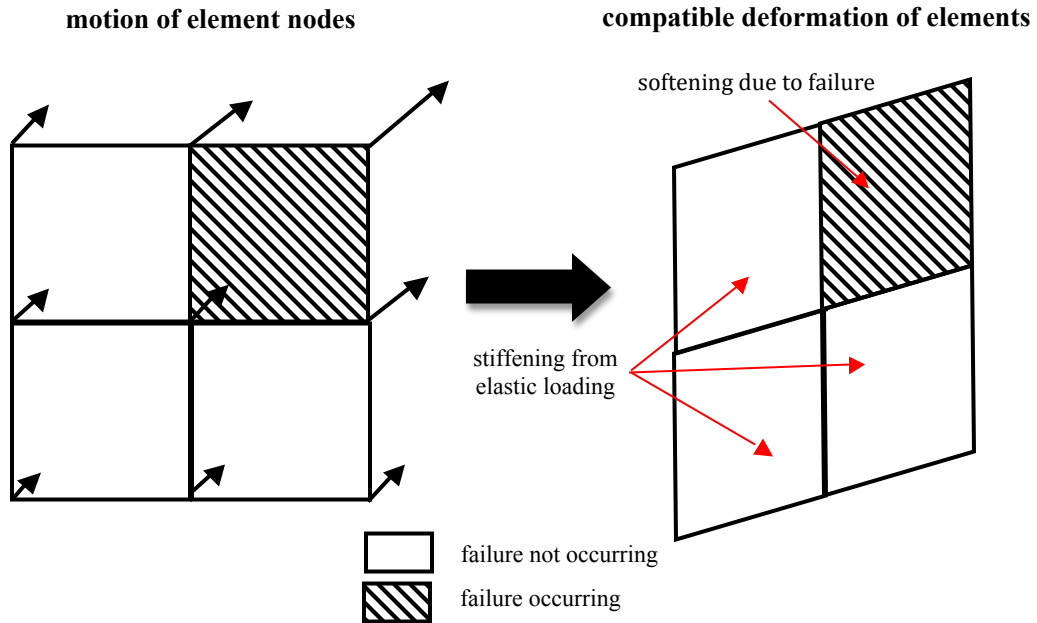


Figure 5.57: Illustration of a compatible deformation of grid cells

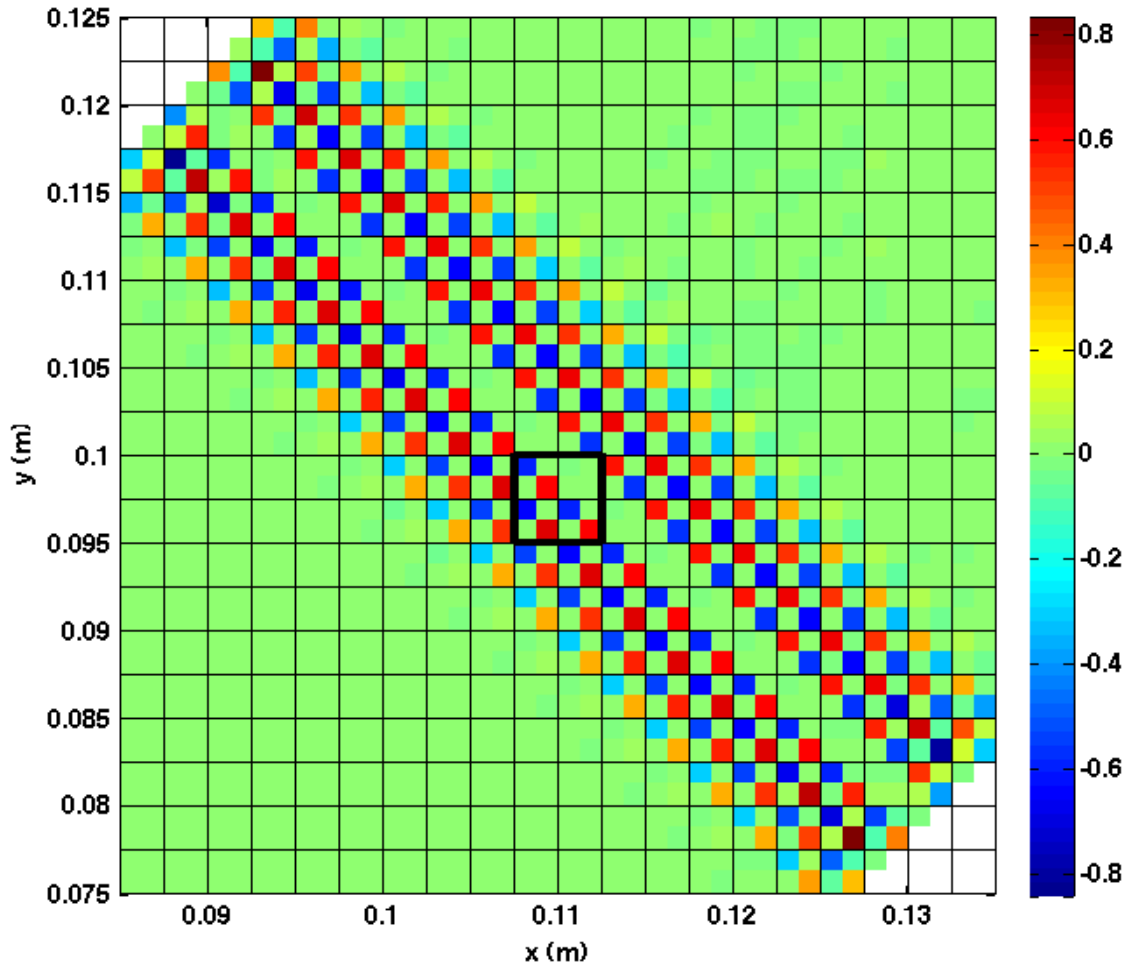


Figure 5.58: Close up of σ_{nt}/τ_{nf} in softening region for $\alpha = 45^\circ$ configuration during softening

5.5.4 Use of Embedded Discontinuities in MPM

As an alternative to using smeared crack MPM for computational fracture, an embedded discontinuity approach is implemented into MPM. This effort is an attempt to overcome the mesh orientation bias of smeared crack MPM results. It is ultimately unsuccessful because the embedded discontinuity method in MPM has the same mesh-dependent behavior as the smeared crack approach. However, the method is summarized in this section for completeness.

A complete description of the embedded discontinuity method, used for this study, is provided by Oliver [41], [44]. Recall the strong discontinuity kinematics representation of material failure presented in section 3.5.2. Now consider the slightly different representation of material failure illustrated in figure 5.59. The displacement field, $\mathbf{u}(\mathbf{x})$, in Ω is defined as follows:

$$\mathbf{u}(\mathbf{x}) = \bar{\mathbf{u}}(\mathbf{x}) + M_\Gamma[[\mathbf{u}]](\mathbf{x}) \quad (5.5.53)$$

The first term of equation (5.5.53), $\bar{\mathbf{u}}(\mathbf{x})$, is the regular (continuous) part of the displacement field. The second term corresponds to the jump in the displacement field, $[[\mathbf{u}]](\mathbf{x})$. The function, $M_\Gamma(\mathbf{x})$, is a unit jump function whose support is the domain, Ω_h , which contains Γ (see figure 5.59). It is defined to be

$$M_\Gamma(\mathbf{x}) = H_\Gamma(\mathbf{x}) - \phi(\mathbf{x}, t) \quad (5.5.54)$$

where $H_\Gamma(\mathbf{x})$ is the Heaviside function defined in equation (3.5.28) and $\phi(\mathbf{x})$ is any continuous function defined such that the following conditions are satisfied:

$$\phi(\mathbf{x}) = \begin{pmatrix} 0 & \forall & \mathbf{x} \in \Omega^-/\Omega_h \\ 1 & \forall & \mathbf{x} \in \Omega^+/\Omega_h \end{pmatrix} \quad (5.5.55)$$

The small strain tensor, $\boldsymbol{\varepsilon}(\mathbf{x})$, is computed from equation (3.2.40) to be

$$\boldsymbol{\varepsilon}(\mathbf{x}) = (\nabla \mathbf{u})^S = \bar{\boldsymbol{\varepsilon}}(\mathbf{x}) + (\nabla M_\Gamma[[\mathbf{u}]])^S \quad (5.5.56)$$

where $\bar{\boldsymbol{\varepsilon}}(\mathbf{x})$ is the regular part of the strain field and the $(\nabla M_\Gamma[[\mathbf{u}]])^S$ term is enhancement to the strain field.

The embedded discontinuity method is used to simulate material failure for the quasi-static problem (see Appendix B for details). The set of equations governing the boundary value problem of the quasi-static deformable solid, Ω , with discontinuity, Γ , depicted in 5.59, include the equilibrium of forces in Ω/Γ , the continuity of traction across Γ , boundary conditions and the constitutive relationship. In the absence of body forces, the equilibrium of internal forces is stated as follows:

$$\nabla \cdot \boldsymbol{\sigma} = \mathbf{0} \quad \forall \mathbf{x} \in \Omega/\Gamma \quad (5.5.57)$$

The boundary is divided into two sets of points such that, $\partial\Omega = \partial\Omega^u \cup \partial\Omega^t$. The displacement (or essential) boundary conditions are applied to $\partial\Omega^u$ and the traction boundary conditions are applied to $\partial\Omega^t$ as follows:

$$\begin{aligned} \mathbf{u}(\mathbf{x}) &= \mathbf{g}(\mathbf{x}) \quad \forall \mathbf{x} \in \partial\Omega^u \\ \boldsymbol{\tau}(\mathbf{x}) &= \mathbf{t}(\mathbf{x}) \quad \forall \mathbf{x} \in \partial\Omega^t \end{aligned} \quad (5.5.58)$$

The condition of traction continuity is

$$\boldsymbol{\sigma} \cdot \mathbf{n}|_{\Omega^+} = \boldsymbol{\sigma} \cdot \mathbf{n}|_{\Omega^-} = \boldsymbol{\sigma} \cdot \mathbf{n}|_\Gamma \quad \forall \mathbf{x} \in \Gamma \quad (5.5.59)$$

where $\boldsymbol{\sigma} \cdot \mathbf{n}|_{\Omega^+}$ ($\boldsymbol{\sigma} \cdot \mathbf{n}|_{\Omega^-}$) represents the value of stress in Ω^+ (Ω^-) in the neighborhood of Γ . The constitutive relationship is denoted symbolically as $\boldsymbol{\sigma} = \boldsymbol{\sigma}(\boldsymbol{\varepsilon})$.

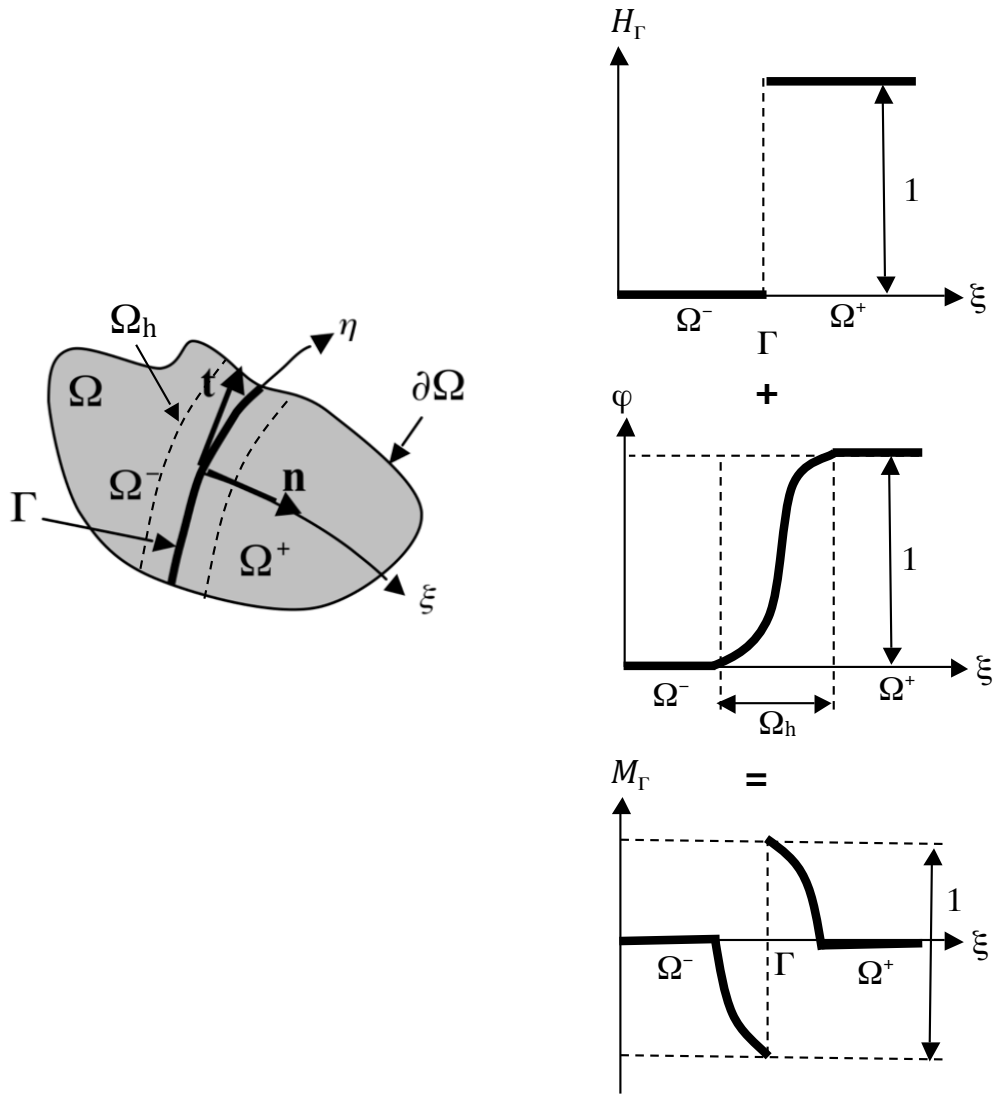


Figure 5.59: Illustration of strong discontinuity kinematics concept

The use of embedded discontinuities to model fracture requires an explicit representation of the failure surface, Γ . A set of n_e grid cells that is intersected by Γ , and defined as $\mathcal{J} = \{e \mid \Omega_e \in \Omega \cap \Gamma \neq \emptyset\}_{e=1}^{n_e}$, is continuously tracked throughout the simulation. An example of \mathcal{J} is displayed in figure 5.60. A 2D illustration of a single element $e \in \mathcal{J}$ is depicted in in figure 5.61. The domain of the element, Ω_e , is separated into Ω_e^- and Ω_e^+ by an elemental discontinuity, Γ_e with length, ℓ_e . Continuity of Γ_e across element boundaries is enforced for all $e \in \mathcal{J}$ so that $\Gamma = \bigcup_{e \in \mathcal{J}} \Gamma_e$.

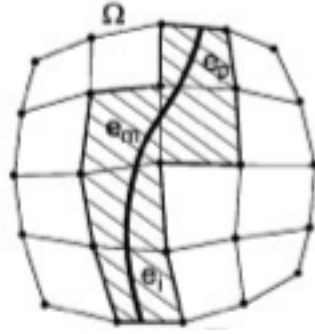


Figure 5.60: Illustration of the set of elements, \mathcal{J} , intersected by the discontinuity taken from [44]

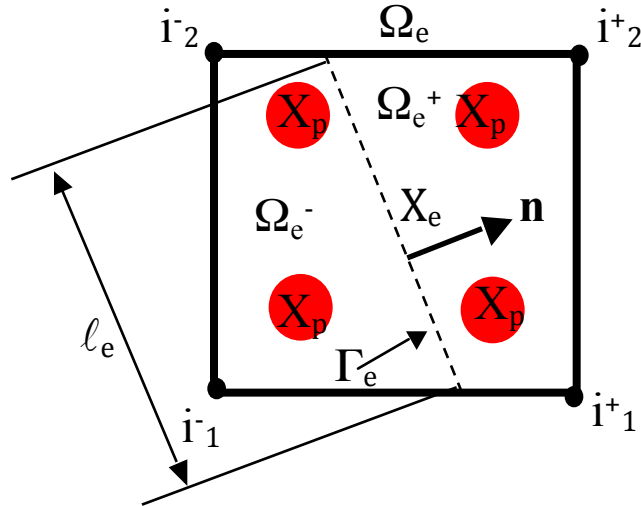


Figure 5.61: Illustration of an element with an embedded discontinuity, $e \in \mathcal{J}$

The development and implementation of quasi-static analysis in MPM is described in detail in Appendix B. The incremental solution for the quasi-static problem is the displacement increment at the nodes, $\Delta \mathbf{u}_i$. The solution approximation is enhanced by additional degrees of freedom that are "embedded" in the n_e elements and correspond to increments in the displacement discontinuity, $\Delta[[\mathbf{u}]]_e$, which are constant over an element $e \in \mathcal{J}$. The enhanced solution approximation is

$$\Delta \mathbf{u}(\mathbf{x}) = \sum_{i=1}^{N_n} \Delta \mathbf{u}_i N_i(\mathbf{x}) + \sum_{e \in \mathcal{J}} M_{\Gamma_e}(\mathbf{x}) \Delta[[\mathbf{u}]]_e \quad (5.5.60)$$

For a given element, e , the function, $M_{\Gamma_e}(\mathbf{x})$ is defined to be

$$M_{\Gamma_e}(\mathbf{x}) = \begin{pmatrix} 0 & \forall e \notin \mathcal{J} \\ H_{\Gamma_e}(\mathbf{x}) - \phi_e(\mathbf{x}) & \forall e \in \mathcal{J} \end{pmatrix} \quad (5.5.61)$$

where, $\phi_e(\mathbf{x})$ is chosen to be the sum of nodal basis functions corresponding to the n_e^+ nodes that belong to Ω_e^+ (see figure 5.61) as follows:

$$\phi_e(\mathbf{x}) = \sum_{i^+=1}^{n_e^+} N_{i^+}(\mathbf{x}) \quad (5.5.62)$$

Since $\Delta[[\mathbf{u}]]_e$ is constant over an element, $\nabla(\Delta[[\mathbf{u}]]_e) = \mathbf{0}$. It follows from equations (5.5.56), (5.5.60) and (5.5.61) that the increment in strain, $\Delta \boldsymbol{\varepsilon}$ is

$$\Delta \boldsymbol{\varepsilon}(\mathbf{x}) = \sum_{i=1}^{N_n} (\Delta \mathbf{u}_i \otimes \nabla N_i(\mathbf{x}))^S + \sum_{e \in \mathcal{J}} \delta_{\Gamma_e}(\mathbf{x}) (\Delta[[\mathbf{u}]]_e \otimes \mathbf{n})^S - \sum_{e \in \mathcal{J}} (\nabla \phi_e(\mathbf{x}) \otimes \Delta[[\mathbf{u}]]_e)^S \quad (5.5.63)$$

where $\delta_{\Gamma_e}(\mathbf{x}) = \nabla H_{\Gamma_e}(\mathbf{x})$ is the Dirac delta function defined in equation (3.5.30). For computational purposes the Dirac delta in equation (5.5.63) is replaced by the reg-

ularized Dirac delta function, δ_{Γ}^L , defined in equation (3.5.33). The strain increment becomes

$$\Delta \boldsymbol{\varepsilon}(\mathbf{x}) = \sum_{i=1}^{N_n} (\Delta \mathbf{u}_i \otimes \nabla N_i(\mathbf{x}))^S + \sum_{e \in \mathcal{J}} \frac{1}{L_c} \mu_{\Gamma_e}(\mathbf{x}) (\Delta [[\mathbf{u}]]_e \otimes \mathbf{n})^S - \sum_{e \in \mathcal{J}} (\nabla \phi_e(\mathbf{x}) \otimes \Delta [[\mathbf{u}]]_e)^S \quad (5.5.64)$$

where μ_{Γ_e} is the collocation function in element, e , defined using equation (3.5.34) as follows:

$$\mu_{\Gamma_e}(\mathbf{x}) = \begin{pmatrix} 0 & \text{for } \mathbf{x} \notin \Gamma_e \\ 1 & \text{for } \mathbf{x} \in \Gamma_e \end{pmatrix} \quad (5.5.65)$$

The traction continuity condition in equation (5.5.59) is satisfied in an average sense over each element $e \in \mathcal{J}$. Equation (5.5.59) is restated by equating the mean value of the traction in Ω_e/Γ_e to the average traction on Γ_e . The result is

$$\frac{1}{\Omega_e} \int_{\Omega_e} \boldsymbol{\sigma} \cdot \mathbf{n} dV = \frac{1}{\ell_e} \int_{\Gamma_e} \boldsymbol{\sigma} \cdot \mathbf{n} d\Gamma \quad \forall e \in \mathcal{J} \quad (5.5.66)$$

Equation (5.5.66) is rearranged using the definition of δ_{Γ}^L in equation (3.5.33) to give the following result:

$$\left(\mu_{\Gamma_e} \frac{1}{L_c} - \frac{\ell_e}{\Omega_e} \right) \int_{\Omega_e} \boldsymbol{\sigma} \cdot \mathbf{n} dV = \mathbf{0} \quad \forall e \in \mathcal{J} \quad (5.5.67)$$

Equation (5.5.67) is satisfied if the following condition holds:

$$L_c = \frac{\Omega_e}{\ell_e} \quad \forall e \in \mathcal{J} \quad (5.5.68)$$

Equation (5.5.68) is the condition used to satisfy average traction continuity for embedded discontinuities.

Implementation of embedded discontinuities in MPM is discussed. All material points, \mathbf{X}_p , are considered to be elastic. Since failure only occurs on Γ , the discrete material failure model is evaluated at the points, \mathbf{X}_e , for $e \in \mathcal{J}$, where \mathbf{X}_e is chosen to be the midpoint of Γ_e (see figure 5.61). The coordinates of \mathbf{X}_e are assumed to remain fixed throughout the simulation. This assumption is appropriate for the present case of small deformations. In the case of large deformations, the displacement of the position, \mathbf{X}_e must be considered.

The values of $\Delta\boldsymbol{\sigma}_e$ and $\Delta[[\mathbf{u}]]_e$ are obtained implicitly using the elastic de-cohesion constitutive algorithm in section 4.5 for all $e \in \mathcal{J}$. Since $\mu_{\Gamma_e}(\mathbf{X}_e) = 1$, the total strain increment, $\Delta\boldsymbol{\varepsilon}_e$ at \mathbf{X}_e , is computed from equation (5.5.64) to be

$$\Delta\boldsymbol{\varepsilon}_e = \sum_{i=1}^{N_n} (\Delta\mathbf{u}_i \otimes \nabla N_i(\mathbf{X}_e))^S + \sum_{e \in \mathcal{J}} \frac{1}{L_c} (\Delta[[\mathbf{u}]]_e \otimes \mathbf{n})^S - \sum_{e \in \mathcal{J}} (\nabla\phi_e(\mathbf{X}_e) \otimes \Delta[[\mathbf{u}]]_e)^S \quad (5.5.69)$$

In order to initialize the material failure algorithm, $\Delta\boldsymbol{\varepsilon}_e$, is computed from equation (5.5.69) with $\Delta[[\mathbf{u}]]_e = \mathbf{0}$.

Once $\Delta[[\mathbf{u}]]_e$ is computed for all $e \in \mathcal{J}$, the material point strain increments, $\Delta\boldsymbol{\varepsilon}_p$, are computed. Since $\mu_{\Gamma_e}(\mathbf{X}_p) = 0$, the total strain increment, $\Delta\boldsymbol{\varepsilon}_p$ at \mathbf{X}_p , is obtained from equation (5.5.64) to be

$$\Delta\boldsymbol{\varepsilon}_p = \sum_{i=1}^{N_n} (\Delta\mathbf{u}_i \otimes \nabla N_i(\mathbf{X}_p))^S - \sum_{e \in \mathcal{J}} (\nabla\phi_e(\mathbf{X}_p) \otimes \Delta[[\mathbf{u}]]_e)^S \quad (5.5.70)$$

The material point stress increment, $\Delta\boldsymbol{\sigma}_p$, is obtained from isotropic linear elasticity as follows:

$$\Delta\boldsymbol{\sigma}_p = \mathbf{C} : \Delta\boldsymbol{\varepsilon}_p \quad (5.5.71)$$

Chapter 5. Evaluation of the Smeared Crack Approach in MPM

In general, numerical implementation of the embedded discontinuity method requires tracking the set, \mathcal{J} . Tracking algorithms are needed to identify the elements in which failure may occur next and what orientation will initiate, given the continuity of Γ and stress states. Specific methods have been developed for FEM [41], [44]. For simplicity, the use of such algorithms is avoided in this study by pre-specifying the set, \mathcal{J} , where failure can initiate and develop. This simplification is sufficient for the 2D embedded discontinuity MPM analysis of the tensile bar problem. The prescribed \mathcal{J} for the bar problem corresponds to a set of elements that is intersected by a transverse line across the middle of the bar with normal vector, \mathbf{n} .

Computational fracture results using embedded discontinuities in MPM are very similar those obtained using a smeared crack representation of fracture. Results from the baseline ($\alpha = 0$) simulation of the bar problem match very well to the analytical solution. Stiffening of global P vs. δ results is observed in $\alpha \neq 0$ cases for relatively small values of α (i.e $\alpha = 5^\circ$). Convergence of solutions is not obtained during post-peak loading once α becomes sufficiently large. It should be noted that, although some embedded discontinuity FEM results for the bar problem do not display post-peak stiffening [44], the irregular grid structure utilized may actually accommodate a tortuous global crack path over \mathcal{J} for which failure surface and grid lines align. In this case the overall good result may only be a consequence of the randomly generated grid. A problem leading to stiffening could still persist in embedded discontinuity FEM using a logically generated rectangular mesh whose lines do not necessarily align with the bar geometry.

Unfortunately, the use of embedded discontinuities in MPM does not provide a remedy to the mesh orientation bias in smeared crack MPM results. The same general conclusion is reached. The method of embedded discontinuities in MPM is only successful when failure surface orientations coincide with the orientation of the grid cell lines.

Chapter 6

Conclusion

Chapter 6. Conclusion

It is important that computational tools be valid methods for solving problems of an intended application, and that their limitations be understood. For this reason the smeared crack material failure representation using MPM has been evaluated as a computational material failure method in general. It has been demonstrated by this research that its use for solving problems of failure in solid mechanics is very limited.

Numerical results of smeared crack MPM analysis suffer from a grid orientation bias. Solution accuracy is achieved only for cases in which the orientations of failure surfaces coincide with the orientations of grid cell lines. This result was demonstrated by a highly idealized problem of mode I fracture of a tensile bar in two dimensions. Good agreement between analytical and numerical results for the case of failure surface and grid line alignment is explained by the similarity between the analytical result for the smeared crack MPM stress computation and the analytical solution of the problem. When failure surfaces and grid cell lines do not align the loss of numerical solution accuracy is manifested as a stiffening of the global response and a spreading of the smeared crack pattern. This unphysical result was determined by a close examination of the stress to be caused by the inherent compatibility of the deformation imposed by the grid cells. Not surprisingly, this problem is identical to the so called "stress locking" observed in smeared crack FEM results. In conclusion, care should be taken for use of smeared crack MPM analysis of problems of material failure due to grid dependence of numerical results.

A remedy to the problem of grid orientation bias in smeared crack MPM results was not obtained from this research. An embedded discontinuity representation of failure was implemented into MPM in an attempt to improve upon the shortcomings of smeared crack MPM analysis. However, the same grid orientation bias is observed for embedded discontinuity results in MPM.

Grid orientation bias is a problem of smeared crack MPM and does not present a

Chapter 6. Conclusion

problem for MPM simulations of deformable solids without failure. A study of an elastic tensile bar demonstrates independence of results with respect to the relative orientation between the body of material points and grid cell lines. Changes in the relative orientation appear only to effect convergence rates for cases in which non-uniform in-cell material point distributions are used. The use of uniform in-cell material point distributions for the elastic tensile bar problem appears to improve solution accuracy, but this effect was not thoroughly explored.

There is no claim of exhaustive research into the possible remedies to the problems of smeared crack MPM analysis, although the findings are not encouraging. In the opinion of the author, future work should focus on the development of new computational fracture representations in MPM, and that any further attempt to fix smeared crack MPM is probably a waste of resources. One possible approach would be to accommodate the grid bias effect and enforce alignment between failure planes and grid cell lines throughout the computation by appropriately changing the grid. This method would be equivalent to re-meshing in FEM from a numerical point of view. The use of element types other than four-node quadrilateral elements (e.g. three-node triangles) could be used in the smeared-crack MPM approach to improve results. It may also be possible to use a smeared mixed-mode failure criterion to generate an overall mode I response when mesh lines and failure surface orientations do not coincide. Failure simulations using MPM could also follow the same developmental path of computational fracture in FEM. A different approach is to adopt the current state of the art failure representations used in the extended finite element method (XFEM). Although direct, this approach is not necessarily the best. MPM is well-suited for simulating problems of failure in solid mechanics, but research to determine a well-suited representation of material failure in MPM is still required.

Appendix A

Non-Linear Solution Methods for Implicit Dynamics in MPM

A.1 Implicit Solution of Non-linear MPM Equations

The solution method for the implicit non-linear system of discrete MPM equations is presented here and follows from the solution methods for implicit dynamics in MPM [66] . An alternative expression for equation (4.2.20) is

$$\mathbf{p}_i^L = \Delta t \mu \Delta \mathbf{f}_i + \mathbf{p}_i^k + \Delta t \mathbf{f}_i^k$$

where $\Delta \mathbf{f}_i = \mathbf{f}_i^L - \mathbf{f}_i^k$.

The non-linearity in (4.2.20) is due to non-linear constitutive models that relate stress to strain. Strain is updated from the nodal velocity (equation (4.3.8)) and the internal forces at the nodes are computed from the stresses (equation (4.2.12)). As a result the quantity $\Delta \mathbf{f}_i$ is generally a non-linear function of the current momentum \mathbf{p}_i^L . From this point forward, the subscript, i , denoting nodal quantities is dropped from equation (4.2.20) and the external forces are assumed to be zero for the sake of simplicity. Equation (4.2.20) is restated to be

$$\mathbf{p}^L = \Delta t \mu \Delta \mathbf{f} + \mathbf{p}^k + \Delta t \mathbf{f}^k \quad (\text{A.1.1})$$

A non-linear function of \mathbf{p}^L , denoted by $\mathbf{F}(\mathbf{p}^L)$, is defined from (A.1.1) to be

$$\mathbf{F}(\mathbf{p}^L) = \mathbf{p}^L - \Delta t \mu \Delta \mathbf{f}(\mathbf{p}^L) + \mathbf{p}^k + \Delta t \mathbf{f}^k \quad (\text{A.1.2})$$

The problem is now to find the unknown quantity \mathbf{p}^L that satisfies

$$\mathbf{F}(\mathbf{p}^L) = \mathbf{0} \quad (\text{A.1.3})$$

Appendix A. Non-Linear Solution Methods for Implicit Dynamics in MPM

Newton's method is employed to find a solution to (A.1.3). In this approach the value of \mathbf{F} , evaluated at some arbitrary value of the independent variable \mathbf{p} , is approximated by a Taylor series expansion of \mathbf{F} about some reference point, denoted by \mathbf{p}_0 . The Taylor series approximation for $\mathbf{F}(\mathbf{p})$ is then substituted into (A.1.3) and the resulting linearized system of equations is

$$\mathbf{J}(\mathbf{p}_0)\mathbf{s} = -\mathbf{F}(\mathbf{p}_0) \tag{A.1.4}$$

where \mathbf{J} is the Jacobian matrix of \mathbf{F} and $\mathbf{s} = \mathbf{p} - \mathbf{p}_0$. The solution to (A.1.4), \mathbf{s} , is an update to the unknown variable \mathbf{p} . Newton's method for solving (A.1.3) is an iterative process. The algorithm is summarized next. The subscript $n \geq 0$ refers to a single Newton iteration step.

Newton Algorithm:

1. Initialize the Newton iteration. Select \mathbf{p}_0 , set $n = 0$ and choose an acceptable error tolerance γ .
2. Evaluate $\mathbf{F}(\mathbf{p}_n)$. If $\|\mathbf{F}(\mathbf{p}_n)\| \leq \gamma$ then the solution $\mathbf{p}^L = \mathbf{p}_n$ has been obtained and the iteration is terminated. Otherwise continue.
3. Compute $\mathbf{J}(\mathbf{p}_n)$
4. Solve the linear system $\mathbf{J}(\mathbf{p}_n)\mathbf{s} = -\mathbf{F}(\mathbf{p}_n)$ for \mathbf{s} .
5. Update the independent variable $\mathbf{p}_{n+1} = \mathbf{p}_n + \mathbf{s}$, increase the Newton iteration $n \rightarrow n + 1$ and return to step 2.

Certain methods are employed in order to simplify the evaluation of specific quantities and reduce the computational cost of the non-linear solution. The GMRES linear solution method (discussed in the next section) is used to solve the linear problem in step 4. GMRES is an iterative method, which generally requires fewer computations than direct solution methods such as LU or QR factorizations. In addition, GMRES does not require the explicit computation of $\mathbf{J}(\mathbf{p}_n)$, but only the matrix vector product $\mathbf{J}(\mathbf{p}_n)\mathbf{s}$. The procedure is also simplified by the use of a difference approximation for the directional derivative of \mathbf{F} in the direction of the solution \mathbf{s} . The approximation is

$$\mathbf{J}(\mathbf{p}_n)\mathbf{s} \approx D_h\mathbf{F}(\mathbf{p}_n, \mathbf{s}) = \left\{ \begin{array}{ll} 0 & \mathbf{s} = \mathbf{0} \\ \|\mathbf{s}\| \frac{\mathbf{F}(\mathbf{p}_n + h\|\mathbf{p}_n\|\mathbf{s}/\|\mathbf{s}\|) - \mathbf{F}(\mathbf{p}_n)}{h\|\mathbf{p}_n\|} & \mathbf{s} \neq \mathbf{0}, \quad \mathbf{p}_n \neq \mathbf{0} \\ \|\mathbf{s}\| \frac{\mathbf{F}(h\mathbf{s}/\|\mathbf{s}\|) - \mathbf{F}(\mathbf{0})}{h} & \mathbf{s} \neq \mathbf{0}, \quad \mathbf{p}_n = \mathbf{0} \end{array} \right\} \quad (\text{A.1.5})$$

where h is the difference approximation parameter. Equation (A.1.5) provides a reasonable approximation to $\mathbf{J}(\mathbf{p}_n)\mathbf{s}$ for small h . In general (and confirmed by the

Appendix A. Non-Linear Solution Methods for Implicit Dynamics in MPM

authors experience) h is problem dependent and an appropriate range of h is obtained by trial and error. An additional benefit of using $D_h \mathbf{F}(\mathbf{p}_n, \mathbf{s})$ is realized when used with complicated constitutive models, for which analytical expressions for the material tangent tensor are unavailable to be evaluated numerically. By replacing $\mathbf{J}(\mathbf{p}_n)\mathbf{s}$ in (A.1.4) by the approximation in (A.1.5), the linear equation in (A.1.4) becomes

$$D_h \mathbf{F}(\mathbf{p}_n, \mathbf{s}) = -\mathbf{F}(\mathbf{p}_n) \tag{A.1.6}$$

The solution method to (A.1.6) is discussed next.

A.2 GMRES

The Generalized Minimum Residual method (GMRES) is a Krylov space method that can be used to solve a non-symmetric $n \times n$ linear system of equations of the general form $\mathbf{Ax} = \mathbf{b}$ in which $\mathbf{A} \in \mathbb{R}^{n \times n}$ and $\mathbf{b} \in \mathbb{R}^{n \times 1}$ are known and $\mathbf{x} \in \mathbb{R}^{n \times 1}$ is the desired solution. GMRES is an iterative method where k denotes the iteration and the k^{th} Krylov subspace is defined to be $K_k = \text{span} \{ \mathbf{b}, \mathbf{Ab}, \mathbf{A}^2\mathbf{b}, \dots, \mathbf{A}^{k-1}\mathbf{b} \}$. In general, GMRES minimizes the residual $\mathbf{r} = \mathbf{Ax} - \mathbf{b}$ by obtaining an approximate solution to the following least squares problem:

$$\min_{\mathbf{x} \in K_k} \|\mathbf{Ax} - \mathbf{b}\| \quad (\text{A.2.1})$$

The material presented here follows from [66, 72] and references therein. A set of orthonormal basis vectors Q_k of K_k is sought such that $K_k = \text{span}(Q_k)$. The set Q_k is defined to be $Q_k = \{ \mathbf{q}_1, \mathbf{q}_2, \mathbf{q}_3, \dots, \mathbf{q}_k \}$ where $\mathbf{q}_i^T \cdot \mathbf{q}_j = \delta_{ij}$ for $i, j \leq k$. The matrix of orthogonal basis vectors of K_k is denoted by \mathbf{Q}_k and defined to be $Q_k = [\mathbf{q}_1 | \mathbf{q}_2 | \mathbf{q}_3 | \dots | \mathbf{q}_k]$. The object is to find an approximate solution \mathbf{x}_k to (A.2.1) that is an orthogonal projection into K_k . The approximate solution is

$$\mathbf{x}_k = \mathbf{Q}_k \mathbf{y} \quad (\text{A.2.2})$$

where $\mathbf{y} \in \mathbb{R}^{k \times 1}$. Using (A.2.2) the least squares problem of (A.2.1) is restated as follows:

$$\min_{\mathbf{x} \in \mathbb{R}^{k \times 1}} \|\mathbf{A}\mathbf{Q}_k\mathbf{y} - \mathbf{b}\| \quad (\text{A.2.3})$$

It is necessary to construct the basis Q_k . Consider the following orthogonal similarity transformation of the matrix \mathbf{A} to a Hessenberg matrix $\mathbf{H} \in \mathbb{R}^{n \times n}$:

Appendix A. Non-Linear Solution Methods for Implicit Dynamics in MPM

$$\mathbf{A} = \mathbf{Q}\mathbf{H}\mathbf{Q}^T \quad (\text{A.2.4})$$

It is also useful to rewrite (A.2.4) as follows:

$$\mathbf{A}\mathbf{Q} = \mathbf{Q}\mathbf{H} \quad (\text{A.2.5})$$

The column space of the orthogonal matrix $\mathbf{Q} \in \mathbb{R}^{n \times n}$ spans the complete Krylov space K_k , but since n is usually very large, the formation of \mathbf{Q} is impractical and not necessary to find \mathbf{x}_k to satisfy (A.2.3) within a reasonable tolerance. Only k basis vectors are needed. In terms of the orthogonal set of vectors in Q_k , equation (A.2.5) can be expressed as follows:

$$\mathbf{A}\mathbf{Q}_k = \mathbf{Q}_{k+1}\mathbf{H}_k \quad (\text{A.2.6})$$

The Hessnburg matrix $\mathbf{H}_k \in \mathbb{R}^{k+1 \times k}$ in (A.2.6) has the following form:

$$\mathbf{H}_k = \begin{bmatrix} H_{11} & H_{12} & \dots & H_{1k} \\ H_{21} & H_{22} & \dots & H_{2k} \\ 0 & H_{32} & \ddots & \vdots \\ \vdots & 0 & \ddots & H_{kk} \\ 0 & \dots & 0 & H_{k+1k} \end{bmatrix} \quad (\text{A.2.7})$$

Equation (A.2.6) can be rewritten in matrix form as follows:

Appendix A. Non-Linear Solution Methods for Implicit Dynamics in MPM

$$\mathbf{A} [\mathbf{q}_1 \ \mathbf{q}_2 \ \mathbf{q}_3 \ \dots \ \mathbf{q}_k] = [\mathbf{q}_1 \ \mathbf{q}_2 \ \dots \ \mathbf{q}_k \ \mathbf{q}_{k+1}] \begin{bmatrix} H_{11} & H_{12} & \dots & H_{1k} \\ H_{21} & H_{22} & \dots & H_{2k} \\ 0 & H_{32} & \ddots & \vdots \\ \vdots & 0 & \ddots & H_{kk} \\ 0 & \dots & 0 & H_{k+1k} \end{bmatrix} \quad (\text{A.2.8})$$

Consider only the k^{th} column of equation (A.2.8). The result is

$$\mathbf{A}\mathbf{q}_k = H_{1k}\mathbf{q}_1 + H_{2k}\mathbf{q}_2 + \dots + H_{kk}\mathbf{q}_k + H_{k+1k}\mathbf{q}_{k+1} \quad (\text{A.2.9})$$

A recursive relationship for constructing the $(k+1)^{\text{th}}$ orthonormal Krylov basis vector \mathbf{q}_{k+1} is obtained by rearranging (A.2.9) as follows:

$$H_{k+1k}\mathbf{q}_{k+1} = \mathbf{A}\mathbf{q}_k - H_{1k}\mathbf{q}_1 - H_{2k}\mathbf{q}_2 - \dots - H_{kk}\mathbf{q}_k \quad (\text{A.2.10})$$

The process of obtaining \mathbf{q}_{k+1} is called Arnoldi iteration. The Arnoldi algorithm, obtained from (A.2.10) for k iterations, is

$$\mathbf{q}_{k+1} = \frac{\mathbf{A}\mathbf{q}_k - \sum_{j=1}^k H_{jk}\mathbf{q}_j}{H_{k+1k}} \quad (\text{A.2.11})$$

$$H_{k+1k} = \left\| \mathbf{A}\mathbf{q}_k - \sum_{j=1}^k H_{jk}\mathbf{q}_j \right\| \quad (\text{A.2.12})$$

The basis vectors in Q_k do in fact form an orthonormal basis for K_k and the vectors in Q_k are generated by Arnoldi iteration [32]. The vectors $\{\mathbf{q}_1, \mathbf{q}_2, \mathbf{q}_3, \dots, \mathbf{q}_k\}$ are constructed from the successive Krylov spaces that are generated by \mathbf{A} and \mathbf{b} , as illustrated in (A.2.10). It is also noted that the algorithm in (A.2.11) and (A.2.12) is

Appendix A. Non-Linear Solution Methods for Implicit Dynamics in MPM

just the Gram-Schmidt process for computing an orthogonal set of basis vectors from an arbitrary set of basis vectors. At first the use of a QR factorization of the Krylov matrix $\mathbf{K}_k = [\mathbf{b}, \mathbf{A}\mathbf{b}, \mathbf{A}^2\mathbf{b}, \dots, \mathbf{A}^{k-1}\mathbf{b}]$ may seem to be the most straightforward approach to constructing an orthogonal basis for K_k . However, this process is unstable because the matrix \mathbf{K}_k is ill-conditioned.

Using (A.2.6) the least squares problem is restated as follows:

$$\min_{\mathbf{x} \in \mathbb{R}^{k \times 1}} \|\mathbf{Q}_{k+1}\mathbf{H}_k\mathbf{y} - \mathbf{b}\| \quad (\text{A.2.13})$$

Since the norm of a vector is unaltered by multiplication with an orthogonal matrix, equation (A.2.13) can be rewritten as follows:

$$\min_{\mathbf{x} \in \mathbb{R}^{k \times 1}} \|\mathbf{H}_k\mathbf{y} - \mathbf{Q}_{k+1}^T\mathbf{b}\| \quad (\text{A.2.14})$$

The Arnoldi iteration for computing of basis vectors in Q_k is initiated by setting $\mathbf{q}_1 = \mathbf{b}/\|\mathbf{b}\|$. As a result the problem in (A.2.14) becomes

$$\min_{\mathbf{x} \in \mathbb{R}^{k \times 1}} \|\mathbf{H}_k\mathbf{y} - \boldsymbol{\beta}\| \quad (\text{A.2.15})$$

where $\boldsymbol{\beta} = \|\mathbf{b}\|\mathbf{e}_1$, $\mathbf{e}_1 \in \mathbb{R}^{k+1 \times k}$ and $\mathbf{e}_1 = [1 \ 0 \ \dots \ 0]^T$.

The first step to solving (A.2.15) is to obtain a QR factorization of \mathbf{H}_k such that $\mathbf{H}_k = \mathbf{V}_k\mathbf{R}_k$ where $\mathbf{V}_k^{-1} = \mathbf{V}_k^T$, $\mathbf{V}_k \in \mathbb{R}^{k+1 \times k+1}$ and $\mathbf{R}_k \in \mathbb{R}^{k+1 \times k}$. The upper triangular matrix \mathbf{R}_k is expressed as $\mathbf{R}_k = \mathbf{V}_k^T\mathbf{H}_k$ and the orthogonal matrix \mathbf{V}_k is formed by the product of Givens rotation matrices, $\mathbf{V}_k^T = \mathbf{G}_k \dots \mathbf{G}_2\mathbf{G}_1$ for which $\mathbf{G}_j^{-1} = \mathbf{G}_j^T$ and $j = 1, \dots, k$. The matrix \mathbf{G}_j is constructed to annihilate the $H_{j+1,j}$ element in the \mathbf{H}_k matrix and has the following form:

Appendix A. Non-Linear Solution Methods for Implicit Dynamics in MPM

$$\mathbf{G}_j = \begin{bmatrix} 1 & 0 & \dots & 0 & \dots & 0 & \dots & 0 \\ 0 & 1 & \dots & 0 & \dots & 0 & \dots & 0 \\ \vdots & \ddots & \ddots & 0 & & 0 & & \vdots \\ 0 & \dots & 0 & G_{jj} & G_{jj+1} & 0 & \dots & 0 \\ 0 & \dots & 0 & G_{j+1j} & G_{j+1j+1} & 0 & \dots & 0 \\ \vdots & & & 0 & 0 & \ddots & & \vdots \\ & & & \vdots & \vdots & & 1 & 0 \\ 0 & 0 & \dots & 0 & 0 & \dots & \dots & 1 \end{bmatrix} \quad (\text{A.2.16})$$

The only entries in \mathbf{G}_j that are not equal to 0 or 1 in (A.2.16) are set to $G_{j+1j+1} = G_{jj} = c_j$, $G_{jj+1} = s_j$ and $G_{j+1j} = -s_j$ where

$$c_j = \frac{H_{jj}}{\sqrt{H_{jj}^2 + H_{j+1j}^2}}, \quad s_j = \frac{H_{j+1j}}{\sqrt{H_{jj}^2 + H_{j+1j}^2}} \quad (\text{A.2.17})$$

In practice Given's rotation matrices are not explicitly computed. Instead only the quantities c_j and s_j are computed and stored.

Once \mathbf{R}_k is formed the problem of (A.2.15) becomes

$$\min_{\mathbf{x} \in \mathbb{R}^{k \times 1}} \|\mathbf{R}_k \mathbf{y} - \mathbf{g}\| \quad (\text{A.2.18})$$

where $\mathbf{g} = \mathbf{V}_k^T \|\mathbf{b}\| \mathbf{e}_1$. By design the R_{k+1k} entry in \mathbf{R}_k is zero, and the $k \times k$ upper triangular sub-system of $\mathbf{R}_k \mathbf{y} = \mathbf{g}$ can be solved to obtain \mathbf{y} and the estimate of the residual is $|g_{k+1}|$. If $|g_{k+1}|$ is within a specified tolerance then the approximate solution is computed to be $\mathbf{x}_k = \mathbf{Q}_k \mathbf{y}$. If the minimum tolerance is not met then another iteration is performed and k is increased by 1. GMRES is designed to be an efficient iterative solver. In practice the matrices \mathbf{G}_j , \mathbf{R}_k and \mathbf{g} are not explicitly constructed

Appendix A. Non-Linear Solution Methods for Implicit Dynamics in MPM

in order to minimize computational effort. Concise algorithms are presented next for the general case and for the specific case in the MPM computational cycle.

GMRES Algorithm (General)

The iterative GMRES algorithm for obtaining a solution to a $n \times n$ linear system of equations is presented here for the general case of $\mathbf{Ax} = \mathbf{b}$ for which $\mathbf{A} \in \mathbb{R}^{n \times n}$ and $\mathbf{b} \in \mathbb{R}^{n \times 1}$ are known and $\mathbf{x} \in \mathbb{R}^{n \times 1}$ is the desired solution.

1. Initialize and store the first orthonormal basis vector to $\mathbf{q}_1 = \mathbf{b}/\|\mathbf{b}\|$ and set $\beta = \|\mathbf{b}\|\mathbf{e}_1$. Choose an appropriate tolerance ε and the maximum number of GMRES iterations k_{max} . Compute first residual error to be $|\beta_{k+1}| = \|\mathbf{b}\|$. Set $k = 1$.
2. Check residual error. If $|\beta_{k+1}| \leq \varepsilon$ or $k \geq k_{max}$ then terminate the procedure and proceed to step 3. Otherwise continue.

(a) Perform k steps of Arnoldi iteration as follows using algorithm in equations (A.2.11) and (A.2.12):

- i. Compute $\mathbf{q}_{k+1} = \mathbf{A}\mathbf{q}_k$
- ii. for $j = 1, \dots, k$ compute $H_{jk} = \mathbf{q}_j^T \mathbf{q}_{k+1}$ and overwrite $\mathbf{q}_{k+1} \rightarrow \mathbf{q}_{k+1} - H_{jk}\mathbf{q}_j$
- iii. Compute $H_{k+1k} = \|\mathbf{q}_{k+1}\|$
- iv. Overwrite and store $\mathbf{q}_{k+1} \rightarrow \mathbf{q}_{k+1}/H_{k+1k}$

(b) Compute and store components of Given's rotation matrices

$$c_j = \frac{H_{jj}}{\sqrt{H_{jj}^2 + H_{j+1j}^2}}, \quad s_j = \frac{H_{j+1j}}{\sqrt{H_{jj}^2 + H_{j+1j}^2}}$$

(c) For $j = 1, \dots, k$ overwrite the components of the k^{th} column of Hessenburg matrix \mathbf{H}_k .

$$\begin{Bmatrix} H_{jk} \\ H_{j+1k} \end{Bmatrix} \rightarrow \begin{bmatrix} c_j & s_j \\ -s_j & c_j \end{bmatrix} \begin{Bmatrix} H_{jk} \\ H_{j+1k} \end{Bmatrix}$$

Appendix A. Non-Linear Solution Methods for Implicit Dynamics in MPM

(d) Overwrite the k^{th} and $(k + 1)^{th}$ components of the $\boldsymbol{\beta}$ vector as follows:

$$\begin{Bmatrix} \beta_k \\ \beta_{k+1} \end{Bmatrix} \rightarrow \begin{bmatrix} c_j & s_j \\ -s_j & c_j \end{bmatrix} \begin{Bmatrix} \beta_k \\ \beta_{k+1} \end{Bmatrix}$$

(e) Increase GMRES iteration $k \rightarrow k + 1$

(f) Return to step 2 to check error tolerance and the number of iterations

3. Solve the upper triangular system $\mathbf{H}_k \mathbf{y} = \boldsymbol{\beta}$ using back substitution.

(a) Compute $y_k = \beta_k / H_{kk}$

(b) For $j = 1, \dots, k + 1$ perform the following computations:

i. Compute $y_{k-j} = \beta_{k-j}$

ii. For $i = (k - j + 1), \dots, k$ overwrite $y_{k-j} \rightarrow y_{k-j} - H_{k-j i} y_i$

iii. Overwrite $y_{k-j} \rightarrow y_{k-j} / H_{k-j k-j}$

4. Compute the solution $\mathbf{x}_k = \sum_{j=1}^k y_j \mathbf{q}_j$

GMRES Algorithm (MPM)

The iterative GMRES algorithm for obtaining a solution to a linear system of equations is presented here for the specific case of the linearized equations encountered in a single non-linear solution step of the following discrete system of MPM equations in equation (A.1.6) displayed again below:

$$D_h \mathbf{F}(\mathbf{p}_n, \mathbf{s}) = -\mathbf{F}(\mathbf{p}_n)$$

In (A.1.6) the subscript n refers to the Newton iteration, \mathbf{p}_n is the current iterate of the global momentum vector and the solution vector is the update to the momentum in the non-linear iteration.

1. Set $\mathbf{b} = -\mathbf{F}(\mathbf{p}_n)$. Initialize and store the first orthonormal basis vector to $\mathbf{q}_1 = \mathbf{b}/\|\mathbf{b}\|$ and set $\beta = \|\mathbf{b}\|e_1$. Choose an appropriate tolerance ε and the maximum number of GMRES iterations k_{max} . Compute first residual error to be $|\beta_{k+1}| = \|\mathbf{b}\|$. Set $k = 1$.
2. Check residual error. If $|\beta_{k+1}| \leq \varepsilon$ or $k \geq k_{max}$ then terminate the procedure and proceed to step 3. Otherwise continue.
 - (a) Perform k steps of Arnoldi iteration as follows using algorithm in equations (A.2.11) and (A.2.12):
 - i. Compute $\mathbf{q}_{k+1} = D_h \mathbf{F}(\mathbf{p}_n, \mathbf{q}_k)$
 - ii. for $j = 1, \dots, k$ compute $H_{jk} = \mathbf{q}_j^T \mathbf{q}_{k+1}$ and overwrite $\mathbf{q}_{k+1} \rightarrow \mathbf{q}_{k+1} - H_{jk} \mathbf{q}_j$
 - iii. Compute $H_{k+1k} = \|\mathbf{q}_{k+1}\|$
 - iv. Overwrite and store $\mathbf{q}_{k+1} \rightarrow \mathbf{q}_{k+1}/H_{k+1k}$

Appendix A. Non-Linear Solution Methods for Implicit Dynamics in MPM

- (b) Compute and store components of Given's rotation matrices

$$c_j = \frac{H_{jj}}{\sqrt{H_{jj}^2 + H_{j+1j}^2}}, \quad s_j = \frac{H_{j+1j}}{\sqrt{H_{jj}^2 + H_{j+1j}^2}}$$

- (c) For $j = 1, \dots, k$ overwrite the components of the k^{th} column of Hessenburg matrix \mathbf{H}_k .

$$\begin{Bmatrix} H_{jk} \\ H_{j+1k} \end{Bmatrix} \rightarrow \begin{bmatrix} c_j & s_j \\ -s_j & c_j \end{bmatrix} \begin{Bmatrix} H_{jk} \\ H_{j+1k} \end{Bmatrix}$$

- (d) Overwrite the k^{th} and $(k+1)^{th}$ components of the $\boldsymbol{\beta}$ vector as follows:

$$\begin{Bmatrix} \beta_k \\ \beta_{k+1} \end{Bmatrix} \rightarrow \begin{bmatrix} c_j & s_j \\ -s_j & c_j \end{bmatrix} \begin{Bmatrix} \beta_k \\ \beta_{k+1} \end{Bmatrix}$$

- (e) Increase GMRES iteration $k \rightarrow k+1$

- (f) Return to step 2 to check error tolerance and the number of iterations

3. Solve the upper triangular system $\mathbf{H}_k \mathbf{y} = \boldsymbol{\beta}$ using back substitution.

- (a) Compute $y_k = \beta_k / H_{kk}$

- (b) For $j = 1, \dots, k+1$ perform the following computations:

i. Compute $y_{k-j} = \beta_{k-j}$

ii. For $i = (k-j+1), \dots, k$ overwrite $y_{k-j} \rightarrow y_{k-j} - H_{k-j i} y_i$

iii. Overwrite $y_{k-j} \rightarrow y_{k-j} / H_{k-j k-j}$

4. Compute the solution $\mathbf{x}_k = \sum_{j=1}^k y_j \mathbf{q}_j$

A.3 Evaluation of the Implicit Non-linear Function and its Directional Derivative

Within the Newton-GMRES iterations it is necessary to evaluate the non-linear function \mathbf{F} . For the Newton algorithm $\mathbf{F}(\mathbf{p}_n)$ is required (see section A.1) for each Newton iteration n . For the GMRES algorithm, the evaluation of \mathbf{F} is necessary to form its directional derivative $D_h\mathbf{F}(\mathbf{p}_n, \mathbf{q}_k)$ for each GMRES iteration k (see section A.2). Quantities associated with the current and previous time step are denoted by superscripts L and 0 respectively. The quantities \mathbf{X}_p^0 , \mathbf{V}_p^0 , $\boldsymbol{\varepsilon}_p^0$, $\boldsymbol{\sigma}_p^0$, \mathbf{p}_i^0 , \mathbf{f}_i^0 and m_i^0 are available from the previous time step. The only quantity that is actually updated during the Newton-GMRES procedure is the momentum for the current time step \mathbf{p}_i^L . All other quantities computed for the current time step during the solver iterations are placeholder quantities that are overwritten at every iteration and are denoted by a tilde. Let $\boldsymbol{\theta}$ be the argument for the function \mathbf{F} . The evaluation of $\mathbf{F}(\boldsymbol{\theta})$ is summarized in the following steps:

1. Compute material point velocity update using equations (4.2.20) and (4.3.6) as follows:

$$\tilde{\mathbf{V}}_p^L = \mathbf{V}_p^0 + \Delta t \sum_{i=1}^{N_i} \frac{1}{m_i^0} \left(\frac{\boldsymbol{\theta} - \mathbf{p}_i^0}{\Delta t} \right) N_i(\mathbf{X}_p^0)$$

2. Compute nodal grid velocity update using equation (4.3.7)

$$\tilde{\mathbf{v}}_i^L = \frac{1}{m_i^0} \sum_{p=1}^{N_p} M_p \tilde{\mathbf{V}}_p^L N_i(\mathbf{X}_p^0)$$

3. Apply boundary conditions to $\tilde{\mathbf{v}}_i^L$ on applicable grid nodes
4. Compute material point strain increment using equation (4.3.8)

Appendix A. Non-Linear Solution Methods for Implicit Dynamics in MPM

$$\Delta \tilde{\boldsymbol{\varepsilon}}_p = \frac{\Delta t}{2} \sum_{i=1} (\tilde{\mathbf{v}}_i^L \otimes \nabla N_i(\mathbf{X}_p^0) + \nabla N_i(\mathbf{X}_p^0) \otimes \tilde{\mathbf{v}}_i^L)$$

5. Compute material point strain update $\tilde{\boldsymbol{\varepsilon}}_p^L = \boldsymbol{\varepsilon}_p^0 + \Delta \tilde{\boldsymbol{\varepsilon}}_p$
6. Evaluate the constitutive model to compute material point stress increment $\Delta \tilde{\boldsymbol{\sigma}}_p$ and update the stress $\tilde{\boldsymbol{\sigma}}_p^L = \boldsymbol{\sigma}_p^0 + \Delta \tilde{\boldsymbol{\sigma}}_p$
7. Compute nodal internal force increment using equation (4.2.12)

$$\Delta \tilde{\mathbf{f}}_i^{int} = - \sum_{p=1}^{N_p} \frac{M_p}{\rho} \Delta \tilde{\boldsymbol{\sigma}}_p \cdot \nabla N_i(\mathbf{X}_p^0)$$

8. Evaluate the implicit non-linear function using equation (A.1.2)

$$\mathbf{F}(\boldsymbol{\theta}) = \boldsymbol{\theta} - \Delta t \mu \Delta \tilde{\mathbf{f}}_i^{int} + \mathbf{p}_i^0 + \Delta t \mathbf{f}_i^{int 0}$$

For a single Newton iteration, $\boldsymbol{\theta} = \mathbf{p}_n$. For the GMRES iterations the argument $\boldsymbol{\theta}$ is either $\boldsymbol{\theta} = \mathbf{p}_n + h \|\mathbf{p}_n\| \mathbf{q}_k$ or $\boldsymbol{\theta} = h \|\mathbf{p}_n\| \mathbf{q}_k$. Since $\|\mathbf{q}_k\| = 1$ for the case of GMRES the difference approximation for the directional derivative of \mathbf{F} in (A.1.5) becomes

$$D_h \mathbf{F}(\mathbf{p}_n, \mathbf{q}_k) = \left\{ \begin{array}{ll} 0 & \mathbf{q}_k = \mathbf{0} \\ \frac{\mathbf{F}(\mathbf{p}_n + h \|\mathbf{p}_n\| \mathbf{q}_k) - \mathbf{F}(\mathbf{p}_n)}{h \|\mathbf{p}_n\|} & \mathbf{q}_k \neq \mathbf{0}, \mathbf{p}_n \neq \mathbf{0} \\ \frac{\mathbf{F}(h \mathbf{q}_k) - \mathbf{F}(\mathbf{0})}{h} & \mathbf{q}_k \neq \mathbf{0}, \mathbf{p}_n = \mathbf{0} \end{array} \right\} \quad (\text{A.3.1})$$

where the quantities \mathbf{p}_n and $\mathbf{F}(\mathbf{p}_n)$ are available from the previous Newton iteration.

Appendix B

Quasi-Static MPM

B.1 Governing Equations

Consider two configurations of a deformable body. The initial or reference configuration of the body is the set of points $\Omega_0 \in \mathbf{R}^3$. The position vector of a material point in the initial configuration is denoted by $\mathbf{X} \in \Omega_0$. The body deforms relative to its initial state. This deformed state is referred to as the current or spatial configuration of the body, and is represented by the set of points $\Omega \in \mathbf{R}^3$. The position vector of a material point in the current configuration is denoted by $\mathbf{x} \in \Omega$. A one-to-one mapping is assumed to exist between the material point positions such that $\mathbf{x} = \mathbf{x}(\mathbf{X})$ and $\mathbf{X} = \mathbf{X}(\mathbf{x})$. The displacement of a material point is $\mathbf{u} = \mathbf{x} - \mathbf{X}$.

The local form of the equilibrium equation is obtained by setting the sum of internal and external forces in Ω equal to zero. The resulting governing equation for equilibrium is

$$\nabla \cdot \boldsymbol{\sigma} + \bar{\mathbf{b}} = \mathbf{0} \quad (\text{B.1.1})$$

where $\boldsymbol{\sigma}$ is the symmetric Cauchy stress tensor and $\bar{\mathbf{b}}$ is the body force per unit volume.

The boundary is divided into two sets of points such that $\partial\Omega = \partial\Omega^u \cup \partial\Omega^t$. The displacement (or essential) boundary conditions are applied to $\partial\Omega^u$ and the traction boundary conditions are applied to $\partial\Omega^t$ as follows:

$$\begin{aligned} \mathbf{u}(\mathbf{x}) &= \mathbf{g}(\mathbf{x}) \quad \forall \quad \mathbf{x} \in \partial\Omega^u \\ \boldsymbol{\tau}(\mathbf{x}) &= \mathbf{t}(\mathbf{x}) \quad \forall \quad \mathbf{x} \in \partial\Omega^t \end{aligned} \quad (\text{B.1.2})$$

The measure of deformation between the initial and deformed configurations is the strain, denoted by $\boldsymbol{\varepsilon}$. The small strain approximation is used for which strain is

Appendix B. Quasi-Static MPM

computed as the symmetric part of the displacement gradient as follows:

$$\boldsymbol{\varepsilon} = \frac{1}{2}[\nabla \mathbf{u} + (\nabla \mathbf{u})^T] \quad (\text{B.1.3})$$

The constitutive relationship, denoted symbolically as $\boldsymbol{\sigma} = \boldsymbol{\sigma}(\boldsymbol{\varepsilon})$, is necessary to form a complete set of equations for obtaining the displacement field solution, $\mathbf{u}(\mathbf{x})$.

The weak (variational) form of equilibrium in equation (B.1.1) is obtained using the usual arguments. The final result is

$$-\int_{\Omega} \rho \nabla \mathbf{w} : \boldsymbol{\sigma}^s dV + \int_{\partial\Omega} \mathbf{w} \cdot \boldsymbol{\tau} dA + \int_{\Omega} \rho \mathbf{w} \cdot \mathbf{b} dV = 0 \quad (\text{B.1.4})$$

where the test function, \mathbf{w} , is an admissible variation of the solution. The specific stress, $\boldsymbol{\sigma}_s$, is defined using the mass density of the material, ρ , to be $\boldsymbol{\sigma}_s = \boldsymbol{\sigma}/\rho$.

B.2 The Discrete MPM Equations

MPM involves the discretization of space, denoted by $\mathbf{x} \in \mathbb{R}^3$, and the body of solid material, denoted by $\Omega \subset \mathbb{R}^3$. Space is discretized by a set of grid cells connected by the set of N_n grid node positions $\{\mathbf{x}_i\}_{i=1}^{N_n}$. The solid body is discretized by the set of N_p material points $\{\mathbf{X}_p\}_{p=1}^{N_p} \subset \Omega$. The subscripts i and p are used to denote quantities associated with grid nodes and material points respectively.

Each material point is associated with a discrete mass M_p . The total mass, m , of the body Ω is simply $m = \sum_{p=1}^{N_p} M_p$. In MPM the mass density, $\rho(\mathbf{x})$, is represented as a distribution of discrete material point masses using the Dirac delta distribution $\delta(\mathbf{x})$ as follows:

Appendix B. Quasi-Static MPM

$$\rho(\mathbf{x}) = \sum_{p=1}^{N_p} M_p \delta(\mathbf{x} - \mathbf{X}_p) \quad (\text{B.2.1})$$

The discrete set of MPM equilibrium equations are formed from the weak form of equilibrium in equation (B.1.4). Substitution of (B.2.1) into (B.1.4) replaces the integrals in (B.1.4) with sums of material quantities evaluated at the material point positions \mathbf{X}_p as follows:

$$-\sum_{p=1}^{N_p} V_p \boldsymbol{\sigma}(\mathbf{X}_p) : \nabla \mathbf{w}(\mathbf{X}_p) + \int_{\partial\Omega} \mathbf{w}(\mathbf{x}) \cdot \boldsymbol{\tau}(\mathbf{x}) dA + \sum_{p=1}^{N_p} V_p \mathbf{w}(\mathbf{X}_p) \cdot \bar{\mathbf{b}}(\mathbf{X}_p) = \mathbf{0} \quad (\text{B.2.2})$$

Since inertial forces are not considered in for the equilibrium case, the use of a mass quantity is not necessary. The quantity, V_p , in equation (B.2.2) is the discrete material point volume.

The variation in equation (B.2.2) is approximated with standard finite element nodal basis functions, $N_i(\mathbf{x})$, $i = 1, 2, \dots, N_n$ which satisfy the partition of unity property such that $\sum_{i=1}^{N_n} N_i(\mathbf{x}) = 1$. The finite element approximation of the displacement field variation is

$$\mathbf{w}(\mathbf{x}) = \sum_{i=1}^{N_n} \mathbf{w}_i N_i(\mathbf{x}) \quad (\text{B.2.3})$$

The test function approximation in equation (B.2.3) is substituted into equation (B.2.2). The final result is

$$\begin{aligned} & -\sum_{i=1}^{N_n} \sum_{p=1}^{N_p} V_p \boldsymbol{\sigma}_p^s : (\mathbf{w}_i \otimes \nabla N_i(\mathbf{X}_p)) + \sum_{i=1}^{N_n} \int_{\partial\Omega} \mathbf{w}_i \cdot \boldsymbol{\tau}(\mathbf{x}) N_i(\mathbf{x}) dA \\ & + \sum_{i=1}^{N_n} \sum_{p=1}^{N_p} V_p \mathbf{w}_i \cdot \bar{\mathbf{b}}(\mathbf{X}_p) N_i(\mathbf{X}_p) = \mathbf{0} \end{aligned} \quad (\text{B.2.4})$$

Appendix B. Quasi-Static MPM

Further simplification of (B.2.4) results in the following:

$$\begin{aligned}
 & - \sum_{i=1}^{N_n} \mathbf{w}_i \cdot \sum_{p=1}^{N_p} V_p \boldsymbol{\sigma}_p^s \cdot \nabla N_i(\mathbf{X}_p) + \sum_{i=1}^{N_n} \mathbf{w}_i \cdot \int_{\partial\Omega} \boldsymbol{\tau}(\mathbf{x}) N_i(\mathbf{x}) dA \\
 & + \sum_{i=1}^{N_n} \mathbf{w}_i \cdot \sum_{p=1}^{N_p} V_p \bar{\mathbf{b}}(\mathbf{X}_p) N_i(\mathbf{X}_p) = \mathbf{0}
 \end{aligned} \tag{B.2.5}$$

Since (B.2.5) holds for all \mathbf{w}_i , discrete MPM equations reduce to the following form:

$$- \sum_{p=1}^{N_p} V_p \boldsymbol{\sigma}_p \cdot \nabla N_i(\mathbf{X}_p) + \int_{\partial\Omega} \boldsymbol{\tau}_p N_i(\mathbf{X}_p) dA + \sum_{p=1}^{N_p} V_p \bar{\mathbf{b}}_p N_i(\mathbf{X}_p) = \mathbf{0} \tag{B.2.6}$$

The internal forces at the nodes are defined to be

$$\mathbf{f}_i^{int} = - \sum_{p=1}^{N_p} V_p \boldsymbol{\sigma}_p \cdot \nabla N_i(\mathbf{X}_p) \tag{B.2.7}$$

The external forces at the nodes are defined to be

$$\mathbf{f}_i^{ext} = \mathbf{b}_i + \hat{\boldsymbol{\tau}}_i \tag{B.2.8}$$

where

$$\hat{\boldsymbol{\tau}}_i = \int_{\partial\Omega} N_i(\mathbf{X}_p) \boldsymbol{\tau}_p dA \tag{B.2.9}$$

and

$$\mathbf{b}_i = \sum_{p=1}^{N_p} V_p \bar{\mathbf{b}}_p N_i(\mathbf{X}_p) \tag{B.2.10}$$

Appendix B. Quasi-Static MPM

Equations (B.2.7) - (B.2.10) are combined to form a simplified expression for the discrete MPM equilibrium equations. The result is

$$\mathbf{F}_i(\mathbf{u}_i) = \mathbf{f}_i^{int} + \mathbf{f}_i^{ext} = \mathbf{0} \quad (\text{B.2.11})$$

where the functional dependence of the nodal displacement solution, \mathbf{u}_i , is emphasized through the use of the function, $\mathbf{F}_i(\mathbf{u}_i)$ in equation (B.2.11).

B.3 Numerical Implementation of Quasi-static MPM

The numerical solution of the quasi-static problem is typically obtained in steps by incrementally applying displacement boundary conditions, external forces or both in order to obtain incremental solutions in displacement, $\Delta\mathbf{u}_i$. The discrete quasi-static equations are solved for each load step denoted by k ($k = 1, \dots, K$). For displacement control loading a boundary displacement increment, $\Delta\mathbf{g}^k$, is applied on $\partial\Omega^u$ for each step such that $\sum_{k=1}^K \Delta\mathbf{g}^k = \mathbf{g}(\mathbf{x})$. In general, load control is achieved by incrementing the external force on the nodes by $\Delta\mathbf{f}_i^{ext k}$ for each load step such that $\sum_{k=1}^K \Delta\mathbf{f}_i^{ext k} = \mathbf{f}_i^{ext}$. This is accomplished by incrementing the corresponding body force $\bar{\mathbf{b}}_i$ for $\mathbf{x}_i \in \Omega$ and surface tractions $\hat{\boldsymbol{\tau}}_i$ for $\mathbf{x}_i \in \partial\Omega^t$ appropriately on the grid nodes. Quantities associated with a discrete load step are denoted with the superscript k . Each discrete load step corresponds to a discrete configuration, Ω^k , of the solid body.

Consider an intermediate equilibrium state of loading at step k for which the material point quantities, \mathbf{X}_p^k , $\boldsymbol{\varepsilon}_p^k$ and $\boldsymbol{\sigma}_p^k$ are known. The known external force at the grid nodes is $\mathbf{f}_i^{ext k} = \sum_{j=1}^k \Delta\mathbf{f}_i^{ext j}$ for predetermined load increments, $\Delta\mathbf{f}_i^{ext j}$ ($j = 1, \dots, k$). The equilibrium state at the $(k+1)^{th}$ loading step is obtained from the

Appendix B. Quasi-Static MPM

nodal displacement increment solution, $\Delta \mathbf{u}_i$, which satisfies the following discrete MPM equation for the incremental quasi-static problem:

$$\mathbf{F}_i(\Delta \mathbf{u}_i) = \mathbf{f}_i^{int\ k+1} + \mathbf{f}_i^{ext\ k+1} = \mathbf{0} \quad (\text{B.3.1})$$

where the external force at the nodes for the $(k+1)^{th}$ loading step is computed to be

$$\mathbf{f}_i^{ext\ k+1} = \mathbf{f}_i^{ext\ k} + \Delta \mathbf{f}_i^{ext\ k+1} \quad (\text{B.3.2})$$

and the following displacement boundary conditions are satisfied:

$$\Delta \mathbf{u}_i = \Delta \mathbf{g}^{k+1}(\mathbf{x}_i) \quad \forall \mathbf{x}_i \in \partial \Omega^u \quad (\text{B.3.3})$$

The nodal internal forces at the $(k+1)^{th}$ loading step are computed from equation (B.2.7) in terms of the corresponding material point stress $\boldsymbol{\sigma}_p^{k+1}$ as follows:

$$\mathbf{f}_i^{int\ k+1} = - \sum_{p=1}^{N_p} V_p \boldsymbol{\sigma}_p^{k+1} \cdot \nabla N_i(\mathbf{X}_p^k) \quad (\text{B.3.4})$$

The incremental displacement solution is approximated using nodal basis functions as follows:

$$\Delta \mathbf{u}(\mathbf{x}) = \sum_{i=1}^{N_n} \Delta \mathbf{u}_i N_i(\mathbf{x}) \quad (\text{B.3.5})$$

The material point strain increment is computed from equations (B.1.3) and (B.3.5) to be

Appendix B. Quasi-Static MPM

$$\Delta \boldsymbol{\varepsilon}_p = \frac{1}{2} \sum_{i=1}^{N_n} \left[\nabla N_i(\mathbf{X}_p^k) \otimes \Delta \mathbf{u}_i + (\nabla N_i(\mathbf{X}_p^k) \otimes \Delta \mathbf{u}_i)^T \right] \quad (\text{B.3.6})$$

The updated strain is

$$\boldsymbol{\varepsilon}_p^{k+1} = \boldsymbol{\varepsilon}_p^k + \Delta \boldsymbol{\varepsilon}_p \quad (\text{B.3.7})$$

The material point stress increment is obtained by evaluation of the constitutive model. Symbolically, the stress increment computation is

$$\Delta \boldsymbol{\sigma}_p = \Delta \boldsymbol{\sigma}_p(\Delta \boldsymbol{\varepsilon}_p) \quad (\text{B.3.8})$$

The updated stress is

$$\boldsymbol{\sigma}_p^{k+1} = \boldsymbol{\sigma}_p^k + \Delta \boldsymbol{\sigma}_p \quad (\text{B.3.9})$$

In general, the function $\mathbf{F}_i = \mathbf{F}_i(\Delta \mathbf{u}_i)$ in equation (B.3.1) is a non-linear function of $\Delta \mathbf{u}_i$. The solution to $\mathbf{F}_i(\Delta \mathbf{u}_i) = \mathbf{0}$ is obtained using the implicit solution method described in Appendix A in which equations (B.3.1) - (B.3.9) are solved iteratively to obtain the new equilibrium state at the $(k+1)^{th}$ load step. Once the solution $\Delta \mathbf{u}_i$ is obtained, the material point position, \mathbf{X}_p , and displacement \mathbf{U}_p , are updated as follows:

$$\mathbf{X}_p^{k+1} = \mathbf{X}_p^k + \sum_{i=1}^{N_n} \Delta \mathbf{u}_i N_i(\mathbf{X}_p^k) \quad (\text{B.3.10})$$

$$\Delta \mathbf{U}_p^{k+1} = \Delta \mathbf{U}_p^k + \sum_{i=1}^{N_n} \Delta \mathbf{u}_i N_i(\mathbf{X}_p^k) \quad (\text{B.3.11})$$

B.4 Evaluation of the Implicit Non-linear Function and its Directional Derivative

Within the Newton-GMRES iterations it is necessary to evaluate the non-linear function \mathbf{F} . For the Newton algorithm the evaluation of $\mathbf{F}(\Delta\mathbf{u}_n)$ is required (see section A.1) for each Newton iteration n . For the GMRES algorithm, the evaluation of \mathbf{F} is necessary to form the directional derivative $D_h\mathbf{F}(\Delta\mathbf{u}_n, \mathbf{q}_k)$ for each GMRES iteration k (see section A.2). Quantities associated with the previous and current load steps are denoted by superscripts 0 and L respectively. The quantities \mathbf{X}_p^0 , $\boldsymbol{\varepsilon}_p^0$ and $\boldsymbol{\sigma}_p^0$ are available from the previous load step. The only quantity that is actually updated during the Newton-GMRES procedure is the displacement increment solution, $\Delta\mathbf{u}_i$. All other quantities computed for the current load step during the solver iterations are placeholder quantities that are overwritten at every iteration and are denoted by a tilde. Let $\boldsymbol{\theta}$ be the argument for the function \mathbf{F} . The evaluation of $\mathbf{F}(\boldsymbol{\theta})$ is summarized in the following steps:

1. Apply kinematic boundary conditions to the argument $\boldsymbol{\theta}$ on applicable grid nodes as follows from equation (B.3.3):

$$\boldsymbol{\theta} = \Delta\mathbf{g}^L(\mathbf{x}_i) \quad \forall \mathbf{x}_i \in \partial\Omega^u$$

2. Compute material point strain increment using equation (B.3.6) as follows:

$$\Delta\tilde{\boldsymbol{\varepsilon}}_p = \frac{1}{2} \sum_{i=1} (\boldsymbol{\theta} \otimes \nabla N_i(\mathbf{X}_p^0) + \nabla N_i(\mathbf{X}_p^0) \otimes \boldsymbol{\theta})$$

3. Compute material point strain update $\tilde{\boldsymbol{\varepsilon}}_p^L = \boldsymbol{\varepsilon}_p^0 + \Delta\tilde{\boldsymbol{\varepsilon}}_p$
4. Evaluate the constitutive model to compute material point stress increment $\Delta\tilde{\boldsymbol{\sigma}}_p$ and update the stress $\tilde{\boldsymbol{\sigma}}_p^L = \boldsymbol{\sigma}_p^0 + \Delta\tilde{\boldsymbol{\sigma}}_p$

Appendix B. Quasi-Static MPM

5. Compute nodal internal force using equation equation (B.3.4) as follows:

$$\tilde{\mathbf{f}}_i^{int. L} = - \sum_{p=1}^{N_p} V_p \tilde{\boldsymbol{\sigma}}_p^L \cdot \nabla N_i(\mathbf{X}_p^0)$$

6. Compute nodal external force using equation equation (B.3.2) as follows

$$\mathbf{f}_i^{ext L} = \mathbf{f}_i^{ext 0} + \Delta \mathbf{f}_i^{ext L}$$

7. Evaluate the implicit non-linear function using equation (B.3.1)

$$\mathbf{F}(\boldsymbol{\theta}) = \tilde{\mathbf{f}}_i^{int. L} + \Delta \mathbf{f}_i^{ext L}$$

For a single Newton iteration, $\boldsymbol{\theta} = \Delta \mathbf{u}_n$. For the GMRES iterations the argument $\boldsymbol{\theta}$ is either $\boldsymbol{\theta} = \Delta \mathbf{u}_n + h \|\Delta \mathbf{u}_n\| \mathbf{q}_k$ or $\boldsymbol{\theta} = h \|\Delta \mathbf{u}_n\| \mathbf{q}_k$. Since $\|\mathbf{q}_k\| = 1$ for the GMRES iteration the difference approximation for the directional derivative of \mathbf{F} in (A.1.5) becomes

$$D_h \mathbf{F}(\Delta \mathbf{u}_n, \mathbf{q}_k) = \left\{ \begin{array}{ll} \mathbf{0} & \mathbf{q}_k = \mathbf{0} \\ \frac{\mathbf{F}(\Delta \mathbf{u}_n + h \|\Delta \mathbf{u}_n\| \mathbf{q}_k) - \mathbf{F}(\Delta \mathbf{u}_n)}{h \|\Delta \mathbf{u}_n\|} & \mathbf{q}_k \neq \mathbf{0}, \quad \Delta \mathbf{u}_n \neq \mathbf{0} \\ \frac{\mathbf{F}(h \mathbf{q}_k) - \mathbf{F}(\mathbf{0})}{h} & \mathbf{q}_k \neq \mathbf{0}, \quad \Delta \mathbf{u}_n = \mathbf{0} \end{array} \right\} \quad (\text{B.4.1})$$

where the quantities $\Delta \mathbf{u}_n$ and $\mathbf{F}(\Delta \mathbf{u}_n)$ are available from the previous Newton iteration.

Appendix C

Preliminary Studies of Fracture Energy Size Effect Simulation

Appendix C. Preliminary Studies of Fracture Energy Size Effect Simulation

The objective of this work is to use MPM to simulate the experimentally observed size effect in mode I fracture energy for concrete using a modified multiple smeared crack material failure representation. Key differences between classical multiple smeared crack models and the modified multiple smeared crack approach are presented. A physical basis for the modification is postulated which retains the fracture energy as a constant material property but accounts for the variation of fracture energy with structural size measured in the laboratory. Preliminary studies demonstrate the feasibility of the approach for simulating the size effect.

C.1 Measurement of Fracture Energy

The fracture energy, G_f , is defined as the energy consumed to form a unit area of crack surface. It is the key material property utilized in discrete constitutive models for localization and fracture. The work of fracture method of measuring G_f for concrete (and other quasi-brittle materials) is illustrated in figure C.1 for the case of a compact tension specimen (CTS) [78], [77]. The specimen is pulled apart by a force P until complete failure. The plane of failure, represented by the dashed line, is assumed to have a surface area equal to the cross sectional area of the specimen ligament A_c . A typical load P vs. load point displacement δ response of the structure is characterized by an increase of load up to a peak value followed by a gradual decrease in load. The softening observed in the response is due to localized deformation in the fracture process zone (FPZ) as discussed previously in section 2.1. The fracture energy is calculated from the P vs. δ response to be

$$G_f = \frac{1}{A_c} \int P d\delta \quad (\text{C.1.1})$$

Although G_f is considered to be a constant material property, experiments show a definite size dependence in the measurement of G_f for geometrically similar test

Appendix C. Preliminary Studies of Fracture Energy Size Effect Simulation

specimens [27], [77]. Test data displaying the size effect in G_f for concrete CTS is displayed in figure C.2. Figure C.1 displays the load vs. crack mouth opening displacement (CMOD) response for geometrically similar test specimens with varying ligament lengths b used to measure G_f . The fracture energy G_f vs. b plot reveals that G_f increases with an increasing value of b (size of sample) and may approach a constant value for sufficiently large b .

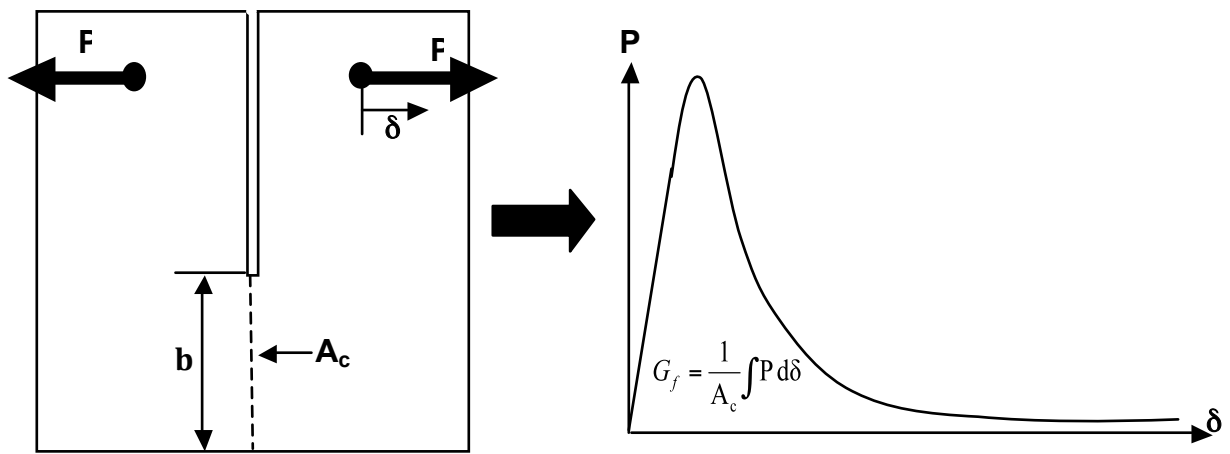


Figure C.1: Illustration of Work of Fracture Method for Measuring G_f

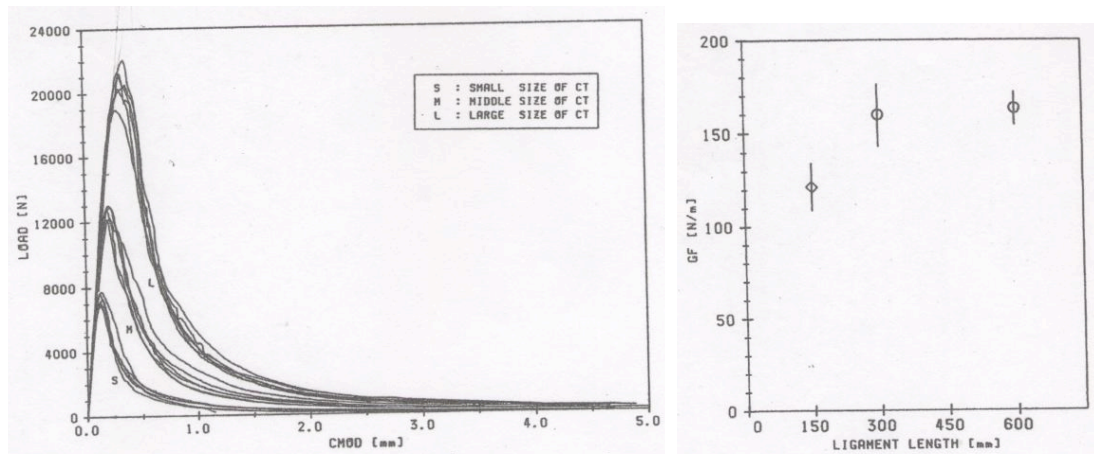


Figure C.2: Experimental Concrete Fracture Data Taken from Wittmann et. al. 1990 [77]

Appendix C. Preliminary Studies of Fracture Energy Size Effect Simulation

For the purposes of modeling material failure using a smeared crack approach, the heterogeneous material is treated as a homogeneous material. The homogeneous approximation is based on the assumption of a representative volume of the material over which material properties are averaged. For concrete the representative volume is on the order of the maximum aggregate size [9] and most concrete applications allow for a smeared analysis because the structural size is usually much greater than the representative volume. In this way macroscopic laboratory testing can be used to obtain material properties that can be applied to structural analysis (i.e. Youngs modulus, Poissons ratio, mass density, etc.). The fracture energy is inherently assumed to be an average material property that applies to the representative volume. So ideally, tension tests of an isolated representative volume would consistently yield a value of mode I G_f within some acceptable experimental error bound. This idealization is illustrated by the tensile test displayed in figure C.3 in two dimensions. However, these tests are not feasible, which has been shown by the problems encountered in direct tensile testing of concrete [54], including the difficulty in uniform loading of tension samples due to non-uniform deformation. For this reason, indirect tension tests such as three point bending of notched beams and compact tension tests have been elected for measuring G_f [48], [49], [78]. The problem with obtaining G_f from these methods is the size effect.

For the present research the fracture energy is still considered to be a constant material property that is applied through a discrete constitutive model. However, a distinction is made between the value of fracture energy measured by a work of fracture method G_f and the fracture energy value obtained by an idealized tension test G_f^* over the isolated representative volume (see figure C.3). The latter value is assumed to be a material property and is calculated to be

$$G_f^* = L \int \sigma d\varepsilon \tag{C.1.2}$$

Appendix C. Preliminary Studies of Fracture Energy Size Effect Simulation

where σ is a uniform tensile stress applied to the volume, ε is the corresponding strain component taken over a characteristic length L of the representative volume. It is important to note that L represents the width of the localization zone over which the cracking effect is smeared. It is automatically assumed that the representative volume encompasses the localization zone.

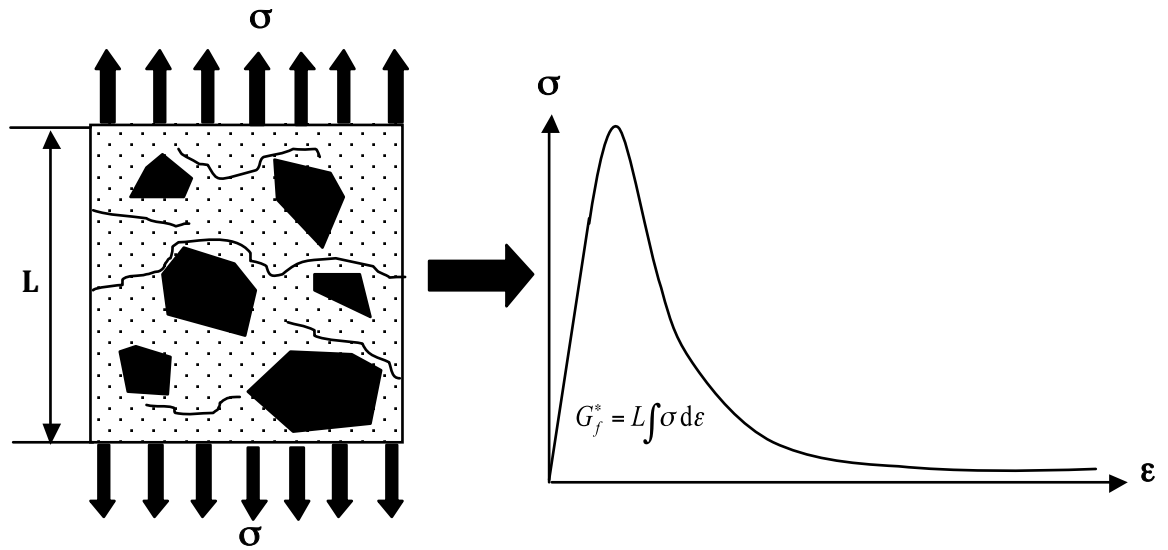


Figure C.3: Idealized tension test of a representative volume of inhomogeneous material to obtain mode I G_f^*

C.2 A Modification to the Classical Multiple Smeared Crack Approach

The smeared crack representation of the discrete constitutive model presented in section 3.5.3 is used for this study. The capability of the constitutive model algorithm to treat multiple smeared cracks at a material point is also utilized (see section 4.5). The commonly used multiple smeared crack representation of failure is referred to as the classical approach, and is described in detail by Rots [54]. The modified multiple smeared crack failure representation described in this section allows for additional energy dissipation mechanisms from failure of cracks over a material point that could simulate the size effect in G_f obtained from work of fracture tests. The associated algorithm requires only minimal modifications to the implementation of the classical approach.

Classical smeared crack approaches do not reproduce the size effect in G_f for simulations of work of fracture experiments. The simulations reproduce exactly the G_f value used in the discrete constitutive model as expected. Let i ($i = 1, 2, \dots$) denote the discrete crack index. The energy dissipated from the failure of a single crack is denoted as E_i^c . The value of G_f from a work of fracture simulation is computed to be

$$G_f = \frac{1}{A_c} \sum_i E_i^c \quad (\text{C.2.1})$$

In order to simulate the size effect, a different value of G_f must be used for a different size specimen. The inability to capture the size effect in simulation is due to specific assumptions of the classical multiple smeared crack model. A conceptually simple modification to this model is proposed to alleviate the shortcoming.

The key differences between the classical multiple smeared crack model and the modi-

Appendix C. Preliminary Studies of Fracture Energy Size Effect Simulation

fied approach utilized for this study are the assumptions regarding energy dissipation prior to failure. The failure of each crack i dissipates a certain amount of energy E_i^c . The classical model limits crack energy dissipation only to one crack over a representative volume (i.e. finite element) at any given point in the loading. The energy available for failure within a representative volume is limited as follows [54]:

$$\sum_i \frac{E_i^c}{A_i} \leq G_f \quad (\text{C.2.2})$$

Failure is associated with a representative volume (usually a finite element) for the case of equality in equation (C.2.2).

It is postulated that the classical multiple smeared crack model can not capture the size effect in G_f measured from work of fracture methods because it inadequately restricts the energy available for failure. The proposed modification does not restrict failure energy availability to a representative volume, but instead to an individual smeared crack i in the volume while multiple smeared crack orientations are allowed to develop at any given time. The energy availability modification is

$$\frac{E_i^c}{A_i} \leq G_f^* \quad (\text{C.2.3})$$

where failure is associated with an individual crack inside a representative volume. In general, equation (C.2.3) does not satisfy the classical failure criterion (equation (C.2.2)). The use of G_f^* rather than G_f in equation (C.2.3) should be noted.

The limitation of energy availability for classical multiple smeared crack models is partially based on experimental claims and partially based on computational convenience. It has been stated that experimental evidence shows that only the most recently initiated crack in a system of non-orthogonal cracks is active [54], [73]. Thus the classical model assumes development of only one crack at a time. However, this

Appendix C. Preliminary Studies of Fracture Energy Size Effect Simulation

choice is also motivated by the computational benefits of such an assumption. Only information for one crack needs to be stored and the history of the previously initiated cracks can be erased. The only necessary history to be tracked throughout the simulation is the accumulated energy dissipation from the cracks (a scalar quantity) because the failure criterion in equation (C.2.2) relies on this quantity. However, no physical basis is provided for the limitation of energy available before fracture in equation (C.2.2). The physical interpretation would be that of failure (supposedly for some orientation) of the entire representative volume occurs once a certain amount of energy is dissipated from crack formation in that volume. This effect is assumed to be independent of the number of cracks in the representative volume and their orientation.

The proposed modification to the multiple smeared crack model removes the energy availability restrictions. The physical interpretation of the revised failure criteria in equation (C.2.3) is that all cracks within a representative volume can develop simultaneously and independent of each other. The same amount of energy is available for the failure of each crack. In essence, the modified model represents the fracture process zone with several cohesive crack surfaces in a given representative volume rather than a single surface that may change orientation. Admittedly there is no physical basis for this assumption either, and to the authors knowledge there is no experimental data to support it. However, the approach does allow for an additional energy dissipation mechanism that may account for the size effect of G_f measured in work of fracture experiments. If the proposed method can be validated with actual size effect data for G_f , a physical basis for its use would be provided. The first goal of the research is to attempt this validation effort and determine whether or not the proposed approach can reproduce the size effect for G_f . Partial success has already been obtained in the preliminary analysis which is discussed in upcoming sections.

C.3 CTS problem Setup in MPM

The problem of interest is the simulation of the experimentally observed increase in fracture energy G_f with increase in size of concrete test specimen using the multiple smeared crack approach in MPM. The test sample geometry and dimensions are taken from the concrete CTS test series of Wittmann et al. [78]. Figure C.4 displays the CTS geometry for which the dimensions are specified in terms of the ligament length b . Small, medium, and large compact tension simulations are performed with ligament lengths of 15, 30, and 60 cm respectively.

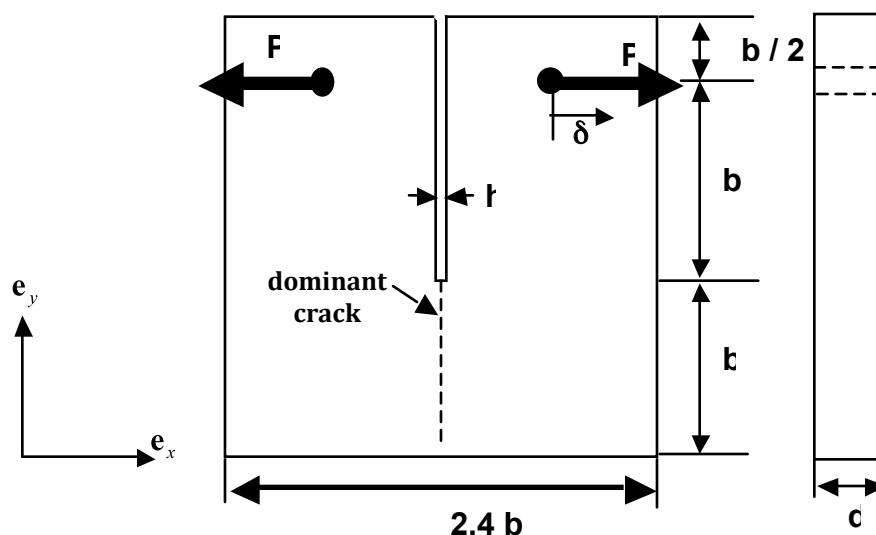


Figure C.4: Compact tension specimen geometry [78]

Figure C.5 displays an MPM configuration of the CTS for $b = 15 \text{ cm}$. The background finite element grid is composed of uniform four node square elements. The body is represented by the set of red material points. Initially four material points are placed uniformly inside each element. As a simplification, the notch width, h , is set equal to the side length of one element. The line of elements directly under the notch, outlined by a dashed box, are referred to as the notch line. Boundary condi-

Appendix C. Preliminary Studies of Fracture Energy Size Effect Simulation

tions are applied through rigid material points that have a prescribed velocity. The two rigid points, in green, are located at the midpoint of the CTS appendages and move at the same speed, v_L , in opposite directions in the \mathbf{e}_x direction. The values of the specimen dimensions and concrete material properties are listed in table C.1. All simulations performed are computed using explicit time integration of the discrete MPM equations ($\mu = 0$ in equation (4.2.20)). A low value of v_L is used in order to simulate a quasi-static loading condition.

Appendix C. Preliminary Studies of Fracture Energy Size Effect Simulation

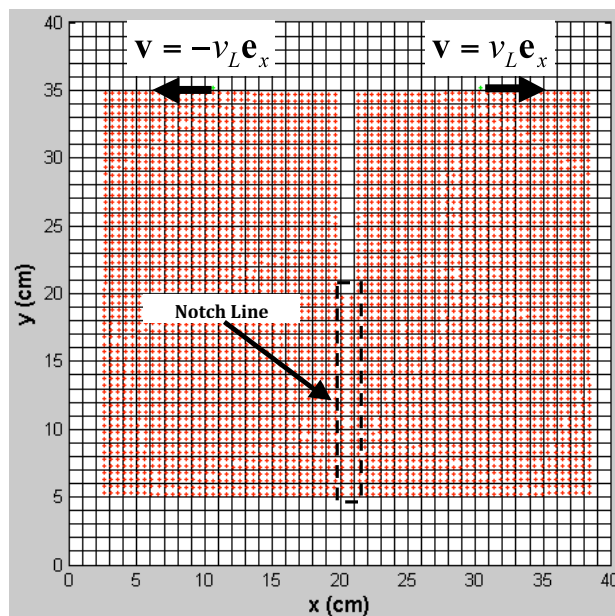


Figure C.5: MPM configuration of CTS for $b = 15 \text{ cm}$

Table C.1: Compact tension specimen problem data

problem data	Symbol	Value	Unit
mass density	ρ	2350	kg/m^3
Young's modulus	E	24.9	GPa
Poisson's ratio	ν	0.18	dimensionless
ultimate tensile strength	τ_{nf}	2.7	MPa
shear strength	τ_{sf}	14.9	MPa
shear strength for large mean pressure	τ_{sm}	90.0	MPa
compressive strength	f'_c	42.7	MPa
fracture energy	G_f	61.35	N/m
coupling parameter	C_n	0.2	dimensionless
coupling parameter	C_s	0.1	dimensionless
coupling parameter	C_ψ	5.0	dimensionless
ligament length	b	15, 30, 60	cm
notch width	h	element side length	cm
specimen depth	d	12	cm
load velocity	v_L	0.02	m/s
material points per cell	N/A	4	N/A

C.4 Simulation of the Ideal Failure of the CTS

The fracture energy computed from simulations of complete failure of the CTS is

$$G_f = \frac{E_f}{bd} \quad (\text{C.4.1})$$

where E_f is the total energy dissipated from crack opening upon complete failure of the CTS and bd is the CTS ligament area. The total crack opening energy of the body is the sum of the energy dissipated from all cracks as follows:

$$E_f = \sum_i E_i^c \quad (\text{C.4.2})$$

The computation of E_f for $i = 1$ is displayed in equation (5.2.40). The value of E_f is also considered to be composed of energy contributions from dominant cracks and non-dominant cracks as follows:

$$E_f = \underbrace{E_{fd}}_{\text{dominant crack}} + \underbrace{E_{fn}}_{\text{non-dominant crack}} \quad (\text{C.4.3})$$

Dominant crack surfaces are defined to be the set of failure surfaces over material points for which the surface traction reduces to zero. Non-dominant crack surfaces are defined as those failure surfaces for which failure is initiated but traction is not reduced to zero. The dominant and non-dominant crack energy contributions are denoted by E_{fd} and E_{fn} respectively in equation (C.4.3).

An ideal fracture test is conducted to ensure that the correct amount of crack opening energy is dissipated. The test is a simulation of a CTS experiment that idealizes failure as the single dominant crack surface as pictured in figure C.1 for which $\mathbf{n} = \mathbf{e}_x$.

Appendix C. Preliminary Studies of Fracture Energy Size Effect Simulation

Upon ideal failure the computed fracture energy G_f should be equal to the true fracture energy G_f^* that is used as a material property. Two restrictions are made for simulating the ideal failure case. First, the discrete constitutive model is applied only to the material points within the notch line elements (see figure C.5) and the remaining material points are considered to be elastic. Secondly, only two failure surfaces defined by normal vectors, $\mathbf{n}_1 = \mathbf{e}_x$ and $\mathbf{n}_2 = \mathbf{e}_y$, are permitted on material points within the notch elements.

Results for the $b = 15\text{ cm}$ case are displayed in figure C.6. The plots on the right of figure C.6 show various energy quantities throughout loading. For complete failure of the CTS, the expected energy dissipated by crack opening is displayed as the constant value $0.12(m) \times 0.15(m) \times 122.7(J/m^2) = 2.2J$. It is also observed that $E_f = E_{fd}$ and $E_{fn} = 0$. This result falls in line with physical interpretation of the ideal fracture in a compact tension test for which the CTS is split into two identical pieces. It is interpreted as complete failure on the dominant crack surfaces for $\mathbf{n}_1 = \mathbf{e}_x$ and no crack opening on the non-dominant surface $\mathbf{n}_2 = \mathbf{e}_y$. Consequently, as the CTS approaches complete failure, $E_f/(bd) \rightarrow G_f^*$. The implication is that $G_f = G_f^*$, the intended result of the ideal CTS failure experiment. The mechanical work, defined as the area under the P vs. δ curve, is also plotted. Note that $W > E_f$ throughout loading due to the additional components of elastic energy and kinetic energy. The energy dissipation behavior of the $b = 15\text{ cm}$ case is representative of the behavior observed for the $b = 30\text{ cm}$ and $b = 60\text{ cm}$ cases.

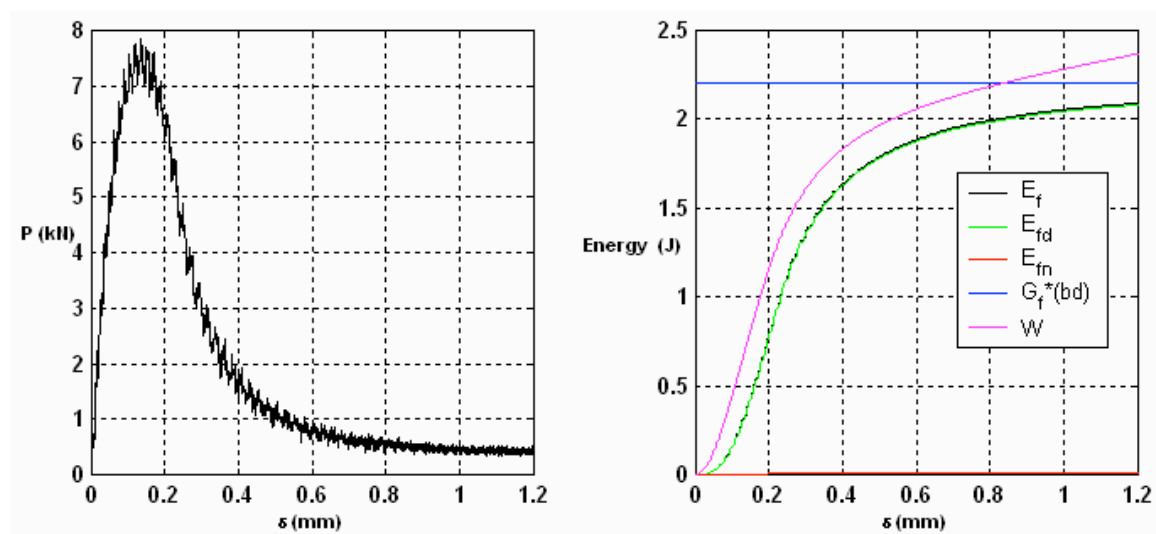


Figure C.6: Ideal CTS failure results for $b = 15 \text{ cm}$

C.5 Preliminary Results for Fracture Energy Size Effect Simulation

Compact tension test simulations of concrete specimens are performed using the multiple smeared crack method in MPM in an attempt to simulate the size effect trend observed in experimentally measured G_f . For all cases the multiple smeared crack model is applied only to material points within the notch line with a maximum of 20 failure orientations allowed over a material point. No predetermined failure surfaces are imposed.

Figures C.7 and C.8 display global responses for the ideal failure simulations and the multiple smeared crack fracture simulations respectively. All simulations are run nearly to failure but not completely failed. Although a maximum number of 20 failure planes were permitted over a given material point, it was observed that no more than 17 surfaces initiated over a given material point for any of the simulations.

Appendix C. Preliminary Studies of Fracture Energy Size Effect Simulation

The results shown in figures C.7 and C.8 correspond to the smallest mesh size used to simulate a given case. Since the notch length is always set equal to the side length of the element, h is also used to denote the side length of the square element.

A brief convergence study (not shown) was performed with a coarse mesh and fine mesh for each case. The respective coarse and fine mesh element sizes correspond to $h = 1\text{ cm}$ and $h = 0.5\text{ cm}$ for the $b = 15\text{ cm}$ case, $h = 2\text{ cm}$ and $h = 1\text{ cm}$ for the $b = 30\text{ cm}$ case and $h = 4\text{ cm}$ and $h = 2\text{ cm}$ for the $b = 60\text{ cm}$ case. The convergence studies incorporate increasingly larger values of h with increasing ligament lengths of the CTS in order to minimize overall computational time. Larger oscillations in the P vs δ response are associated with relatively larger values h . This effect is observed in the results in figures C.7-C.8 since the specimens with a larger value of b are associated with relatively larger value of h . In general, good agreement between coarse and fine mesh results were observed up to the point of the loading where the force drops down and begins to flatten out. At this point the force was observed to rise again for the coarse mesh simulations; an unphysical result which requires further investigation.

Appendix C. Preliminary Studies of Fracture Energy Size Effect Simulation

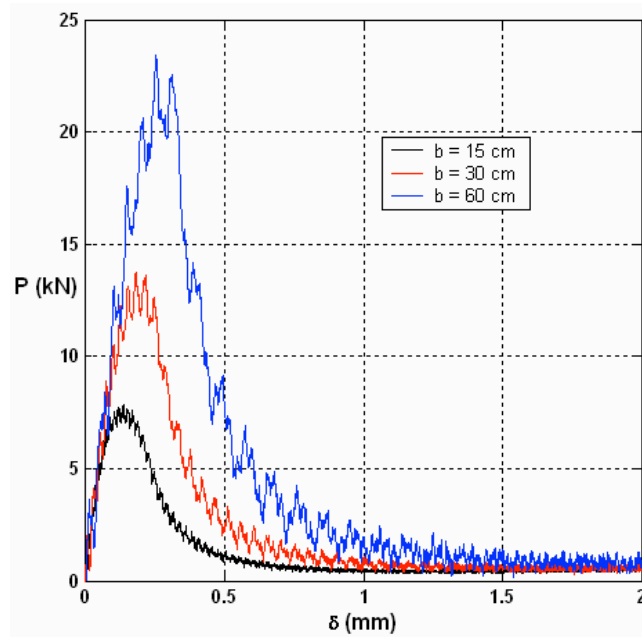


Figure C.7: P vs. δ response for the ideal CTS failure

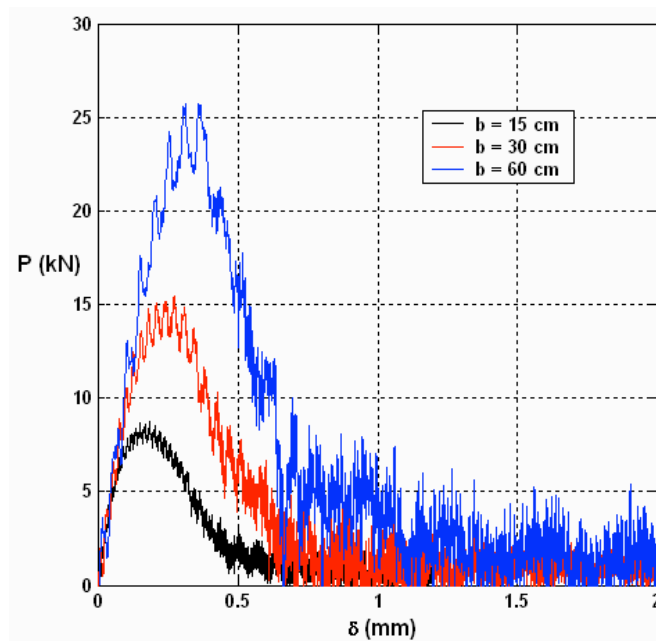


Figure C.8: P vs. δ response for CTS failure using multiple cracks

Appendix C. Preliminary Studies of Fracture Energy Size Effect Simulation

The calculated fracture energy results from the multiple smeared crack fracture simulations are displayed in table C.2. A simulated size effect trend is obtained. The second column contains the calculated fracture energy $G_f = E_f/(bd)$ which increases with increasing values of ligament length b (size). This increase in G_f with increasing b is accompanied by an increase in the percentage of total crack opening energy contribution from non-dominant cracks (column 5). One physical interpretation of this result is that the non-dominant cracks represent the effect of microcracks in the FPZ and that more microcracks form in the FPZ for bigger test samples. This interpretation falls in line with the theory that the size effect in occurs because the boundaries of sufficiently small test specimens inhibit full development of the FPZ [77], [56]. The larger the sample, the larger the FPZ, and therefore more microcracks are present and more energy is dissipated. It should also be noted that the quantity $E_{fd}/(bd)$ in column 3 approaches the value, $G_f^* = 122.7$, as the samples approach complete failure. This result represents the ideal fracture case.

It is clear from the results in table C.2 that use of the modified multiple smeared crack approach results in the correct size effect trend; the increase in G_f with increasing size b . These results demonstrate the potential of the failure simulation approach for predict the size effect in G_f . However, validation of this approach requires a successful comparison with experimental size effect data.

Table C.2: Results for G_f computed from simulations

b (cm)	$\frac{E_f}{(bd)}$ (J/m^2)	$\frac{E_{fd}}{(bd)}$ (J/m^2)	% $\frac{E_{fd}}{E_f}$	% $\frac{E_{nd}}{E_f}$
15	147	120	82	18
30	165	114	69	31
60	178	103	58	42

References

- [1] I. Babuska and J.M. Melenk. The partition of unity method. *International Journal for numerical Methods in Engineering*, 40:727–758, 1997.
- [2] S.G. Bardenhagen, J.E. Guilkey, K.M. Roessig, J.U. Brackbill, W.M. Witzel, and J.C. Foster. An improved contact algorithm for the material point method and application to stress propagation in granular material. *CMES*, 2:509–522, 2001.
- [3] Z.P. Bazant. Instability, ductility and size effect in strain-softening. *Journal of Engineering Mechanics*, 102:331–344, 1976.
- [4] Z.P. Bazant. Size effect in blunt fracture: concrete, rock, metal. *Journal of Engineering Mechanics*, 110:518–535, 1984.
- [5] Z.P. Bazant. Fracture mechanics of concrete. In *Mechanics of fracture and progressive cracking in concrete structures*, pages 1–85. Martinus Nijhoff Publishers, Dordrecht, 1985.
- [6] Z.P. Bazant. Determination of fracture energy from size effect and brittleness number. *Materials Journal*, 84(6):463–480, 1987.
- [7] Z.P. Bazant. Concrete fracture models: testing and practice. *Engineering Fracture Mechanics*, 69:165–205, 2002.
- [8] Z.P. Bazant and T.B. Belytschko. Wave propagation in a strain-softening bar: exact solution. *Journal of Engineering Mechanics*, 3(3):381–389, 1985.
- [9] Z.P. Bazant and B.H. Oh. Crack band theory for fracture of concrete. *RILEM Materials and Structures*, 16:155–177, 1983.
- [10] T. Belytschko, J. Fish, and E. Engelmann. A finite element with embedded localization zones. *Computer Methods in Applied Mechanics and Engineering*, 70:59–89, 1988.

References

- [11] D. Bigoni and T. Hueckel. Uniqueness and localization – i. associative and non-associative elastoplasticity. *Int. J. Solids Structures*, 28(2):197–213, 1991.
- [12] J.U. Brackbill and H.M. Ruppel. Flip: A method for adaptively zoned, particle-in-cell calculations of fluid flows in two dimensions. *J. Comput. Phys.*, 65:314–343, 1986.
- [13] I. Carol, P. Prat, and C.M. Lopez. A normal/shear cracking model. application to discrete crack analysis. *ASCE Journal of Engineering Mechanics*, 123(8):765–773, 2001.
- [14] L. Cedolin, S. Dei Poli, and L. Iori. Experimental determination of the fracture process zone in concrete. *Cement and Concrete Research*, 13:557–567, 1983.
- [15] E. Cosserat and F. Cosserat. *Theorie des Corps Deformable*. Hermann, Paris, 1909.
- [16] R. de Borst. *Computational aspects of smeared crack analysis. Constitutive Modeling of Concrete Structures*. Pinerage Press, Swansea, 1986.
- [17] R. de Borst. *Nonlinear analysis of frictional materials*. PhD thesis, Delft University of Technology, Delft, The Netherlands, 1986.
- [18] R. de Borst, M.A. Gutierrez, G.N. Wells, J..J.C. Remmers, and H. Askes. Cohesive-zone models, higher-order continuum theories and reliability methods for computational failure analysis. *Int. J. Numer. Meth. Engng*, 60:289–315, 2004.
- [19] R. de Borst and P. Nauta. Smeared crack analysis of reinforced concrete beams and slabs failing in shear. In F. Damjanic et al., editor, *Computer-Aided Analysis and Design of Concrete Structures*, pages 261–273. Pinerage Press, Swansea, United Kingdom, 1984.
- [20] R. de Borst and P. Nauta. Non-orthogonal cracks in a smeared finite element model. *Engineering Computations*, 2:35–46, 1985.
- [21] R. de Borst, L.J. Sluys, H.R. Muhlhaus, and J. Pamin. Fundamental issues in finite element analysis of localization of deformation. *Engineering Computations*, 10:99–122, 1993.
- [22] P.H. Evans and M.S. Marathe. Microcracking and stress-strain curves for concrete in tension. *Materials and Structures*, (1):61–64, 1968.
- [23] R.E. Goodman, R.L. Taylor, and T.L. Brekke. A model for the mechanics of jointed rock. *Journal of the Soil Mechanics and Foundations Division ASCE*, 94:637–695, 1968.

References

- [24] R. Hill. A general theory of uniqueness and stability in elastic-plastic solids. *Journal of the mechanics and Physics of Solids*, 6:236–249, 1958.
- [25] R. Hill. Acceleration waves in solids. *Journal of the mechanics and Physics of Solids*, 10:1–16, 1962.
- [26] A. Hillerborg. Numerical methods to simulate softening and fracture of concrete. In *Fracture Mechanics of Concrete*, pages 141–170. Martinus Nijhoff Publishers, Dordrecht,, 1985.
- [27] A. Hillerborg. Results of three comparative test series for determining the fracture energy of concrete. *Mater. Struct.*, 18(33-39), 1985.
- [28] A. Hillerborg, M. Modeer, and P.E. Petersson. Analysis of crack formation and crack growth in concrete by means of fracture mechanics and finite elements. *Cement and Concrete Research*, 6:773–782, 1976.
- [29] A.R. Ingraffea and V. Saouma. Numerical modeling of discrete crack propagation in reinforced and plain concrete. In *Fracture Mechanics of Concrete*, pages 171–225. Martinus Nijhoff Publishers, Dordrecht, 1985.
- [30] M. Jirasek. Comparative study on finite elements with embedded discontinuities. *Comput. Methods Appl. Mech. Engrg.*, 188:307–330, 2000.
- [31] M. Jirasek, S. Rolshoven, and P. Grassl. Size effect on fracture energy induced by non-locality. *International Journal for Numerical and Analytical Methods in Geomechanics*, 28:653–670, 2004.
- [32] C.D. Meyer. *Matrix Analysis and Applied Linear Algebra*. SIAM Philadelphia, PA, 2000.
- [33] S. Mindess and S. Diamond. A preliminary sem study of crack propagation in mortar. *Cement and Concrete Research*, 10:509–519, 1980.
- [34] N. Moes, J. Doblrow, and T. Belytschko. A finite element method for crack growth without remeshing. *International Journal for Numerical methods in engineering*, 46:131–150, 1999.
- [35] J. Mosler and G. Meschke. Embedded crack vs. smeared crack models: a comparison of elementwise discontinuous crack path approaches with emphasis on mesh bias. *Computer Methods in Applied Mechanics and Engineering*, 193:3351–3375, 2004.
- [36] M.K. Neilsen and H.L. Schreyer. Bifurcations in elastic-plastic materials. *Int. J. Solids Structures*, 30(4):521–544, 1993.

References

- [37] D. Ngo and A.C. Scordelis. Finite element analysis of reinforced concrete beams. *J. Am. Concrete Inst.*, 64(14):152–163, 1967.
- [38] J.A. Nrain. Material point method calculations with explicit cracks. *Computer Modeling in Engineering and Science*, 30(4):521–544, 2003.
- [39] J. Oliver. A consistent characteristic length for smeared cracking models. *International Journal for Numerical methods in engineering*, 28:431–474, 1989.
- [40] J. Oliver. Modeling strong discontinuities in solid mechanics via strain softening constitutive equations. part 1: fundamentals. *International Journal for Numerical methods in engineering*, 39:3575–3600, 1996.
- [41] J. Oliver. Modeling strong discontinuities in solid mechanics via strain softening constitutive equations. part 2: numerical simulation. *International Journal for Numerical methods in engineering*, 39:3601–3623, 1996.
- [42] J. Oliver, A.E. Huespe, and M.D.G. Pulido. *El metodo de las discontinuidades fuertes en deformaciones finitas, Metodos Numericos En Ingenieria V. SEMNI*, Espana, 2002.
- [43] J. Oliver, A.E. Huespe, M.D.G. Pulido, and E. Chaves. From continuum mechanics to fracture mechanics: the strong discontinuity approach. *Engineering Fracture Mechanics*, 69:113–136, 2002.
- [44] J. Oliver, A.E. Huespe, and E. Samaniego. A study on finite elements for capturing strong discontinuities. *International Journal for Numerical methods in engineering*, 56:2135–2161, 2003.
- [45] M. Ortiz and A. Pandolfi. Finite-deformation irreversible cohesive elements for three-dimensional crack-propagation analysis. *International Journal For Numerical Methods in Engineering*, 44:1267–1282, 1999.
- [46] N.S. Ottosen and K. Runesson. Properties of discontinuous bifurcation solutions in elasto-plasticity. *Int. J. Solids Structures*, 27(4):401–421, 1991.
- [47] K. Peterson. *Modeling arctic sea ice using the material-point method and a elastic-decohesive rheology*. PhD thesis, University of New Mexico, Albuquerque, New Mexico, U.S.A, 2008.
- [48] P.E. Petersson. Fracture energy of concrete; method of determination. *Cement and Concrete Research*, 10:78–89, 1980.
- [49] P.E. Petersson. Fracture energy of concrete; practical performance and experimental results. *Cement and Concrete Research*, 10:91–101, 1980.

References

- [50] H.E. Read and G.A. Hegemier. Strain softening of rock, soil and concrete – a review article. *Mech. of Mat.*, 3:271–294, 1984.
- [51] H.W. Reindhardt. Fracture mechanics of an elastic softening material like concrete. *HERON*, 29(2), 1984.
- [52] H.W. Reindhardt, Cornelissen H.A.W., and D.A. Hordijk. Tensile tests and failure analysis of concrete. *J. Struct. Engng.*, 112(11):2462–2477, 1986.
- [53] J.R. Rice. The localization of plastic deformation. In W.T. Koiter, editor, *Theoretical and Applied Mechanics*, pages 204–220. North Holland Publishing Company, Amsterdam, 1976.
- [54] J.G. Rots. *Smearred Computational modeling of concrete fracture*. PhD thesis, Delft University of Technology, Delft, The Netherlands, 1988.
- [55] J.G. Rots. Smearred and discrete representations of localized fracture. *International Journal of Fracture*, 51:45–59, 1991.
- [56] J.G. Rots, P. Nauta, G.M.A. Kusters, and J. Blaauwendraad. Smearred crack approach and fracture localization in concrete. *Heron*, 30(1):1–47, 1985.
- [57] J.W. Rudnicki and J.R. Rice. Conditions for the localization of deformation in pressure-sensitive dilatant materials. *J. Mech. Phys. Solids*, 23:371–394, 1975.
- [58] H.L. Schreyer. Modeling surface orientation and stress at failure of concrete and geological materials. *Journal For Numerical And Analytical Methods In Geomechanics*, 31:144–171, 2007.
- [59] H.L. Schreyer and Z. Chen. One-dimensional softening with localization. *J. Appl. Mech.*, 53:791–797, 1986.
- [60] H.L. Schreyer and M.K. Neilsen. Analytical and numerical tests for loss of material stability. *International Journal For Numerical Methods in Engineering*, 39:1721–1736, 1996.
- [61] H.L. Schreyer and M.K. Neilsen. Discontinuous bifurcation states for associated smooth plasticity and damage with isotropic elasticity. *Int. J. Solids Structures*, 33(20-22):3239–3256, 1996.
- [62] J.C. Simo and T.J.R Hughes. *Computational Inelasticity*. Springer-Verlag New York, Inc., 1998.
- [63] J.C. Simo, J. Oliver, and F. Armero. An analysis of strong discontinuities induced by strain-softening in rate-dependent inelastic solids. *Computational Mechanics*, 12:277–296, 1993.

References

- [64] J.C. Simo and S. Rifai. A class of mixed assumed strain methods and the methods of incompatible modes. *Int. J. Numer. Methods Eng.*, 29:1595–1638, 1990.
- [65] L.J. Sluys. *Wave propagation, localization and dispersion in softening solids*. PhD thesis, Delft University of Technology, Delft, The Netherlands, 1992.
- [66] D. Sulsky and A. Kaul. Implicit dynamics in the material-point method. *Comp. Meths. Appld. Mechs. Engrg.*, 139:1137–1170, 2004.
- [67] D.L Sulsky, Z. Chen, and H.L. Schreyer. A particle method for history-dependent materials. *Comput. Methods Appl. Mech.*, 118:179–196, 1994.
- [68] D.L. Sulsky and H.L. Schreyer. Axisymmetric form of the material point method with applications to upsetting and taylor impact problems. *Comput. Meths. Appld. Mechs. Engrg.*, 139:409–429, 1996.
- [69] D.L. Sulsky and H.L. Schreyer. Mpm simulation of dynamic material failure with a decohesion constitutive model. *European Journal of Mechanics A/Solids*, 23:423–445, 2004.
- [70] D.L. Sulsky, H.L. Schreyer, K. Peterson, M.D. Coon, and R. Kwok. Using the material-point method to model sea ice dynamics. *J. Geophys. Res.*, 112, 2007.
- [71] D.L Sulsky, S. Zhou, and H.L. Schreyer. Application of a particle-in-cell method to solid mechanics. *Comput. Phys.*, 87:236–252, 1995.
- [72] L.N. Trefethen and D. Bau III. *Numerical Linear Algebra*. SIAM Philadelphia, PA, 1997.
- [73] F.J. Vecchio and M.P. Collins. The modified compression-field theory for reinforced concrete elements subjected to shear. *J. Am. Concrete Inst.*, 83(2):219–231, 1986.
- [74] P.F. Walsh. Fracture of plain concrete. *The Indian Concrete Journal*, 46(11):469,470, and 476, 1979.
- [75] G.N. Wells. *Discontinuous modeling of strain localization and failure*. PhD thesis, Delft University of Technology, Delft, The Netherlands, 2001.
- [76] G.N. Wells and L.J. Sluys. A new method for modeling cohesive cracks using finite elements. *International Journal for Numerical Methods in Engineering*, 50:2667–2682, 2001.
- [77] F.H. Wittmann, H. Mihashi, and N. Nomura. Size effect on fracture energy of concrete. *Engineering Fracture Mechanics*, 35:107–115, 1990.

References

- [78] F.H. Wittmann, K. Rorugo, E. Bruhwiler, H. Mihashi, and P. Simain. Fracture energy and strain softening of concrete as determined by means of compact tension specimens. *Mater. Struct.*, 21:21–32, 1988.
- [79] Q. Zuo. *Bifurcation and stability analysis of elasto-plastic materials and elastic structures*. PhD thesis, University of New Mexico, Albuquerque, New Mexico, U.S.A, 1995.